

TURBULENT BOUNDARY-LAYER CONTROL WITH  
DBD PLASMA ACTUATORS USING SPANWISE  
TRAVELLING-WAVE TECHNIQUE

Richard D. Whalley, B.Eng.

THESIS SUBMITTED TO THE UNIVERSITY OF NOTTINGHAM FOR  
THE DEGREE OF DOCTOR OF PHILOSOPHY

July 2011

# Abstract

Turbulent boundary-layer control has been investigated experimentally using a low-speed wind tunnel at the University of Nottingham, with an overall aim of achieving skin-friction drag reduction. The important part of this investigation is to understand the mechanism of drag reduction and the associated changes in the structure of the turbulent boundary layer. It was demonstrated with Direct Numerical Simulations (DNSs) nearly a decade ago that by applying a spanwise travelling wave in the near-wall region of a turbulent wall flow can lead to a skin-friction drag reduction on the order of 30%. To date, spanwise travelling waves are predominantly created by a Lorentz force, limiting the study of this technique to water flows and numerical investigations. As an aeronautical application of this innovative flow control technique, an investigation into the use of Dielectric-Barrier-Discharge (DBD) plasma actuators to generate spanwise travelling waves in air has been conducted. DBD plasma actuators have received enormous interest over the past ten years within the flow control community due to their unique properties. DBD plasma actuators are completely electrical and ionize the nearby air to couple momentum to the surrounding flow. Hence, DBD plasma actuators require no moving parts, which makes their design simple and without the need for complicated ducting, holes or cavities. They are fast acting, of low power, low in weight, cheap to manufacture and can be fitted to existing airframes. As the body force that the DBD plasma actuator creates is at the wall, DBD plasma actuators are an ideal candidate for wall-based flow control techniques such as the spanwise travelling wave-technique. In this study, DBD

plasma actuators have been found to have the ability to greatly modify the near-wall region of the turbulent boundary layer with a potential to reduce skin-friction drag. The near-wall structures modified by the spanwise travelling waves were studied using the PIV technique, while the associated turbulence statistics were carefully documented using hot-wire anemometry. On initiation of DBD plasma in the turbulent boundary layer, streamwise vortices were generated. Spreading of low-speed fluid by the streamwise vortices that were travelling in the spanwise direction was observed, which seems to have greatly attenuated the turbulence production process. This is very much in line with the finding of DNS studies, where wide low-speed ribbons replaced the low-speed streaks.

# Acknowledgements

I am indebted to my supervisor, Professor Kwing-So Choi for his endless support, expertise and guidance during the course of this study; I continue to learn a lot from him. I would also like to thank my colleagues who have shared their wealth of experience. Thanks must go to Dr. Faycal Bahri, Dr. Peng Xu, Dr. Yong-Duck Kang and Dr. Timothy Jukes. I would like to extend my thanks to the technicians of L4—in particular to Andrew Matthews, David Smith and Paul Johns—who have provided an unlimited supply of help and knowledge on tasks both great and small.

I would like to thank my parents, grandparents and sisters who have always remained proud of me and provided me with unwavering support for so many years. Finally, I must thank Sarah for her unconditional love and support, especially whilst writing this thesis.

This work has been jointly funded by the European Physical Sciences Research Council and the EU 6<sup>th</sup> framework program—AVERT.

# Contents

<b>Abstract</b>	<b>i</b>
<b>Acknowledgements</b>	<b>iii</b>
<b>List of Tables</b>	<b>vii</b>
<b>List of Figures</b>	<b>viii</b>
<b>Nomenclature</b>	<b>xvii</b>
<b>1 Introduction</b>	<b>1</b>
1.1 Thesis Outline . . . . .	2
<b>2 Literature Review</b>	<b>4</b>
2.1 Turbulent Boundary Layers . . . . .	4
2.1.1 Near-wall Region . . . . .	5
2.1.2 Outer Region . . . . .	9
2.1.3 Hairpin Vortices and the Turbulence Regeneration Cycle .	11
2.2 Skin-friction Drag Reduction Techniques . . . . .	16
2.2.1 Overview . . . . .	18
2.2.2 Spanwise Travelling Waves . . . . .	20
2.3 Dielectric-Barrier-Discharge Plasma . . . . .	25
2.3.1 DBD Plasma Actuators . . . . .	25
2.3.2 Flow Control with DBD Plasma . . . . .	38

<b>3</b>	<b>Experimental Set-up</b>	<b>44</b>
3.1	Wind Tunnel . . . . .	44
3.2	Removable Test Plate . . . . .	45
3.3	Hot-wire Anemometry . . . . .	48
3.3.1	Hot-wire Probe Calibration . . . . .	52
3.3.2	Cold-wire Probe Calibration . . . . .	56
3.4	Traversing System . . . . .	56
3.5	Data Acquisition . . . . .	57
3.6	Flow Visualisation . . . . .	59
3.7	PIV System . . . . .	61
3.7.1	Seeding Mechanism for the Turbulent Boundary Layer . . . . .	64
3.7.2	2D PIV Measurements . . . . .	64
3.7.3	Stereoscopic PIV Measurements . . . . .	67
3.8	Spanwise Travelling-Wave Actuator Sheets . . . . .	72
3.9	Plasma Power Supply . . . . .	75
<b>4</b>	<b>Starting Vortex</b>	<b>79</b>
4.1	Kinematics and Dynamics of the Starting Vortex . . . . .	79
4.2	Chapter Summary . . . . .	110
<b>5</b>	<b>Spanwise Travelling Waves in Quiescent Air</b>	<b>112</b>
5.1	Travelling-Wave Actuator Sheets . . . . .	112
5.2	2D PIV Measurements of Spanwise Travelling Waves in Quiescent Air . . . . .	113
5.3	Chapter Summary . . . . .	133
<b>6</b>	<b>Hot-wire Anemometry Measurements of Spanwise Travelling Waves in the Turbulent Boundary Layer</b>	<b>136</b>
6.1	Canonical Turbulent Boundary layer . . . . .	137
6.2	Turbulent Boundary-Layer Measurements with Spanwise Travel- ling Waves . . . . .	143

6.2.1	Thermal Boundary-Layer Measurements . . . . .	146
6.2.2	Velocity Measurements . . . . .	158
6.2.2.1	Temperature Correction and Considerations . . . . .	158
6.2.2.2	Streamwise Velocity Measurements . . . . .	175
6.2.2.3	Energy Spectra and Probability Density Function . . . . .	182
6.2.2.4	Conditional Sampling - VITA Analysis . . . . .	186
6.3	Chapter Summary . . . . .	199
<b>7</b>	<b>PIV Measurements of Spanwise Travelling Waves in the Turbulent Boundary Layer</b>	<b>203</b>
7.1	Phase-averaged PIV Measurements . . . . .	204
7.2	Time- and Spanwise-averaged PIV Measurements . . . . .	250
7.3	Chapter Summary . . . . .	261
<b>8</b>	<b>Conclusions and Future Recommendations</b>	<b>262</b>
8.1	Conclusions . . . . .	262
8.2	Novel Outcomes . . . . .	265
8.3	Future Recommendations . . . . .	267
8.4	Publications . . . . .	269
	<b>Bibliography</b>	<b>271</b>

# List of Tables

2.1	Reynolds stress quadrants, adopted from Wallace <i>et al.</i> (1972) . . .	9
4.1	Experimental conditions studied. . . . .	82
4.2	Characteristic velocity scale and plasma force coefficient. . . . .	91
4.3	Scaling law fits . . . . .	97
5.1	Experimental conditions studied with spanwise travelling waves in quiescent air . . . . .	115

# List of Figures

2.1	Near-wall streaky structure, Kline <i>et al.</i> (1967) . . . . .	6
2.2	Multiple ejections, Corino and Brodkey (1969) . . . . .	7
2.3	Burst events, Blackwelder and Kaplan (1976) . . . . .	10
2.4	The turbulent boundary layer, Gad-el Hak and Bandyopadhyay (1994) . . . . .	11
2.5	Falco Eddies, Falco (1977) . . . . .	12
2.6	Conceptual model of sweeps/ejections, Robinson (1991) . . . . .	13
2.7	PIV in the turbulent boundary layer, Adrian <i>et al.</i> (2000) . . . . .	13
2.8	Schematic of a hairpin vortex, Adrian <i>et al.</i> (2000) . . . . .	14
2.9	Nested hairpins, Adrian <i>et al.</i> (2000) . . . . .	15
2.10	Hairpin packets, Zhou <i>et al.</i> (1999) . . . . .	17
2.11	Conceptual model of burst events, Choi (1989) . . . . .	18
2.12	Instantaneous flow visualisation of the near-wall region at $y^+ = 4$ , Du <i>et al.</i> (2002) . . . . .	23
2.13	Drag reduction as a function of $I, T^+$ and $\Delta$ , Du <i>et al.</i> (2002) . . . . .	23
2.14	DBD plasma actuator, Corke <i>et al.</i> (2010) . . . . .	26
2.15	Demonstration of the plasma body force, Roth and Sherman (1998)	27
2.16	V-I characteristics of a DC low pressure electrical discharge tube, Roth (1995) . . . . .	29
2.17	The regions of ionization in DBD plasma actuators, Corke <i>et al.</i> (2007) . . . . .	30
2.18	Discharge patterns, Gibalov and Pietsch (2000) . . . . .	31

2.19	Voltage and current waveforms for a DBD plasma actuator, Moreau (2007) . . . . .	32
2.20	Voltage and current from a DBD plasma actuator, Boeuf <i>et al.</i> (2007b) . . . . .	32
2.21	Phase-locked PIV, Kim <i>et al.</i> (2007) . . . . .	34
2.22	Scaling of velocity with applied voltage, Enloe <i>et al.</i> (2004b), Forte <i>et al.</i> (2006), Jukes <i>et al.</i> (2006a) . . . . .	36
2.23	A symmetric DBD plasma actuator, Jukes <i>et al.</i> (2008) . . . . .	37
2.24	Starting vortex with DBD plasma, Jukes <i>et al.</i> (2006a) . . . . .	38
2.25	Annular actuators, Santhanakrishnan and Jacob (2006a) . . . . .	39
2.26	Sliding discharge, Moreau <i>et al.</i> (2008) . . . . .	39
2.27	Aerofoil flow-separation control, Roth (2003) . . . . .	40
2.28	Flow-separation control of an aerofoil, Okita <i>et al.</i> (2008) . . . . .	41
2.29	Flow visualisation of spanwise wall oscillation with DBD plasma, Jukes (2007) . . . . .	42
3.1	Wind tunnel test facility . . . . .	46
3.2	Upper surface of the test section . . . . .	47
3.3	Trailing-edge flap . . . . .	47
3.4	Turbulent trip . . . . .	47
3.5	Details of the Perspex test plate for mounting plasma actuator sheets	49
3.6	Dantec CTA system with multiple plug in units enclosed in a copper Faraday cage . . . . .	50
3.7	Hot-wire anemometry probes and holder . . . . .	51
3.8	Mitigation of radiated electrical noise . . . . .	53
3.9	Optimisation of a hot-wire probe from a square wave test . . . . .	54
3.10	A picture demonstrating hot-wire calibration . . . . .	55
3.11	Hot-wire calibration curves . . . . .	55
3.12	Cold-wire calibration . . . . .	56
3.13	Energy spectra in a canonical turbulent boundary layer . . . . .	59

3.14	Calculation of the integral time scale . . . . .	60
3.15	Photron Fastcam SA-3 high-speed camera . . . . .	62
3.16	Copper vapour laser . . . . .	62
3.17	Experimental arrangement for quiescent air PIV . . . . .	63
3.18	Drawing of the seeder used in the PIV measurements of the turbulent boundary layer . . . . .	65
3.19	Picture of the seeder used in the PIV measurements of the turbulent boundary layer . . . . .	66
3.20	Experimental arrangement for the 2D PIV measurements . . . . .	67
3.21	Experimental arrangement for the stereoscopic PIV measurements . . . . .	68
3.22	PIV calibration target . . . . .	69
3.23	An example of PIV laser alignment . . . . .	69
3.24	Photron APX-RX high-speed camera and Scheimpflüg adapter . . . . .	69
3.25	Time-averaged mean velocity profile of the turbulent boundary layer . . . . .	70
3.26	Drawing of the travelling-wave actuator sheet . . . . .	74
3.27	Pictures of the travelling-wave actuator sheet . . . . .	74
3.28	Voltage and current waveforms of the high voltage plasma power supply . . . . .	76
4.1	Schematic representation of a DBD plasma actuator . . . . .	80
4.2	Laminar wall jet created by a DBD plasma actuator, Jukes <i>et al.</i> (2006a) . . . . .	81
4.3	Flow visualisation and PIV vorticity fields of the plasma induced starting vortex . . . . .	83
4.4	Flow visualisation around the vicinity of a DBD plasma actuator . . . . .	84
4.5	Flow visualisation of Kelvin-Helmholtz instability, Whalley and Choi (2010a) . . . . .	85
4.6	Comparison of PIV velocity fields . . . . .	86
4.7	Comparison of PIV vorticity fields . . . . .	87
4.8	Characteristic velocity scale for Case A . . . . .	89

4.9	Characteristic velocity scale for Case B and Case C . . . . .	89
4.10	Normalised velocity fields and vorticity fields at $t^* = 6000$ . . . . .	92
4.11	Normalised velocity fields and vorticity fields at $t^* = 8000$ . . . . .	93
4.12	Definition of spatial scales . . . . .	95
4.13	Vortex core scalings . . . . .	96
4.14	Momentum of the starting vortex . . . . .	99
4.15	Self-similarity of the starting vortex . . . . .	102
4.16	Self-similar structure of the starting vortex . . . . .	105
4.17	Circulation of the starting vortex . . . . .	106
4.18	Mechanism of the starting vortex . . . . .	109
5.1	Schematic representation of 4-phase spanwise travelling waves . . . . .	114
5.2	BNC signal generator for the travelling waves . . . . .	114
5.3	PIV of unidirectional travelling waves in quiescent air . . . . .	117
5.4	Spanwise velocity profile at $y = 5$ mm with unidirectional forcing, $T = 208$ ms . . . . .	119
5.5	Spanwise velocity profile at $y = 5$ mm with unidirectional forcing for $T = 124$ ms to $T = 208$ ms . . . . .	120
5.6	Generic two-bump forcing profile used by Du <i>et al.</i> (2002). . . . .	121
5.7	Spanwise velocity profiles through the vortex core with unidirec- tional forcing . . . . .	122
5.8	Breakdown of the spanwise travelling-wave excitations . . . . .	123
5.9	PIV of bidirectional travelling waves in quiescent air . . . . .	126
5.10	Spanwise velocity profile with bidirectional forcing, $T = 208$ ms . . . . .	128
5.11	Spanwise velocity profiles with unidirectional forcing, $T = 124$ ms to $T = 208$ ms . . . . .	129
5.12	Spanwise velocity profiles through the vortex core with bidirec- tional forcing . . . . .	130
5.13	Mechanism of the bidirectional travelling wave . . . . .	134

6.1	A picture showing a Dantec 55P15 boundary-layer type probe being traversed towards the wall . . . . .	138
6.2	Hot-wire measurement locations Z1 to Z4 . . . . .	138
6.3	Near-wall and streamwise velocity profiles of the boundary layer .	141
6.4	Mean streamwise velocity profiles at Z1 to Z4 of the boundary layer	142
6.5	Averaged streamwise and turbulence intensity velocity profiles of the boundary layer . . . . .	144
6.6	Averaged skewness and kurtosis profiles in the boundary layer . .	145
6.7	Temperature time-series at $y^+ = 5$ using exponential and error function fits . . . . .	149
6.8	Temperature time-series at $y^+ = 5$ using quadratic fits . . . . .	150
6.9	Temperature time-series at $y^+ = 5$ using linear and cubic function fits . . . . .	151
6.10	RMS temperature profiles throughout the boundary layer . . . . .	153
6.11	Mean temperature difference measurements, $\Delta T$ , in the boundary layer . . . . .	156
6.12	Non-dimensional thermal boundary-layer profile . . . . .	157
6.13	Temperature correction . . . . .	160
6.14	Effect of temperature compensation with different function fits . .	161
6.15	Velocity time-series showing the effect of thermal corrections . . .	162
6.16	Effects of the thermal boundary layer on the unidirectional forcing no-control data . . . . .	164
6.17	Effects of the thermal boundary layer on the bidirectional forcing no-control data . . . . .	165
6.18	Hot-wire measurement locations, Z1 to Z3, in relation to the $x$ - $z$ plane PIV data at $y^+ = 5$ . . . . .	166
6.19	Thermal effects in the near-wall region . . . . .	169
6.20	Hot-wire geometry and heat balance for an incremental element, Bruun (1995) . . . . .	171

6.21	Streamwise velocity profiles with travelling waves . . . . .	176
6.22	Averaged streamwise and turbulence intensity profiles with travelling waves . . . . .	178
6.23	Mean streamwise velocity profile with spanwise oscillation . . . . .	180
6.24	Comparison of turbulence intensity profiles . . . . .	181
6.25	Averaged skewness and kurtosis profiles with travelling waves . . . . .	183
6.26	Energy spectra through the boundary layer with travelling waves . . . . .	185
6.27	Time-series and corresponding PDF at $y^+ = 5$ with travelling waves . . . . .	187
6.28	Time-series and corresponding PDF at $y^+ = 10$ with travelling waves . . . . .	188
6.29	Time-series and corresponding PDF at $y^+ = 30$ with travelling waves . . . . .	189
6.30	Time-series and corresponding PDF at $y^+ = 60$ with travelling waves . . . . .	190
6.31	No-control data VITA detection at $y^+ = 5$ . . . . .	193
6.32	No-control data VITA events and ensemble average at $y^+ = 5$ . . . . .	194
6.33	Unidirectional VITA detection at $y^+ = 5$ . . . . .	194
6.34	Unidirectional VITA events and ensemble average at $y^+ = 5$ . . . . .	195
6.35	Ensemble-averaged VITA events with travelling waves . . . . .	198
6.36	An example of VITA for sweep events with an oscillating wall, Choi and Clayton (2001) . . . . .	199
6.37	Frequency of sweep events as a function of threshold $k$ with travelling waves . . . . .	200
7.1	A comparison of instantaneous canonical flow and unidirectional forcing at $\frac{1}{2}T^+$ in the $x-z$ plane . . . . .	206
7.2	A comparison of data in the $z-y$ and $x-z$ planes at $\frac{1}{2}T^+$ with unidirectional forcing . . . . .	209
7.3	A comparison of instantaneous canonical flow and unidirectional forcing at $\frac{1}{2}T^+$ in the $x-z$ plane . . . . .	211

7.4	A comparison of data in the $z$ - $y$ and $x$ - $z$ planes with bidirectional forcing at $\frac{3}{4}T^+$ . . . . .	214
7.5	Visualisations of a controlled turbulent wall flow with a travelling wave, Karniadakis and Choi (2003) . . . . .	216
7.6	Streamwise and spanwise velocity and a representation of the skin-friction field . . . . .	218
7.7	Instantaneous skin-friction field, Zhao <i>et al.</i> (2004) . . . . .	218
7.8	Phase-averaged streamwise velocity, spanwise velocity and wall-normal vorticity in the $x$ - $z$ plane with unidirectional forcing . . .	221
7.9	Phase-averaged streamwise velocity, spanwise velocity and wall-normal vorticity in the $x$ - $z$ plane with unidirectional forcing through phase (ii) . . . . .	222
7.10	Phase-averaged streamwise velocity, spanwise velocity and wall-normal vorticity in the $x$ - $z$ plane with bidirectional forcing . . . .	224
7.11	Phase-averaged streamwise velocity, spanwise velocity and wall-normal vorticity in the $x$ - $z$ plane with bidirectional forcing through phase (iii) . . . . .	225
7.12	Spanwise velocity profiles with unidirectional forcing at $y^+ = 5$ . .	229
7.13	Spanwise velocity profiles with bidirectional forcing at $y^+ = 5$ . .	230
7.14	Phase-averaged streamwise vorticity in the $z$ - $y$ plane with unidirectional forcing through phase (ii) . . . . .	235
7.15	Phase-averaged streamwise vorticity in the $z$ - $y$ plane with bidirectional forcing through phase (ii) . . . . .	236
7.16	Phase-averaged streamwise velocity and vorticity in the $x$ - $z$ plane with unidirectional forcing . . . . .	239
7.17	Phase-averaged streamwise velocity and vorticity in the $x$ - $z$ plane with bidirectional forcing . . . . .	239
7.18	Phase-averaged wall-normal velocity and streamwise vorticity in the $z$ - $y$ plane with unidirectional forcing . . . . .	241

7.19	Phase-averaged wall-normal velocity and streamwise vorticity in the $z$ - $y$ plane with bidirectional forcing . . . . .	242
7.20	Phase-averaged spanwise velocity and streamwise vorticity in the $z$ - $y$ plane with unidirectional forcing . . . . .	243
7.21	Phase-averaged spanwise velocity and streamwise vorticity in the $z$ - $y$ plane with bidirectional forcing . . . . .	243
7.22	Phase-averaged $-\langle uw^+ \rangle$ Reynolds stress, streamwise velocity fluctuation and streamwise vorticity in the $z$ - $y$ plane with unidirectional forcing . . . . .	245
7.23	Phase-averaged $-\langle uw^+ \rangle$ Reynolds stress, streamwise velocity fluctuation and streamwise vorticity in the $z$ - $y$ plane through with bidirectional forcing . . . . .	246
7.24	Phase-averaged $-\langle vw^+ \rangle$ Reynolds stress, spanwise velocity fluctuation and streamwise vorticity in the $z$ - $y$ plane with unidirectional forcing . . . . .	247
7.25	Phase-averaged $-\langle vw^+ \rangle$ Reynolds stress, spanwise velocity fluctuation and streamwise vorticity in the $z$ - $y$ plane with bidirectional forcing . . . . .	247
7.26	Phase-averaged $-\langle uv^+ \rangle$ Reynolds stress, streamwise velocity fluctuation and streamwise vorticity in the $z$ - $y$ plane with unidirectional forcing . . . . .	248
7.27	Phase-averaged $-\langle uv^+ \rangle$ Reynolds stress, streamwise velocity fluctuation and streamwise vorticity in the $z$ - $y$ plane with bidirectional forcing . . . . .	249
7.28	A comparison of time-averaged data in the $z$ - $y$ and $x$ - $z$ planes with uni and bidirectional forcing . . . . .	252
7.29	Spanwise-averaged data of Figure 7.28 showing streamwise vorticity, velocity and wall-normal velocity . . . . .	255

7.30	A comparison of time-averaged Reynolds stress in the $z$ - $y$ plane with uni and bidirectional forcing . . . . .	256
7.31	Spanwise-averaged data of Figure 7.28 showing $-\langle \overline{uv}^+ \rangle$ , $-\langle \overline{vw}^+ \rangle$ and $-\langle \overline{uw}^+ \rangle$ Reynolds stress. . . . .	259

# Nomenclature

$a$	polynomial coefficient
$A_w$	area of a hot wire
$b$	polynomial coefficient
$c$	wave speed; polynomial coefficient
$C_f$	skin-friction coefficient
$C_p$	plasma force coefficient
$d$	polynomial coefficient
$d_\tau$	diameter of a PIV seeding particle
$d_p$	diameter of a CCD camera pixel
$D$	detector function
$E$	voltage
$f$	frequency
$f_c$	cut-off frequency
$F$	force
$h$	turbulent trip height
$H$	shape factor $\frac{\delta^*}{\theta}$
$I$	travelling-wave amplitude; impulse
$K$	Kurtosis
$k$	VITA threshold
$k_w$	thermal conductivity
$L$	length scale for $C_p$
$l$	length of a hot wire

$l_c$	hot wire cold-length
$M$	force-amplitude parameter; momentum
$n$	exponent for Cantwell's analysis
$N$	number of independent samples
$P$	power
$q$	constant
$\dot{Q}_e$	total heat transfer
$\dot{Q}_c$	heat transfer due to conduction
$\dot{Q}_{cp}$	heat transfer to the hot-wire prongs
$\dot{Q}_r$	heat transfer due to radiation
$\dot{Q}_{fc}$	heat transfer due to forced convection
$\dot{Q}_s$	heat transfer due to heat storage
$R_{uu}$	auto-correlation function
$Re_x = \frac{U_\infty x}{\nu}$	Reynolds number based on streamwise distance
$Re_\theta = \frac{U_\infty \theta}{\nu}$	Reynolds number based on momentum thickness
$Re_\tau = \frac{u_\tau \delta}{\nu}$	Reynolds number based on friction velocity
$Re_h = \frac{hU_\infty}{\nu}$	Reynolds number based on trip height
$S$	Skewness
$s$	distance between opposing electrodes
$t$	time
$t_{AC}$	period of plasma waveform
$T$	temperature; period of travelling wave; plasma duration
$T_a$	ambient temperature
$T_{ens}$	ensembling window length
$T_i$	integral time scale
$T_s$	sampling time
$T_w$	window length
$u_\tau$	friction velocity
$U$	streamwise velocity

$U_m$	maximum velocity scale (starting vortex)
$U_{max}$	maximum velocity
$V$	wall-normal velocity
$W$	spanwise velocity
$Z_{\frac{\alpha}{2}}$	Gaussian probability density
$x$	streamwise distance
$X_c$	vortex core $x$ -location
$Y_c$	vortex core $y$ -location
$y$	wall-normal distance
$z$	spanwise distance
$\lambda$	wavelength of the travelling wave
$\rho$	density
$\rho_{uu}$	auto-correlation coefficient of $u$
$\tau$	auto-correlation time-scale
$\delta$	boundary-layer thickness
$\delta^*$	displacement thickness
$\theta$	momentum thickness
$\nu$	kinematic viscosity
$\mu$	dynamic viscosity
$\Delta$	travelling-wave penetration depth
$\Delta_c$	thermal boundary-layer thickness with no-control
$\Delta_p$	thermal boundary-layer thickness with control
$\sigma$	standard deviation
$\alpha$	polynomial coefficient
$\beta$	polynomial coefficient
$\varepsilon$	dielectric constant
$\omega$	vorticity
$\Gamma$	circulation
$\kappa$	constant

$\xi$	spatial scale, starting vortex
$\eta$	spatial scale, starting vortex
Parenthesis	
$\langle u \rangle$	phase-averaged or spanwise-averaged
Superscripts	
+	indicates viscous scaling or inner scaling of viscous time, length and velocity, $t^+ = \frac{tu_\tau^2}{\nu}$ , $y^+ = \frac{yu_\tau}{\nu}$ , $u^+ = \frac{u}{u_\tau}$
*	indicates starting vortex scaling, $t^* = \frac{tu_m^2}{\nu}$
$\bar{U}$	mean velocity
' (prime)	RMS value
$\hat{u}$	local mean value; Cantwell's scaling
$\hat{\bar{u}}$	true mean value
Subscripts	
$\infty$	free-stream condition
0	at the wall
$x$	indicates in the $x$ -direction (streamwise)
$y$	indicated in the $y$ -direction (wall-normal direction)
$z$	indicates in the $z$ -direction (spanwise direction)
Prefixes	
$B(u)$	probability density function of $u$
$\Delta$	indicates a change in quantity
Var	indicates variance
$\sigma [u]$	uncertainty in $u$

# Chapter 1

## Introduction

Turbulent boundary layers can be found in many industrial situations, from the flow over aircraft or hydrodynamic vehicles to the transportation of oil within pipelines. Turbulent boundary layers in engineering applications are somewhat unavoidable, with Reynolds numbers being sufficiently high for the flow to be in a turbulent regime. Over 50% of the total drag on a long-haul commercial aircraft is due to turbulent skin friction. Therefore, the flow control techniques to reduce turbulent skin-friction drag are important for the aeronautical industry. Huge benefits in costs and pollution can be gained if we can obtain just a small percentage in drag reduction. The Advisory Council for Aeronautics Research in Europe (ACARE) proposed significant reductions in airframe drag, engine CO<sub>2</sub>, and a “pro-green” aircraft (ACARE, 2004). They have set targets for air transport systems which include a 50% reduction in CO<sub>2</sub> and noise, and an 80% reduction in NO<sub>x</sub> by 2020. Optimised aerodynamic performance through lower skin friction is one way to achieve these targets. This would conserve fossil fuels, produce less pollution in the atmosphere and offer economic benefits to commercial airlines and airframe manufacturers.

The spanwise travelling-wave technique is one of the techniques that is capable of achieving high amounts of drag reduction. Spanwise travelling waves have been studied both numerically and experimentally using Lorentz forcing and

have obtained up to a 30% reduction in turbulent skin-friction drag. Similar to Lorentz forcing, Dielectric-Barrier-Discharge (DBD) plasma is a surface based technique, which makes it an ideal candidate for travelling-wave excitation in the turbulent boundary layer. However, Lorentz forcing and plasma forcing are fundamentally different; plasma forcing is applicable to airflows whereas Lorentz forcing is limited to a conducting medium. Lorentz forcing has a maximum force at the wall which decays exponentially. By contrast, on initiation of DBD plasma starting vortices are created which eventually lead to the creation of a laminar wall jet. DBD plasma actuators are a very novel actuator type, having simple geometries, no moving parts and are completely electrical. They have very fast response times, can adhere to existing airframes and have the ability to create a flow and modify existing flows around aerodynamic bodies.

## 1.1 Thesis Outline

Chapter 2 provides an overview of DBD plasma actuators, turbulent boundary layers, skin-friction drag reduction mechanisms and details the existing literature on the spanwise travelling-wave technique. In §2.1.1, coherent motions present in the near-wall region of the turbulent boundary layer will be introduced and explained. In §2.1.2, the outer region of the turbulent boundary will be introduced and in §2.1.3, hairpin vortices and some of the proposed mechanisms for the self-sustaining nature of wall-bounded turbulence will be introduced and explained. In §2.2.1, an overview of skin-friction drag reduction techniques will be presented with emphasis on the skin-friction drag reduction mechanisms. This section documents passive flow-control devices, such as riblets, compliant coatings and Large-Eddy-Break-Up devices (LEBU) and active flow-control devices, such as spanwise wall oscillation, local blowing and suction and Micro-Electro-Mechanical-Systems (MEMS) technology. In §2.2.2, the available literature on the spanwise travelling-wave technique will be presented and the proposed mech-

anisms of skin-friction reduction introduced. In §2.3.1, the working principle of the DBD plasma actuator will be presented along with different DBD plasma actuator configurations. In §2.3.2, flow control using DBD plasma will be presented, with illustrations of flow-separation control over an aerofoil and turbulent boundary-layer control using spanwise wall-oscillation technique. Further references will be cited for bluff body flow-separation control, noise attenuation and the control of laminar to turbulent transition. In Chapter 3, the experimental testing facility used for the present study will be presented along with the experimental equipment, techniques and data analysis procedures. In Chapter 4, a single DBD plasma actuator is applied in quiescent air and the effects are studied using flow visualisation and Particle Image Velocimetry (PIV). It will be shown that on application of DBD plasma in quiescent air, a starting vortex is created, which will be shown to scale in a self-similar fashion. DBD plasma actuator arrays are developed in Chapter 5 to generate spanwise travelling waves, which are initially studied in quiescent air using PIV. In this chapter, two different forcing configurations will be developed—uni and bidirectional forcing—and the mechanisms of the spanwise travelling-wave excitations will be presented and discussed. In Chapters 6 and 7, the spanwise travelling-wave actuator arrays that have been developed in Chapter 5 are applied to the turbulent boundary layer and the changes in turbulent boundary-layer structure are studied using hot-wire anemometry and PIV. It will be shown that the turbulent boundary-layer structure can be modified up to  $y^+ = 200$ , with significant changes in structure observed in the near-wall region of the boundary layer. In Chapter 8, the key conclusions that have been documented throughout the thesis will be given, along with some suggestions for future work.

# Chapter 2

## Literature Review

In this chapter, a literature review will be presented covering the themes of the turbulent boundary layer and Dielectric-Barrier-Discharge (DBD) plasma. It is intended to be an introduction and provide the reader with sufficient understanding to supplement the discussions detailed within the thesis. An overview of the turbulent boundary layer will be given in §2.1 followed by some examples in §2.2 of how the turbulent boundary layer can be controlled to achieve skin-friction drag reduction. DBD plasma will be introduced in §2.3 with an emphasis on DBD plasma actuators with some examples of flow control with DBD plasma illustrated in §2.3.2.

### 2.1 Turbulent Boundary Layers

Despite decades of research, there is still an on-going debate over the self-sustaining mechanism of wall turbulence (Jiménez and Pinelli, 1999; Bernard *et al.*, 1993; Chernyshenko and Baig, 2005; Adrian, 2007). However, it is well accepted that the turbulent boundary comprises “coherent motions” with the roll of near-wall turbulence events —such as the sweeps and ejections— being undeniable in the production of turbulence. Robinson (1991) defines a “coherent motion” as:

a three dimensional region of the flow over which at least one fundamental flow variable (velocity component, density, temperature

etc.) exhibits significant correlation with itself or with another variable over a range of space and/or time that is significantly larger than the smallest scales of the flow.

If we are to achieve successful turbulent boundary-layer control, it is of great importance for us to understand the coherent motions within the turbulent boundary layer. It is these motions that we must target for elimination.

### 2.1.1 Near-wall Region

The near-wall region of the turbulent boundary layer was studied by Kline *et al.* (1967) and found to have a very distinctive structure. Figure 2.1 shows a photograph taken from Kline *et al.* (1967) of a plane parallel to the wall at a wall-normal distance of  $y^+ = \frac{yu_\tau}{\nu} = 4.5$  ( $u_\tau$  is the friction velocity and  $\nu$  is the kinematic viscosity). The boundary-layer flow is moving from top to bottom and the hydrogen bubble technique was used for visualisation. It can be seen that there is a streaky structure apparent in the flow with the collections of hydrogen bubbles being low-speed fluid. This observation led Kline *et al.* (1967) to remark that the viscous sublayer was not as two-dimensional as first thought and instead contained unsteady three-dimensional motions. The streaky structure was found to persist up to  $y^+ \approx 50$  and had a characteristic spanwise spacing of  $z^+ = 100$ . Kline *et al.* (1967) observed that the low-speed streaks meandered through the flow and lifted up away from the surface with growing oscillation to  $y^+ \approx 8 - 12$ . After which, the oscillation amplified and typically between  $10 < y^+ < 30$ , the low-speed streak terminated with the expulsion of low-speed fluid into the outer region of the boundary layer. It had previously been shown by Klebanoff (1954), that the majority of the turbulence energy production occurred in the buffer region. Kline *et al.* (1967) pointed out that the ejection of low-speed fluid into the outer region of the boundary layer could play an important role in determining the entire structure of the turbulent boundary layer and in particular could dominate the energy transfer processes between the inner and outer regions.

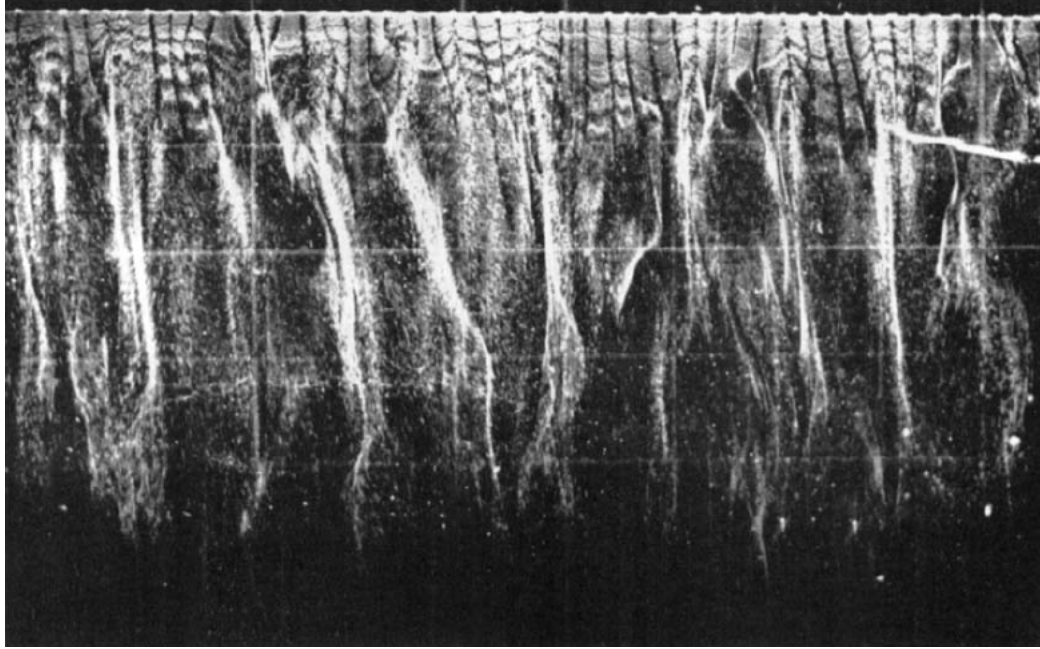


Figure 2.1: Near-wall streaky structure of the turbulent boundary layer at  $y^+ = 4.5$ . The boundary-layer flow is from top to bottom and is visualised using the hydrogen bubble technique. Taken from Kline *et al.* (1967).

Corino and Brodkey (1969) performed high-speed visualisations of a pipe flow that was seeded with markers, in essence a qualitative version of Particle Image Velocimetry (PIV). They found similar findings to Kline *et al.* (1967), however, an important addition was made; this was the notion of a sweep. They concluded a sequence of events that repeated itself in the near-wall region. This began with the observation of a decelerated region, Figure 2.2. The decelerated region spread over a large extent of the wall and was flanked by a region of high-speed fluid. The high-speed fluid accelerated the decelerated region and caused the ejection of low-speed fluid from the decelerated region. It was noted that at times, several ejections could occur from the same decelerated region. After the ejections, high-speed fluid which was moving either parallel or towards the wall would sweep the low-speed region out of the near-wall region. This sequence was then repeated. Corino and Brodkey (1969) stated that the events occurred as described, although there were variations of this sequence. They recognised the importance of the ejection events and estimated that they contributed to 70% of the total production of the Reynolds stress in the near-wall region. The

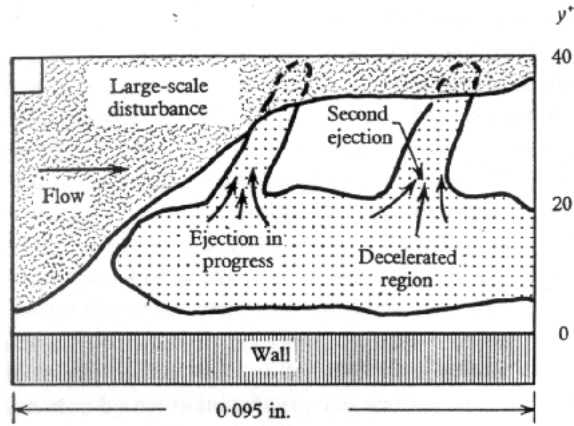


Figure 2.2: Observation of multiple ejections. Taken from Corino and Brodkey (1969).

remaining 30% was put down to the sweeping motion that occurred after the ejection of the low-speed fluid.

Kim *et al.* (1971) studied the near-wall region of a low-speed water flow using a combined approach of hot-wire anemometry and dye injection along with the hydrogen bubble technique. They observed that the near-wall region consisted of low- and high-speed velocity, hence appearing to have the streaky structure as found by Kline *et al.* (1967). They found similar results to Corino and Brodkey (1969) and made an attempt to describe the near-wall events with three stages, (i) to (iii). Stage (i) was the observation of the low-speed streak that was lifted away from the wall, stage (ii) was the oscillation of the low-speed streak which lead to stage (iii) the break-up of the low-speed streak into a chaotic motion. They termed the three stages a “burst” and they found that the majority of the turbulence production occurred at  $y^+ < 100$  during this bursting process.

Offen and Kline (1975) proposed that the inrush of high-speed fluid into the wall (similar to the sweep event) initiated the lift-up of the low-speed streak in the near-wall region. The low-speed streak would, as described by Kim *et al.* (1971), move upwards away from the wall and break-up due to instability, which would be followed by another inrush of high-speed fluid, which forms the beginning of the new low-speed streak. The ejection leads to a sweep which leads to an ejection and the cycle is repeated to form the complete bursting cycle. Hence, Offen and

Kline (1975) were the first researchers who proposed the major elements of a regenerative cycle of near-wall turbulence.

At the same time as the flow visualisation studies, more quantitative measurements of the turbulent boundary layer were taking place using hot-wire anemometry. Wallace *et al.* (1972) used a cross-wire to measure the  $u$  and  $v$  components of velocity in a fully developed channel flow and conditionally analysed the signals to calculate the  $-uv$  Reynolds stresses over the four possible combinations of  $u$  and  $v$ . These combinations are shown in Table 2.1, with the quadrant notations, Q1 to Q4, introduced by Lu and Willmarth (1973). Wallace *et al.* (1972) were able to show that at  $y^+ = 15$  the Q2 and Q4 events (ejections and sweeps) accounted for 140% of the total Reynolds stress in the boundary layer, with each event having an equal contribution of 70% to the Reynolds stress. This was slightly different than the observation of Corino and Brodkey (1969) who found that the ejection events contributed to 70% of the total Reynolds stress and the sweep events for the remaining 30%. Wallace *et al.* (1972) pointed out that this discrepancy was due to the negative contribution to the total Reynolds stress from the Q1 and Q3 events. Using the hydrogen bubble technique, Grass (1971) found similar observations to Corino and Brodkey (1969) and also to the measurements of Wallace *et al.* (1972), concluding that the Reynolds stress contributions for the ejection and sweep-type motions were of the same order for  $y^+ < 60$ . Wallace *et al.* (1972) also noted that although the sweep and ejection events offered equal weighting to the total measured Reynolds stress at  $y^+ = 15$ , the sweep events dominated the total Reynolds stress for  $y^+ < 15$  and the ejection events dominated for  $y^+ > 15$ . Willmarth and Lu (1972) and Lu and Willmarth (1973) also carried out measurements over the four Reynolds stress quadrants. They concluded that the Q2 events (ejections) contributed 77% to the Reynolds stress and the Q4 events (sweeps) contributed to 55% over the majority of the boundary layer which was in agreement with other studies (Corino and Brodkey, 1969; Grass, 1971). However, this conflicted with the study of Wallace *et al.*

Table 2.1: Reynolds stress contributions adopted from Wallace *et al.* (1972) (quadrant numbering of Lu and Willmarth (1973) added).

Quadrant	Sign of $u$	Sign of $v$	Sign of $-uv$	Type of motion
Q1	+	+	-	Interaction (outward)
Q2	-	+	+	Ejection
Q3	-	-	-	Interaction (wallward)
Q4	+	-	+	Sweep

(1972), who had found larger proportion of sweep events over ejection events for  $y^+ < 15$ . Lu and Willmarth (1973) attributed this to the different experimental test facilities that had been used, with Wallace *et al.* (1972) having used an open water channel flow and the other measurements being taken in boundary-layer flows.

Blackwelder and Kaplan (1976) brought a new approach to looking at the structure of the turbulent boundary layer by using the Variable-Interval Time-Averaging (VITA) technique (see Chapter 6, §6.2.2.4, Eqn. 6.10). This technique essentially moves a small window across the fluctuating component of velocity. When the running variance of the small window is larger than a threshold value, an event is detected and that part of the velocity signal inside the window is used as part of the conditional average (Bruun, 1995). Blackwelder and Kaplan (1976) used rakes of hot wires orientated in the wall-normal direction with a detector probe at  $y^+ = 15$ . They observed that before the burst was detected, there was an inflection in the velocity profile as seen in Figure 2.3, a similar result was seen in the study of Kline *et al.* (1967). They showed that the bursting event (detected at  $y^+ = 15$ ) was well correlated over the height of the boundary layer, which suggested that the burst events affected a large region of the boundary layer, Figure 2.3.

### 2.1.2 Outer Region

The outer region of the turbulent boundary layer is usually defined as the region  $y/\delta > 0.15$ , where inertial effects are dominant and the effects of viscosity are

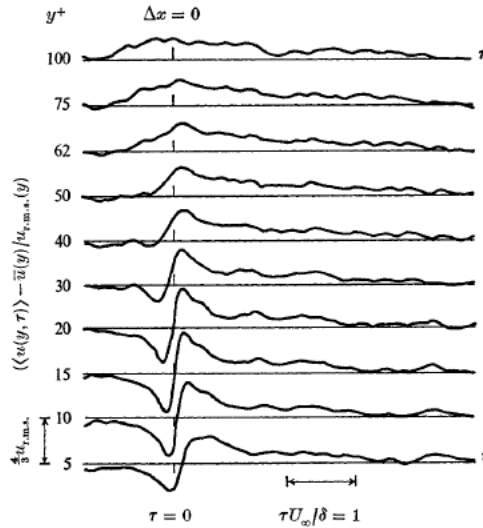


Figure 2.3: Bursting events taken from the VITA analysis of Blackwelder and Kaplan (1976).

small (Panton, 2001). An example of the outer region of the turbulent boundary layer is shown in Figure 2.4 and is taken from Gad-el Hak and Bandyopadhyay (1994). This figure shows flow visualisation obtained with fluorescent dye when a flat plate is being towed in a water channel. There are two turbulent boundary layers developed, one on top of the plate and the other on the bottom of the plate. The boundary layer on top of the plate is the one of interest and clearly shows that the turbulent boundary layer consists of bulges of fluid. These bulges of fluid interact with the free stream, entraining fluid into the turbulent boundary layer. In between the bulges there are large valleys of irrotational fluid. It is important to realise that the turbulent boundary layer is not as smooth as the time-averaged quantities of velocity makes the boundary layer appear. The turbulent bulges are on the order of the boundary-layer thickness,  $\delta$ , in the streamwise, spanwise and wall-normal directions.

Flow visualisation from Falco (1977) showed that “typical eddies” or as they are sometimes referred to, “Falco Eddies,” are created on the upstream sides of the turbulent bulges, Figure 2.5. Falco (1977) suggested that the turbulent bulges and eddies moved towards the wall and could be responsible for the sweep-type motions that have been seen in the near-wall region. The interaction between the

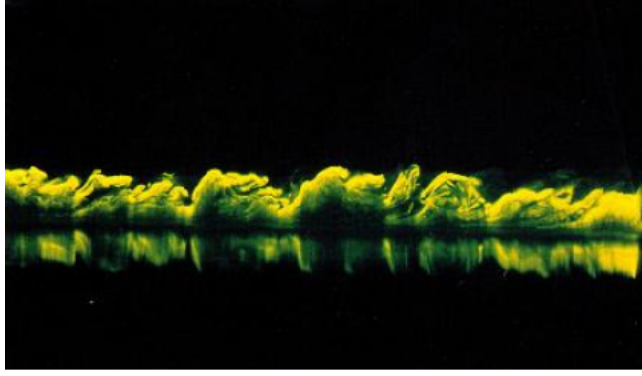


Figure 2.4: Flow visualisation of the turbulent boundary layer. Taken from Gad-el Hak and Bandyopadhyay (1994).

inner and the outer regions of the turbulent boundary layer is not well understood, although the inrush of high-speed fluid and the violent expulsion of low-speed fluid into the outer region have previously been seen. Panton (2001) stated that as the large-scale turbulent bulges pass the wall, they impose pressure fluctuations on the near-wall region which could be influencing the near-wall events.

### 2.1.3 Hairpin Vortices and the Turbulence Regeneration Cycle

One of the most important features of the turbulent boundary layer are vortical structures. This comes as no surprise since a vortex has the ability to pump fluid into and away from the wall across the mean velocity gradient and hence, it is important in the production of turbulent kinetic energy. Theodorsen (1952) proposed that the turbulent boundary layer comprises horseshoe or ring shaped vortices that are responsible for the transfer of momentum within the boundary layer. Head and Bandyopadhyay (1981) performed smoke flow visualisation in the turbulent boundary layer by placing a laser sheet at an angle of  $45^\circ$  to the flow direction. They found that the turbulent boundary layer was comprised of coherent motions (Cantwell, 1981; Robinson, 1991). The coherent motions are hairpin-type vortices that extend from the wall to the height of the boundary layer. Head and Bandyopadhyay (1981) commented that the hairpin structures seem

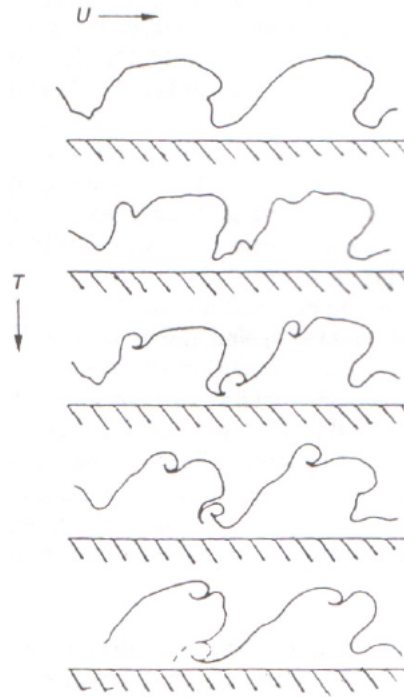


Figure 2.5: The outer boundary layer showing typical Falco Eddies at the back of turbulent bulges. Taken from Falco (1977).

to consistently be arranged at  $45^\circ$  to the wall and could agglomerate together to generate hairpin packets. The visualisation studies of Head and Bandyopadhyay (1981) have offered the motivation for more recent quantitative studies of the turbulent boundary layer (Hutchins *et al.*, 2005; Hambleton *et al.*, 2006).

Robinson (1991) suggested that the hairpin vortices could be split up into three parts, these being the legs, neck and head of the hairpin vortex. He suggested that there could be a link between the quasi-streamwise vortices, hairpin vortices and the near-wall low-speed streaks. Figure 2.6 shows that the legs of the hairpin vortices could be the quasi-streamwise vortices in the turbulent boundary layer. If the legs of hairpin vortices were extending towards the wall, as depicted in Figure 2.6, it was suggested that these could be responsible for the sweep and ejection events in the turbulent boundary layer. Hence, the quasi-streamwise vortices (legs of hairpin vortices) collect low-speed fluid within the viscous sub-layer on the upwash side of their legs, causing the appearance of the low-speed streaks (Kline *et al.*, 1967), which ultimately lead to ejection events (Corino and Brodkey, 1969); the violent expulsion of low-speed fluid into the outer regions of

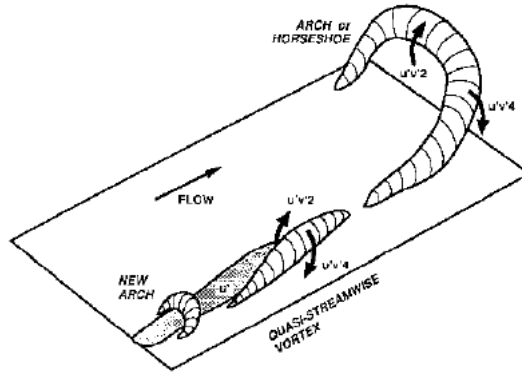


Figure 2.6: Conceptual model of the relationship between the sweep and ejection events with quasi-streamwise vortices in the near-wall region and arch-shaped vortices in the outer region. Taken from Robinson (1991).

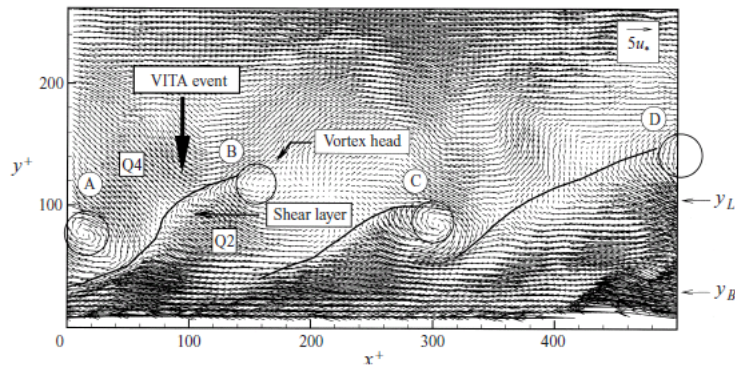


Figure 2.7: Four hairpin vortex signatures aligned in the streamwise direction. Taken from Adrian *et al.* (2000).

the boundary layer. The sweep events, which have been shown to be the major contributor to turbulent skin friction (Kravchenko *et al.*, 1993; Orlandi and Jiménez, 1993), occur on the downwash side of the hairpin legs, where high-speed fluid from the outer regions of the boundary layer transfers momentum into the wall.

Using high-resolution PIV in the  $x$ - $y$  plane of the turbulent boundary layer, Adrian *et al.* (2000) were able to study and confirm the notion of the hairpin packet, Figure 2.7. This figure shows the signature of four hairpin vortices with the heads of the hairpin vortices shown by the circles A to D. It can be seen that each hairpin vortex creates an angle at approximately  $45^\circ$  to the wall. However, as the vortices approach the wall the angle becomes shallower. Hence, Figure 2.7 shows the existence of a hairpin packet in the turbulent boundary layer and

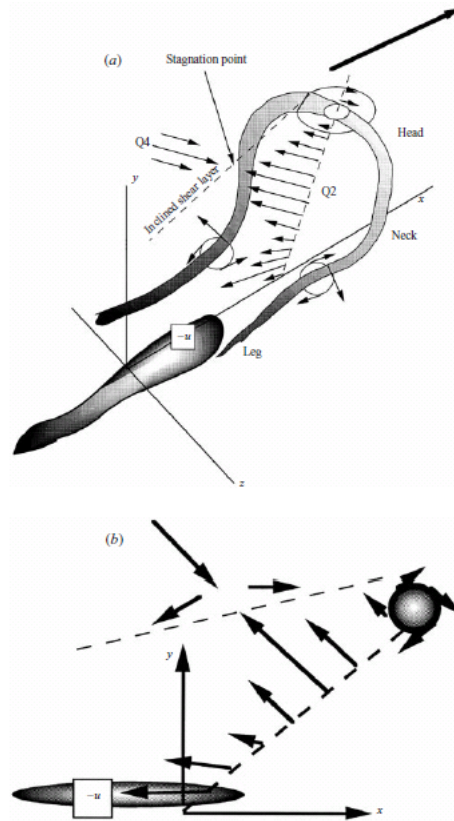


Figure 2.8: Showing a) schematic of a hairpin vortex attached to the wall with induced motions and b) a slice in the  $x$ - $y$  plane through the hairpin vortex. Taken from Adrian *et al.* (2000).

Adrian *et al.* (2000) claimed that at least one hairpin packet appeared in 85% of all the PIV data that was taken. In Figure 2.8, an idealised hairpin vortex of Adrian *et al.* (2000) is shown. It can be seen that there is a Q2 event (ejection) under the vortex head that makes an angle at  $45^\circ$  to the wall. The arrows show the direction of vortex pumping from the neck of the hairpin vortex. In this model, the legs of the hairpin vortex are the quasi-streamwise vortices that are extending down towards the wall and are collecting and lifting the low-speed fluid in the near-wall region. There is also a stagnation zone which is a shear layer that has formed due to the interaction between the Q2 (ejection) and the Q4 (sweep) events. Through the PIV data, Adrian *et al.* (2000) observed that the most frequent and observable flow feature throughout the turbulent boundary layer was the hairpin vortex which ranged from  $y^+ = 50$  to the top of the boundary layer.

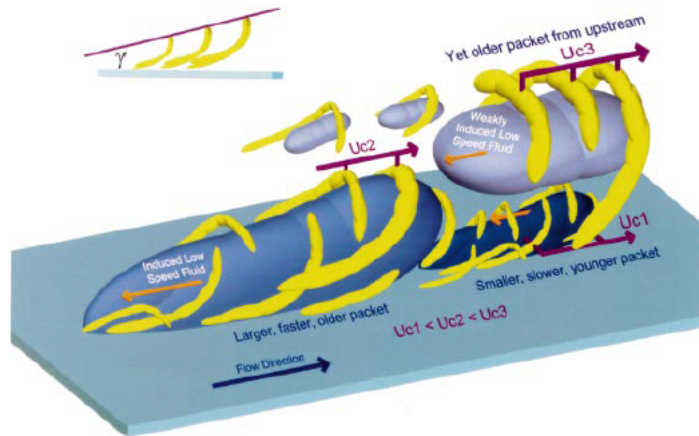


Figure 2.9: Conceptual scenario of nested hairpin or cane-type vortices growing up from the wall in a turbulent boundary layer. Taken from Adrian *et al.* (2000).

There are many conceptual models on how turbulence is able to self-sustain and these can be divided into parent-offspring or instability based mechanisms (Panton, 2001). Here, two parent-offspring mechanisms will be focused on. It has already been noted that Head and Bandyopadhyay (1981) and also Adrian *et al.* (2000) have seen packets of hairpin vortices. Adrian *et al.* (2000) found that the hairpin packets could contain up to 10 hairpin vortices which would all convect with a similar speed and could stretch for streamwise distances as long as  $2\delta$ . Adrian *et al.* (2000) also thought that hairpin packets could exist within one another. This is shown in Figure 2.9 with a conceptual image of nested hairpin packets. In this figure, there are young, small packets of hairpins that are located close to the wall which are being over run by older, faster hairpin packets. The idea of a hairpin packet could be used to explain the events in the near-wall region. It has already been demonstrated that perhaps the legs of the hairpin vortices (the quasi-streamwise vortices) are collecting the low-speed fluid in the near-wall region, forming the near-wall low-speed streaks and causing bursting events. It was noted by Kline *et al.* (1967) that the near-wall streaky structure lasts for typically 1000 wall units in the streamwise direction, yet a single hairpin vortex lasts for typically 100 wall units (Zhou *et al.*, 1999). With the idea of the hairpin packet that could contain up to 10 hairpins, this could account for the meandering low-speed streaks in the near-wall region extending

for long streamwise distances. It could also explain the observations of Corino and Brodkey (1969), who observed several ejection events during the bursting cycle (Figure 2.2), as there could be several ejection-type motions occurring within the hairpin packet. Interestingly, Zhou *et al.* (1999) observed in their DNS studies that a single hairpin has the ability to generate a hairpin packet if it is strong enough, causing several other hairpins upstream and downstream of the primary hairpin, Figure 2.10. The ability of a hairpin to self-generate as shown by Zhou *et al.* (1999) and consequently observed by Adrian *et al.* (2000), could offer a plausible explanation for the self-sustaining mechanism of turbulence. Based on flow visualisation studies, Choi (1989) provided another conceptual model for the self-sustaining mechanism of turbulence, this is shown in Figure 2.11 and can be explained over three stages. During stage 1, a spanwise vortex filament is deformed by a bursting event that occurs upstream. During stage 2, the deformed vortex filament moves downstream where it develops into a hairpin loop moving away from the wall. During stage 3, the hairpin loop develops due to self-induction and forms a hairpin vortex that moves away from the wall at an angle of around  $45^\circ$ . During this ejection process, neighbouring hairpin vortices also move away from the wall causing the legs of the hairpins to come in close proximity and form counter-rotating pairs, which induce a sweep event and cause high-speed fluid to be splashed on to the wall leading to an increase in skin friction. The induced sweep event would then cause the perturbation for the next oncoming vortex filament and the sequence is repeated.

## 2.2 Skin-friction Drag Reduction Techniques

This section offers a brief look into some successful skin-friction drag reduction techniques in §2.2.1 and a more detailed look into the skin-friction drag reduction achieved with the spanwise travelling-wave technique in §2.2.2.

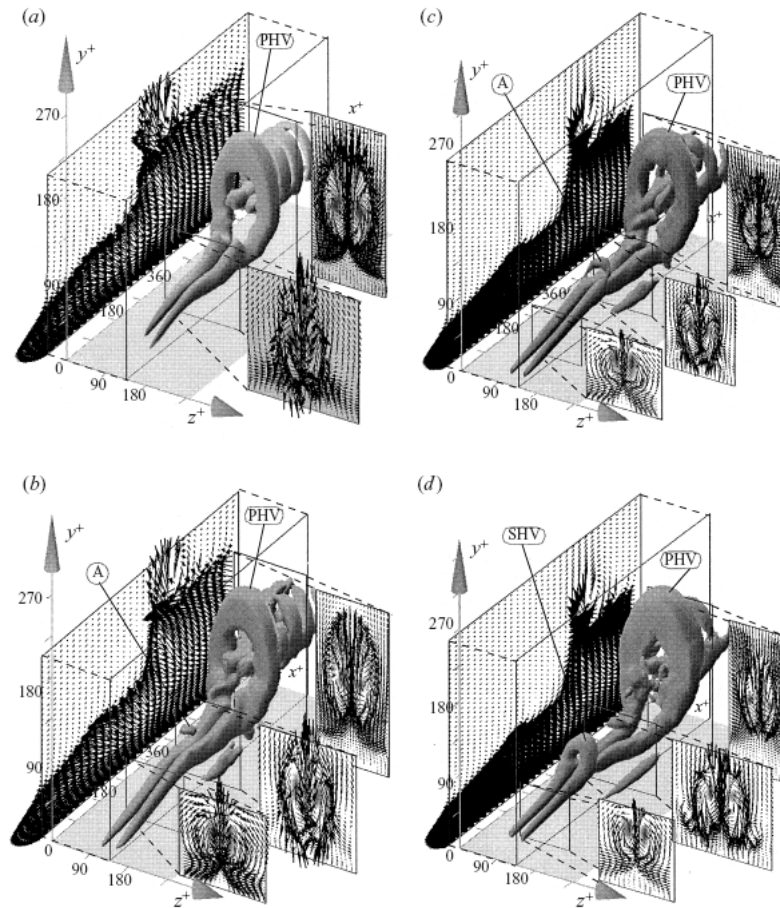


Figure 2.10: DNS of a turbulent channel flow showing the generation of a secondary hairpin vortex (SHV) upstream of the head of the primary hairpin vortex (PHV). The SHV initiates from location A in b) and c). There is also formation of hairpin vortices downstream of the head of the PHV. Taken from Zhou *et al.* (1999).

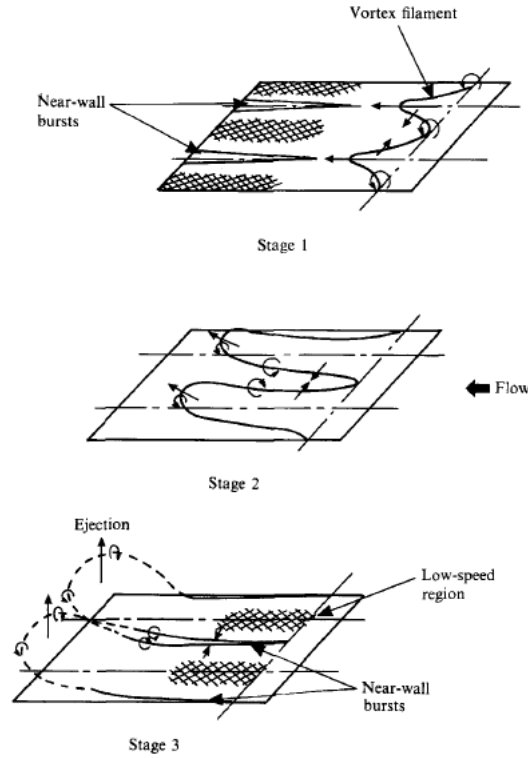


Figure 2.11: Conceptual model of burst events. Taken from Choi (1989).

### 2.2.1 Overview

A highly successful skin-friction drag reduction technique is the addition of polymers or surfactants to liquid flows. It has been found that the long molecular chains of polymers and the string-like chains of surfactants have the ability to hinder turbulence production. Oil soluble polymers are currently used in industry, being placed in the Trans-Alaska Pipeline to aid the throughput of oil. Skin-friction reductions of up to 70% have been reported in the literature with the drag reduction mechanism thought to be linked to the extension of molecular chains which interact with the bursting cycle (Virk, 1975).

Inspired by nature from shark's skin, riblets are small longitudinal grooves that are aligned in the flow direction. The most practical groove to manufacture is the V-shaped groove. The riblets have characteristic spacing with the groove height and spanwise spacing being on the same order and found to be optimal when typically 15 viscous units. Riblets can reduce the skin-friction drag by around 8%. Choi (1989) deduced that the riblets act as small fences which restrict

the movement of the quasi-streamwise vortices near the wall. Consequently, the strength of the near-wall bursts are reduced and occur prematurely at higher frequency, leading to reductions in both turbulence intensity and skin friction.

Another inspiration from nature was compliant coatings which were inspired from dolphin's skin (Kramer, 1961). Compliant coatings have small deformable surfaces and are predominantly applied in liquid flows. Typically drag reduction of up to 10% can be achieved and it is thought that the deformable surface acts to weaken ejection events. Choi *et al.* (1997) stated that the natural frequency of the compliant coating needed to match the flow conditions, a non-dimensional period of  $50 < t^+ < 150$  was suggested.

Transverse motions in the near-wall region of the turbulent boundary layer have received a lot of interest over recent years. One of the most successful techniques being spanwise wall oscillation. This technique initiated through a numerical simulation from Jung *et al.* (1992), who showed that, by applying a spanwise oscillation at the wall with a period of  $T^+ = 100$ , a skin-friction drag reduction of 40% could be achieved. This was later performed experimentally by Choi *et al.* (1998) who found a 45% reduction in turbulent skin-friction drag. When a flow is subjected to wall oscillation, a thin Stokes' layer is created —this is viscous fluid flow, which is oscillating close to the wall due to the oscillatory motion of the wall. Choi *et al.* (1998) suggested that the drag reduction mechanism for the spanwise wall oscillation was the twisting of the periodic Stokes' layer in the near-wall region, which causes negative spanwise vorticity and a reduction in the near-wall velocity gradient, leading to a reduction in wall shear stress. Choi *et al.* (1998) suggested that a non-dimensional spanwise wall speed was a more appropriate parameter than the oscillation period for determining the skin-friction drag reduction. Recently streamwise travelling waves (Quadrio *et al.*, 2009; Huang *et al.*, 2010) have been applied to a turbulent channel flow using Direct Numerical Simulation (DNS) where it has been found that drag reduction up to 48% can be achieved. Quadrio *et al.* (2009) placed a streamwise

travelling wave at the wall of a turbulent channel flow by specifying a spanwise wall velocity that varied with time and was modulated sinusoidally in the streamwise direction. It was found that skin-friction drag reduction could be obtained when the streamwise travelling wave moved forwards or backwards. When the travelling wave was moving with a wave speed comparable to the convection velocity of the near-wall turbulence, there was a drag increase. It was noted that when the streamwise travelling waves were effective in reducing the drag, they operated in a similar fashion to spanwise wall oscillation. Another interesting numerical simulation concerning near-wall spanwise motions was the standing wave simulation of Viotti *et al.* (2009). Here, a spanwise velocity was applied at the wall that did not vary with time but was modulated in the streamwise direction sinusoidally. Hence, this could be thought of as the same wave as Quadrio *et al.* (2009) but with a wave speed of zero. It was shown that with the standing wave the skin-friction drag could be reduced by more than 50%. These simulations are interesting because they rely on surface based motions at the wall. DBD plasma is a surface based technique, hence it is possible that the streamwise travelling wave and the standing wave could both be implemented with DBD plasma actuators.

Other turbulent drag reduction techniques include Micro-Electro-Mechanical-Systems (MEMS) (Rathnasingham and Breuer, 2003), micro-bubbles (Merkle and Deutsch, 1989), Large-Eddy-Break-Up devices (LEBU) (Savill and Mumford, 1988) and blowing/suction control (Antonia *et al.*, 1995). A recent review of actuators for active flow control can be found in Cattafesta III and Sheplak (2010). The above list is by no means exhaustive, it merely provides a flavour of the vast areas of research that govern the discipline of turbulent drag reduction.

### 2.2.2 Spanwise Travelling Waves

A spanwise travelling wave was implemented in a turbulent channel flow and studied using DNS by Du and Karniadakis (2000) and Du *et al.* (2002). The ideal travelling-wave forcing equation that was used in their simulations was,

$$F_z = I e^{-\frac{y}{\Delta}} \sin\left(\frac{2\pi}{\lambda} z - \frac{2\pi}{T} t\right), \quad (2.1)$$

where  $F_z$ , was the spanwise force that was imposed at the wall and  $I$ , was the amplitude of the travelling wave. The travelling-wave force was maximum at the wall and decayed exponentially with respect to a penetration depth,  $\Delta$ . The wavelength of the travelling wave was denoted by  $\lambda$  and the time period by  $T$ . It is important to realise that the spanwise travelling wave is inherently linked to a spanwise wall oscillation and a standing wave that is modulated in the spanwise direction. If we think of a spanwise travelling wave with an infinite wavelength,  $\lambda \rightarrow \infty$ , then Eqn. 2.1 would reduce to a spanwise wall oscillation,

$$F_z = I e^{-\frac{y}{\Delta}} \sin\left(\frac{2\pi}{T} t\right). \quad (2.2)$$

Similarly, if we think of a spanwise travelling wave that has an infinite time period,  $T \rightarrow \infty$ , then Eqn. 2.1 would reduce to a standing wave modulated in the spanwise direction,

$$F_z = I e^{-\frac{y}{\Delta}} \sin\left(\frac{2\pi}{\lambda} z\right). \quad (2.3)$$

Hence, the spanwise travelling wave could be thought of as a standing wave, which was made to oscillate —travel— along the spanwise direction.

Du *et al.* (2002) found that application of the spanwise travelling waves to a turbulent channel flow led to large changes in the near-wall structure. Figure 2.12 shows two images of instantaneous velocity at  $y^+ = 4$  taken from Du *et al.* (2002). In each of these figures, the flow is moving from left to right and the spanwise travelling wave (bottom image) is moving from bottom to top as indicated by the arrows in the image. The red regions denote high-speed flow and blue regions denote low-speed flow. The top image of Figure 2.12 is with no-control and shows the characteristic near-wall streaky structure of low- and high-speed fluid. The bottom image shows the effect of spanwise travelling-wave control, where the near-wall streaks nearly become eliminated and form wide ribbons of

low-speed fluid. Du *et al.* (2002) stated that this was a significant new finding as it is very difficult to alter the near-wall streak spacing. Even in the most drag reducing flows, like spanwise wall oscillation, the streaks are merely twisted in the near-wall region and are not eliminated as was the case with the spanwise travelling-wave control. The maximum skin-friction reduction that was obtained in the spanwise travelling wave study of Du *et al.* (2002) was 30% and is shown in Figure 2.13 for a range of travelling-wave parameters. The 30% drag reduction was achieved by applying periods of  $T^+ = \frac{Tu_z^2}{\nu} = 25, 50$  or 100 depending on the penetration depth and amplitude of the Lorentz force. Du *et al.* (2002) proposed that if a product of force amplitude,  $I$ , period,  $T^+$  and penetration depth,  $\Delta$  equals unity,  $I \times T^+ \times \Delta = 1$ , a skin-friction drag reduction of 30% should be obtained. However, not all combinations of  $(I, T^+)$  were valid. Low amplitudes of forcing with large periods,  $I = 0.25, T^+ = 200$ , led to drag increase as the travelling-wave motion, the phase speed, was too low. This implied that a correct range of forcing period needs to be found with the correct forcing amplitude to produce a spanwise travelling wave capable of skin-friction reduction. Furthermore, penetration depths,  $\Delta^+ > 10$ , greater than the viscous sublayer, were seen to increase skin friction. Du *et al.* (2002) suggested that the mechanism for the skin-friction reduction was to be due to the stabilisation of the near-wall streaks which led to changes in the turbulence regeneration cycle.

Xu and Choi (2006) studied experimentally a spanwise travelling wave with Lorentz forcing in a water channel and obtained a skin-friction reduction on the order of 30% with forcing periods of  $T^+ = 42$  and 82 when the near-wall fluid was displaced more than 115 wall units in the spanwise direction. This spanwise spatial scale is on the order of spacing between low-speed streaks and provides a constraint for the minimum wavelength needed for skin-friction reduction,  $\frac{1}{2}\lambda^+ > 115$ . Xu and Choi (2006) also performed flow visualisations of the near-wall region during travelling-wave excitation and found that the near-wall streaky structures, the low-speed streaks were substantially altered in a similar way to

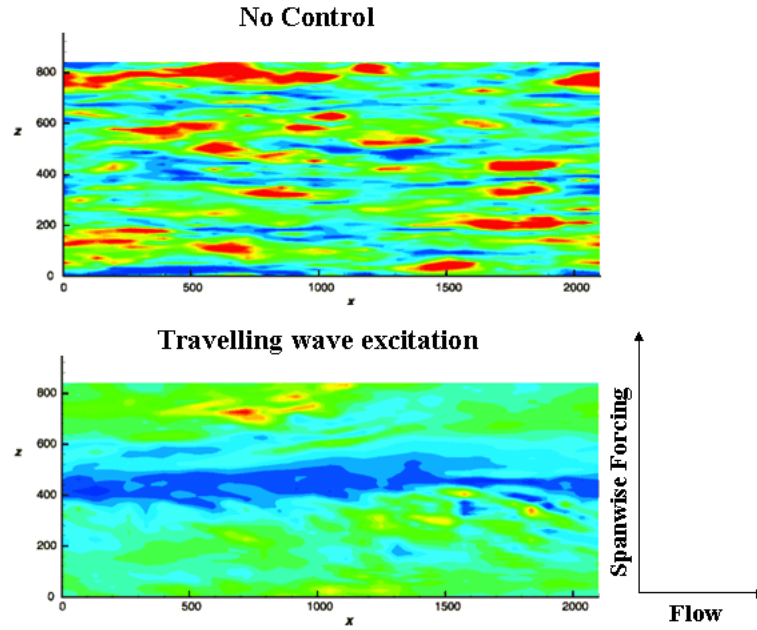


Figure 2.12: Instantaneous flow visualisation of the near-wall region at  $y^+ = 4$  (top image) no-control and (bottom image) spanwise travelling-wave control with Lorentz forcing. Red regions denote high speed and blue regions denote low speed. Adopted from Du *et al.* (2002).

---

$\Delta$	$T^+$	$I$	Product	Approx. drag change
$\frac{1}{30}$	50	1	1	-30%
$\frac{1}{25}$	50	1	2	0%
$\frac{1}{25}$	100	1	4	+70%
$\frac{1}{25}$	25	1	1	-30%
$\frac{1}{25}$	50	0.5	1	-30%
$\frac{1}{25}$	100	0.25	1	-30%
$\frac{1}{25}$	100	0.1	0.4	-25%
$\frac{1}{10}$	5	4	2	-10%
$\frac{1}{100}$	50	1	0.5	-20%
$\frac{1}{100}$	100	1	1	-30%

---

Figure 2.13: Drag reduction as a function of  $I, T^+$  and  $\Delta$ . Table adopted from Du *et al.* (2002).

Du *et al.* (2002).

Furthermore, numerical simulations of a travelling wave by a flexible wall have been studied by Zhao *et al.* (2004) with a forcing period of  $T^+ = 50$ , where a skin-friction drag reduction of 30% was achieved. They believed that the main mechanism for the drag reduction is the change in boundary vorticity flux due to the flexible wall's acceleration that causes a thin Stokes' layer of concentrated streamwise vorticity, which suppresses quasi-streamwise vortices from the viscous sublayer and causes a regularised skin-friction pattern at the wall. Zhao *et al.* (2004) also saw the amalgamation of the low-speed streaks into wide ribbons of low-speed fluid. Hence, the large changes in the near-wall structure appear as a key feature of the turbulent boundary-layer control with the spanwise travelling-wave technique. After the numerical simulation of a flexible wall by Zhao *et al.* (2004), Itoh *et al.* (2006) studied experimentally a flexible wall in a turbulent boundary layer of 8 m/s. The spanwise travelling wave was actuated with a 10  $\mu\text{m}$  thick polythene sheet forced by a 1.5 W loud speaker at 100 Hz, producing a time period of  $T^+ = 100$  and a travelling wave with out of plane motion. They found a skin-friction reduction of 7.5%, however they noted that the wave speed of the travelling wave was very large,  $c^+ = \frac{\lambda^+}{T^+} = 28$ . This was due to a large wavelength ( $\lambda^+ = 2800$ ) that was fixed by the constraints of the polythene sheet.

A new and interesting DNS of the spanwise travelling waves in a turbulent channel flow has been conducted by Huang *et al.* (2011). They found that application of a spanwise travelling wave to a turbulent channel flow leads to the production of a streamwise vortex that travels in the spanwise direction and reorganises the turbulent boundary-layer structure leading to a drag reduction of over 30%. They have also found that the streamwise vortex is important in the collecting and spreading of low-speed fluid in the near-wall region of the turbulent boundary layer and hence in the formation of the wide ribbons of low-speed fluid that have been seen in several spanwise travelling-wave experiments (Du and Karniadakis, 2000; Du *et al.*, 2002; Zhao *et al.*, 2004; Xu and Choi, 2006).

## 2.3 Dielectric-Barrier-Discharge Plasma

This section is centered around the topic of Dielectric-Barrier-Discharge (DBD) plasma actuators as this is the actuator type that has been used throughout this thesis. Here, an overview will be provided of DBD plasma actuators in §2.3.1 and some examples of how DBD plasma has been used for flow control in §2.3.2.

### 2.3.1 DBD Plasma Actuators

DBD plasma actuators are completely electrical devices that create a body force (ionic wind) by the movement of charged particles inside an electric field. Hence, DBD plasma actuators require no moving parts, which makes their design simple and without the need for complicated ducting, holes or cavities. They are fast acting with response times on the order of 10's of  $\mu\text{s}$  and they are low in power needing typically 10's of  $\text{W}/\text{m}$  (or 100's of  $\text{W}/\text{m}^2$ ). The plasma actuators are very low in weight, being on the order of 10's of grams depending on their size, they are cheap to manufacture and can be fitted to existing airframes.

DBD plasma actuators consist of an upper and lower electrode separated by a thin dielectric material, with the upper electrode exposed to the air and the lower electrode encapsulated by the aerodynamic surface. An example of this configuration is shown in Figure 2.14a). On application of several kV of AC power at kHz frequency between the upper and lower electrodes, the air around the upper electrode becomes ionized. This ionized air is known as plasma, which is why these types of actuators are referred to as plasma actuators. Typically the upper and lower electrodes range from 10's-100's of  $\mu\text{m}$  in thickness and the dielectric materials range from 100's of  $\mu\text{m}$  to several mm in thickness. The applied voltages can range from several kV to 10's of kV at frequencies of several kHz to 100's of kHz. The plasma appears as a light purple glow which is low in intensity, requiring a darkened space to be seen by the naked eye. An example of the DBD plasma discharge is shown in Figure 2.14b). The plasma extends

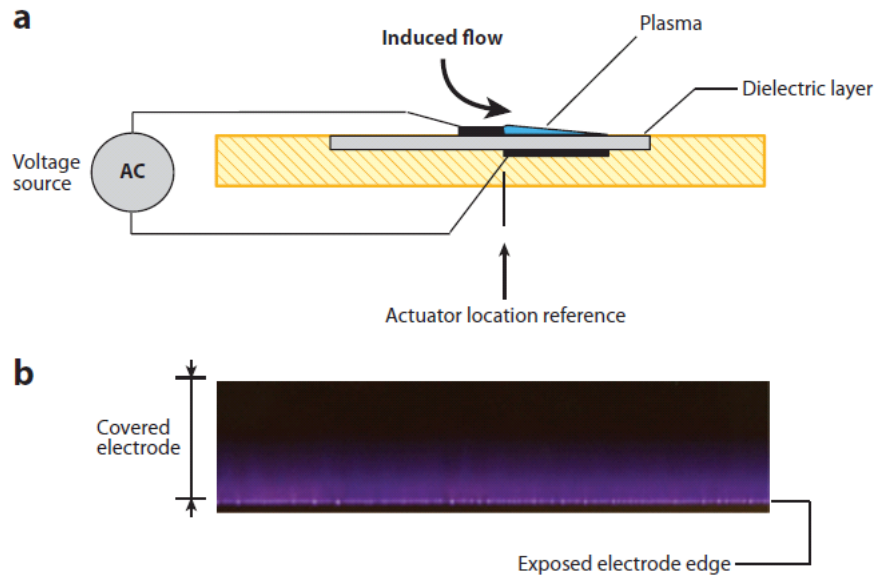


Figure 2.14: DBD plasma actuator a) cross-section and b) photograph showing the ionized air. Taken from Corke *et al.* (2010).

typically for a few mm away from the upper electrode and across the dielectric. The plasma generates a body force which couples momentum to the surrounding air to induce a jet flow (Enloe *et al.*, 2004a), which is caused by the movement of plasma ions to and from the dielectric surface and is usually referred to as an ionic wind (Robinson, 1962). An example of the momentum coupling created on application of DBD plasma is shown in Figure 2.15. This image is taken from Roth and Sherman (1998) who were the first group to develop a DBD plasma actuator that was capable of working at atmospheric pressure for the application of flow control. In Figure 2.15a), there is a laminar jet moving in the horizontal direction. When the DBD plasma is switched on, Figure 2.15b), the laminar jet is heavily deflected towards the wall and is pushed in the horizontal direction (to the right) by the actuation of the plasma. This clearly shows that on application of DBD plasma a body force can be coupled to the air to generate a flow.

The term “plasma” was first introduced into the physics vernacular by Langmuir (1928) who used it to describe a region of electrically neutral discharge (Kunhardt, 2000). A plasma is created when a sufficient amount of energy is supplied to a volume of gas. In the case of generating DBD plasmas, the energy source is the applied electric field between the upper and lower electrodes, which

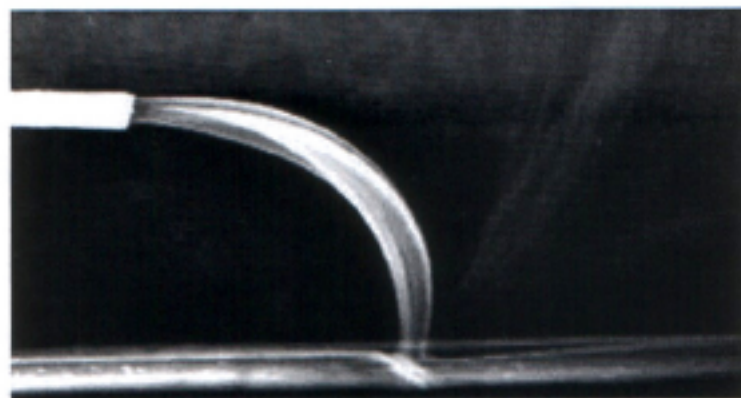
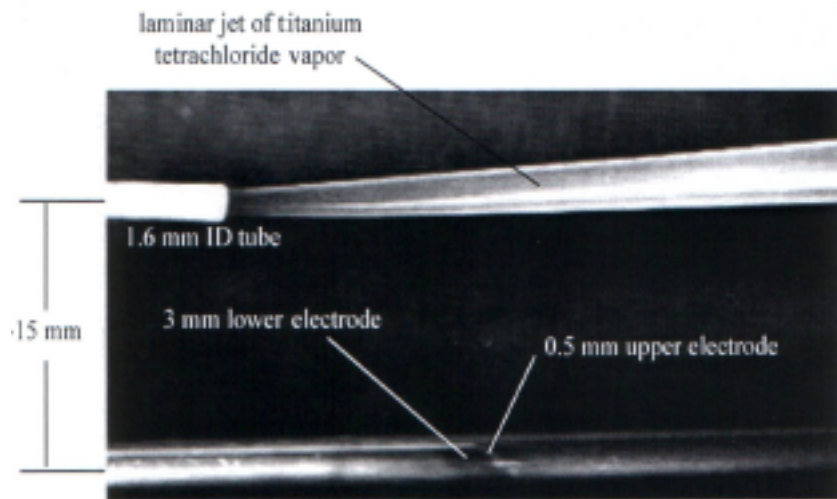


Figure 2.15: Demonstration of the body force due to an asymmetric DBD plasma actuator in quiescent air a) plasma off and b) plasma on. Taken from Roth and Sherman (1998).

needs to have a sufficient electric potential to be able to cause the ionization of the air. An example of the voltage and current characteristics of a DC low pressure electrical discharge tube is shown in Figure 2.16 and is taken from Roth (1995). This figure is very general and shows the transition through different types of plasmas, including the glow discharge regime (F-G) which the DBD plasma actuators are a part of. With reference to Figure 2.16, as the voltage is initially increased (A-B), the naturally occurring electrons and ions move due to the applied electric field causing a current to be drawn. Through (B-C) the electrons and ions are removed from the discharge tube and the current becomes saturated. The electrons do not have enough energy to create new ionization. As the voltage is further increased through (C-E), the electrons acquire enough energy and are emitted from the cathode and cause the ionization of the surrounding neutral gas particles leading to an exponential increase in current as a function of voltage. This is called the Townsend regime and between (D-E) corona discharges will occur due to the asperities on the electrodes until the breakdown voltage is reached at point (E). The plasma that is created from (A-E) is referred to as a dark discharge. This is because the plasma cannot be seen by the naked eye (apart from the corona discharge and the spark that would occur at the breakdown voltage). Increasing the voltage beyond the breakdown voltage will cause the plasma to transition to the glow discharge regime (E-H). This is where the voltage and current are large enough to create sufficient amounts of excitation of the neutral background gas, allowing the discharge to be seen by the eye. After some transition between (E-F), the normal glow discharge region is found between (F-G) which is the region of interest for the DBD plasma actuators. The discharge at this point appears as a light purple glow as already shown in Figure 2.14. Increasing the voltage even further beyond the glow regime causes the cathode to be heated by the high current to incandescence causing glow-to-arc transition (H-I) and the beginning of the arc discharge regime.

The DBD plasma discharge is thought to be neutral (Orlov and Corke, 2005;

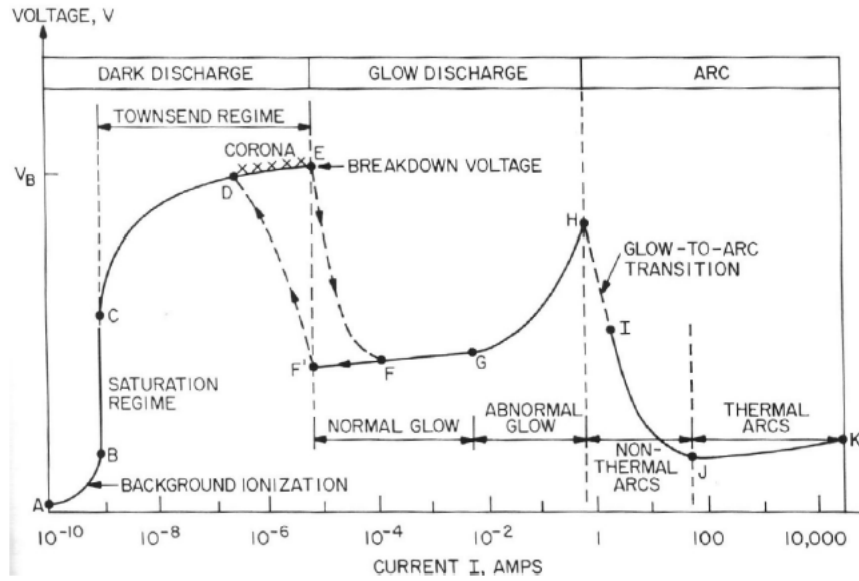


Figure 2.16: Voltage and current characteristics of a DC low pressure electrical discharge tube. Taken from Roth (1995).

Orlov *et al.*, 2006) with the discharge containing equal numbers of positive and negative charges which each respond to the applied electric field. Hence, negative charges that are present in the plasma discharge, such as electrons and negative ions would move towards the positively charged electrode. Similarly, the positive charges present in the discharge such as the positive ions would move towards the negatively charged electrode. An illustration of the movement of the negative charges during a single AC cycle of a DBD plasma actuator is shown in Figure 2.17. In this example, the DBD plasma actuator is operated using a sinusoidal voltage. In the case when the high voltage waveform is on the negative part of the AC cycle (referred to as the forward-stroke) and is above the breakdown voltage of the surrounding air, electrons are emitted from the exposed electrode and deposited on the dielectric surface. This occurs during the blue rectangle (a-b) in Figure 2.17. The deposited electrons cause charge build up on the dielectric surface which opposes the charge of the exposed electrode, quenching the plasma discharge and stopping the plasma from collapsing into an arc. In other words, DBD plasma actuation is a self-limiting process (Enloe *et al.*, 2004b). For the plasma discharge to continue, an increasing voltage would have to be applied to the upper electrode. On the positive side of the AC cycle (referred to as the

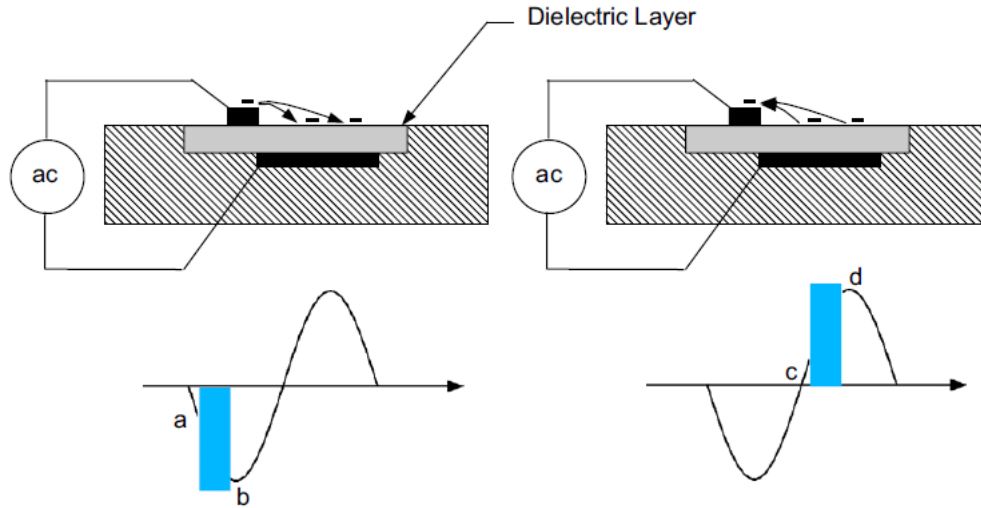


Figure 2.17: The regions of ionization in DBD plasma actuators. Taken from Corke *et al.* (2007).

backward-stroke) when the electric potential is large enough, the electrons which were deposited on the dielectric surface move back to the positive electrode from which they were initially emitted. The region of ionization is shown in the blue rectangle (c-d) and similar to the forward-stroke, the ionization stops when the voltage at the upper electrode stops becoming more positive. Hence, the plasma discharge takes place twice per AC cycle.

To the eye the DBD plasma discharge looks homogeneous and uniform. However it was shown by Gibalov and Pietsch (2000) that the DBD is highly filamentary containing microdischarges or streamers. These are shown in Figure 2.18a) to c) where positive DC voltage, negative DC voltage and an AC voltage were applied across a DBD plasma actuator respectively. The discharges contained small channels which had widths on the order of 1 mm that spread out across the dielectric surface. These microdischarges can be seen in the voltage and current waveforms applied to the DBD plasma actuator. An example is shown in Figure 2.19, where spikes can be seen on the current curve (black line) which coincide with the region of plasma formation. Hence, the microdischarges cause large current spikes during the DBD plasma discharge, with more filamentary structures seen on the backward-stroke of the waveform, as shown in Figure 2.18a). The filamentary nature of the DBD plasma discharge was also observed by Wilkinson

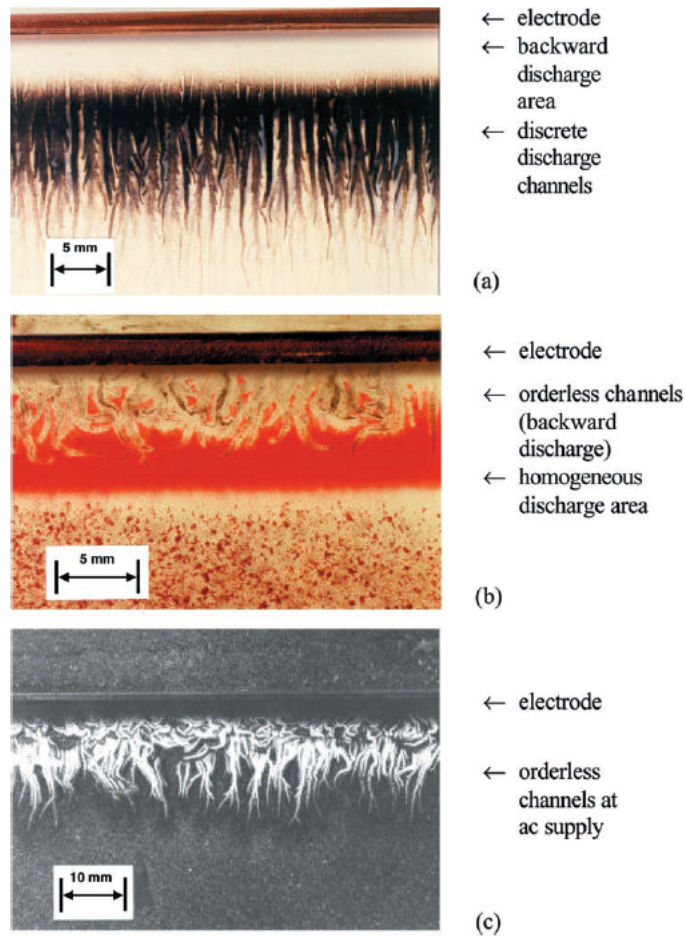


Figure 2.18: Discharge patterns on the dielectric surface of DBD plasma actuator seen by dust figures, a) positive 20 kV at the upper electrode, b) negative 20 kV at the upper electrode and c) an AC voltage of 10 kV. Taken from Gibalov and Pietsch (2000).

(2003) and Enloe *et al.* (2004a,b). The DBD plasma actuator was modelled by Boeuf and Pitchford (2005) and Boeuf *et al.* (2007b) where it was found that during each AC cycle the DBD plasma consists of glow and corona-like discharges. The glow discharges were qualified as microdischarges or streamers of large amplitude, short duration current pulses, Figure 2.20. The glow discharge regions were separated by low current, longer duration corona-like discharges. It was thought that the corona-like discharge phases have a dominant contribution to the total body force exerted by the plasma since their durations are much longer and act over a larger volume.

A frequently debated topic with DBD plasma is the role of the positive and negative half cycles (backward and forward stroke) on the body force generated

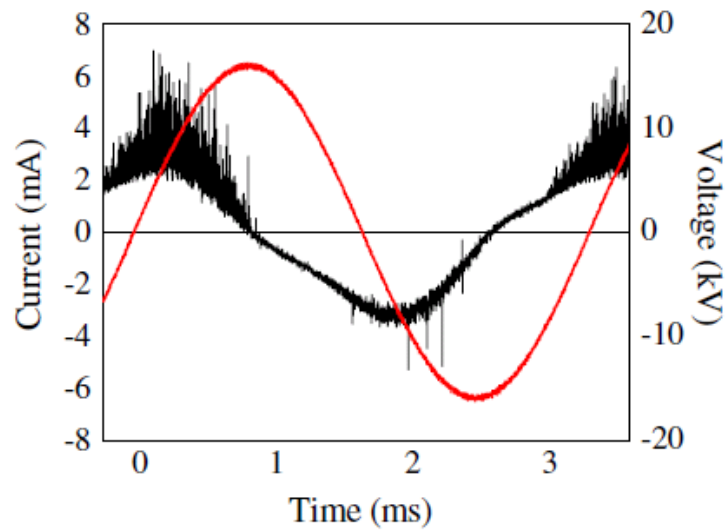


Figure 2.19: Voltage (red line) and current (black line) waveforms for a DBD plasma actuator. Taken from Moreau (2007).

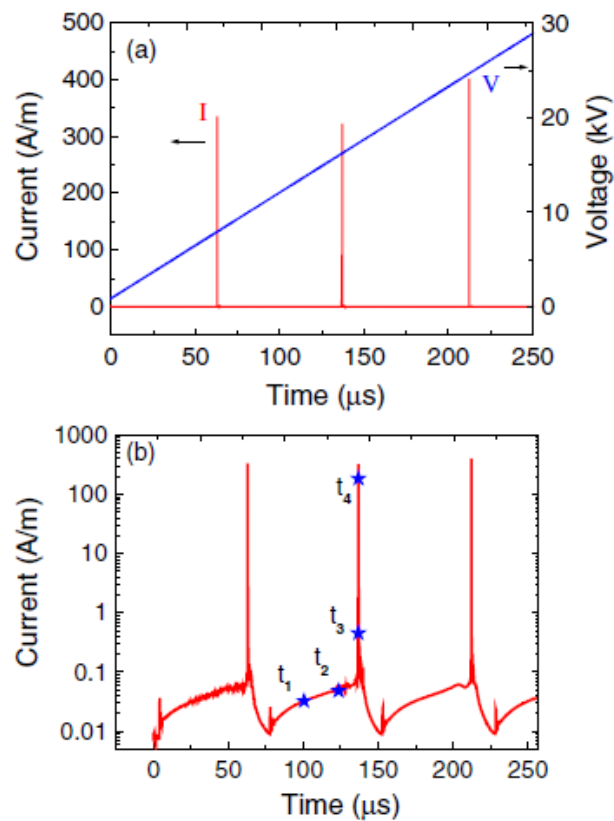


Figure 2.20: Voltage and current from a numerical simulation of a DBD plasma actuator, a) voltage and current and b) current on a logarithmic scale. Taken from Boeuf *et al.* (2007b).

during DBD plasma forcing. It has been discussed that charged particles move in opposite directions during each half of the AC cycle and it has been demonstrated that still a resultant body force acts away from the upper electrode in the direction of plasma forcing, Figures 2.14 and 2.15. Numerical simulations of DBD plasma actuation in inert and Nitrogen gases (Boeuf and Pitchford, 2005; Boeuf *et al.*, 2007b; Jayaraman *et al.*, 2008), document that the predominant force is on the positive-going portion of the forcing cycle (the backward stroke). Font and Morgan (2005) simulated the propagation of a streamer from the upper electrode to the dielectric and from the dielectric back to the upper electrode. They were also able to show that the force during the negative-going portion of the AC cycle (the forward stroke) acted in the opposite direction due to presence of positive ions. In contrast, the recent experimental results (Forte *et al.*, 2006; Enloe *et al.*, 2008; Kim *et al.*, 2007) suggest that the predominant force is on the negative-going portion of the forcing cycle, the forward-stroke. Enloe *et al.* (2008) used a Michelson interferometer to measure the oscillatory motion of a second-order mechanical system driven by a DBD plasma actuator to show that the majority, 97%, of the momentum coupling occurs during the negative-going portion of the forcing cycle. Qualitatively, the same result was found by Kim *et al.* (2007) who phase-locked PIV measurements with the plasma forcing cycle. Figure 2.21 shows the phase-locked PIV measurements of Kim *et al.* (2007). As the upper electrode is on the negative-going portion of the AC cycle, Figure 2.21a), there is clearly an increase in velocity over the dielectric to the right of the upper electrode. As the upper electrode changes polarity and the AC cycle shifts to the positive-going portion of the AC cycle, the velocity to the right of the upper electrode has decreased yet still remains positive, Figure 2.21b). As the AC cycle returns to the negative-going portion of the AC cycle, Figure 2.21c), the velocity to the right of the upper electrode is increased once more, with this cycle of undulating positive and more positive velocity found on each part of the AC cycle. Forte *et al.* (2006) performed time-resolved Laser-Doppler-Anemometry

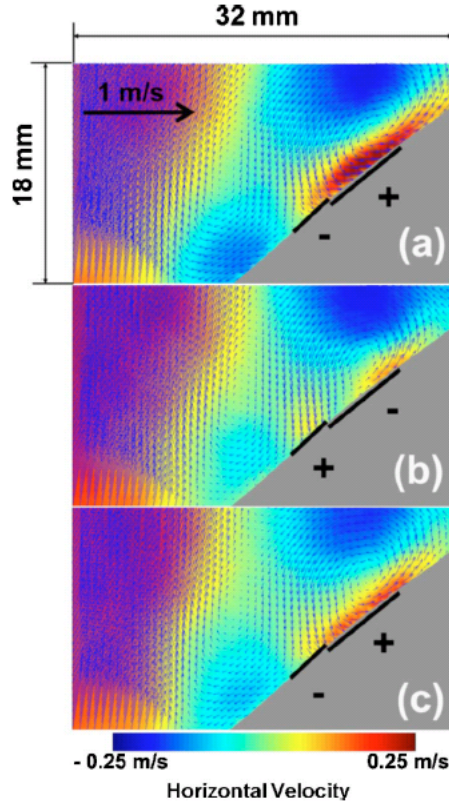


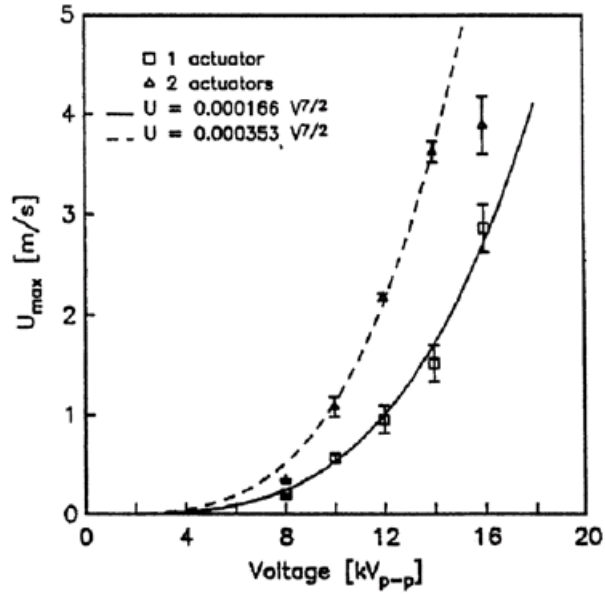
Figure 2.21: Phase-locked PIV measurements in the near field of a DBD plasma actuator. Taken from Kim *et al.* (2007).

(LDA) of the induced flow from an asymmetric DBD plasma actuator in still air. They too found that the induced velocity was largest during the negative-going portion of the AC cycle and it remained positive on both sides of the AC cycle. It is therefore thought that the reason for the difference in results between the numerical and experimental studies is the omission of negative ions in the inert gas and Nitrogen gas modelling (Enloe *et al.*, 2008; Kim *et al.*, 2007). It is well known that plasma discharge in oxygen, hence air, produces both positive and negative ions which could offer the reason for the major force contributor being found in the negative half cycle experimentally. Recently, Boeuf *et al.* (2007a) and Likhanskii *et al.* (2008) modelled the DBD plasma actuator in air, identifying the key role of the negative ions which were absent in previous DBD plasma models. They found that the integrated tangential force was downstream of the plasma actuator for both the forward and backward stroke of plasma forcing.

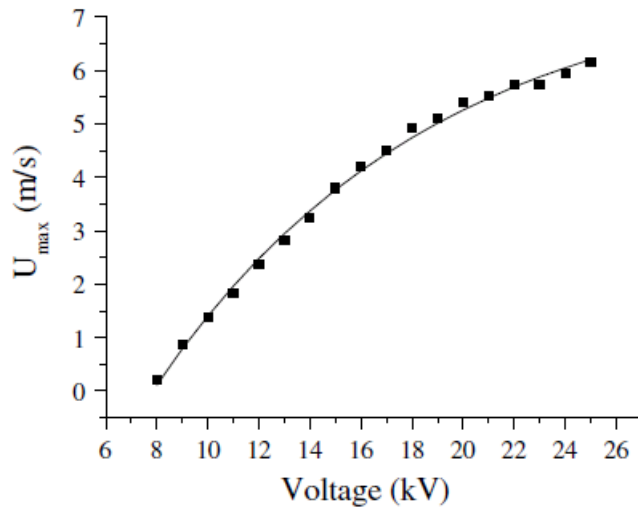
The maximum velocity that can be induced by a plasma actuator has been

studied by many authors (Forte *et al.*, 2006; Enloe *et al.*, 2004a; Jukes *et al.*, 2006a). Figure 2.22a) is taken from Enloe *et al.* (2004a) who used PIV to obtain the maximum velocity of a DBD plasma actuator as a function of applied voltage. They found that maximum velocity scaled with  $E^{3.5}$ , where  $E$  is the applied voltage. They also found that doubling the number of actuators caused double the maximum velocity. Although this might be true for two actuators it is expected that after several actuators firing together, the maximum attainable speed must reach an asymptote. Figure 2.22b) is taken from Forte *et al.* (2006), where LDA was used as the measurement technique and it can be seen that the velocity does not appear to scale with  $E^{3.5}$ , instead it increases asymptotically to a maximum velocity of around 7 m/s with an applied voltage of 26 kV. A further study is presented in Figure 2.22c) and is taken from Jukes *et al.* (2006a) who used hot-wire anemometry to measure the maximum velocity and found that for an asymmetric actuator the velocity scaled with  $E^2$ . Jukes *et al.* (2006a) also studied the maximum velocity with a symmetric actuator (Figure 2.23) and found that the maximum velocity was smaller for a given applied voltage when compared with an asymmetric actuator although it scaled more rapidly,  $E^{3.69}$ . Although the three presented figures differ, what is clear from these studies is that by applying a higher voltage a higher velocity can be obtained. The discrepancies between the three studies could be due to the different actuator geometries and materials that have been employed in the tests. It could also be due to the measuring techniques being different for all three studies along with the plasma power supplies.

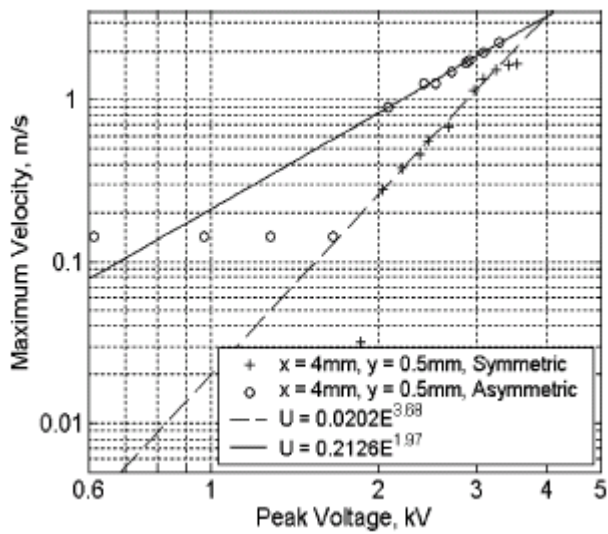
Velocity and temperature measurements were made around a symmetric actuator by Jukes *et al.* (2006a, 2008). Figure 2.23 shows a schematic of a symmetric DBD plasma actuator. The upper electrode is situated in the centre of the lower electrode causing plasma to form on both sides of the upper electrode. The DBD plasma actuator can be operated in two modes. The first mode is continuous, where the plasma actuator is operated with 100% duty cycle. The second mode is pulsed. Figure 2.24a) shows the application of plasma in a continuous mode



a)



b)



c)

Figure 2.22: The scaling of velocity with applied voltage, taken from a) Enloe *et al.* (2004b), b) Forte *et al.* (2006) and c) Jukes *et al.* (2006a).

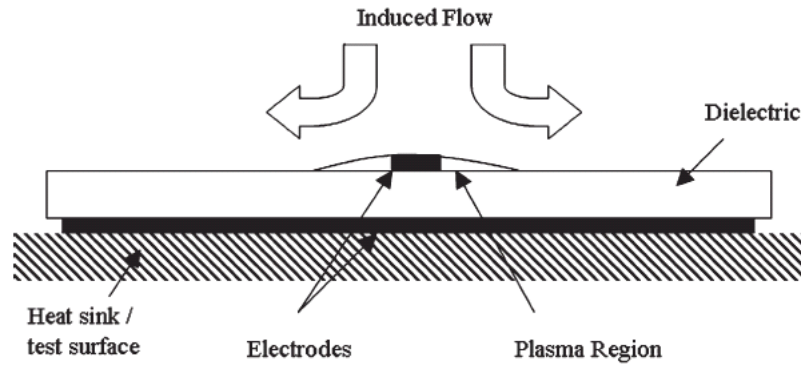


Figure 2.23: A symmetric DBD plasma actuator. Taken from Jukes *et al.* (2008).

where two starting vortices can be seen emanating from either side of the upper electrode. In a pulsed mode, Figure 2.24b), a train of individual starting vortices are produced, one for every time the plasma is pulsed, these will eventually agglomerate downstream of the plasma forcing into a larger vortex. Once the starting vortices have sufficiently moved far downstream a laminar wall jet is developed. Jukes *et al.* (2008) also performed thermal imaging around the symmetric actuator and found that the air was heated to approximately  $4^\circ$  above ambient temperature with an applied voltage of  $7 \text{ kV}_{\text{p-p}}$  (peak to peak) at  $25 \text{ kHz}$ . It was not expected that the flow was thermally driven due to the low amount of heat that was generated.

DBD plasma actuators can have different geometrical designs. Here, a couple of different styles of actuators will be given purely to show that the DBD plasma actuator does not have to be of an asymmetric or symmetric style, or have only two electrodes. So far the asymmetric and symmetric DBD plasma actuators that have been discussed both generate wall jets that are tangential to the wall. The actuator shown in Figure 2.25 is an example of an annular ring. In this case on application of DBD plasma, the wall jets move inwards towards the centre of the ring and the air is pushed vertically upwards to create a wall-normal jet (Santhanakrishnan and Jacob, 2006b; Segawa *et al.*, 2008). The streamlines of the cross-section of the mushroom type vortex that is produced is shown in Figure 2.25b). An example of a new design of plasma actuator is

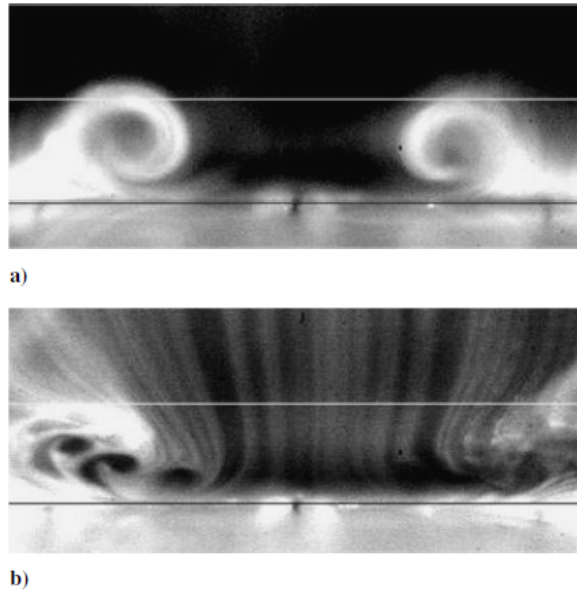


Figure 2.24: The starting vortex from a symmetric DBD plasma actuator, a) steady operation and b) pulsed operation. Taken from Jukes *et al.* (2006a).

shown in Figure 2.26 and has been termed a sliding discharge (Moreau *et al.*, 2008). In the arrangement there are three electrodes, Figure 2.26a). A conventional DBD plasma discharge is created by electrodes #1 and #3 and is shown in Figure 2.26b). When a high DC voltage is supplied to actuator #2, the discharge slides and fills the entire gap between the two upper electrodes (which in this case is 40 mm), creating plasma over a large volume. The sliding discharge was able to increase the obtainable maximum velocity as well as the area of coverage in the experiments of Moreau *et al.* (2008) by a factor of two with little noticeable increase in power, which may have some potential for flow control in the future. An in-depth review of non-thermal plasma actuators can be found in Moreau (2007).

### 2.3.2 Flow Control with DBD Plasma

Over the past decade DBD plasma has been used extensively for aerodynamic flow control (Corke *et al.*, 2010), ranging from flow-separation control of aerofoils (Post and Corke, 2003; Roth, 2003; Corke and Post, 2005; Patel *et al.*, 2008; He and Corke, 2009) and circular cylinders (Jukes and Choi, 2009b; McLaughlin *et al.*,

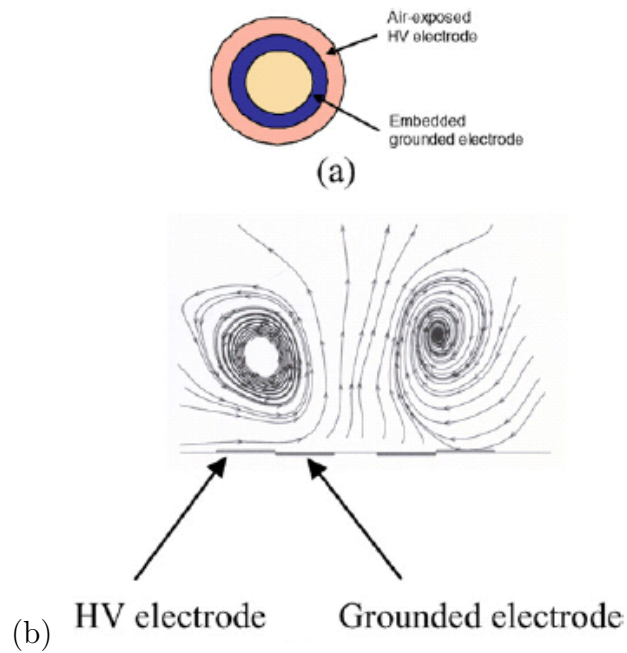


Figure 2.25: An illustration of an annular actuator capable of creating a wall-normal jet, a) schematic of the actuator and b) streamlines of the induced vortices and jet. Taken from Santhanakrishnan and Jacob (2006b).

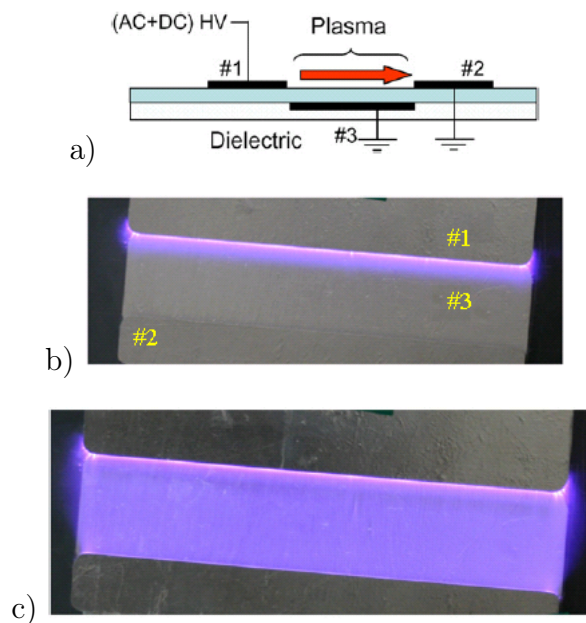


Figure 2.26: Sliding discharge, a) schematic of the DBD plasma actuator (side view), b) standard DBD operation (plan view) and c) sliding discharge (plan view). Taken from Moreau *et al.* (2008).

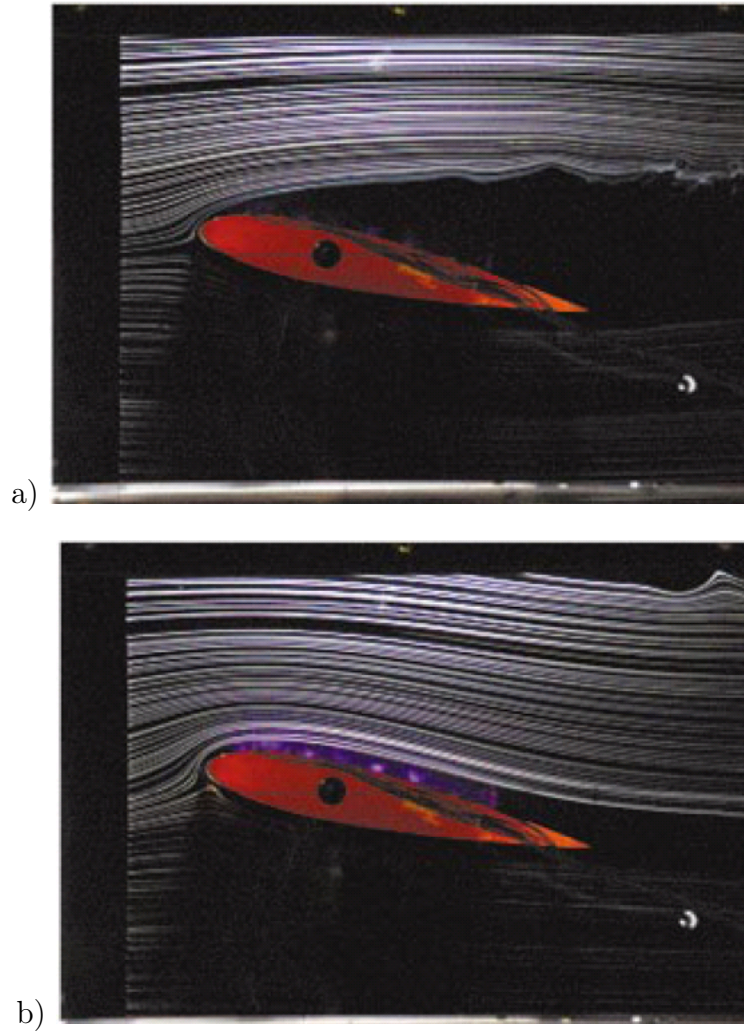


Figure 2.27: Flow-separation control over an aerofoil, a) plasma off and b) plasma on. Taken from Roth (2003).

2004; Munska and McLaughlin, 2003), to noise attenuation of cavity flows (Huang and Zhang, 2008) and the control of turbulent boundary layers (Wilkinson, 2003; Jukes, 2007). It has been shown that DBD plasma actuators can act as efficient turbulent trips (Porter *et al.*, 2007) and can also be used to delay laminar-to-turbulent transition by actively cancelling Tollmein-Schlichting waves artificially produced in the laminar boundary layer (Grundmann and Tropea, 2007, 2008, 2009).

In Figure 2.27 flow visualisation has been taken from Roth (2003), who applied DBD plasma along the upper surface of a NACA 0015 aerofoil which was at an angle of attack of  $12^\circ$  in a free-stream velocity of 2.85 m/s. In Figure 2.27a) the

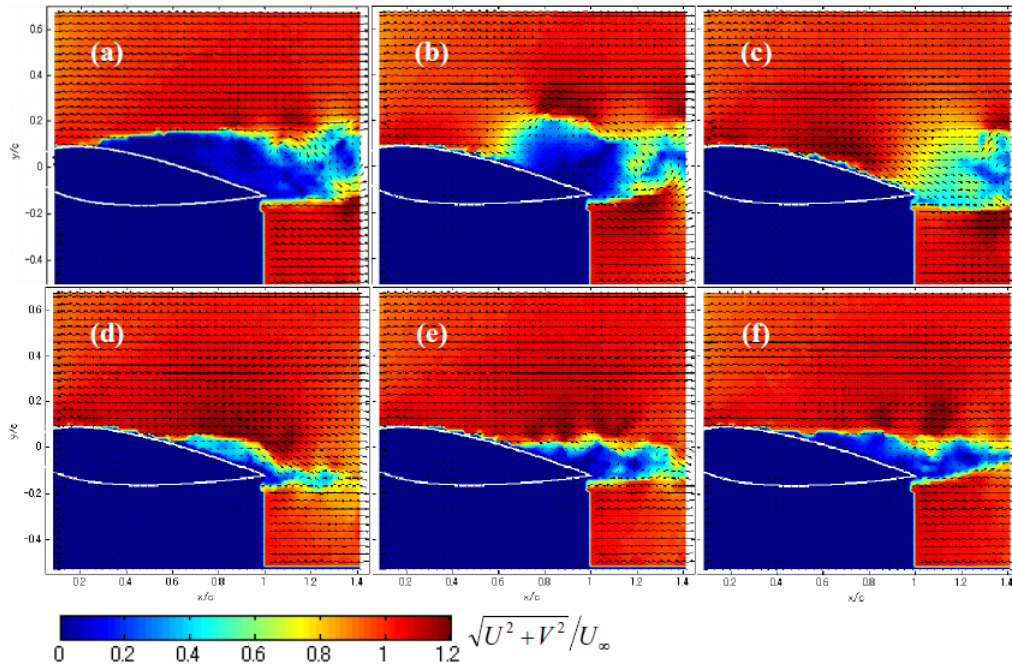


Figure 2.28: Flow-separation control of a NACA 0024 aerofoil. Taken from Okita *et al.* (2008).

flow is separated and the wake at the back of the aerofoil can clearly be seen. On application of DBD plasma forcing in the flow direction, momentum was added to the separated boundary layer, Figure 2.27b), causing the the flow to become reattached, increasing lift and reducing the drag.

Another example of the change in flow structure over an aerofoil with DBD plasma is shown in Figure 2.28. These figures have been taken from Okita *et al.* (2008) who applied an asymmetric DBD plasma actuator to the upper surface of a NACA 0024 aerofoil. The DBD plasma actuator was of an asymmetric style and was placed at 30% of the chord length downstream from the leading edge. The plasma actuator was placed at a yaw angle to the flow. In Figure 2.28a) the flow is separated which is clearly identifiable by the low-speed wake region over the top of the aerofoil. As the plasma is activated, the flow becomes reattached, Figure 2.28b) and c). The plasma is then switched off and it can be seen in Figures 2.28d) to e) that the flow returns back to its naturally separated state. Inside the flow, the DBD plasma actuator would create a large-scale streamwise vortex which would entrain the high-speed flow from the outer boundary layer

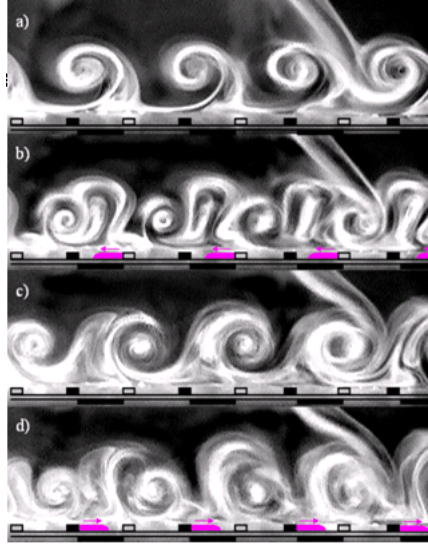


Figure 2.29: Flow visualisation of spanwise wall oscillation with DBD plasma, a)  $t = \frac{2\pi}{3}$ , b)  $t = \pi$ , c)  $t = \frac{5\pi}{3}$  and d)  $t = 2\pi$ . Taken from Jukes (2007).

into the near-wall region causing flow reattachment. Hence, the DBD plasma was used as an active vortex generator.

A spanwise oscillation with DBD plasma was generated by Wilkinson (2003) with the aim of applying DBD plasma to the turbulent boundary layer to achieve skin-friction drag reduction. Wilkinson (2003) generated the spanwise oscillation by using a pair of lower electrodes positioned under one upper electrode. A frequency modulating input was supplied to the lower electrodes to form plasma on either side of the upper electrode which oscillated in time. An initial study was performed using hot-wire anemometry in quiescent air. However, due to the frequency modulation, there were times during the cycle when the plasma formed on both sides of the upper electrode causing the wall jets to collide which created a wall-normal jet. This was thought to be unsatisfactory and the spanwise oscillation was not tested in the turbulent boundary layer. Spanwise oscillation with DBD plasma was also conducted by Jukes (2007), who used two sets of asymmetric plasma actuators to generate a spanwise oscillation. Figure 2.29 shows flow visualisation in quiescent air with the direction of the actuated plasma actuators as indicated in the figure. The first set of asymmetric DBD plasma actuators caused a set of co-rotating vortices, Figure 2.29a). On application of the second

set of asymmetric actuators, Figure 2.29b), a set of counter-rotating vortices were formed that consumed the co-rotating vortices from the previous actuation. The same process continues through Figure 2.29c) and d). The spanwise oscillation was placed in the turbulent boundary layer with a free-stream velocity of 1.8 m/s and studied using hot-wire anemometry. It was found that a skin-friction drag reduction of up to 45% could be achieved. It was thought that the spanwise oscillation with DBD plasma was twisting the quasi-streamwise vortices in the near-wall region, producing a negative spanwise vorticity and reduced the near-wall gradient, similar to the boundary-layer control with spanwise-wall oscillation (Choi, 2002). It was postulated that the starting vortices generated on initiation of DBD plasma could still be present in the turbulent boundary-layer flow, although their role on the drag reduction mechanism was unclear.

It has been shown that DBD plasma actuators are simple, electrical devices that do not require the need for complicated holes, ducting or cavities. The DBD plasma actuators have very quick response times and due to their material, can be fitted to existing airframes. Hence, the DBD plasma actuator can be operated only when required and does not have profile drag penalty as it is a surface-based device. This makes DBD plasma actuators an ideal candidate for wall-based flow-control techniques, such as the spanwise travelling-wave technique. In Chapter 4, a single asymmetric DBD plasma actuator will be studied in quiescent air, so that the flow field created with the DBD plasma actuator can be studied and the associated flow physics understood. Once, the flow physics created by a single DBD plasma actuator have been examined, actuator arrays will be developed in Chapter 5 to create spanwise travelling waves in air. In Chapters 6 and 7, the spanwise travelling wave actuator arrays will be implemented inside the turbulent boundary layer, where the changes in turbulent boundary-layer structure will be carefully documented.

# Chapter 3

## Experimental Set-up

Experiments have been conducted in both quiescent air and inside a turbulent boundary layer using hot-wire anemometry, smoke-flow visualisation and Particle Image Velocimetry (PIV). Details of these diagnostic tools and the wind tunnel facility will be outlined in this chapter.

### 3.1 Wind Tunnel

The turbulent boundary-layer measurements to be described in Chapters 6 and 7 have been conducted inside a low-speed, closed-loop wind tunnel, Figure 3.1. The wind tunnel is driven by a 7.5 kW motor, contains a fan and a series of mesh screens and honeycomb to enhance flow uniformity and to reduce turbulence. There was a 7:1 contraction from the settling chamber to test section and the maximum attainable flow speed was 10 m/s using the current controller.

The wind tunnel had an octagonal geometry with the test section having a cross-section of 508 mm x 508 mm. The boundary layer was developed on the underside of a 3 m long flat plate positioned in the upper part of the wind tunnel, Figure 3.2. The flat plate was fabricated from polished MDF that was 20 mm in thickness and had a super-elliptic leading edge with a semi-major axis of 75 mm. A nearly zero pressure gradient was kept along the test section by adjustment of a trailing-edge flap and by the slightly diverging walls of the test

section, Figure 3.3. A trip was placed 100 mm downstream of the leading edge of the flat plate, Figure 3.4. The trip consisted of a series of 3 mm diameter rods which were 10 mm in height and extended for 60 mm in the streamwise direction. The Reynolds number based on trip height,  $Re_h = \frac{hU_\infty}{\nu}$ , was 1100 and effectively tripped the flow into a turbulent regime.

Measurements were typically taken 2.3 m downstream of the leading edge of the flat plate, where the boundary was fully developed and turbulent. The free-stream velocity,  $U_\infty$ , was set to 1.7 m/s producing a boundary-layer thickness,  $\delta$ , of 90 mm and a viscous sublayer thickness of 1 mm. The Reynolds numbers based on streamwise distance,  $Re_x = \frac{U_\infty x}{\nu}$ , on momentum thickness,  $Re_\theta = \frac{U_\infty \theta}{\nu}$  and friction velocity,  $Re_\tau = \frac{u_\tau \delta}{\nu}$  were  $2.6 \times 10^5$ , 1024 and 435 respectively and the free-stream turbulence intensity,  $\frac{u'}{U_\infty}$ , was 0.24%. The wind tunnel was placed in a climate control room which had a Denco air conditioner unit that kept the ambient temperature to  $17 \pm 0.5^\circ\text{C}$  for the hot-wire measurements and to  $20 \pm 0.5^\circ\text{C}$  for the PIV measurements.

## 3.2 Removable Test Plate

The plasma actuator sheets (that will be introduced in §3.8) were flush mounted into the wind tunnel with the aid of the Perspex test plate shown in Figure 3.5, which acts as a good insulator if the plasma sheet failed leading to arcing. The Perspex test plate was 408 mm x 336 mm and was 10 mm in thickness. Two 408 mm x 20 mm slats of 10 mm thickness were bonded with Tensol to the lower surface on the outside edges of the test plate. The two slats had in total 4,  $\text{Ø}6$  mm tapped holes for studding and thumb screws which were used to lower the test plate into the wind tunnel, 1.9 m downstream of the leading edge of the flat plate, Figure 3.1c).

The travelling-wave actuator sheets were bonded with doubled sided adhesive tape to the Perspex test plate. There was a small 287 mm x 30 mm pocket

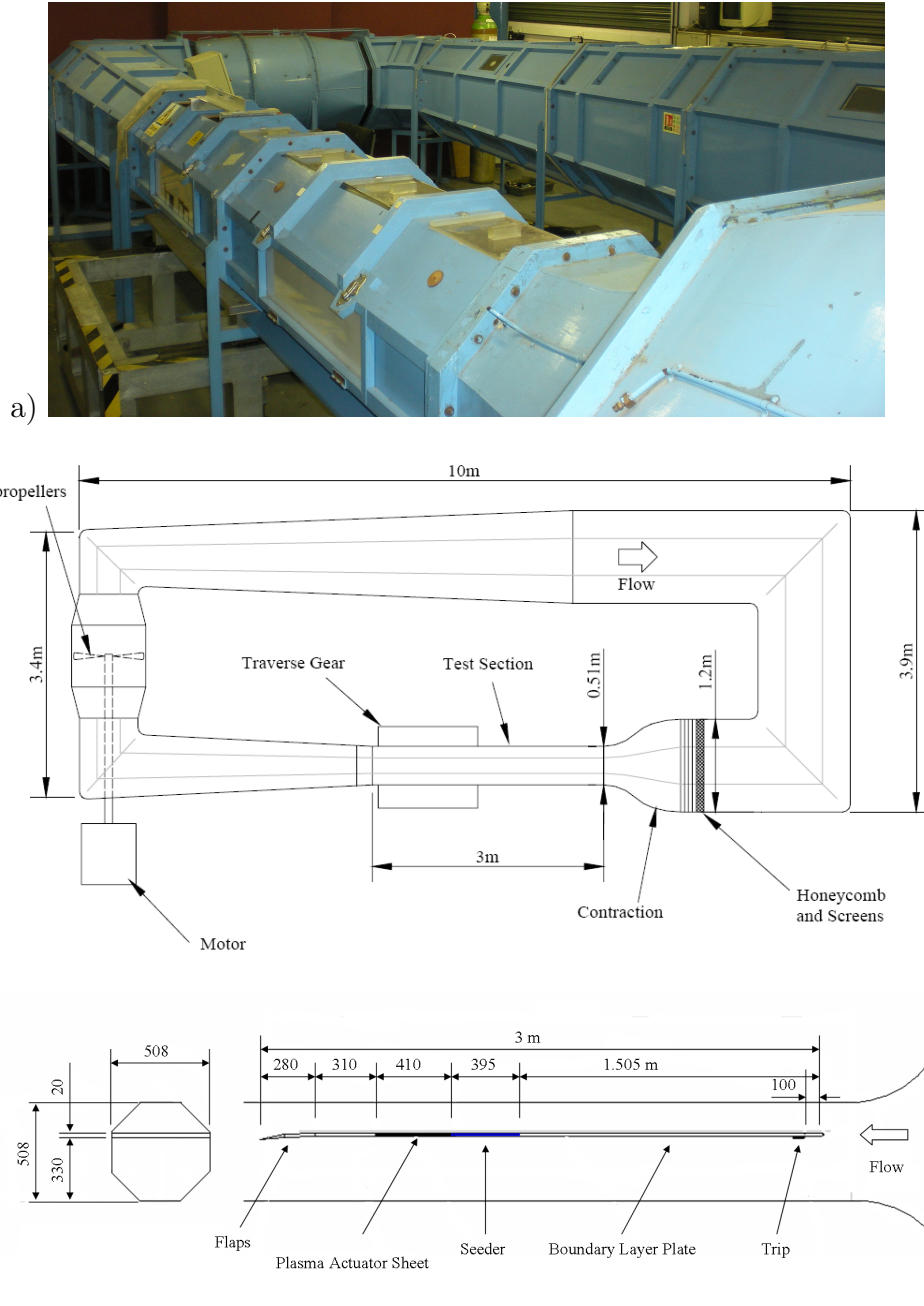


Figure 3.1: Wind tunnel test facility a) picture of the closed-loop wind tunnel, b) schematic of the closed-loop wind tunnel and c) cross-section of the test section.



Figure 3.2: Upper surface of the test section.



Figure 3.3: Trailing-edge flap.



Figure 3.4: Turbulent trip.

milled through the test plate to allow the electrical connections to the plasma actuator sheet. A small step of 250  $\mu\text{m}$  can be seen in Detail A of Figure 3.5. The plasma actuator sheets were 250  $\mu\text{m}$  in thickness and were flush mounted against the Perspex step. This was designed so that the hot-wire measurements of Chapter 6 could be performed on a solid insulating wall allowing the wall location to be obtained (Hutchins and Choi, 2002). Hot-wire measurements over the Mylar dielectric have been known to cause errors with the interpretation of the wall location (Jukes, 2007), since the dielectric deforms as the hot wire is traversed towards the dielectric surface. The step change between the actuator sheet and Perspex plate was on the order of 50  $\mu\text{m}$  ( $y^+ = 0.3$ ), therefore hydraulically smooth. Any gaps were filled with an epoxy based filler and then smoothed using emery paper.

### 3.3 Hot-wire Anemometry

Hot-wire anemometry has been used to study turbulent boundary-layer control with spanwise travelling waves in Chapter 6. Hot-wire anemometers measure the flow velocity by sensing the convective heat transfer from a heated thin wire which is exposed to the flow. The change in convective heat transfer can be detected by either measuring the change in resistance of the wire as it is altered by the flow velocity (constant current mode) or by measuring the change in current that is needed to keep the wire at constant temperature (constant temperature mode) (Bruun, 1995).

The hot-wire anemometry system used was a Dantec 56B10 main frame, which allowed multiple plug in units, Figure 3.6. The Dantec unit is enclosed in a copper Faraday cage, which prevented electro-magnetic noise contaminating the hot-wire signals. For velocity measurements, Dantec 56C01 Constant Temperature Anemometers (CTAs) were used with Dantec 56C17 bridge units with Dantec 56N20 signal conditioners. For temperature measurements, a Dantec 56C20 tem-

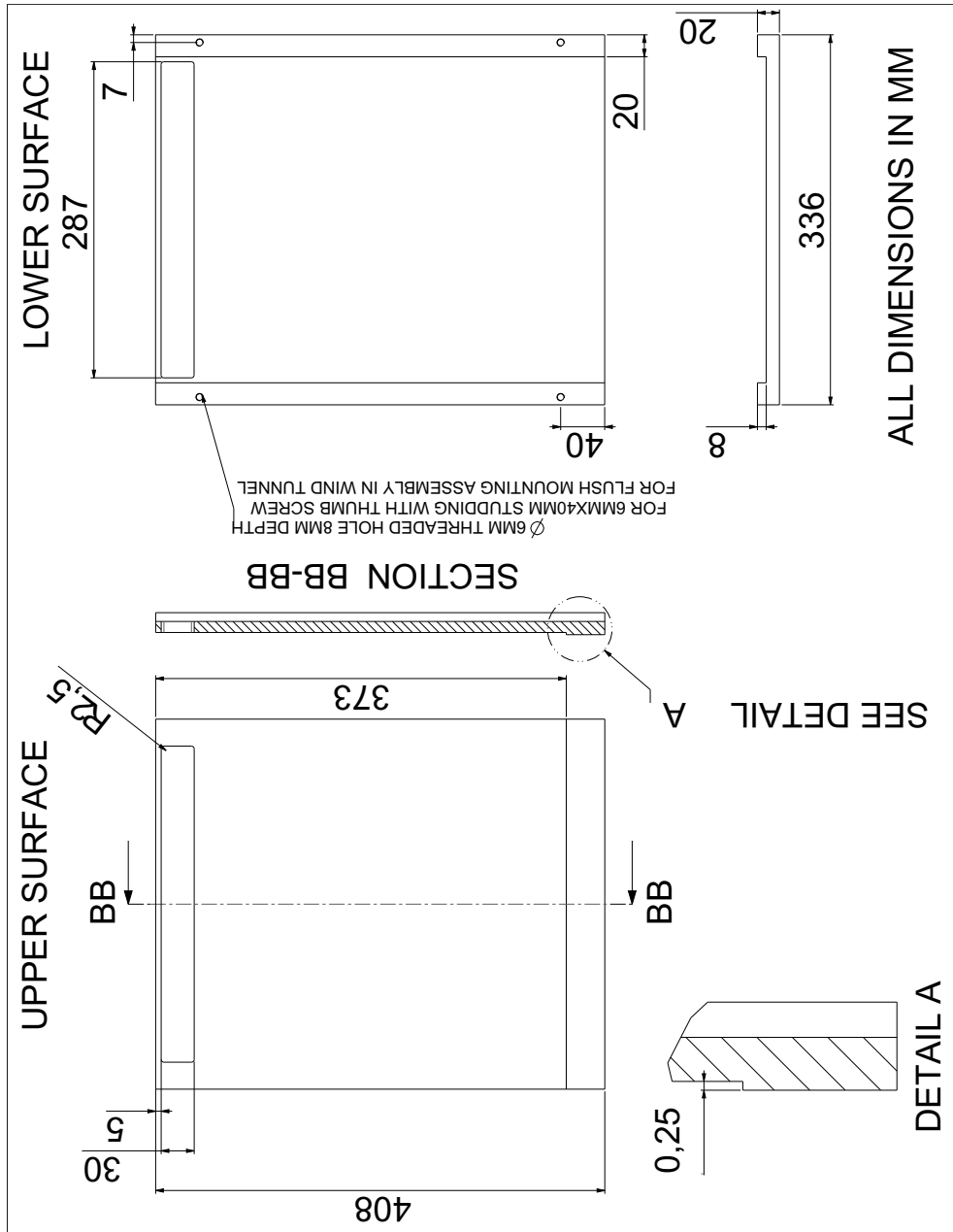


Figure 3.5: Details of the Perspex test plate that has been used to flush mount the plasma actuator sheets inside the wind tunnel.



Figure 3.6: Dantec CTA system with multiple plug in units enclosed in a copper Faraday cage.

perature bridge was used in constant current mode. Temperature measurement in a constant current mode is usually termed cold-wire anemometry.

A Dantec 55P15 boundary-layer probe with a swan-neck, Figure 3.7a), was used for the velocity measurements in the boundary layer. This allows measurements to be taken close to the wall. This type of probe has a platinum-plated tungsten wire which has a diameter of  $5\ \mu\text{m}$  and is 1.25 mm in length. The 55P15 probe was operated with an overheat ratio of 1.8, which gave the probe a high operating temperature, typically around  $230^\circ\text{C}$ . This enabled high sensitivity to velocity changes whilst minimising sensitivity to ambient temperature change. The 55P15 probe was plugged into the 56C17 bridge and operated in constant temperature mode such that the probe formed one arm of a Wheatstone bridge. The flow over the wire, induces a change in the convective heat transfer which causes changes to the temperature and resistance of the wire. This leads to an off-balance in the Wheatstone bridge which is detected by an operational amplifier. The off-balance is corrected by applying a change in voltage and current to the hot-wire probe which maintains the wire at constant temperature. The change in voltage applied to the wire can be measured at the rear of the 56B10 main frame.

A Dantec 55P31 cold-wire probe, Figure 3.7b), was used for the temperature measurements in the boundary layer. This probe has a platinum wire which has

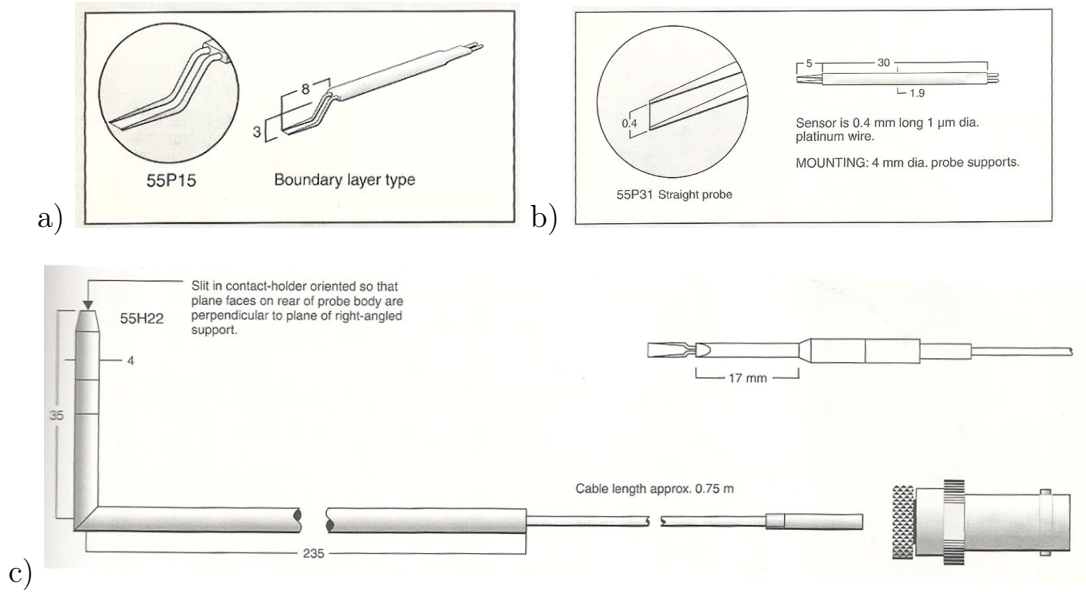


Figure 3.7: Hot-wire anemometry probes and holder a) 55P15 hot wire for velocity measurements, b) 55P31 cold wire for temperature measurements and c) 55H22 L-shaped hot-wire probe support. Courtesy of Dantec Dynamics.

a diameter of  $1 \mu\text{m}$  and is  $0.4 \text{ mm}$  in length. The probe was operated in constant current mode at  $0.2 \text{ mA}$  with an overheat ratio close to 1. This maintained the wire very close to ambient temperature. The 55P31 probe was controlled by the 56C20 temperature bridge and connected so that the probe formed one arm of a Wheatstone bridge. The heated or cooled flow would cause a change in the resistance of the wire, causing an off-balance in the Wheatstone bridge. The bridge (and hence cold wire) was compensated by applying a corrective change in voltage. This change in voltage was directly proportional to the temperature change of the fluid and the change in resistance of the wire as the probe was held at constant current. The change in voltage could be measured at the rear of the 56B10 main frame.

Each of the Dantec 55P15 and 55P31 probes was held in place during boundary layer traverses by a Dantec 55H22 L-shaped probe support, Figure 3.7c). Prior to sampling, the hot-wire signals were passed through a Dantec 56N20 signal conditioner. The signal conditioner had a 2<sup>nd</sup> order low-pass Butterworth filter, a 1<sup>st</sup> order high-pass filter and had a gain amplifier to minimise the signal-to-noise ratio (SNR). For the hot-wire data in this study, a low-pass filter of

300 Hz and a gain of 5 was applied to each hot-wire signal.

On application of DBD plasma, large amounts of high frequency electromagnetic noise is generated ( $> 50$  kHz), which could potentially contaminate the hot-wire signals. To prevent the hot-wire signals from being susceptible to electrical interference, the entire CTA was housed in a copper Faraday cage, Figures 3.6 and 3.8a), and appropriately grounded. Ferrite cores, Figure 3.8b), were applied to each end of all BNC cables used with the hot-wire anemometry system (Jukes, 2007). These were used to absorb any high frequency noise that was being passed down or radiated on to any BNC line which was transmitting data. To test the levels of noise on the hot-wire signals, a 55P15 boundary-layer probe was placed 1 mm from the wall and 10 mm away from the DBD plasma in quiescent air. It was found that the electrical interference generated with DBD plasma led to a velocity change on the order of  $\Delta U = 0.005$  m/s. This is a negligible level of noise interference. Hence, the hot-wire signals were considered devoid of noise due to electrical interference. Typically for turbulent flows with a turbulence intensity,  $\frac{u'}{U}$ , of less than 20%, the error in the velocity measurements is approximately 2% (Bruun, 1995; Lee, 2008). The maximum turbulence intensity in the boundary layer is 12%, hence the velocity measurements have error less than 2%.

### 3.3.1 Hot-wire Probe Calibration

Prior to calibration, each hot wire was optimised as part of the bridge. To optimise the hot wires, a square wave was applied to the hot-wire bridges. The applied square wave simulated a step change in velocity and allowed the frequency response of the hot-wire probes to be determined. The optimal response of a hot-wire probe is shown in Figure 3.9a) taken from Bruun (1995). The response from each hot wire was optimised by changing the anemometer unit gain, filter and high frequency balance until a response as shown in Figure 3.9a) was achieved. The optimised response from a Dantec 55P15 boundary-layer probe is shown in Figure 3.9b), and has a cut-off frequency,  $f_c$ , of 80 kHz. The measured hot-wire

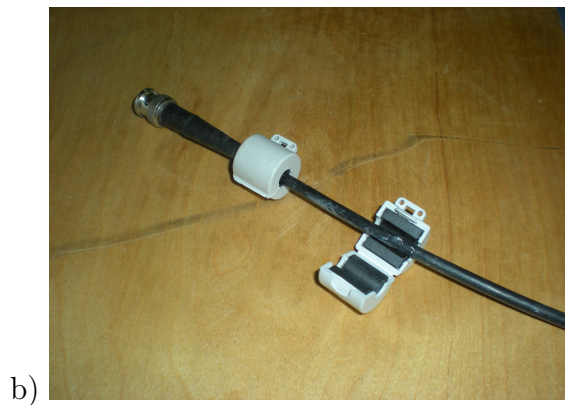


Figure 3.8: Mitigation of radiated electrical noise a) copper Faraday cage, b) ferrite cores and c) EMI shielding.

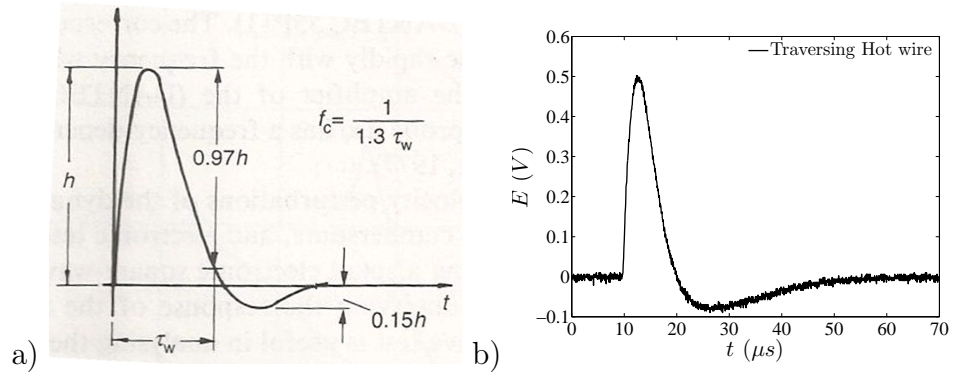


Figure 3.9: Optimisation of a hot-wire probe from a square wave test, a) optimal response from Bruun (1995) and b) optimised response from a 55P15 boundary-layer probe ( $f_c = 80$  kHz).

response, Figure 3.9b), is very similar to the optimised hot-wire response taken from Bruun (1995), Figure 3.9a).

For the boundary-layer tests to be described in Chapter 6, two Dantec 55P15 boundary-layer probes were used. One probe was used to obtain the boundary-layer profile (traversing probe) and another was positioned in the free stream (free-stream probe). The ambient temperature drift was monitored using a LM35 Precision temperature sensor, which had an accuracy of  $\pm 0.5^\circ\text{C}$ , allowing the hot-wire data to be compensated accordingly.

The positions of all sensors during a calibration are shown in Figure 3.10. The hot-wire probes were calibrated against a Dantec 54T28 FlowMaster. The FlowMaster was precalibrated by the manufacturer, having an accuracy of  $\pm 0.02$  m/s and corrected itself for ambient temperature drift using a thermistor. The traversing probe ②, free-stream probe ④ and FlowMaster ③ were positioned at the same plane in the wind tunnel, 50 mm apart and 150 mm from the upper wall. This ensured that the probes were outside of any boundary layer, secondary flows and located in the free stream. A temperature sensor monitoring ambient temperature can be seen at ①. The general calibration procedure was to sample the hot wire and FlowMaster voltage signals simultaneously for 10 seconds at 17 different free-stream velocities which ranged from 0-2.5 m/s. Care was taken to check for hysteresis of the calibrations by taking points up and down the full velocity

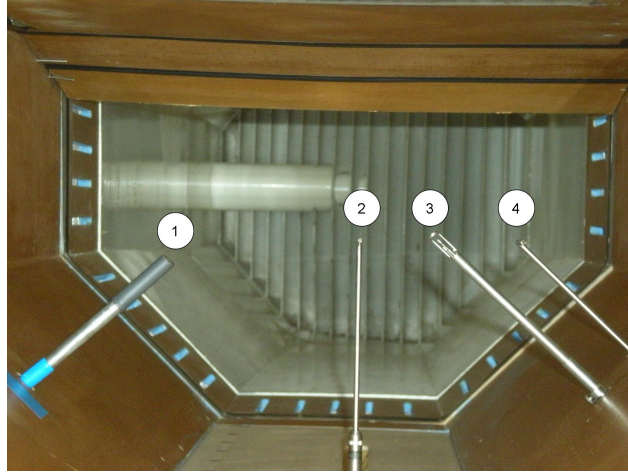


Figure 3.10: A picture taken inside the wind tunnel demonstrating hot-wire calibration, showing ① temperature sensor, ② traversing hot-wire probe, ③ Flow-Master and ④ free-stream hot-wire probe.

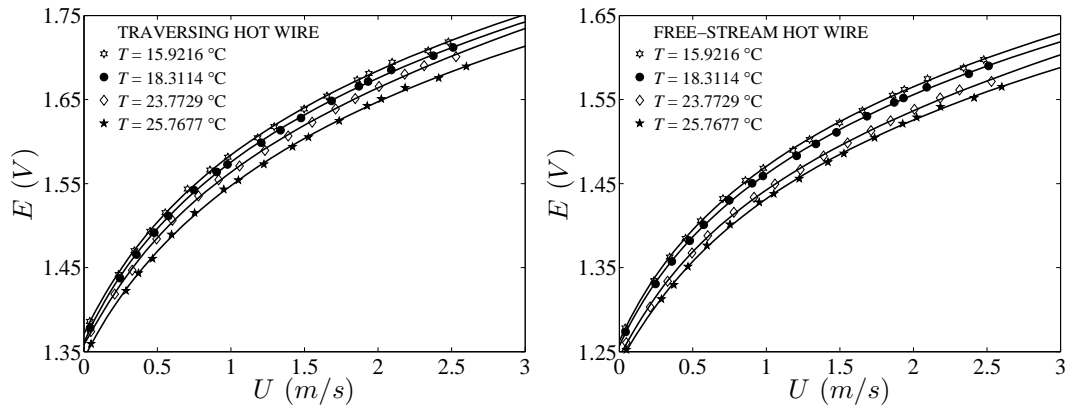


Figure 3.11: Hot-wire calibration curves over a range of temperatures, a) traversing probe and b) free-stream probe.

range. Hot wires are sensitive to ambient temperature drift, therefore the temperature for each calibration was recorded. The experimental results were then corrected by linearly interpolating between calibration curves. Examples of the hot-wire probes calibration curves fitted with 4<sup>th</sup> order polynomials for a temperature range of 16°C-26°C can be found in Figure 3.11. In this figure, there are 4 calibration curves presented for clarity, in total 10 calibration curves were taken each separated by approximately 1°C. The hot-wire calibrations were taken over a 10°C range as it is known that on application of DBD plasma a thermal boundary layer is created (Jukes, 2007).

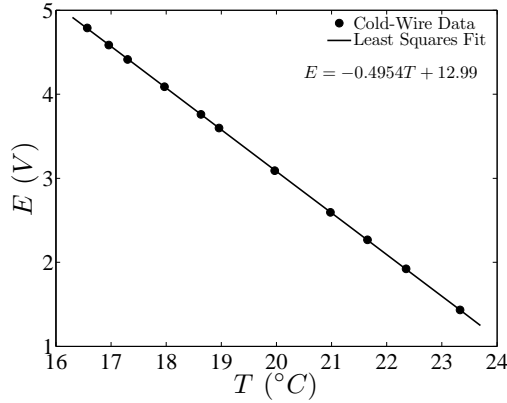


Figure 3.12: Cold-wire calibration.

### 3.3.2 Cold-wire Probe Calibration

The Dantec 55P31 cold-wire probe was used in constant current mode for the thermal boundary-layer measurements inside the turbulent boundary layer with DBD plasma, §6.2.1. It was possible to calculate the sensitivity of the probes to temperature by applying a 1% change in current to the cold wire, which simulated a 1% change in wire resistance, where it was found that the sensitivity of the probe was  $-0.474 \text{ V}/^\circ\text{C}$ . This was verified by calibrating the cold-wire probe against the LM35 temperature sensor, Figure 3.12. The calibration found a sensitivity of  $-0.495 \text{ V}/^\circ\text{C}$ , which was within 5% of the calculated sensitivity. The temperature sensor used during the calibration had an accuracy of  $\pm 0.5^\circ\text{C}$ , hence the calculated sensitivity was thought to be more reliable and used for data analysis.

## 3.4 Traversing System

The traversing probe was mounted on a three-axis traverse mechanism, which consisted of three stepper motors fitted with ball-race worm drives which produced little backlash. The stepper motors were powered and controlled by CD25 Digiplan controllers, programmable with an IEEE488 interface to a PC. The stepper motors moved the probe independently in the  $x$  (streamwise),  $y$  (wall-normal) and  $z$  (spanwise) directions. The resolution of the stepper motors in the  $x$  and

$z$  directions was  $2.5 \mu\text{m}$ , and  $1.25 \mu\text{m}$  in the  $y$ -direction. It was found that the stepper motor power cables produced electro-magnetic interference (EMI) which potentially could contaminated the hot-wire signals. To stop any radiated noise, EMI shield, Figure 3.8c), was used on the stepper motor transmission cables.

### 3.5 Data Acquisition

The hot-wire signals were simultaneously sampled and converted into binary format with an 8 channel 16-bit Iotech 488/8SA analogue-to-digital converter (ADC). The ADC had programmable inputs with ranges of  $\pm 1$ ,  $\pm 2$ ,  $\pm 5$  and  $\pm 10$  V. The ADC (and traverse mechanism) were controlled using QB programs.

The sampling frequency used throughout this study was 1 kHz. It can be seen through the energy spectra in Figure 3.13 that the turbulence has a cut-off frequency at around 300 Hz. Hence, a sampling rate of 1 kHz is over double the Nyquist frequency needed to resolve the smallest scales within the flow. To establish the length of time needed to sample the flow, analysis taken from Tennekes and Lumley (1972) and Bruun (1995) is used. The total sampling time,  $T_s$ , required at each location in the turbulent boundary layer can be expressed as,

$$T_s = N\Delta t, \quad (3.1)$$

where  $N$  is the total number of independent samples required and,

$$\Delta t = 2T_i. \quad (3.2)$$

$T_i$  is the integral time scale —average time-scale of energy-containing eddies— and correspondingly  $\Delta t$  is the optimum sampling interval. To evaluate the integral time scale,  $T_i$ , an auto-correlation function,  $R_{uu}(\tau)$ , is defined such that,

$$R_{uu}(\tau) = \lim_{T \rightarrow \infty} \frac{1}{T} \int_0^T u(t) u(t + \tau) dt, \quad (3.3)$$

where  $u(t)$  is the fluctuating streamwise velocity time-series at a given point in the turbulent boundary layer and  $R_{uu}(\tau)$  represents the interdependence (or correlation) of  $u(t)$  with  $u(t + \tau)$ . The auto-correlation function is then normalised to obtain the auto-correlation coefficient,  $\rho_{uu}(\tau)$ ,

$$\rho_{uu}(\tau) = \frac{R_{uu}(\tau)}{R_{uu}(0)}, \quad (3.4)$$

the integral of which forms the integral time scale,  $T_i$ ,

$$T_i = \int_0^{\infty} \rho_{uu}(\tau) d\tau. \quad (3.5)$$

The integral time scale,  $T_i$ , computed at the location of maximum turbulence intensity,  $y^+ = 15$ , is shown in Figure 3.14 along with the fluctuating streamwise velocity signal at that point. It can be seen that the integral time scale is equal to 45 ms in this case. This implies that a sampling frequency of  $\frac{1}{\Delta t}$  would suffice at obtaining the mean velocity and turbulence intensity of the flow provided  $N$  independent samples were taken. This is true, but as can be seen in Figure 3.13, the turbulence contains small time scales (and hence length scales) that a frequency of  $\frac{1}{\Delta t}$  would not resolve, hence a sampling frequency of 1 kHz has been used.

The measured mean value,  $\bar{U}$ , could be said to lie in a confidence interval somewhere between the true mean value,  $\hat{U}$ ,  $\pm$ some uncertainty. This could be expressed with the use of the normal distribution as,

$$\hat{U} - Z_{\frac{\alpha}{2}} \sigma [\bar{U}] < \bar{U} < \hat{U} + Z_{\frac{\alpha}{2}} \sigma [\bar{U}], \quad (3.6)$$

where  $Z_{\frac{\alpha}{2}}$  is the Gaussian probability density and  $\sigma [\bar{U}]$  is the uncertainty in  $\bar{U}$  and is defined as,

$$\sigma [\bar{U}] = \frac{1}{\sqrt{N}} \frac{u'}{\bar{U}}. \quad (3.7)$$

Hence, to determine the total number of independent samples,  $N$ , required to

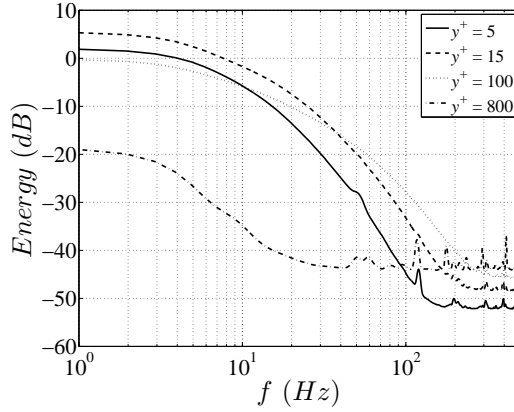


Figure 3.13: Energy spectra throughout the turbulent boundary layer sampled at 1 kHz for 1 hour.

obtain an accuracy for the measured mean,  $\bar{U}$ , within  $\pm 1\%$  of the true mean,  $\widehat{U}$ , with 99% confidence, Eqn. 3.6 can be expressed as,

$$\frac{\bar{U}}{\widehat{U}} = 1 \pm 2.57 \left[ \frac{1}{\sqrt{N}} \frac{u'}{\bar{U}} \right] = 1 \pm 0.01. \quad (3.8)$$

The turbulence intensity,  $\frac{u'}{\bar{U}}$ , at  $y^+ = 15$  is 12%. This allows Eqn. 3.8 to be solved and it is found that 1006 independent samples are required to obtain a measured velocity within  $\pm 1\%$  of the true mean velocity with 99% confidence. Through Eqn. 3.1 this equates to having a total sampling time,  $T_s$ , of 90 seconds. Therefore, a total sampling time of 90 seconds has been used at each location in the boundary layer.

### 3.6 Flow Visualisation

Flow visualisation is one of the oldest scientific techniques used in fluid mechanics, most likely first used by Leonardo Da Vinci who sketched the motions of eddies in a turbulent flow when a free water jet plunged into a pool. Flow visualisation is a useful way of visualising the entire complex motions inside a flow, which at times can be missed with point measurement techniques such as hot-wire or laser-doppler anemometry. A notable example of the flow visualisation technique is the work of Reynolds (1883), who injected dye into a pipe to study the transition from

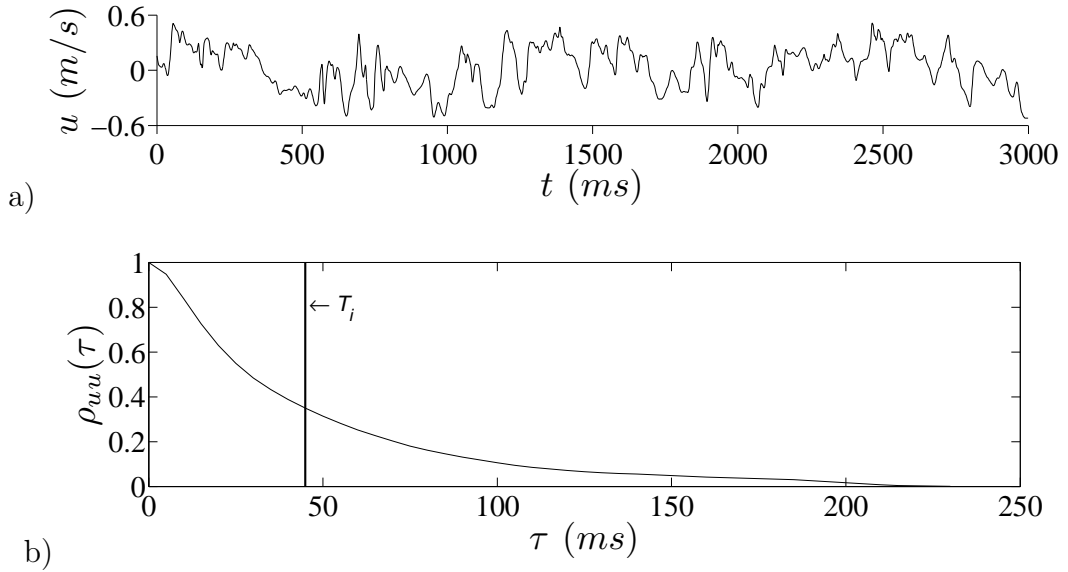


Figure 3.14: Calculation of the integral time scale. a) Velocity fluctuation at  $y^+ = 15$  and b) auto-correlation coefficient of  $y^+ = 15$  data.

laminar flow to a turbulent flow. More recently, smoke-flow visualisation was used in a turbulent boundary layer by Head and Bandyopadhyay (1981) to show the existence of hairpin structures. The results of their study provided motivation for further quantitative analysis of the turbulent boundary-layer structure (Hutchins *et al.*, 2005).

Smoke-flow visualisation was used to study the transient flow field when a DBD plasma actuator is fired in quiescent air, Chapter 4. The flow visualisation experiments were conducted inside a 1.5 m long 508 mm x 508 mm octagonal chamber in a wind tunnel, Figure 3.1. The plasma actuator was positioned in the centre of the chamber. The flow visualisation was performed with a Photron Fastcam SA-3 high-speed camera (1024 x 1024 pixels), Figure 3.15, which was synchronised to a pulsed copper vapour laser that was aligned with the actuator mid-span, Figure 3.16. The laser had a maximum output of 30 W and had a wavelength of 511 nm. The laser was delivered by a fibre-optic cable, which fanned out through a series of optics and produced a 1 mm thick light sheet, Figure 3.17a). Typically 30% power loss was experienced due to the fibre-optic delivery of the laser sheet. Images were taken with a frequency of 1 kHz, with each camera frame exposed to a 30 ns laser pulse. The air was seeded by a fog generator

which created a water based smoke with particles of 1  $\mu\text{m}$  nominal diameter. The camera was set to view a 60 mm x 30 mm area with image calibration performed using a calibration target with a typical conversion of 60  $\mu\text{m}/\text{pixel}$  with  $\pm 0.5\%$  variation over the image area.

The spanwise travelling waves were initially studied in quiescent air, Chapter 5, using the copper vapour laser and Photron Fastcam SA-3 high-speed camera which has been described. For these experiments, PIV was performed using ILA software where image pairs were taken at a frame rate of 500 Hz with the time delay between frames being typically 200-400  $\mu\text{s}$ . Each image was exposed with a 30 ns laser pulse and velocity vectors were computed on a 32 x 32 pixel interrogation area with 50% overlap using a recursive cross-correlation technique, generating 2600 vectors per image pair. Image calibration was performed using a calibration target to an accuracy of  $\pm 0.2\%$  with a typical conversion of 100  $\mu\text{m}/\text{pixel}$ . This gave a spatial resolution of 1.6 mm x 1.6 mm.. The air was seeded using 1  $\mu\text{m}$  nominal diameter glycerin particles and the 1 mm thick light sheet was aligned with the actuator mid-span illuminating the  $z$ - $y$  plane, Figure 3.17b). The black strips on the plasma actuator sheet are matt black paint to stop the reflection of laser light from the white Mylar sheet. The matt black paint could not be painted over the region where the DBD plasma was discharged, as it may change the characteristics of the plasma and hence the travelling-wave excitation.

### 3.7 PIV System

A time-resolved PIV system from TSI has been used for two sets of experiments. The transient flow field created by a DBD plasma actuator in quiescent air has been studied using 2D PIV with results being described in Chapter 4. The turbulent boundary layer with spanwise travelling-wave excitation has been studied using 2D and stereoscopic PIV, the results from these experiments can be found



Figure 3.15: Photron Fastcam SA-3 high-speed camera used for the flow visualisation studies of Chapter 4 and the PIV studies in Chapter 5.



Figure 3.16: Copper vapour laser used in the flow visualisation studies of Chapter 4 and the PIV studies in Chapter 5.

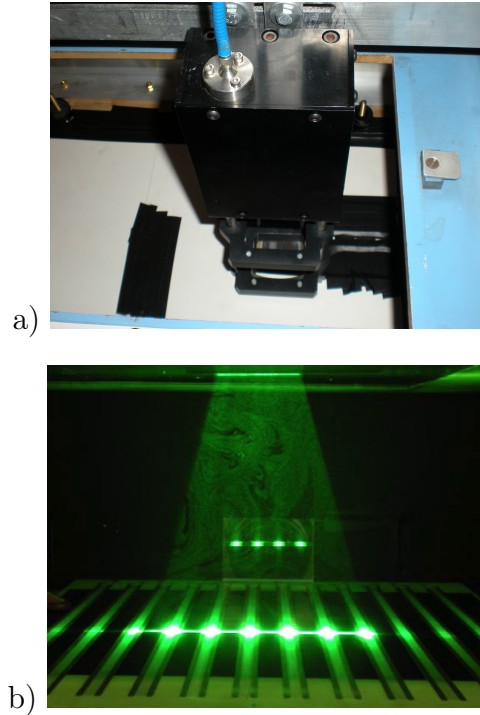


Figure 3.17: Experimental arrangement for the PIV measurements of the spanwise travelling waves in quiescent air. a) Fibre-optic cable delivery and optics and b) 1 mm fanned light sheet for PIV measurements.

in Chapter 7. As previously described in §3.6, the copper vapour laser and Photron Fastcam SA-3 high-speed camera were coupled to create an alternative PIV system which was used to study the spanwise travelling waves in quiescent air.

The time-resolved PIV system from TSI consisted of a Photron APX-RX high-speed camera (1024 x 1024 pixels), a New Wave Research Pegasus PIV laser [45 W Nd:YLF (Neodymium-doped Yttrium Lithium Fluoride)] and a TSI 9307-6 atomiser. The New Wave Research Pegasus laser had a wavelength of 578 nm and a maximum power output of 45 W, which generated 10 mJ/pulse of energy at a bursting frequency of 1 kHz. The laser light was delivered by a laser arm which produced a 1 mm thick fanned light sheet with a focal length of 0.5 m. The data taken with this system was processed using TSI, INSIGHT 3G software.

### 3.7.1 Seeding Mechanism for the Turbulent Boundary Layer

A custom made seeder was fabricated to disperse the seeding particles uniformly into the turbulent boundary layer without causing any disruption to the flow. A drawing of the seeder can be found in Figure 3.18 and a picture in Figure 3.19. The seeder was manufactured from a Perspex plate which was 10 mm in thickness and had dimensions of 395 mm x 336 mm. Three pockets which were 226 mm x 55 mm, were milled into the Perspex plate. Inside each pocket, a 1 mm ( $x^+ = 5$ ) spanwise slot was machined with a slitting saw at an angle of  $15^\circ$  to the flow direction. Each 1 mm slot was separated by a streamwise distance of 120 mm ( $x^+ = 610$ ). A vacuum-formed acrylic cover, 1.5 mm in thickness, was screw fixed above the three pockets with an inlet for a seeding hose. Olive oil droplets with 1  $\mu\text{m}$  nominal diameter filled the chamber created by the acrylic cover, forcing the seeding to disperse through the 1 mm slots and into the flow. Two slats which had dimensions of 395 mm x 20 mm were bonded along the edges of the Perspex plate with Tensol. Each slat had two  $\text{\O}6$  mm threaded holes for studding and thumb screw assembly, enabling the seeder to be flush mounted in the upper section of the wind tunnel. The seeder was positioned directly upstream of the travelling-wave actuator sheet, Figure 3.1c), so that the two Perspex plates (one for the seeding mechanism, and one for the plasma actuator sheet) were positioned side by side in a streamwise orientation.

### 3.7.2 2D PIV Measurements

The time-resolved PIV measurements of the DBD plasma actuator in quiescent air (Chapter 4), were conducted in a 300 mm x 300 mm chamber which was 1.6 m long. The plasma actuator was positioned on the floor of the chamber. Olive oil particles of 1  $\mu\text{m}$  nominal diameter were used to seed the air and the laser was aligned with the actuator mid-span. The camera was set to view a 70 mm x 40 mm area. Image calibration was performed using a calibration target with a typical conversion of 70  $\mu\text{m}/\text{pixel}$  ( $1024 \times 70 \times 10^{-6} = 70 \text{ mm}$ ) with  $\pm 0.2\%$  variation over

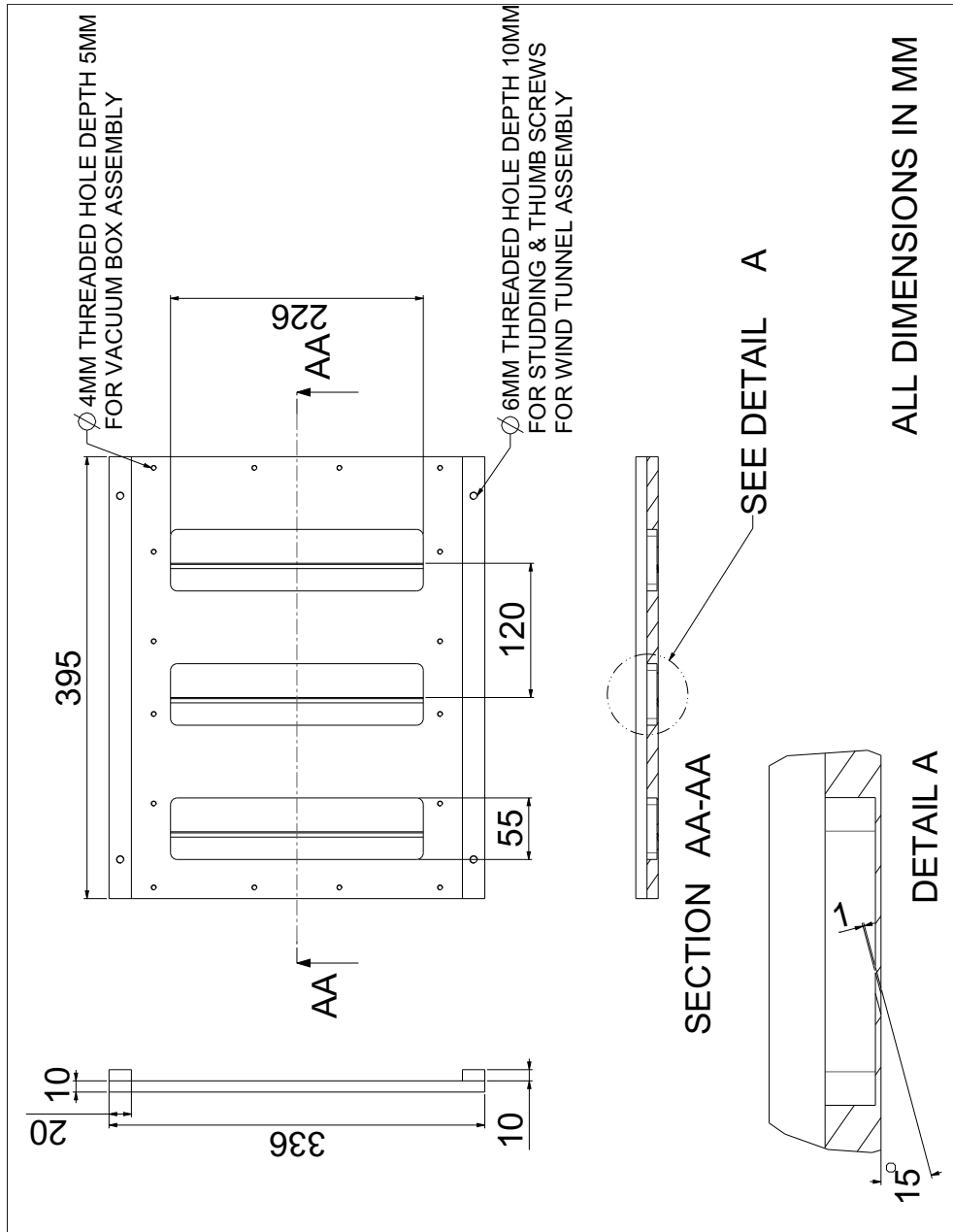


Figure 3.18: Drawing of the seeder used in the PIV measurements of the turbulent boundary layer.

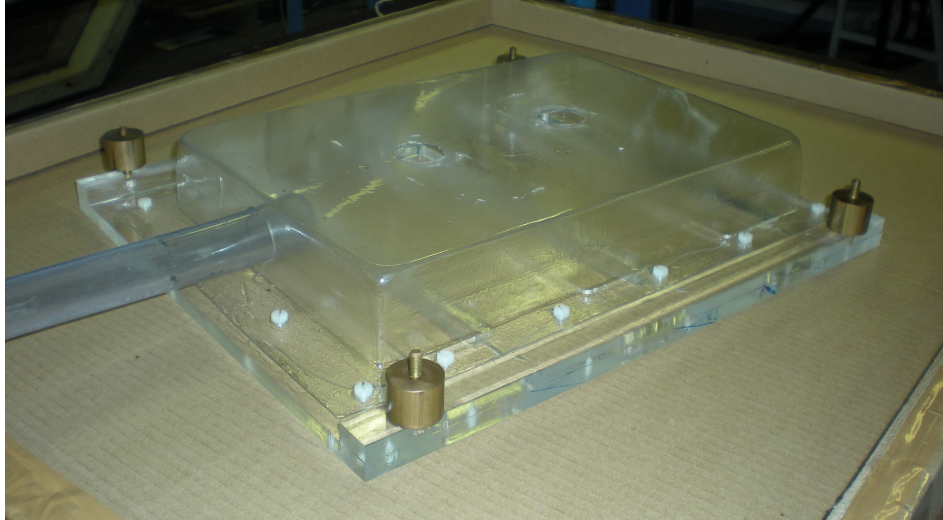


Figure 3.19: Picture of the seeder used in the PIV measurements of the turbulent boundary layer.

the measurement area. Image pairs were taken at a frame rate of 500 Hz, where the time delay between images was typically 200-400  $\mu\text{s}$  with each image exposed to a 10 ns laser pulse. Image processing resulted in less than 2% erroneous vectors before validation. The data were processed on a 20 x 20 pixel interrogation area with 50% overlap using a recursive cross-correlation technique, which generated 6000 vectors per image pair at spatial resolution of 0.7 mm x 0.7 mm.

Measurements in the  $x$ - $z$  plane of the turbulent boundary layer (Chapter 7) were conducted using time-resolved PIV. Images were taken with a 105 mm Sigma f/2.8 lens, with the aperture fully open. Image pairs were taken at a frame rate of 750 Hz with the time delay between frames being typically 200  $\mu\text{s}$ . Each image was exposed with a 10 ns laser pulse. PIV velocity vectors were computed on a 32 x 32 pixel interrogation area with 50% overlap using a recursive cross-correlation technique, generating 4000 vectors per image pair. This resulted in less than 3% erroneous vectors prior to validation. Image calibration was performed using a calibration target to an accuracy of  $\pm 0.2\%$  with a typical conversion of 100  $\mu\text{m}/\text{pixel}$ . This gave a spatial resolution of 1.6 mm x 1.6 mm (8 x 8 wall units). A picture of the experimental arrangement demonstrating the position of the camera and laser can be found in Figure 3.20.



Figure 3.20: Experimental arrangement for the 2D PIV measurements in the  $x$ - $z$  plane of the turbulent boundary layer.

### 3.7.3 Stereoscopic PIV Measurements

Measurements in the  $z$ - $y$  plane were conducted using time-resolved stereoscopic PIV. The stereoscopic PIV system was identical to the 2D PIV system with an additional Photron APX-RX high-speed camera (1024 x 1024 pixels). Each camera was used with a 105 mm Sigma f/2.8 lens. For the stereoscopic measurements, image pairs were taken at a frame rate of 750 Hz with the time delay between frames being typically 75  $\mu$ s. Each image was exposed with a 10 ns laser pulse. PIV velocity vectors were computed on a 32 x 32 pixel interrogation area with 50% overlap using a recursive cross-correlation technique, generating 4000 vectors per image pair. This resulted in less than 3% erroneous vectors prior to validation. Image calibration was performed using a calibration target to an accuracy of  $\pm 0.2\%$ , with a typical conversion of 95  $\mu$ m/pixel. This gave a spatial resolution of 1.5 mm x 1.5 mm (7.5 x 7.5 wall units). A picture of the experimental arrangement demonstrating the position of the cameras and laser can be found in Figure 3.21.

A PIV calibration target was supplied with the TSI system, Figure 3.22, which was useful for the stereoscopic measurements. The calibration target had a mirror positioned on its side. This was to allow accurate alignment of the calibration target and the cameras inside the wind tunnel. If the calibration



Figure 3.21: Experimental arrangement for the stereoscopic PIV measurements in the  $z$ - $y$  plane of the turbulent boundary layer.

target was positioned in the same plane as the light sheet, the laser was reflected back towards itself with no deflection, Figure 3.23a). However, if the calibration target and laser were misaligned, the laser light would be reflected back at the laser with some angle, Figure 3.23b). From Figure 3.22 it can be seen that the calibration target was layered, having sets of white dots spaced 10 mm apart on two different planes on both sides of the target (a four-plane calibration target). The four planes enabled the stereoscopic calibration of the PIV system with a single image, removing the need of traversing the calibration target in the  $z$ -direction to obtain the length scale for the 3<sup>rd</sup> velocity component.

For the stereoscopic PIV measurements, Scheimpflüg adapters were used with each camera to ensure that each PIV image was in focus. A picture showing the Scheimpflüg adapters and Photron APX-RX cameras is shown in Figure 3.24. Typically a stereoscopic angle of  $6^\circ$  was used on both high-speed cameras throughout the boundary-layer measurements. Due to the forward scattering of laser light as the cameras were no longer normal to the laser light sheet, the  $f$  number for the camera lenses was increased. This helped focusing the images as the depth of field was increased. Throughout the stereoscopic measurements an  $f$  number of 8 has been used.

The third component of velocity measured with the stereoscopic PIV, is the



Figure 3.22: PIV calibration target.

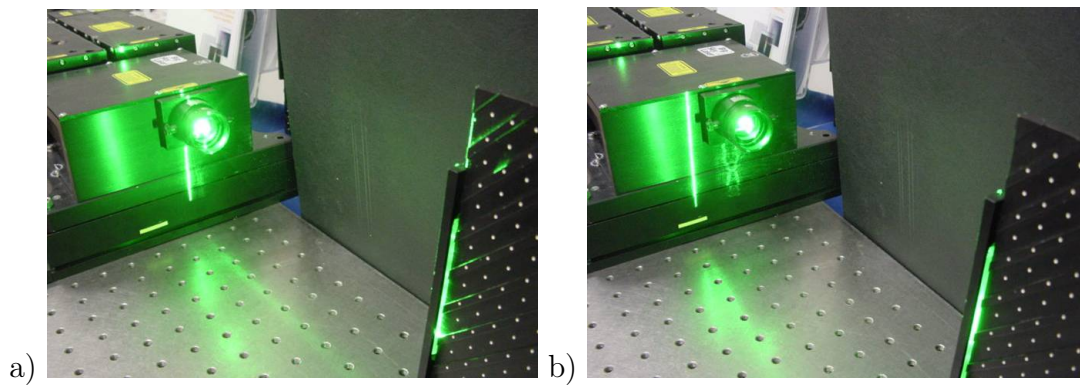


Figure 3.23: An example of a) correct alignment of a laser and calibration target and b) incorrect alignment of a laser and calibration target. Courtesy of TSI.

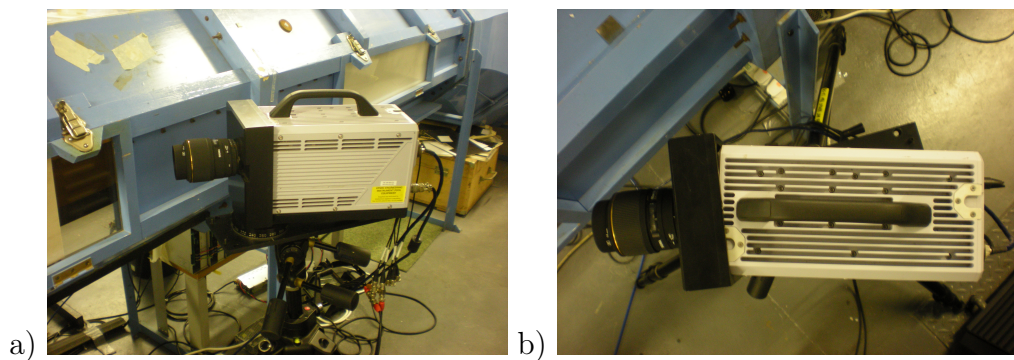


Figure 3.24: Photron APX-RX high-speed camera and Scheimpflug adapter for stereoscopic PIV measurements a) side view and b) plan view.

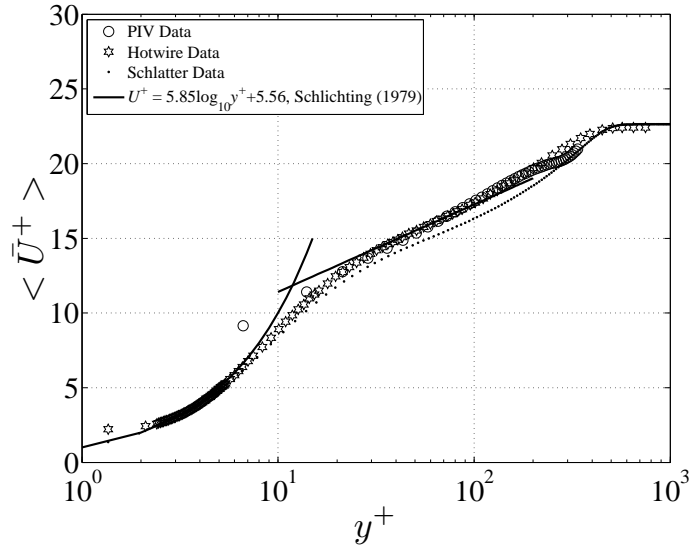


Figure 3.25: Comparison of the canonical time-averaged velocity profile of the turbulent boundary layer with stereoscopic PIV and hot-wire anemometry.

velocity component passing through the laser light sheet. In the  $z$ - $y$  plane measurements this was the  $U$ -component of velocity. To verify the  $U$ -component of velocity measured with the stereoscopic setup, a logarithmic velocity plot of  $U$  against  $y$  is shown in Figure 3.25. Here, the stereoscopic PIV data were taken 2.1 m downstream of the leading edge of the flat plate (which is the centre of the plasma actuator sheet). The data were obtained from a time-average over 7500 independent realisations of the flow, which was then averaged over the 500 wall units in the spanwise direction of the turbulent boundary layer. Alongside the stereoscopic PIV data, hot-wire anemometry (Chapter 6) of the canonical turbulent boundary layer ( $Re_\tau = 450$ ) and DNS data of a turbulent boundary layer from Schlatter *et al.* (2009) ( $Re_\tau = 500$ ) can be seen. The stereoscopic PIV data collapses to the logarithmic velocity profile of Schlichting (1979) and collapses to the hot-wire anemometry data presented for  $20 < y^+ < 200$ . The first PIV data point located at  $y^+ = 6$  appears spurious. This is due to the data point being very close the wall, where the higher velocity away from the wall influences the average velocity movement in the interrogation area, which is  $7.5 \times 7.5$  wall units. The Clauser plot method (Clauser, 1954) was used to obtain the friction velocity,  $u_\tau$  (see Chapter 6), which was within 1.6% of the friction velocity ob-

tained with the hot-wire data. The Clauser plot method assumes that a known log law profile can be fit to the turbulent boundary layer. Here, the log law of Schlichting (1979) has been used. Schlichting’s log law assumes a gradient,  $\frac{1}{\kappa}$ , of 5.85 and an intercept of 5.56. By matching the log law profile to the logarithmic region of the turbulent boundary layer, the friction velocity and hence the local skin-friction coefficient can be estimated. It should be noted that the Clauser plot is only valid for turbulent flows that have not been manipulated.

It is interesting to note that on observation of the canonical data, which is presented in Figure 3.25, there is a noticeable difference between the data that has been obtained by hot-wire anemometry/stereo PIV and the data of Schlatter *et al.* (2009). Both data sets have similar Reynolds numbers and therefore a large difference between the data sets is not expected. Erm and Joubert (1991) studied the effect of three different turbulent trips on low Reynolds number flows, with Reynolds number in the range  $715 < Re_\theta < 2810$ . The turbulent trips that were used in their study were (i) circular wire, (ii) distributed grit and (iii) cylindrical pins. In the current study, the turbulent trip consisted of cylindrical pins, Figure 3.4. Erm and Joubert (1991) found that for a given free-stream velocity there was a correct trip height that would yield correct stimulation of the flow into a turbulent regime. If the trip height was too small, the flow would not acquire enough energy from the trip to develop into a fully developed turbulent flow and was described as being an “under-stimulated” boundary layer. In contrast, a trip height that was too large, would cause an “over-stimulation” of the boundary layer. Erm and Joubert (1991) found that at low Reynolds numbers,  $Re_\theta = 1020$ —which is almost identical to the Reynolds number of the present investigation,  $Re_\theta = 1024$ —noticeable differences in the mean-velocity profiles could occur if cylindrical pins not having the correct height were used to trip the boundary layer. The turbulent boundary layer developed from the distributed grit and the circular wire—both under- or over-stimulating trips—through a range of Reynolds numbers showed only small differences to the mean velocity profile. At

higher Reynolds number,  $Re_\theta \approx 2810$ , there were negligible differences on the velocity profiles generated for under- or over-stimulated boundary layers with either of the three tripping devices. Hence, the reason for the difference in the canonical data presented in the Figure 3.25, could be due to an over-stimulation of the boundary layer caused by the (cylindrical pins) turbulent trip used in the current study. This could also explain why the canonical data in the logarithmic region of the boundary layer, Figure 3.25, shows a slight divergence away from the log law proposed by Schlichting (1979).

There is always a trade-off with having sufficient mean particle movement within the laser sheet plane, whilst minimising the particles lost that are travelling through the light sheet in a stereoscopic PIV set-up. The  $U$ -component of velocity is under-estimated by 0.1 m/s ( $\sim 1$  wall unit) for  $y^+ > 200$ . This uncertainty is within the 3-5% error level of PIV measurements (Westerweel, 1997). However, it is possible for  $y^+ > 200$  as the free-stream velocity is being approached, that the  $\Delta t$  between image pairs is large enough to cause particles to be lost through the laser sheet. This would cause an underestimate in velocity as the more slowly moving particles are left inside the interrogation area contributing to the cross-correlation peak (Smits and Lim, 2000).

### 3.8 Spanwise Travelling-Wave Actuator Sheets

The plasma actuator sheet used in the spanwise travelling-wave experiments consisted of a 250  $\mu\text{m}$  Mylar dielectric, with 24 copper electrodes arranged in asymmetric configurations powered by a set of high voltage sinusoidal plasma power supplies. A drawing of the upper and lower surfaces of the actuator sheet is shown in Figure 3.26. The actuator sheet dimensions were 408 mm x 336 mm ( $x^+ = \frac{xu_\tau}{\nu} = 2100$  and  $z^+ = 1730$ ). The upper and lower electrodes were 2.5 mm and 6 mm ( $z^+ = 13$  and 30) in width respectively, had an active length of 336 mm ( $x^+ = 1720$ ) and protruded 18  $\mu\text{m}$  ( $y^+ = 0.09$ ) from the dielectric surface. As the

protrusion of the electrodes is much smaller than the viscous sublayer ( $y^+ = 5$ ) the dielectric surface remains hydraulically smooth.

The actuator sheet was insulated with a thin coat of lacquer on its underside and bonded to a 10 mm Perspex substrate, §3.2. This ensured that there was plasma formation on the upper surface of the electrode sheet only and prevented additional wear of the actuator sheet and further ozone production. The actuator design was fabricated by photo-chemically etching a double sided copper laminate of Mylar, which had a dielectric constant,  $\epsilon$ , of 3.1. The same electrode sheet design, Figure 3.26, could be wired to create the two travelling wave forcing configurations. These configurations will be described in Chapter 5. Holes of 1 mm in diameter were drilled through each of the 24 electrodes on the actuator sheet. Figure 3.27a) and b), show a close up of the upper and lower surfaces of an actuator sheet respectively, indicating where holes were drilled. Each hole was filled with silver conductive paint that created an electrically conductive path from the upper to the lower surface of the actuator sheet. This allowed the high voltage connections for the plasma to be made on the lower surface of the actuator sheet, Figure 3.27c). The plasma actuator sheet could then be flush mounted in the wind tunnel for the turbulent boundary-layer tests of Chapters 6 and 7, with electrical connections causing no obstruction to the flow. Discontinuities between the flush mounted actuator and the wind tunnel test section were on the order of 200  $\mu\text{m}$ . Any discontinuity was smoothed using Scotch tape which was 58  $\mu\text{m}$  in thickness.

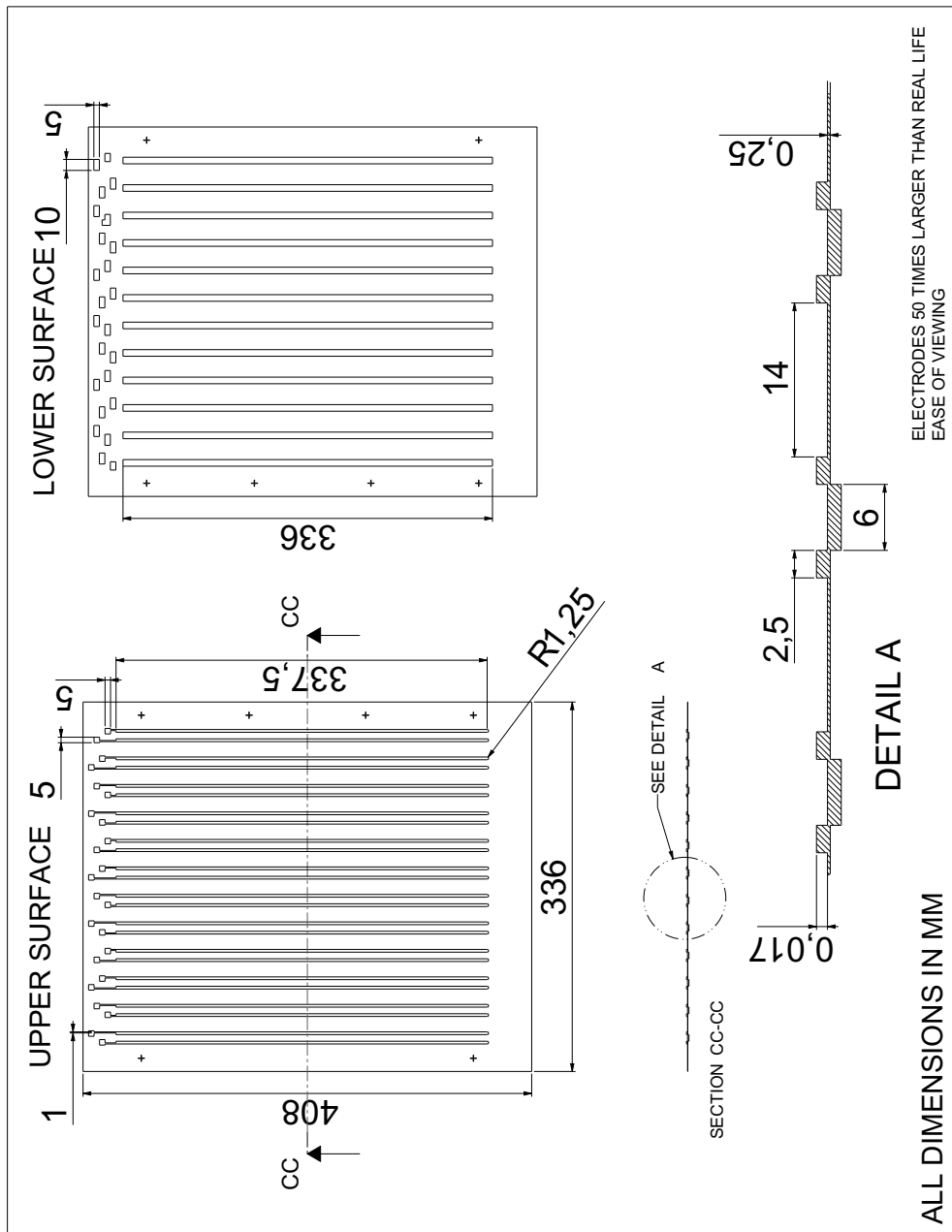


Figure 3.26: A drawing of the travelling-wave actuator sheet.

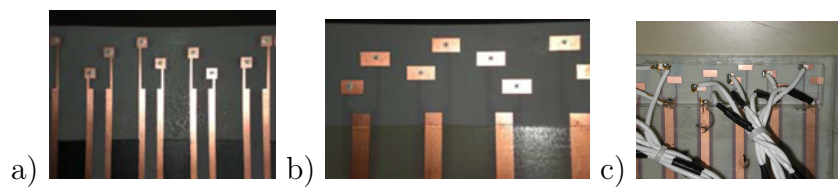


Figure 3.27: Travelling-wave actuator sheet. a) Upper surface, b) lower surface and c) electrical connections on the lower surface of the plasma sheet.

### 3.9 Plasma Power Supply

To generate the DBD plasma, a high voltage AC power supply was used. The high voltage power supply was a PSI-MCPG2503C power amplifier device purchased from KI Tech Ltd. The power supply operated from DC 36 V, had a maximum power output of 150 W and produced a sinusoidal voltage output. The plasma power supply could typically generate a high voltage output of up to 8 kV<sub>p-p</sub> with a frequency of up to 25 kHz. However, the voltage output and optimum frequency were dependent on the load attached to the power supply. This was a contribution of many factors, such as the length of the plasma actuators, the thickness of the dielectric material and the type of material that was used for the dielectric. With all the measurements presented, 250  $\mu\text{m}$  thick Mylar was used as the dielectric, which has a dielectric constant,  $\epsilon$ , of 3.1 and a breakdown voltage of 17 kV/mm.

An example of the voltage and current waveforms produced by the plasma power supply can be seen in Figure 3.28. In this figure, a voltage,  $E$ , of 7 kV<sub>p-p</sub> at a frequency,  $f$ , of 25 kHz is applied to two DBD plasma actuators that have a combined length of 672 mm. The spiky regions seen in the current signal indicate that the voltage has reached a high enough potential and plasma is forming.

The power supplied to the DBD plasma actuators can be defined as,

$$P = f \int_0^{t_{AC}} (EI) dt. \quad (3.9)$$

On integration of the voltage and current waveforms in Figure 3.28, it is found that the power supplied to the DBD plasma actuators is 35 W. Note that this is for a total actuator length of 672 mm, meaning that with an applied voltage of 7 kV<sub>p-p</sub> at 25 kHz, the power consumed by the DBD plasma actuators is 52 W/m.

To compute the efficiency of a plasma actuator, the fluidic power generated by the actuator needs to be obtained. In Chapter 4, it will be shown that the force coupled into quiescent air by a single plasma actuator is on the order of

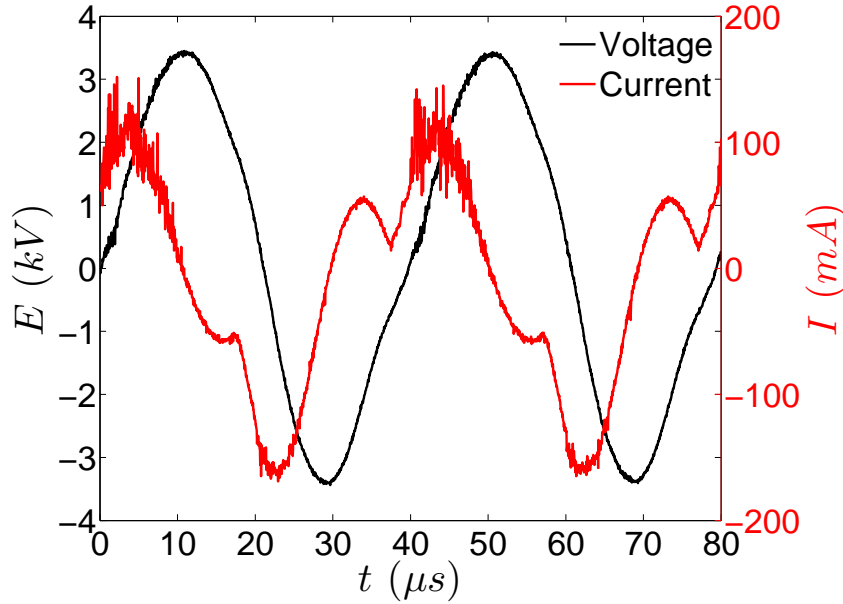


Figure 3.28: Voltage and current waveforms of the high voltage plasma power supply. The waveforms have been averaged over 512 AC cycles to remove random noise.

1 mN/m and the plasma wall-jet velocity is on the order of 1 m/s. Hence, the fluidic power generated by the plasma actuator is on the order of 1 mW/m. It has been expressed that the plasma actuators required for the boundary-layer tests require 52 W/m, hence the plasma actuator power requirement is on the order of 10 W/m, which gives an actuator efficiency on the order of  $10^{-4}$ . Efficiency of this order of magnitude has also been found by Enloe *et al.* (2004b).

When an active method of flow control is being used, it is useful to have an estimation of the fluidic power that will be potentially saved by the skin-friction drag reduction technique. The power saving can then be compared to the electrical power input required to operate the active flow-control device. For this calculation, it is useful to express the power required by the DBD plasma actuators in W/m<sup>2</sup>. It has been shown that the power required to operate two DBD plasma actuators on the travelling-wave actuator sheet is 35 W. The travelling-wave actuator sheet generates 4-phase spanwise travelling waves —25% duty cycle— and has a total of 24 electrodes, which are operated over an area of 300 mm x 336 mm. Therefore, the maximum power required to power the plasma actuator sheet is 105 W, which is approximately 1 kW/m<sup>2</sup>.

The fluidic power per square metre saved by the skin-friction drag reduction technique can be obtained by the following equation,

$$P = \Delta\tau_w U_\infty, \quad (3.10)$$

where,  $\Delta\tau_w$ , is the change in wall shear stress due to drag reduction and  $U_\infty$ , is the free-stream velocity. The change in wall shear stress can be obtained by,

$$\Delta\tau_w = \rho \left( u_{\tau,\text{can}}^2 - u_{\tau,\text{plasma}}^2 \right), \quad (3.11)$$

where  $\rho$ , is the density of the fluid and  $u_\tau$ , is the friction velocity. The friction velocity for the canonical boundary-layer,  $u_{\tau,\text{can}}$  can be approximated by,

$$u_{\tau,\text{can}} \approx \frac{U_\infty}{22}, \quad (3.12)$$

and the friction velocity for the manipulated boundary layer,  $u_{\tau,\text{plasma}}$  can be calculated by,

$$u_{\tau,\text{plasma}} = \frac{1}{2} \rho U_\infty \sqrt{\alpha C_{f,\text{can}}}. \quad (3.13)$$

Here,  $C_{f,\text{can}}$  is the skin-friction co-efficient for the canonical boundary-layer, which can be calculated from,

$$C_{f,\text{can}} = 2 \left( \frac{u_\tau}{U_\infty} \right)^2, \quad (3.14)$$

and  $\alpha$  is a constant which depends on the amount of skin-friction drag reduction. By substitution of Eqns. 3.12, 3.13 and 3.14 into Eqn. 3.11 yields,

$$\Delta\tau_w = \rho \left( 1 - \frac{1}{2} \alpha \right) \left( \frac{U_\infty}{22} \right)^2. \quad (3.15)$$

The spanwise travelling-wave technique can achieve up to a 30% reduction in turbulent skin-friction drag, which can be simulated by setting  $\alpha$  equal to 0.7.

The free-stream velocity for the wind tunnel tests is 1.7 m/s. Hence, on substitution of these values along with Eqn. 3.15 into Eqn. 3.10, the fluidic power saved by the spanwise travelling-wave technique is on the order of 0.01 W/m<sup>2</sup>. It has been shown that the plasma actuator sheet requires on the order of 1000 W/m<sup>2</sup>. To make DBD plasma viable for industrial applications, much work is needed in improving the efficiency of the plasma actuators. This will require optimisation of the dielectric materials and actuator geometries, along with improved power supplies to remove unwanted power losses. In this thesis, we are interested in developing the spanwise travelling-wave technique using DBD plasma, so that it becomes applicable for aeronautical applications. Understanding the changes in structure of the turbulent boundary layer by studying the flow physics, will allow us to refine and optimise this innovative flow-control technique in the future. This coupled with improvements in material science, actuator geometry and electronics, may make the spanwise travelling-wave technique created with DBD plasma a viable aeronautical flow-control technique for the future.

# Chapter 4

## Starting Vortex

In this section, the actuation of DBD plasma from an asymmetric actuator in quiescent air will be presented. A single asymmetric DBD plasma actuator is the simplest DBD plasma actuator that can be studied. It is important to understand the formation processes and the evolution of the starting vortex as it may play a dominant role when DBD plasma is used for turbulent boundary-layer control. The kinematics and the dynamics of the starting vortex are studied using a high-speed time-resolved PIV system and flow visualisation.

### 4.1 Kinematics and Dynamics of the Starting Vortex

DBD plasma actuators consist of two electrodes separated by a thin dielectric layer, Figure 4.1. Typically one electrode is exposed to the ambient fluid and the other is encapsulated by the aerodynamic surface. On application of several kV and kHz from an AC source, local ionization around the exposed electrode couples momentum to the surrounding neutral gas particles and induces a body force on the ambient fluid (Enloe *et al.*, 2004a).

A DBD plasma actuator can be operated in a continuous mode (100% duty cycle) or in a pulsed mode. Each actuation of DBD plasma leads to the creation

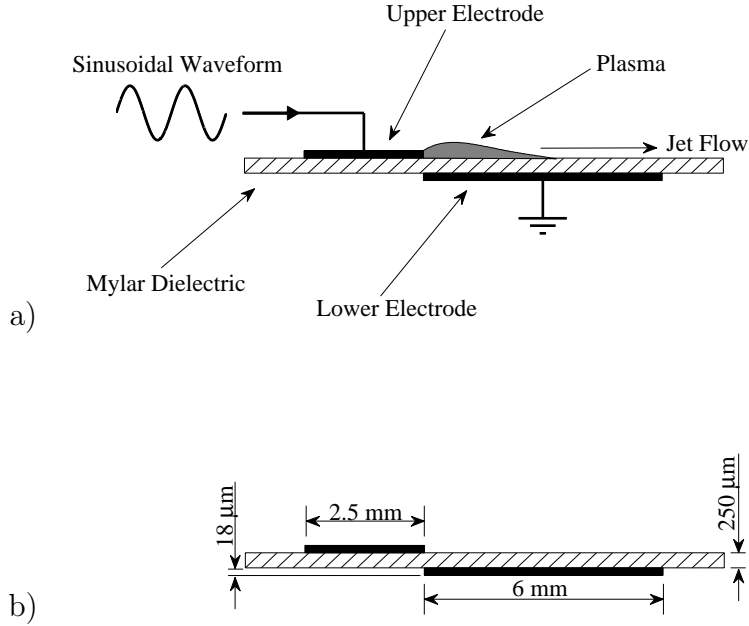


Figure 4.1: Schematic representation of a DBD plasma actuator used in the present study a) cross-section and b) typical dimensions.

of a starting vortex (Post, 2004). By pulsing the DBD plasma actuator on a ms scale, trains of starting vortices can be induced which agglomerate downstream of the plasma actuator into a single, larger vortex (Jukes *et al.*, 2006a). After an initiation phase of several 100's of ms (which depends on the applied voltage, frequency and actuator geometry) for both a continuous or pulsed operated DBD plasma actuator, the starting vortex has sufficiently moved far downstream of the plasma actuator and leads to the formation of a wall jet. The wall jet —fluid flow along the wall— when non-dimensionalised appropriately collapses to the analytical solution for a laminar wall jet, Figure 4.2.

The DBD plasma actuator used in the present study had an asymmetric configuration, Figure 4.1, which consisted of a 250  $\mu\text{m}$  thick Mylar dielectric (dielectric constant,  $\varepsilon = 3.1$ ) which was sandwiched by two electrodes. The upper and lower electrodes were made from copper which were 2.5 mm and 6 mm in width respectively. Each copper electrode was 18  $\mu\text{m}$  in thickness and had a total length of 160 mm. The plasma actuator was mounted on a Perspex substrate of 10 mm thickness with double sided adhesive tape to ensure plasma formation from the upper electrode only. To generate the DBD plasma, a sinusoidal voltage

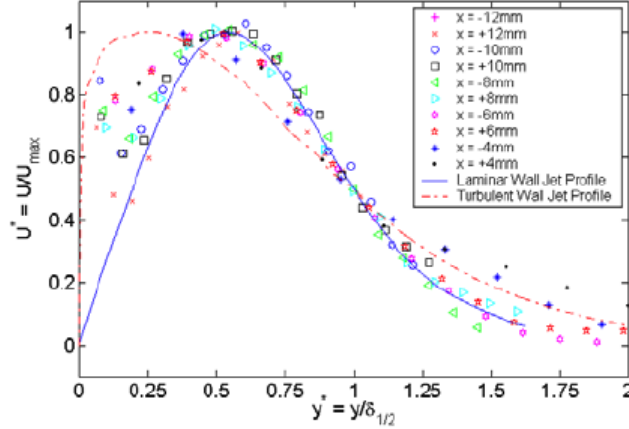


Figure 4.2: Laminar wall jet created by a DBD plasma actuator. Taken from Jukes *et al.* (2006a).

waveform with an applied voltage,  $E$ , of 5.50 - 7.20 kV<sub>p-p</sub> at a frequency  $f$ , of 20 - 25 kHz was applied to the plasma actuator with continual forcing (100% duty cycle) for a duration,  $T$ , of 150, 300 or 600 ms. A summary of the conditions tested can be found in Table 4.1.

Figure 4.3 shows a series of images, flow visualisation and vorticity fields for an applied voltage,  $E$ , of 5.50 kV<sub>p-p</sub> at a frequency,  $f$ , of 20 kHz and with plasma duration,  $T$ , of 300 ms of continual plasma forcing to the actuator. These two data sets are for the same experimental test condition but have been taken separately. The plasma initiates at  $(x, y) = 0$ , the end of the upper electrode with  $y = 0$  mm being the location of the wall. The plasma extends for around 2-3 mm in the horizontal direction (to the right). It can be seen in the flow visualisation (left column) that on initiation of DBD plasma a starting vortex is created. As the plasma actuator is operated for 100% duty cycle (continuously operated) a single starting vortex is formed. The starting vortex, through Figure 4.3a) to e), rolls up to form a coherent structure. As the vortex rolls up, the number of turns outlined by the smoke streaklines is increased due to entrainment and the core location is the centre of a tightly compacted spiral of white smoke. As time increases through Figure 4.3a) to e) the starting vortex moves along in the positive  $x$ -direction and away from the wall in the positive  $y$ -direction. It can be seen in this example that on comparison of the flow visualisation and the PIV

Table 4.1: Experimental conditions studied.

Cases	Plasma Parameters		Plasma Duration, $T$ (ms)		
	$E$ (kV <sub>p-p</sub> )	$f$ (kHz)	150	300	600
A	5.50	20	✓	✓	✓
B	7.20	20	✓	✓	-
C	5.50	25	✓	✓	-

data, the location of the vortex core differs by approximately 2 mm between the two techniques. This exemplifies the uncertainty in the location of the vortex core due to the repeatability of the experiments.

Allen and Chong (2000) studied experimentally the vortex formed in front of a piston as it moves through a cylinder. They commented on the necessary generation of secondary vorticity on the piston face to preserve the no-slip boundary condition as the piston is set into motion. The secondary vorticity was wrapped around the piston vortex and it was thought that this induced the movement of the primary structure away from the piston face. The vorticity of the starting vortex for the same test configuration as the flow visualisation is shown in the right column of Figure 4.3. Figure 4.3a) shows 120 ms into plasma actuation where the vortex core location can be seen by the region of primary vorticity. A region of secondary vorticity can be seen along the wall underneath the starting vortex to preserve the no-slip boundary condition. The secondary vorticity is being stretched and wrapped around the starting vortex throughout the images of Figure 4.3a) to e) in a similar fashion to the piston vortex of Allen and Chong (2000), offering an explanation for the apparent growth of a starting vortex away from the wall. As time increases through Figure 4.3a) to e) the magnitude of both primary and secondary vorticity decreases as the vortex moves along and away from the wall.

Figure 4.4 shows flow visualisation around the vicinity of a plasma actuator which is actuated with  $E = 5.50$  kV<sub>p-p</sub> at  $f = 20$  kHz. Figure 4.4a) shows 2 ms into plasma actuation, where the starting vortex can be seen. The starting

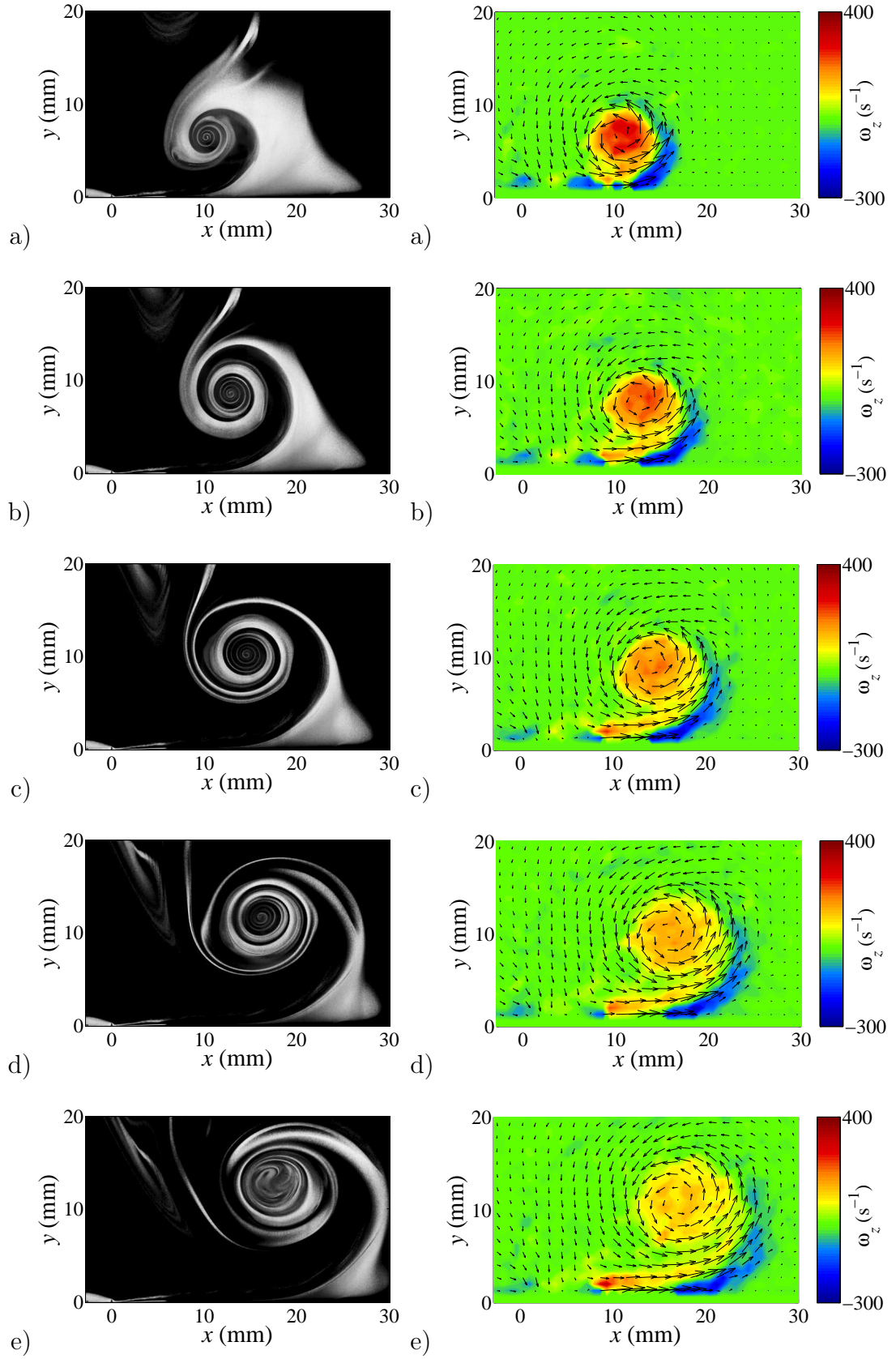


Figure 4.3: Flow visualisation (left column) and PIV vorticity fields (right column) of the plasma induced starting vortex with  $E = 5.50$  kV<sub>p-p</sub> at  $f = 20$  kHz and  $T = 300$  ms at a) 120 ms, b) 160 ms, c) 200 ms, d) 240 ms, e) 280 ms.

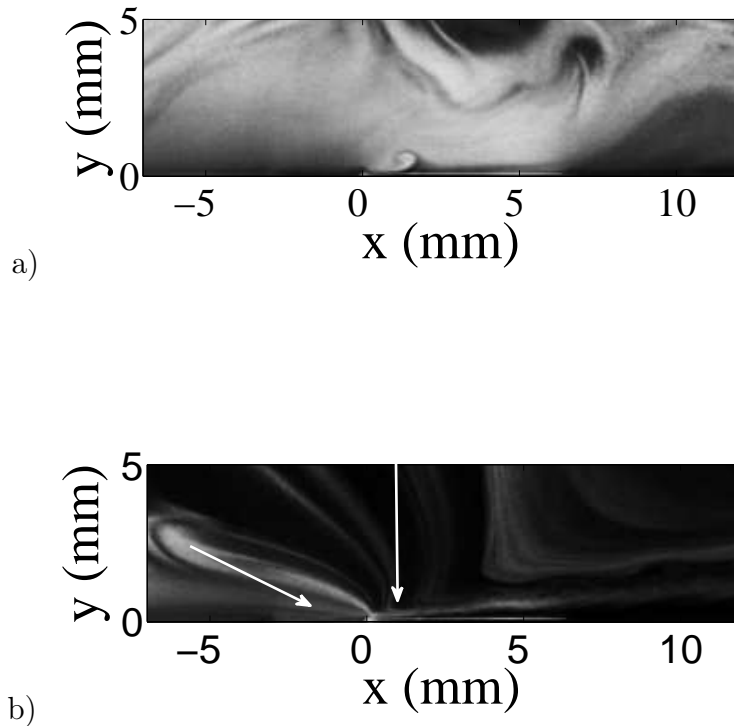


Figure 4.4: Flow visualisation around the vicinity of a DBD plasma actuator with  $E = 5.50 \text{ kV}_{\text{p-p}}$  at  $f = 20 \text{ kHz}$ , a) initial formation of the starting vortex 2 ms into plasma actuation and b) 240 ms into plasma actuation, smoke streaklines showing entrainment caused by the plasma jet.

vortex is located around  $x = 2 \text{ mm}$  and  $y = 0.5 \text{ mm}$ . Hence, it would appear that the starting vortex is created instantaneously on the initiation of DBD plasma. Figure 4.4b) illustrates entrainment, a key feature of the plasma actuator. This image is taken 240 ms into plasma actuation and shows a close-up view around the plasma actuator. The smoke streaklines can be seen bending into the plasma region above the plasma actuator (plasma discharge begins at  $x = 0 \text{ mm}$ ) and from behind the plasma actuator. The two white arrows indicate the regions of entrainment. As the DBD plasma actuator imparts momentum and not mass to the ambient fluid, entrainment is a key feature. The streaklines are indicating the regions of entrainment by the plasma actuator as the fluid which is ejected laterally by the plasma wall jet must be replenished by continuity.

Another feature of the starting vortex that has been found using flow visualisation are Kelvin-Helmholtz (K-H) instabilities. In Figure 4.5a) an image of starting vortices created by two opposing plasma actuators is presented. The wall

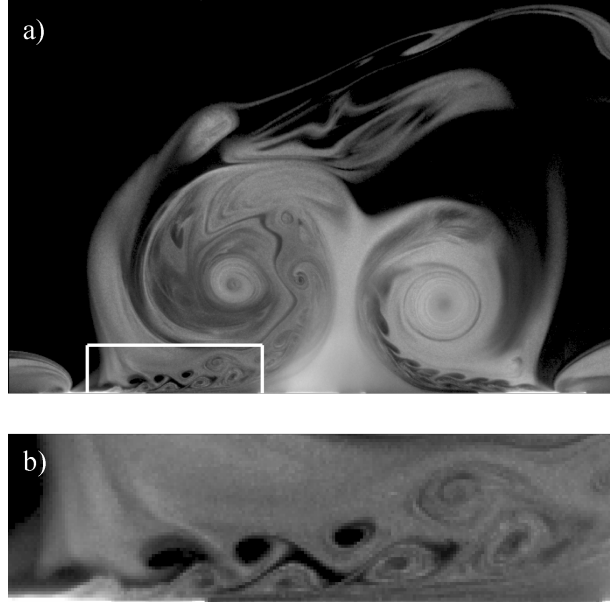


Figure 4.5: Flow visualisation of colliding vortices at  $E = 5.50 \text{ kV}_{\text{p-p}}$  at  $f = 25 \text{ kHz}$ , a) 170 ms after plasma initiation and b) showing the Kelvin-Helmholtz instability. Taken from Whalley and Choi (2010a).

jets from the plasma actuators collide to form a wall-normal jet at the centre of the picture. As a result, the starting vortices are pushed away from the wall as they develop. Trains of vortices due to the K-H instability are clearly seen in the jets (see Figure 4.5b) for an enlarged picture), which are ingested by the starting vortices. It should be noted that the frequency of instability is nearly two orders of magnitude lower than that of the alternating-current power supply. Hence, the vortices inside the shear layer are not due to plasma forcing frequency.

In Figures 4.6 and 4.7, a comparison of the velocity and vorticity fields for the three cases which have been studied can be seen respectively. As shown in Table 4.1,  $E = 5.50 \text{ kV}_{\text{p-p}}$  at  $f = 20 \text{ kHz}$  (left column) will be referred to as Case A,  $E = 3.60 \text{ kV}_{\text{p-p}}$  at  $f = 20 \text{ kHz}$  (middle column) will be referred to as Case B and  $E = 5.50 \text{ kV}_{\text{p-p}}$  at  $f = 25 \text{ kHz}$  (right column) will be referred to as Case C. The images begin 60 ms into plasma actuation and are presented every 60 ms until the plasma actuation ceases after 300 ms. It can be seen in all cases that on initiation of DBD plasma a starting vortex is created which grows and moves along and away from the wall with time. All cases have an asymmetric velocity distribution around the vortex, with higher velocity magnitude on the

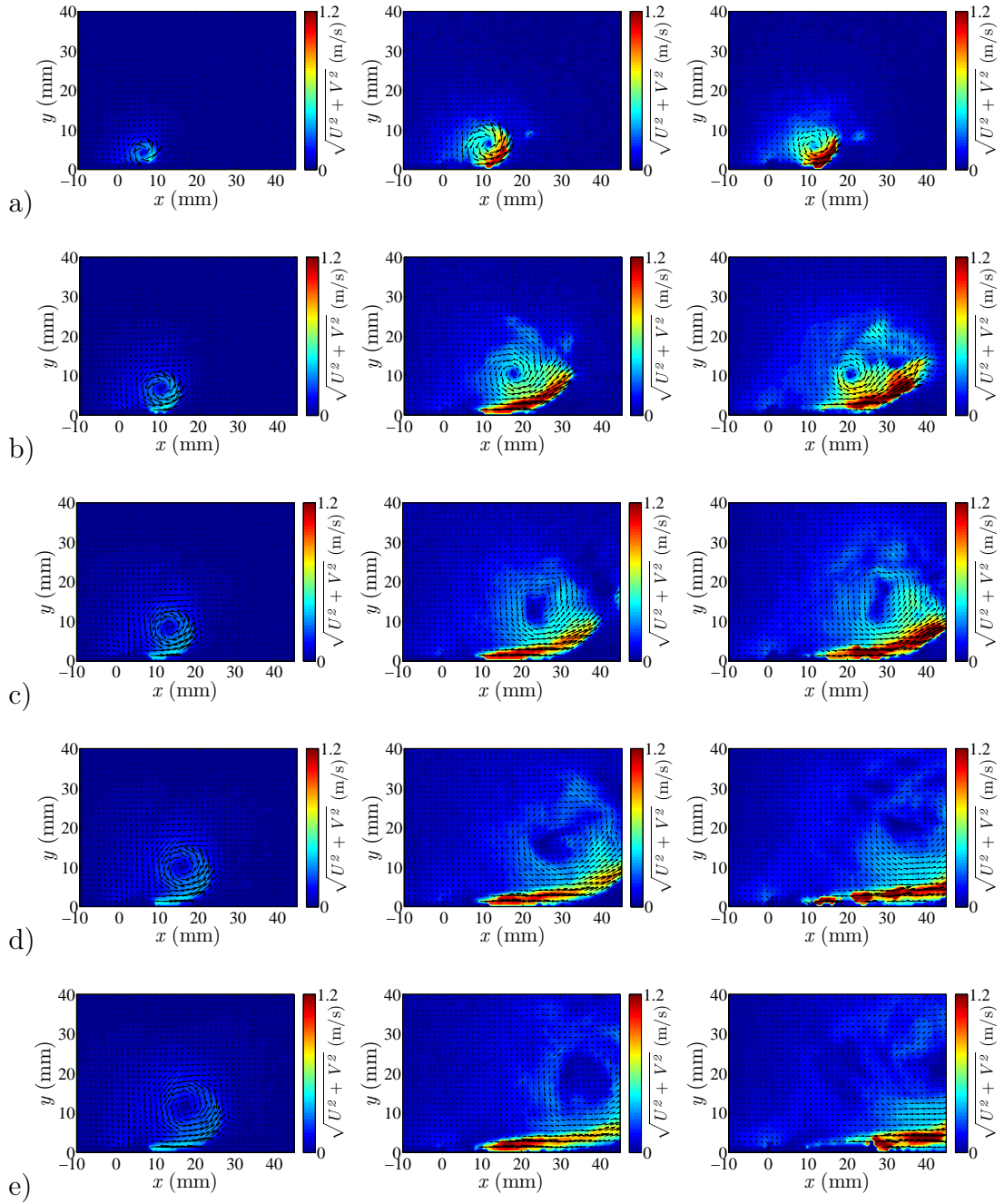


Figure 4.6: A comparison of PIV velocity fields for the starting vortex with Case A (left column), Case B, (middle column) and Case C (right column) at a) 60 ms, b) 120 ms, c) 180 ms, d) 240 ms, e) 300 ms.

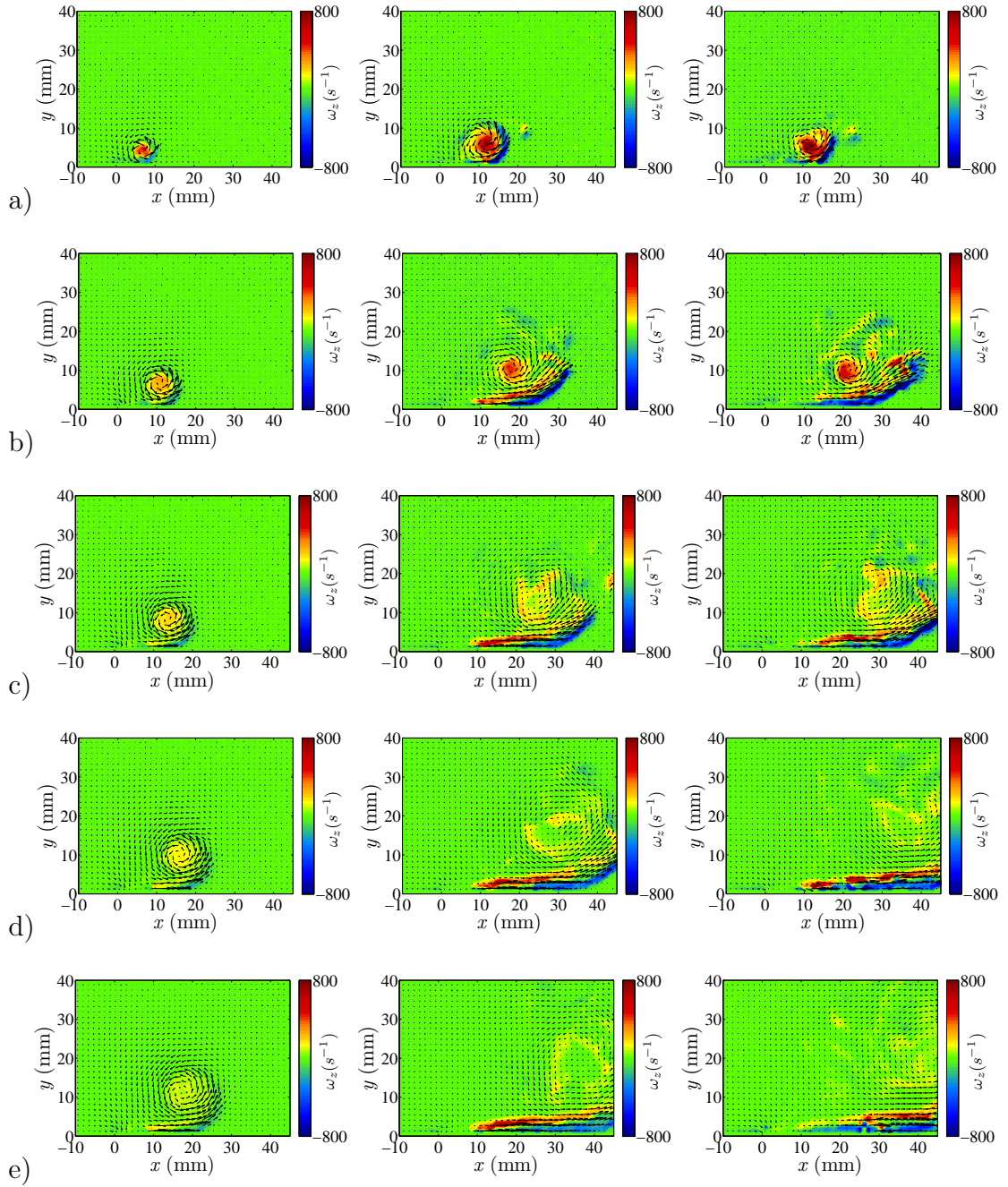


Figure 4.7: A comparison of PIV vorticity fields for the starting vortex with Case A (left column), Case B (middle column) and Case C (right column) at a) 60 ms, b) 120 ms, c) 180 ms, d) 240 ms, e) 300 ms.

underside of the vortex where the wall jet is located. The vortex core location can be seen by the low-speed region in the centre of the asymmetric velocity distribution. The lowest plasma forcing, Case A (left column), creates a starting vortex with a velocity magnitude on the order of 0.5 m/s. As the applied voltage or frequency is increased, Case B (middle column) and Case C (right column), stronger starting vortices are created which have a velocity magnitude on the order of 1 m/s and have larger values of vorticity when compared with Case A (left column). Increasing the applied voltage or frequency (Cases B and C) causes the starting vortex to move along and away from the wall more quickly with time, hence develop more quickly, as expected. The velocity fields and vorticity fields for Case B (middle column) and Case C (right column) appear qualitatively and quantitatively similar. Both cases have velocity magnitudes on the same order (1 m/s) and both cases see the starting vortex positioned approximately in the same location in space at each location in time. After 120 ms of plasma actuation, Figures 4.6b) and 4.7b), both the starting vortices appear to detach from the wall jet which is present on the underside of each vortex. This could be due to vortex induction as the strength of the starting vortices are higher for Cases B and C. When compared with Case A, the lowest applied voltage and frequency used, the starting vortex remains very stable throughout the actuation of the plasma and laminar-like. This could be due to lack of secondary vorticity that is present. Hence, increasing the plasma parameters by either an increase in applied voltage (Case B) or an increase in frequency (Case C) appears to create a more unstable vortex.

To be able to compare the velocity and vorticity fields across the experimental cases, a velocity scale,  $U_m$ , is needed so that the spatial and temporal scales of the starting vortex can be non-dimensionalised appropriately. In Figure 4.8 the maximum velocity,  $U_{max}$ , in each PIV frame throughout 600 ms of plasma actuation for Case A is shown. The maximum  $U$ -component of velocity in each PIV frame was located in the wall jet underneath the vortex core. In Figure 4.8a),

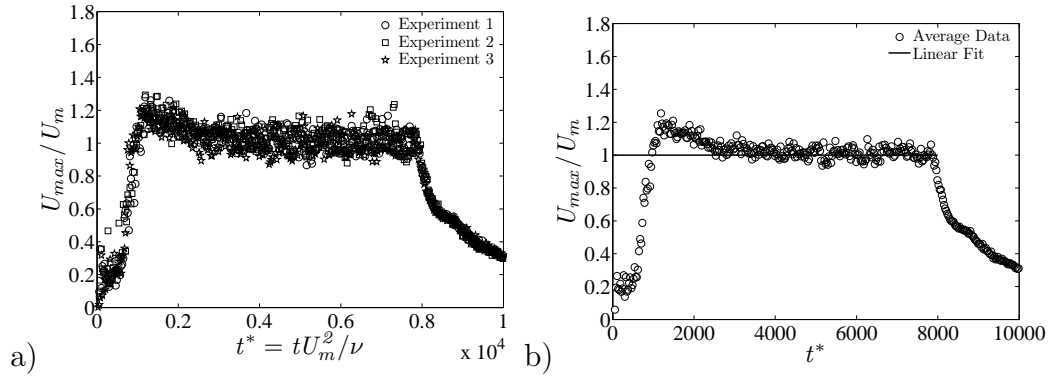


Figure 4.8: Characteristic velocity scale obtained from PIV velocity fields for Case A with  $T = 600$  ms showing a) data from three experiments and b) averaged data.

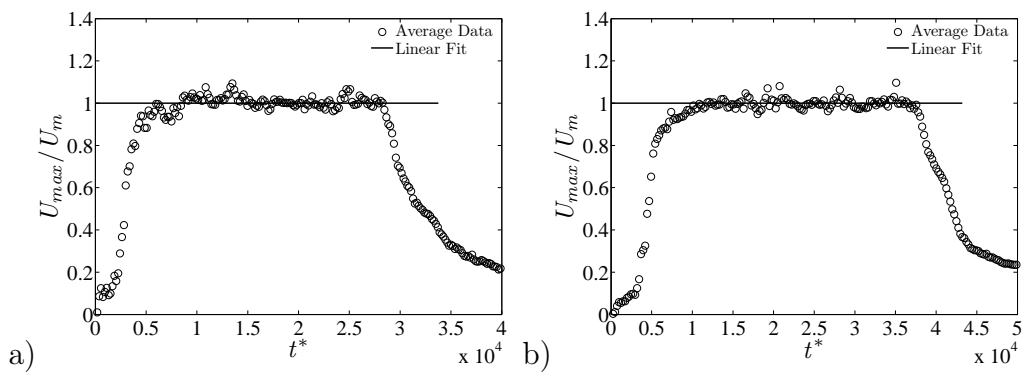


Figure 4.9: Characteristic velocity scale obtained from PIV velocity fields for a) Case B and b) Case C with  $T = 300$  ms.

data taken from 3 experiments is shown and in Figure 4.8b) the data from the 3 experiments is averaged. It can be seen in Figure 4.8b) that the maximum velocity increases from zero, overshoots and then becomes constant at around  $t^* = \frac{tU_m^2}{\nu} = 5000$ . The constant velocity defines the velocity scale  $U_m$ , and  $\nu$ , is the kinematic viscosity. At  $t^* = 8100$  ( $t = 600$  ms) the plasma actuation is stopped and the maximum velocity begins to return to zero. This phenomenon of maximum velocity overshooting and then becoming constant has also been observed by Jukes and Choi (2009a) when DBD plasma was actuated in quiescent air over a circular cylinder. The averaged maximum velocity obtained throughout 300 ms of plasma forcing for Cases B and C is shown in Figure 4.9. As the applied voltage or frequency is increased larger than Case A, the maximum velocity does not overshoot. Instead, the maximum velocity increases from zero and becomes constant at around  $t^* = 5000$  for both cases —the physical reason for the velocity becoming constant at  $t^* = 5000$  is not known at the present time. The plasma actuation ceases at  $t^* = 28000$  and  $37000$  for Figure 4.9a) and b) respectively, after which time maximum velocity can be seen returning to zero. Hence for all cases studied, the maximum velocity obtained from the PIV images becomes constant at  $t^* = 5000$ . The velocity scale,  $U_m$ , for each case can be found in Table 4.2. The smallest velocity scale is for the smallest applied voltage and frequency (Case A) with  $U_m = 0.45$  m/s. As the plasma parameters are increased by an increase in voltage (Case B) and an increase in frequency (Case C) the velocity scale increases to  $U_m = 1.19$  m/s and  $1.36$  m/s respectively.

A plot of the normalised velocity and vorticity fields at  $t^* = 6000$  and  $8000$  can be found in Figures 4.10 and 4.11 respectively. In these figures the distances have been non-dimensionalised by  $\frac{U_m}{\nu}$  and the velocities have been non-dimensionalised by  $U_m$ . The vorticity has been non-dimensionalised by  $\frac{\nu}{U_m^2}$ , where  $U_m$  is the maximum wall jet velocity and  $\nu$  is the kinematic viscosity. The plots at equal  $t^* = 6000$  and  $8000$  show similar shapes and distributions of non-dimensional velocity and vorticity. Throughout Figures 4.10 and 4.11 the velocity profiles (left

Table 4.2: Characteristic velocity scale and plasma force coefficient.

Cases	$E_{p-p}$ (kV)	$f$ (kHz)	$U_m$ (m/s)	$F_p$ (mN/m)	$C_p$
A	5.50	20	0.45	0.15	0.058
B	7.20	20	1.19	1.62	0.211
C	5.50	25	1.36	2.18	0.219

column) show positive velocity underneath the vortex core and negative velocity above the vortex core. The positive velocity is a result of the wall jet which is located on the underside of the vortex, adjacent to the wall due to plasma forcing. The negative velocity is due to the induction of the vortex and a characteristic of a vortex velocity profile. The vorticity fields show both primary and secondary vorticity. The maximum primary vorticity generally indicates the location of the vortex core, at least in quiescent air. However, care must be taken when using maximum primary vorticity as an indicator for the vortex core. As can be seen in Figure 4.11a), the maximum primary vorticity (red region) in this case is situated above the wall jet close to the plasma actuation region and does not represent the location of the vortex core. The secondary vorticity is present throughout all the images for both  $t^* = 6000$  and  $8000$ . As the vortex grows in size from  $t^* = 6000$  to  $8000$  the secondary vorticity can be seen stretched and wrapped around the starting vortex, beginning at the wall underneath the vortex and ending at a wall-normal distance greater than the vortex core location. The plots for the lowest wall jet velocity, Figures 4.10a) and 4.11a) show better resolution as the physical scale of the vortex is larger when compared with the higher wall jet cases.

Allen and Naitoh (2007) studied the transient growth of a junction vortex that was created when an impulsively started moving wall slid underneath a stationary wall. Allen and Naitoh (2007) demonstrated that the junction vortex displayed self-similarity with the vortex core scaling with  $t^{\frac{5}{6}}$  for a range of wall speeds. It has been demonstrated that on the initiation of DBD plasma, a starting vortex is created which rolls up to create a coherent structure, Figure 4.3. The starting vortex appears qualitatively similar to the junction vortex of Allen and Naitoh

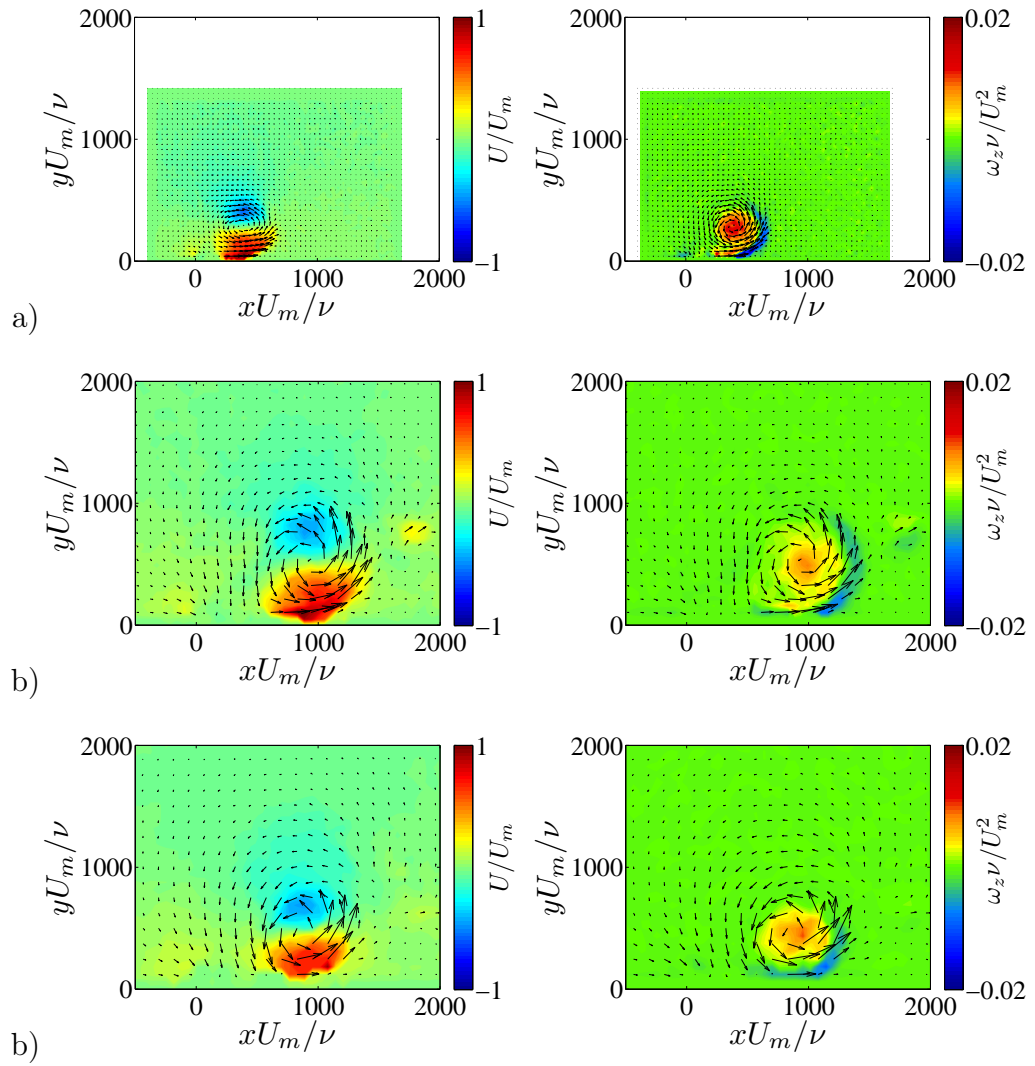


Figure 4.10: Normalised velocity fields (left column) and vorticity fields (right column) at  $t^* = 6000$  for a) Case A and b) Case B and c) Case C.

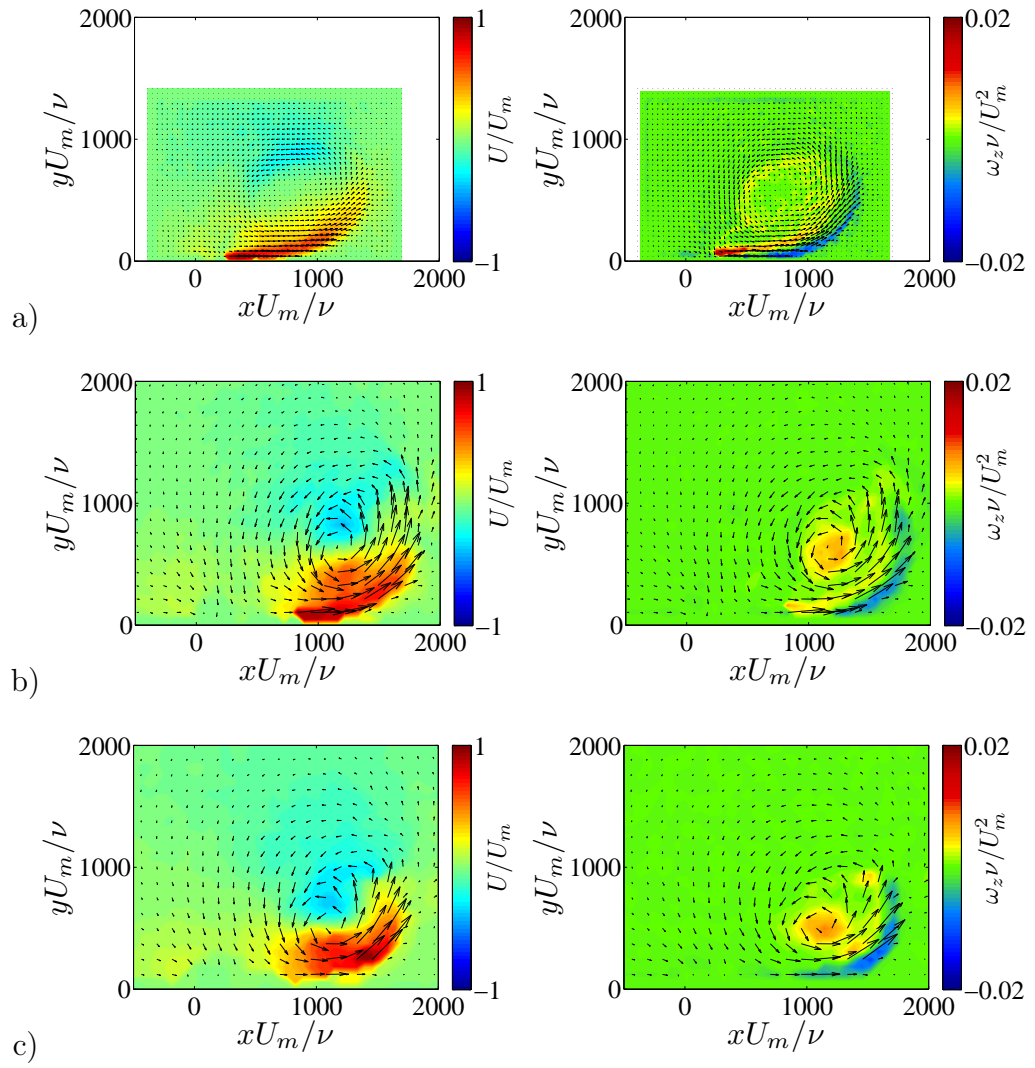


Figure 4.11: Normalised velocity fields (left column) and vorticity fields (right column) at  $t^* = 8000$  for a) Case A and b) Case B and c) Case C.

(2007), in the sense that fluid is rolled up into a coherent structure and moves along and away from the wall under continual plasma forcing. In Figures 4.10 and 4.11, non-dimensional velocity and vorticity was presented for the starting vortex over three cases (Cases A, B and C). Each starting vortex when normalised had similar shapes and similar distributions of both velocity and vorticity. Hence, the starting vortex generated by DBD plasma could scale in a self-similar fashion, similar to the junction vortex of Allen and Naitoh (2007).

To see if the starting vortex generated by DBD plasma scaled in a self-similar way, measurements of the the vortex core locations with time were made. The vortex core location,  $(X_c, Y_c)$ , is defined as being the horizontal distance from the end of the upper electrode and the wall-normal distance from the surface to the vortex core respectively, Figure 4.12. The measurements of the starting vortex core,  $X_c$  and  $Y_c$  have been made with a combination of flow visualisation and PIV for all the conditions presented in Table 4.3 for each technique. Using PIV, three experiments for each test case were phase-averaged —this is taking an average at the same point in time across the three cases— every 2 ms with the core being located using a minimum velocity criterion. The vortex core is of low velocity, therefore smoothing the  $x, y$  velocity field in this region with a Gaussian kernel and plotting over a 2D surface indicated the vortex core location by a local velocity minimum. The PIV velocity field can be measured to an accuracy of 3-5% (Westerweel, 1997) with the vortex core being located with an accuracy of  $\pm$ half the spatial resolution of the interrogation area,  $\pm 0.35$  mm. The flow visualisation measurements obtained similar results with an uncertainty in  $X_c$  and  $Y_c$  of  $\pm 1$ -2 mm and  $\pm 0.8$  mm respectively. This was evaluated by computing twice the standard deviation of the  $(X_c, Y_c)$  measurements for the 20 - 25 flow visualisation events that were phased-averaged for each case. The measurements of the vortex core have been scaled with  $\frac{U_m}{\nu}$ , where  $U_m$  is the maximum wall jet velocity (Table 4.2) and  $\nu$  is the kinematic viscosity.

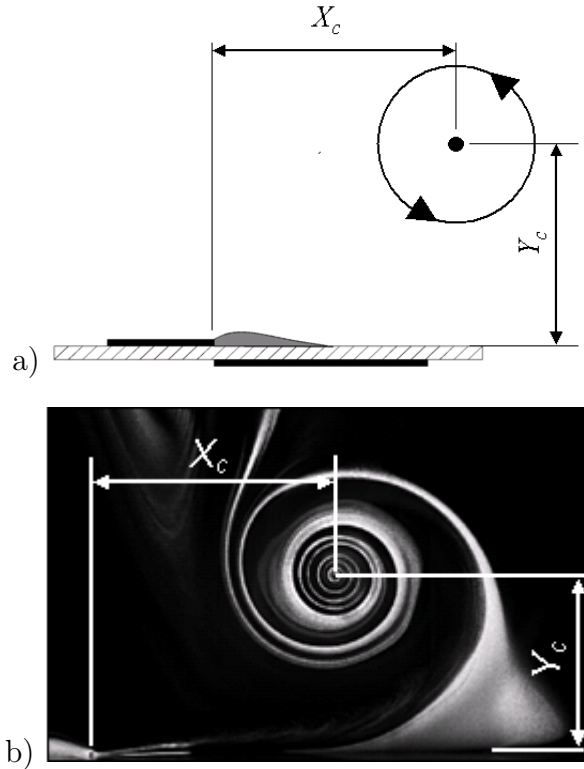


Figure 4.12: Definition of spatial scales a) diagram and b) picture.

## Self-similar Scaling

The development of the vortex core is presented in Figure 4.13, where 14 data sets are on each plot, 7 from the flow visualisation studies and 7 from the PIV studies. It was possible with PIV to measure the vortex core location throughout the entire plasma actuation period,  $T$ . Measurements of the vortex core location with flow visualisation were possible typically up to 150 - 250 ms, after this the smoke tracer dissipated and the core location could no longer be obtained. Hence, for the presented results the scaling of the core begins at the initiation of plasma,  $t = 0$  ms, and ends when the plasma actuation ceases, after  $T = 150, 300$  or  $600$  ms for PIV measurements and up to 150 - 250 ms for the flow visualisation measurements. The vortex core movement away and along the wall,  $(X_c, Y_c)$ , can be seen in Figure 4.13a), b) and c). The data fits a general power law of the form:

$$\frac{(X_c, Y_c) U_m}{\nu} = \kappa \left( \frac{t U_m^2}{\nu} \right)^q. \quad (4.1)$$

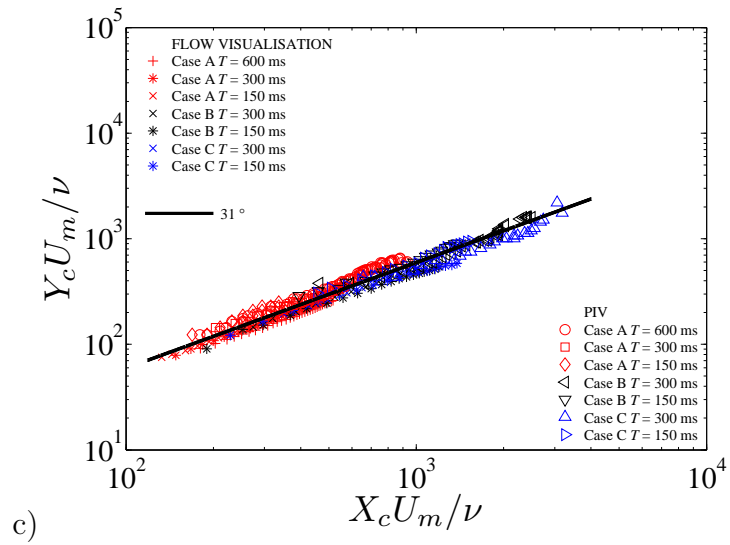
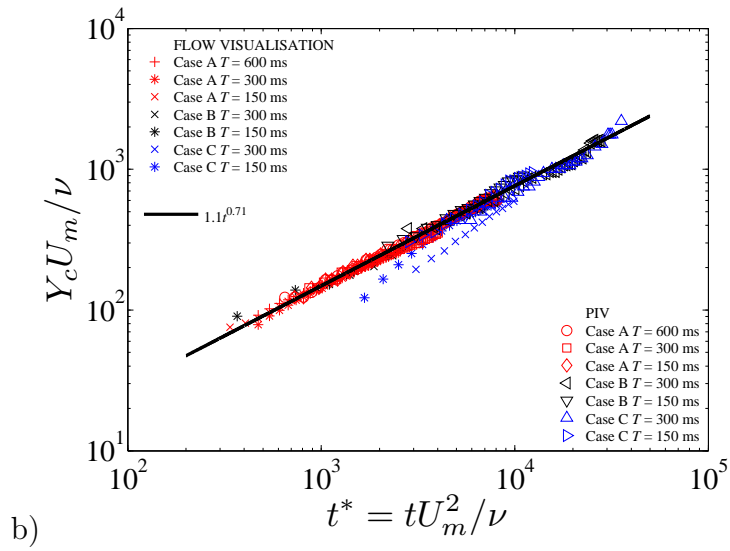
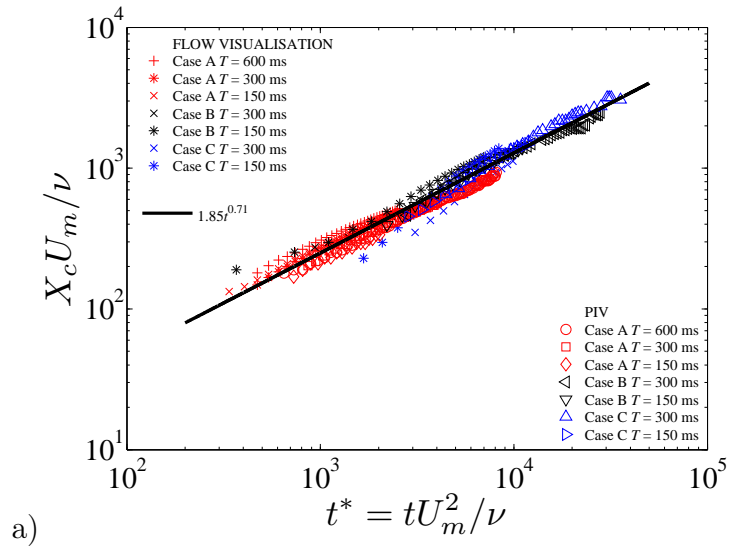


Figure 4.13: Vortex core scalings. a)  $X_c$  vs.  $t$ , b)  $Y_c$  vs.  $t$ , c)  $Y_c$  vs.  $X_c$ .

Table 4.3: Scaling law fits

	$X_c$	$Y_c$
$\kappa$	1.85	1.10
$q$	0.71	0.71

It can be seen in Figure 4.13a) and b) that the vortex core moves at constant rates in both the horizontal and vertical directions respectively with a scaling rate of  $t^{0.71}$ . The core locations made with flow visualisation and PIV are in excellent agreement. The values for the constants,  $\kappa$  and  $q$  in Eqn. 4.1 are shown in Table 4.3. Figure 4.13c) shows a plot of  $Y_c$  against  $X_c$  which indicates that the vortex moves with an angle of  $31^\circ$  to the horizontal.

To understand the physics behind the scaling rate of  $t^{0.71}$  it is important to link the kinematics and dynamics of the starting vortex. Cantwell (1986) studied analytically the evolution of a starting vortex at the head of a viscous starting jet. Cantwell (1986) was able to calculate the rate at which the transient structure should scale at the head of the jet and was able to relate the scaling rate to an impulse that was applied to the flow. Cantwell (1986) considered the jet to be produced initially from rest with a line force at the origin of the infinite domain and found that the impulse applied to the flow was,

$$I(t) = \frac{Mt^{(n-1)}}{(n-1)} \quad (4.2)$$

where  $M$  was a force-amplitude parameter and had dimensions of  $L^3T^{-n}$  and the exponent  $n$  was defined by the forcing type used to create the jet. For a jet that was created by a short impulse,  $n = 1$ , for a jet created by a constant force,  $n = 2$  and for a jet created by a linearly increasing forcing,  $n = 3$ . Cantwell (1986) used the Euler equations to form similarity groups based on an infinite domain (lack of experimental length scale) and the impulse (Eqn. 4.2) applied to the flow being invariant when under transformation. The forms of the similarity groups for length scales and velocity scales were,

$$\begin{aligned}\xi &= \frac{x}{M^{\frac{1}{3}}t^{\frac{n}{3}}} \\ \hat{U}(\xi) &= \frac{U}{M^{\frac{1}{3}}t^{\frac{n}{3}-1}},\end{aligned}\tag{4.3}$$

where the values of  $M$  and  $n$  need to be determined by the forcing of the jet. These similarity groups, if applicable to the flow field, will allow a prediction for the scaling rates of the spatial and velocity scales of the flow field, which will allow a comparison to experimental observations. The same analysis was performed by Allen and Naitoh (2007) to predict the scaling rate of the velocity field and the scaling rate for the junction vortex core. Allen and Naitoh (2007) used an analytical expression for the velocity layer forming over an impulsively started plate to establish a momentum equation that was time dependent. From the momentum equation they were able to solve for  $M$  and  $n$  in Eqn. 4.3 to show that with Cantwell's analysis the spatial scales of their junction vortex should scale with  $t^{\frac{5}{6}}$  and the velocity field should scale with  $t^{-\frac{1}{6}}$ . Hence, the prediction for the spatial scaling of the junction vortex in Allen and Naitoh's experiment and the experimental observations were in excellent agreement (both scaling with  $t^{\frac{5}{6}}$ , at least in the  $x$ -direction) and the prediction that the velocity field scaling with  $t^{-\frac{1}{6}}$  was moderately successful when applied to their experimental data.

To establish the momentum that the plasma actuator couples to the flow, the momentum in the  $x$ -direction is obtained from the time-resolved PIV velocity fields by integrating the  $U$ -component of velocity over the area of each PIV image. Hence, the momentum per unit length can be obtained by,

$$M_x = \rho \int_A U dA.\tag{4.4}$$

The momentum in the direction of plasma forcing throughout the actuation of DBD plasma is shown in Figure 4.14. The use of the momentum balance, Eqn. 4.4, to establish a forcing coefficient for the plasma has previously been

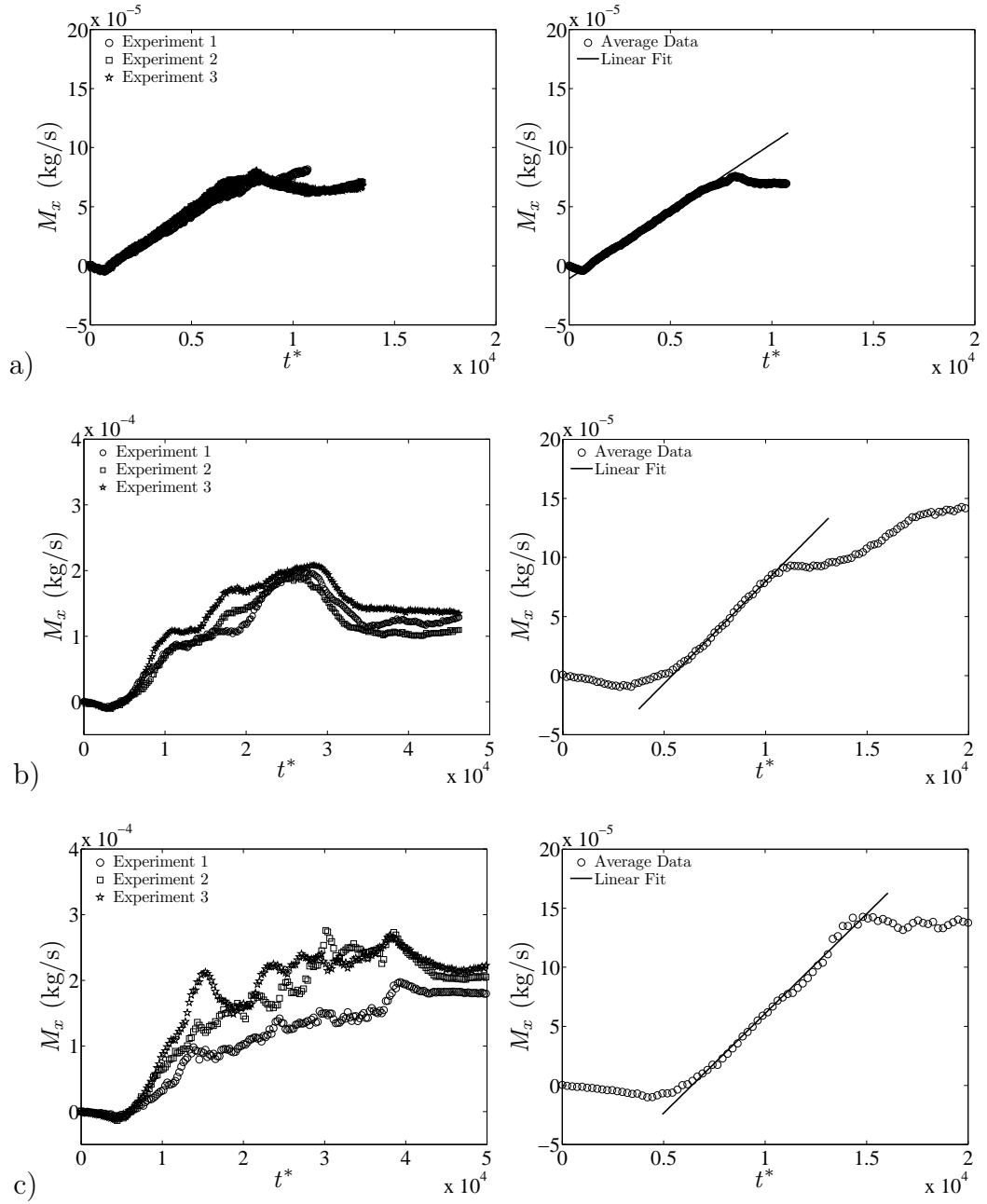


Figure 4.14: Momentum induced by the starting vortex over three experimental runs (left column) and average data with linear fit (right column), a) Case A with  $T = 600$  ms, b) Case B with  $T = 300$  ms and c) Case C with  $T = 300$  ms.

used by Jukes and Choi (2009a). The temporal evolution of momentum,  $M_x$ , for Case A (Table 4.1) with  $T = 600$  ms of continual forcing can be seen in Figure 4.14a), with momentum from three repeated experiments (left column) and the average of the three experiments (right column). The momentum is linear with time and a straight line can be fitted through the data indicating that the plasma is coupling momentum to the flow with constant forcing. The plasma stops actuation at  $t^* = 8100$  ( $t = 600$  ms) where the momentum begins to decrease. It can be seen at the initiation of plasma there appears to be negative momentum. This appears in all the cases of Figure 4.14 and is due to the glare from the white Mylar surface. As the plasma initiates the starting vortex is small and is located close to the plasma actuator. The glare from the Mylar stops PIV data from being attainable at the wall. Hence, the upper half of the vortex is only measured by the PIV, which is the region of reverse flow over the top of the vortex core. This negative  $U$ -component of velocity is what creates the negative momentum initially. As the vortex grows sufficiently away from the plasma actuator region, the glare no longer becomes a large issue and the momentum begins to increase due to higher velocity found underneath the starting vortex in the wall jet. The momentum for Cases B and C with 300 ms of continual plasma forcing with data from three events (left column) and the average of the three experiments (right column) are shown in Figure 4.14b) and c) respectively. In these two figures, the momentum needs to be analysed more carefully as fluid is being lost outside of the PIV measurement area due to the higher jet velocity created as the voltage and frequency applied to the plasma actuator is increased. Fluid being lost outside the PIV measurement area for Cases B and C was shown in Figure 4.6b) to c). Hence, for Figure 4.14b) (Case B) the data are unreliable for calculating momentum for  $t^* > 11000$  ( $t > 117$  ms) and for Figure 4.14c) (Case C) for  $t^* > 15000$  ( $t > 121$  ms). The region of data that is reliable for Cases B and C is shown in the right column of Figure 4.14b) and c), where a linear fit has been applied to the momentum. The scale of the plots where the

linear fit has been made to the momentum data (Figure 4.14 right column) is the same. Hence, by observation of the gradient it can be seen that the gradient of Case C > Case B > Case A. As the momentum is linear with time, this implies a constant force in the  $x$ -direction,  $F_x$ , supplied to the flow by the plasma actuator. By differentiating the momentum equation of each linear fit, the force per unit length can be obtained, these values can be found in Table 4.2. It can be seen in this table, that the forces throughout Cases A, B and C are on the order of mN. The lowest plasma force, 0.15 mN/m, is generated by the lowest applied voltage and frequency (Case A). The force generated by Cases B and C are fairly similar with 1.62 mN/m and 2.18 mN/m respectively. As the force,  $F_x$  is known, it is possible to define a forcing coefficient for the plasma,  $C_p$ ,

$$C_p = \frac{F_x}{\frac{1}{2}\rho U_m^2 L}, \quad (4.5)$$

where,  $F_x$  is the force in the  $x$ -direction,  $\rho$  is the density of the air,  $U_m$  is the maximum wall jet velocity and  $L$  is a characteristic length scale. The length scale,  $L$ , is defined as the distance in the  $x$ -direction to the vortex core from the end of the upper electrode ( $X_c$ ), at the time when the maximum velocity scale,  $U_m$ , has been reached. It was observed in Figures 4.8 and 4.9 that the maximum velocity scale occurred at around  $t^* = 5000$  for all cases. The values for the force coefficient,  $C_p$ , can be found in Table 4.2, which range from  $C_p = 0.058$  for Case A up to  $C_p = 0.211$  and  $0.219$  for Cases B and C respectively.

It has been shown that the plasma actuator couples momentum to the fluid linearly with time. Hence, the plasma couples momentum to the fluid with constant force. For a jet with constant forcing the exponent,  $n$ , in Cantwell's analysis is 2. By substitution of  $n = 2$  into Eqn. 4.3 yields explicit similarity groups for the scaling of the starting vortex,

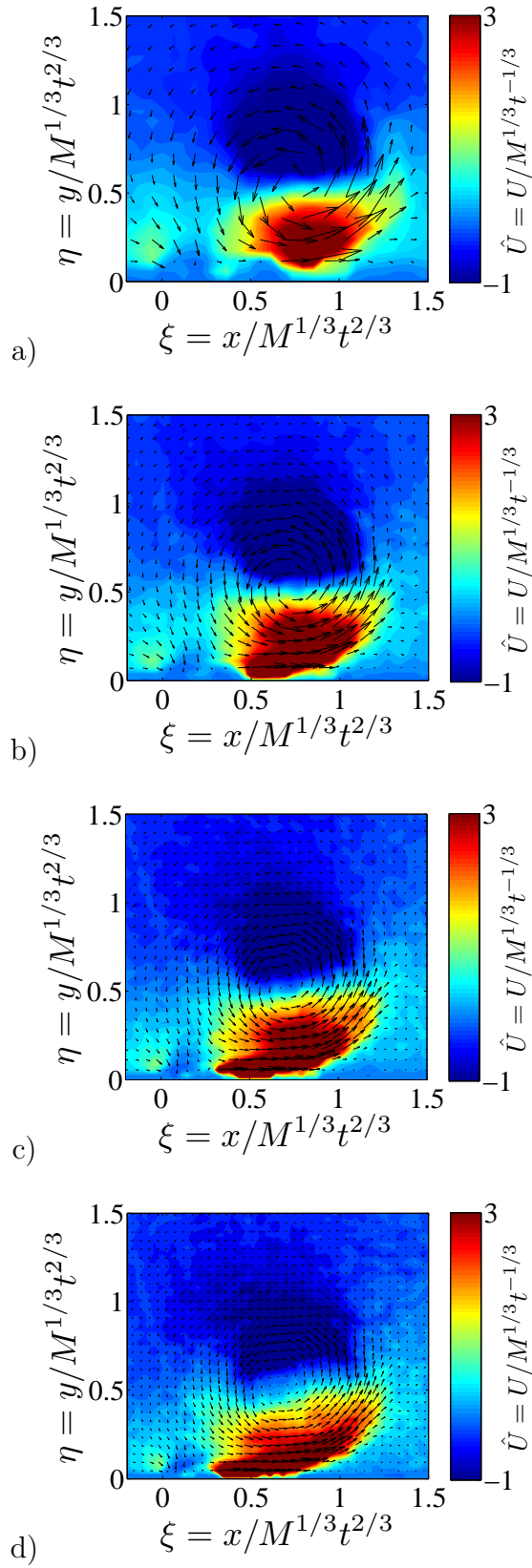


Figure 4.15: Self-similarity of the starting vortex for Case A at a)  $t^* = 1350$ , b)  $t^* = 2700$ , c)  $t^* = 4050$  and d)  $t^* = 5400$ .

$$\begin{aligned}\xi &= \frac{x}{M^{\frac{1}{3}}t^{\frac{2}{3}}} \\ \hat{U}(\xi) &= \frac{U}{M^{\frac{1}{3}}t^{-\frac{1}{3}}}.\end{aligned}\tag{4.6}$$

This analysis suggests that the vortex core should scale with  $t^{\frac{2}{3}}$ , which is in excellent agreement to that observed experimentally,  $t^{0.71}$ . Hence the analysis taken from Cantwell (1986) has linked the reason for the apparent scaling of a vortical structure at the head of a jet to the momentum which is imparted on the fluid by the jet. It has been found that the momentum coupled to the flow with a DBD plasma actuator varies linearly with time, implying that the plasma actuator is coupling the momentum to the fluid with a constant force. It has been noted that the momentum coupled to the flow is non-linear for the junction vortex experiment,  $\left(t^{\frac{3}{2}}\right)$ , which implies that the moving belt is coupling momentum to the fluid somewhere between a constant force and ramp force (Allen and Naitoh, 2007). This could be the physical reason why the transient structure generated by the junction flow and the DBD plasma do not scale by the same self-similar scaling rate; the momentum coupling to flow by the moving belt and DBD plasma actuators scale differently with time. In other words, it could be because the DBD plasma applies a constant force to the quiescent air and the moving belt applies somewhere between a constant force and ramp force.

The analysis of Cantwell also suggests that the velocity field should scale with  $t^{-\frac{1}{3}}$ . Figure 4.15 shows PIV data for a large range of  $t^*$  which have been scaled spatially using  $\xi = \frac{x}{M^{\frac{1}{3}}t^{\frac{2}{3}}}$ ,  $\eta = \frac{y}{M^{\frac{1}{3}}t^{\frac{2}{3}}}$  and with the velocity field scaled with  $\hat{U}(\xi) = \frac{U}{M^{\frac{1}{3}}t^{-\frac{1}{3}}}$ . It can be seen through Figure 4.15a) to d) where  $t^*$  ranges from 1350 to 5400 that the velocity fields all have a similar shape and distribution of velocity and the vortex core throughout all the images is held at a constant location of  $(\xi, \eta) = (0.7, 0.5)$ . Hence, Figure 4.15 indicates that the velocity field of the starting vortex has been scaled successfully with  $t^{-\frac{1}{3}}$  and is showing the start-

ing vortex generated by DBD plasma shows self-similarity. As the velocity field data collapses to the same shape when scaled spatially with  $t^{\frac{2}{3}}$  and with velocity scaled with  $t^{-\frac{1}{3}}$ , it is possible to take a time-average through the PIV images to determine a self-similar structure for the starting vortex. This is presented in Figure 4.16. Typically in this figure the velocity field is time-averaged from 50 ms to the end of plasma actuation and over the three PIV events. For the data shown in Figure 4.16, this amounts to 400-800 realisations of the velocity field for each time-average depending how long the plasma is actuated for. Figure 4.16a) is for Case A with 600 ms of continual plasma forcing, Figure 4.16b) is for Case B and Figure 4.16c) is for Case C. The values of the velocity scale for all three cases can be found in Table 4.2. The vertical black line in Figure 4.16a) to c) is the location through the vortex core ( $\xi = 0.7$ ), a plot of this velocity profile is shown in Figure 4.16d). Through a) to c) it is clear that the self-similar structure of the starting vortex for all conditions studied has an asymmetric velocity distribution. There is clearly a high-speed velocity region underneath the vortex core due to the plasma wall jet and a region of reversed flow with lower magnitude above the vortex core. For all cases presented the velocity profiles collapse reasonably well. The slight discrepancy between Case A to Cases B and C could be due to the lack of secondary vorticity generated during Case A, hence there is expected to be less of an interaction between the starting vortex and the secondary vorticity. The velocity profiles do not resemble a laminar wall jet at this stage as the velocity distribution is dominated by the starting vortex. To obtain a laminar wall jet profile, the plasma would have to be forced for a longer time period, allowing the vortical structure to convect away from the plasma region, an example of the wall jet profile is shown in Figure 4.2 and is taken from Jukes *et al.* (2006a).

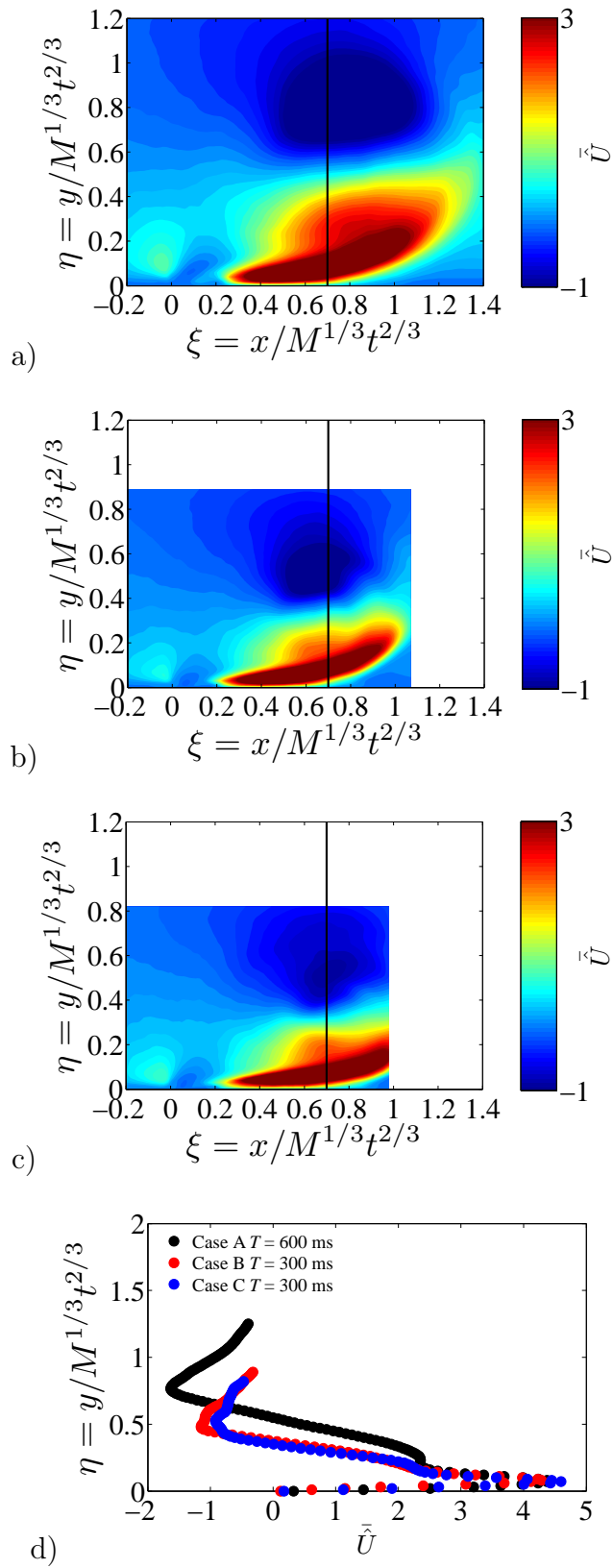


Figure 4.16: Self-similar structure of the starting vortex. a) Case A, b) Case B c) Case C, d) a plot through the vortex core.

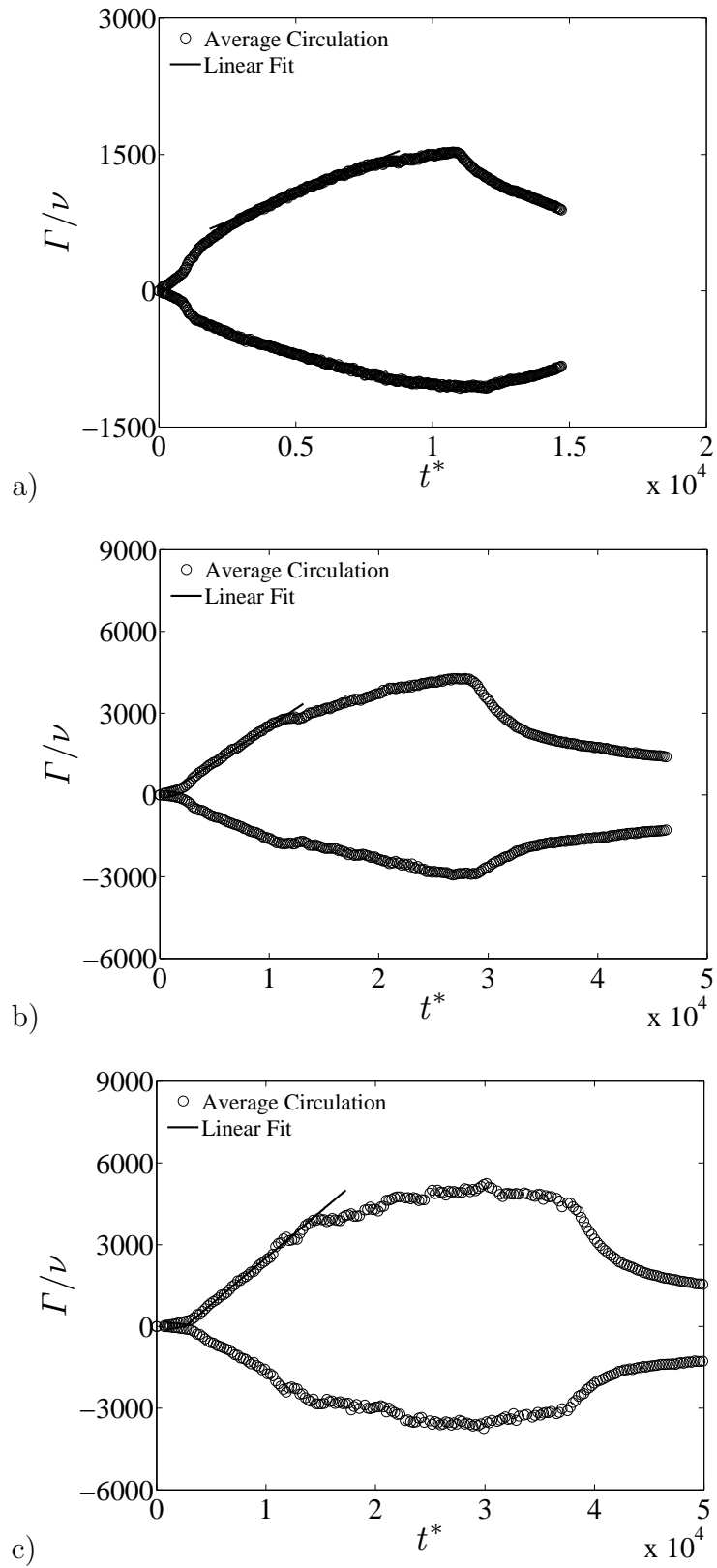


Figure 4.17: Circulation created by the starting vortex a) Case A with  $T = 600$  ms, b) Case B with  $T = 300$  ms and c) Case C with  $T = 300$  ms.

## Circulation

As we have seen in Figure 4.7, the starting vortex generates both primary and secondary vorticity. Integration of these quantities leads to the circulation developed by the starting vortex. Figure 4.17 represents the positive and negative circulation at a) Case A, b) Case B and c) Case C. The plasma ceases actuation at  $T = 600$  ms ( $t^* = 8100$ ) for Case A,  $T = 300$  ms ( $t^* = 28300$ ) for Case B and for  $T = 300$  ms ( $t^* = 37000$ ) for Case C. As the energy supplied to the DBD plasma actuator increases, by increasing the applied voltage and/or frequency, the momentum coupling to the flow increases. The increase in energy generates an increase in vorticity and the strength of the vortex increases accordingly. In all cases there appears to be an exponential start-up in the circulation data. These data could be spurious and were found in the momentum data (Figure 4.14) also. As the plasma initiates, the glare from the Mylar surface does not allow the PIV to resolve the starting vortex until it has sufficiently convected downstream of the plasma actuator. As the plasma initiates, a large impulse is given to the fluid. Laterally ejected fluid is replenished by strong downwash and entrainment due to mass continuity. This shearing motion generates vorticity, hence circulation, and causes the generation of the starting vortex. The vortex at this early stage has small velocity and length scales, is located close to the plasma region and is strongly affected by the momentum addition of the plasma jet. The starting vortex begins to grow and is convected along and away from the wall, away from the location of the plasma, hence away from the source of momentum. The time scale for the linear increase in circulation coincides with the time scale for linear increase in momentum. It should be noted that for Figure 4.17b) and c), fluid is lost from the control volume for  $t^* > 11000$  and  $15000$  respectively. Hence, it appears that the circulation is decreasing at a slower linear rate, but this may not be the case. It could simply be that the full contribution of vorticity in the computation of the circulation is not present as fluid is lost outside of the measurement area of the PIV. It is also apparent from Figure 4.17 that the magnitude

of the secondary vorticity is on the same order as the primary vorticity for all the cases presented. On comparison of Figures 4.17a) with b) and c), there are large differences in the magnitude of circulation. The larger the applied voltage and/or frequency, the greater the circulation and strength of the starting vortex. Although the circulation is of the same order of magnitude for both cases, increasing voltage and/or frequency by 25% yields the circulation of the vortex to increase by factor of 2.

## The Mechanism of the Starting Vortex

The mechanism of the starting vortex is described in Figure 4.18 using four images. As the upper electrode of the DBD plasma reaches the breakdown voltage, plasma ions are transferred to and from the dielectric surface and a plasma discharge extends for a few mm to the right of the upper electrode over the dielectric material, imparting a body force on the surrounding ambient gas. The plasma couples momentum to the fluid and not mass, therefore entrainment is a key feature of the DBD plasma actuator. This is represented in Figure 4.18a), where the plasma body force is acting in the horizontal direction adjacent to the wall. To replenish the fluid that has been ejected laterally by the plasma body force, entrainment occurs directly above the plasma region. As the plasma initiates and the plasma body force is generated in the horizontal direction, the force generated by the vertical entrainment of fluid will be of the same order. This will create a circulating region in the vicinity of the plasma actuator and will cause the formation of the starting vortex, Figure 4.18b). As fluid is being pushed in the horizontal direction whilst fluid is being entrained in the vertical direction, two velocity gradients are being created, namely  $\frac{\partial v}{\partial x}$  by the vertical entrainment of fluid and  $\frac{\partial U}{\partial y}$  by the plasma body force thrusting fluid in the horizontal direction. The two velocity gradients contribute to the vorticity generated by the plasma actuator and hence to the circulation of the starting vortex. To preserve

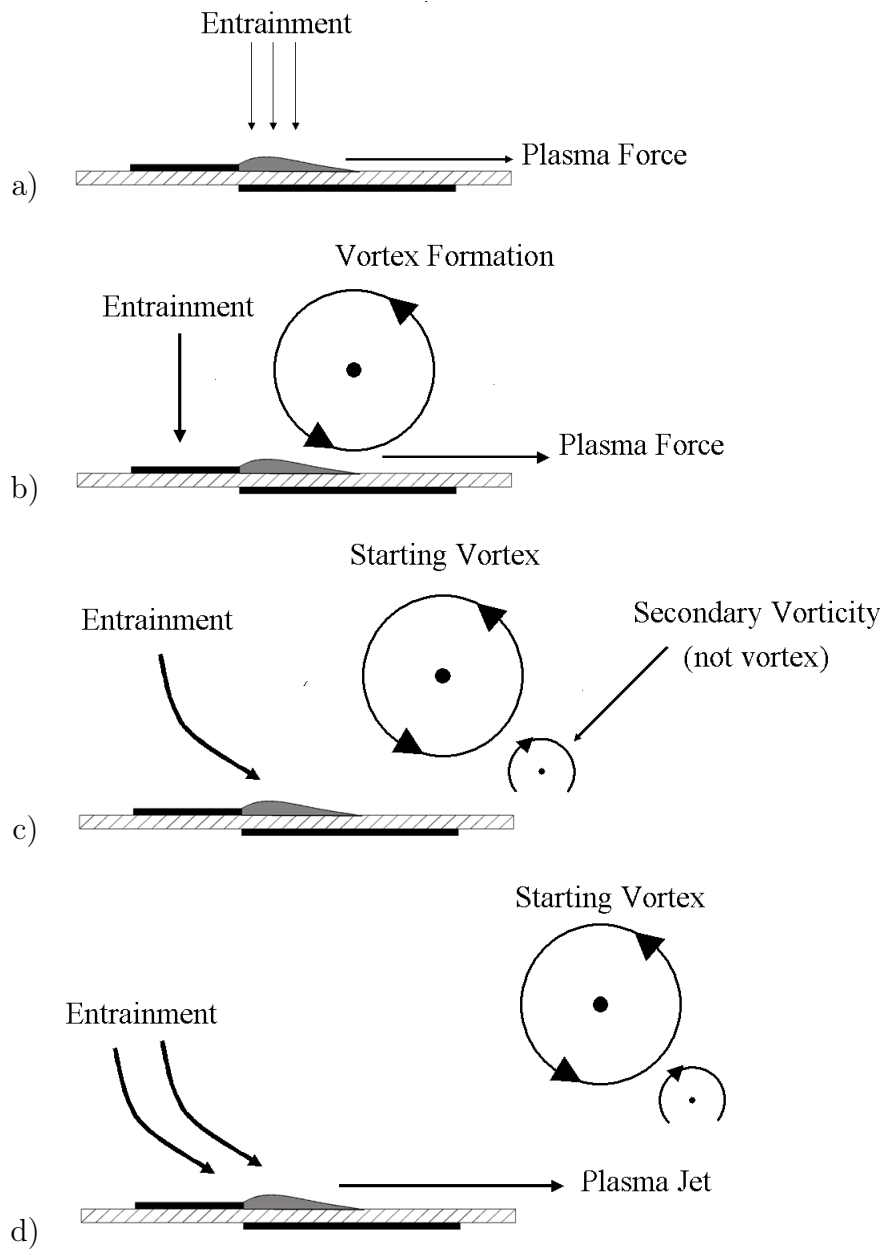


Figure 4.18: Mechanism of the starting vortex a) plasma initiation, b) vortex formation, c) generation of secondary vorticity and d) plasma wall jet.

the no-slip boundary condition, secondary vorticity is generated at the wall, Figure 4.18c). As the starting vortex is pushed along and away from the wall the secondary vorticity will be wrapped around the starting vortex. Now the plasma wall jet is established the entrainment of fluid to replenish the laterally ejected fluid is not solely from above the plasma region. In other words, the entrainment vector is no longer  $90^\circ$  to the wall, it begins to make an angle with the horizontal, Figure 4.18c). As the plasma continues to actuate, the starting vortex, Figure 4.18d), is thrust further in the horizontal direction and is convected away from the wall, growing in size and circulation.

## 4.2 Chapter Summary

It has been found that on initiation of DBD plasma in quiescent air a starting vortex is created, which rolls up to form a coherent transient structure, qualitatively similar to the junction vortex of Allen and Naitoh (2007). It has been shown that the location of the core of the starting vortex scales with  $t^{0.71}$  in both the horizontal and vertical directions, and the starting vortex moves at angle of  $31^\circ$  to the wall for all cases presented. The growth rate of the starting vortex has been related to the momentum which is imparted by the plasma actuator, which results in the prediction that the vortex core should scale with  $t^{\frac{2}{3}}$  (Cantwell, 1986), which is in excellent agreement with the experimental observations. The velocity field has been predicted to scale with  $t^{-\frac{1}{3}}$  and it has been shown that this prediction is in excellent agreement with the experimental data. Hence, the starting vortex generated on initiation of DBD plasma shows signs of self-similar scaling. The mechanism of the starting vortex is thought to be due to continuity, with laterally ejected fluid created by the plasma wall jet being replenished by entrainment above the plasma region, creating circulation. Secondary vorticity generated to preserve the no-slip boundary condition has been seen throughout all the conditions studied. The secondary vorticity is found to be wrapped around

the starting vortex and aid the movement of the starting vortex away from the wall.

# Chapter 5

## Spanwise Travelling Waves in Quiescent Air

The effects of actuating a single, asymmetric DBD plasma actuator have been shown in Chapter 4. In this section, an electrode design is developed to create 4-phase spanwise travelling waves for turbulent boundary-layer control. The electrode design consists of several asymmetric DBD plasma actuators arranged to create travelling waves with two forcing configurations. The travelling waves are initially studied in quiescent air to determine whether it is possible to create spanwise travelling-wave excitations with DBD plasma.

### 5.1 Travelling-Wave Actuator Sheets

The spanwise travelling-wave actuator sheets (see §3.8) could be actuated with two forcing configurations, unidirectional and bidirectional. Unidirectional forcing actuated in one direction per phase, bidirectional forcing actuated with two opposite directions per phase, with each travelling wave forcing over a wavelength,  $\lambda = 100$  mm. The entire sheet consisted of  $3\lambda$ . Figure 5.1 shows a schematic of uni and bidirectional forcing. Opposing electrodes for bidirectional forcing were separated by a distance,  $s = 56$  mm. Each phase of the travelling waves were actuated for a time period of  $\frac{1}{4}T$ . The amplitudes of the travelling waves could

be altered by changing the applied voltage and frequency supplied to the DBD plasma actuators and the phase speed of travelling waves could be altered by changing the length of time each plasma actuator was fired. The spatial and temporal scales used in the experiments were based on the conditions studied by Xu and Choi (2006) where a 30% reduction in turbulent skin-friction drag was obtained using Lorentz forcing.

The ideal travelling wave forcing equation is,

$$F_z = I e^{-\frac{y}{\Delta}} \sin\left(\frac{2\pi}{\lambda} z - \frac{2\pi}{T} t\right), \quad (5.1)$$

where  $F_z$  is the force imposed at the wall in the spanwise direction and  $I$  is the amplitude of the travelling wave. The travelling-wave force is maximum at the wall and decays exponentially to a penetration depth,  $\Delta$ . The wavelength of the travelling wave is denoted by,  $\lambda$ , and the time period is,  $T$ . This forcing equation is continuous and is frequently used in DNS studies of turbulent boundary-layer control (Du *et al.*, 2002; Zhao *et al.*, 2004). However, an ideal travelling-wave excitation, Eqn. 5.1, is very difficult to implement practically as actuators are located and actuated at discrete locations in space and time.

## 5.2 2D PIV Measurements of Spanwise Travelling Waves in Quiescent Air

For the experiments in this section, a travelling wave over one wavelength was created by powering the 8 central electrodes with 8 plasma power supplies. The plasma power supplies operate most efficiently when the AC operating frequency is tuned to match the operating frequency of the load, causing resonance. This depends on the load (capacitance) and the transformer of the power supply. The optimum AC frequency can be found by observing the AC voltage waveform as the AC operating frequency is incremented at low voltage; when the system is

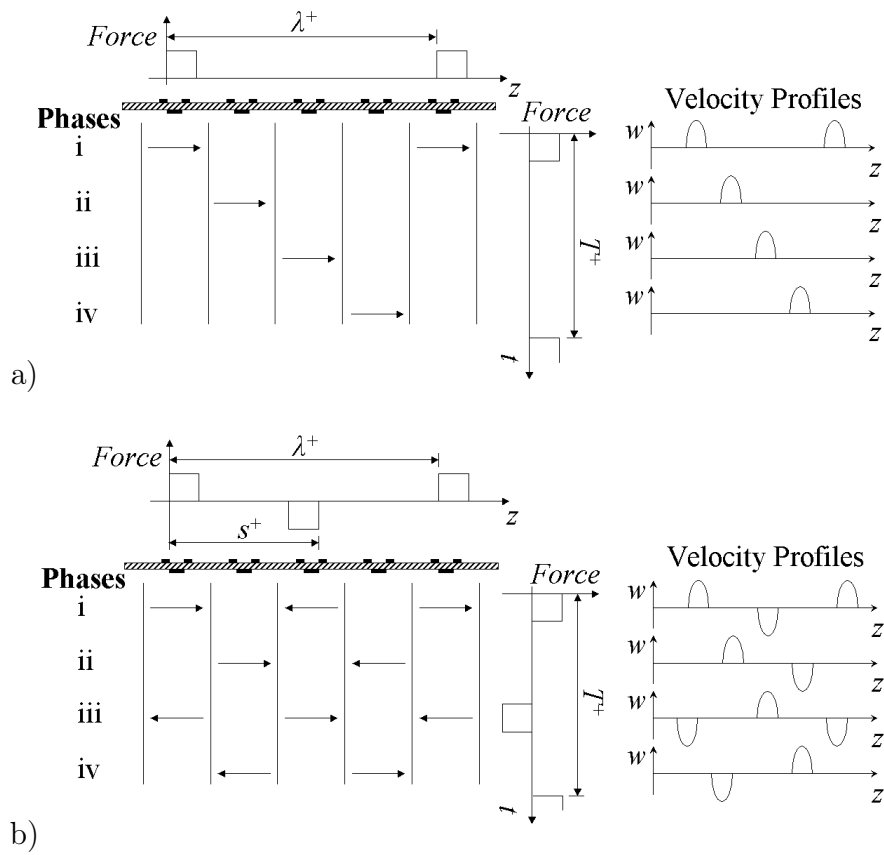


Figure 5.1: Schematic representation of 4-phase spanwise travelling waves. a) Unidirectional forcing and b) bidirectional forcing.

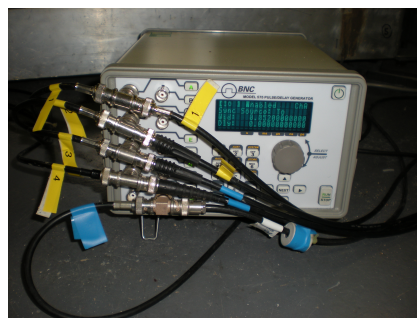


Figure 5.2: Signal generator used to create the 4-phase spanwise travelling waves.

Table 5.1: Experimental conditions studied for uni and bidirectional spanwise travelling waves in quiescent air.

Plasma Parameters		Travelling-Wave Period, $T$ (ms)			
$E_{p-p}$ (kV)	$f$ (kHz)	124	148	184	208
7.00	25	✓	✓	✓	✓
6.72	25	✓	✓	✓	✓
6.50	25	✓	✓	✓	✓
6.30	25	✓	✓	✓	✓

tuned, the peak-peak voltage will be at a maximum and the voltage waveform will have a smooth sinusoidal profile. Each power supply transformer has a fixed optimum frequency for a given load. It is, of course, still possible to operate the power supply at a frequency other than the optimum frequency, although, care must be taken not to heavily distort the AC waveform, as the regions of plasma formation may alter. For the spanwise travelling-wave actuator sheets, the optimum AC frequency was found to be 25 kHz. Therefore, throughout the experiments the sinusoidal voltage input to the plasma power supplies was varied from  $E = 6.30 - 7.00$  kV<sub>p-p</sub> at a fixed frequency of  $f = 25$  kHz, which was monitored using a Tektronix TDS2024 200MHz oscilloscope. The time period,  $T$ , of the travelling wave was varied from 124 - 208 ms with an 8 channel BNC 575 series Pulse generator, Figure 5.2. The test conditions for the spanwise travelling waves in quiescent air can be found in Table 5.1.

A unidirectional forcing configuration was tested by Du *et al.* (2002) in their DNSs using a square wave positive pulse for the forcing function. A slight increase in skin-friction drag was predicted. They did not explore the parameter space, hence only a single simulation was run and unfortunately the reason for the skin friction increase was not discussed by the authors. Therefore, it is not known whether a unidirectional forcing configuration would always yields skin friction increase or could be optimised to achieve skin-friction drag reduction. As very little information is known on the mechanism for the possible increase in skin friction for unidirectional forcing it is one of our objectives to investigate this

further.

## Unidirectional Forcing PIV Data

Phase-averaged PIV images (of five independent travelling-wave periods) of a spanwise travelling wave with unidirectional forcing in quiescent air are shown in Figure 5.3 through velocity magnitude and vorticity measurements. In each of these figures there are four images, one taken at the end of each of the 4-phases (i) to (iv). The plasma is operated with an applied voltage,  $E = 7.00 \text{ kV}_{\text{p-p}}$  at a frequency,  $f = 25 \text{ kHz}$  for a time period,  $T = 208 \text{ ms}$ , with each actuator capable of creating a  $1 \text{ m/s}$  wall jet with these plasma parameters. The location of the plasma actuators and the direction of the DBD plasma jets are indicated under each image. The travelling-wave direction is from left to right. On actuation of DBD plasma a starting vortex is created (Whalley and Choi, 2010a), which develops and moves along and away from the wall in the positive  $z$ -direction as seen in phase (i). The core of the starting vortex is located at  $y = 10 \text{ mm}$ . The secondary vorticity is generated due to the no-slip boundary condition (Allen and Naitoh, 2007), which is seen wrapped around the primary roller. This is qualitatively similar to the piston vortex of Allen and Chong (2000), where the secondary vorticity was found to induce the movement of the piston vortex away from the surface of the piston. Hence, it is thought that the secondary vorticity generated by the starting vortex is aiding the starting vortex to move away from the wall (Allen and Chong, 2000). Phase (ii) shows the creation of a new starting vortex. This entrains the previously formed starting vortex generated from phase (i) to cause the two co-rotating vortices to coalesce, thrusting the fluid further in the spanwise direction. At the end of phase (iii), the wall jet begins to separate from the wall and wraps up around the starting vortex, due to the induction of the starting vortex. The travelling wave appears to move the fluid effectively in the spanwise direction by entraining the fluid from the previous phase and adding

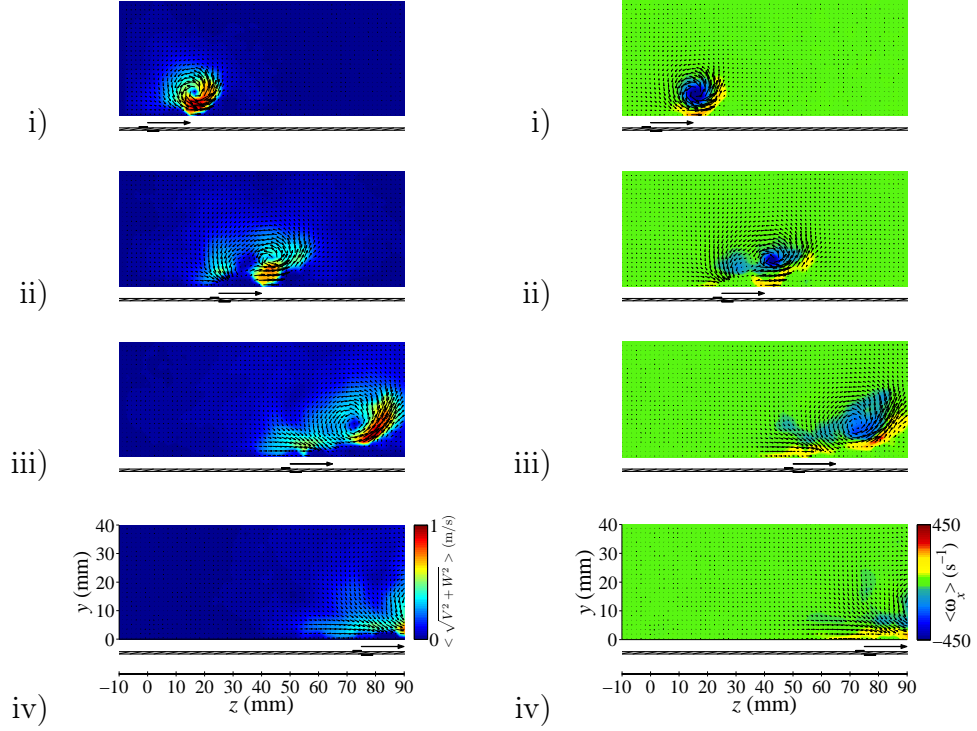


Figure 5.3: PIV results to show the effect of travelling waves in quiescent air with unidirectional forcing on velocity magnitude (left hand column) and streamwise vorticity (right hand column) at i)  $\frac{1}{4}T$ , ii)  $\frac{1}{2}T$ , iii)  $\frac{3}{4}T$  and iv)  $T$ .  $\lambda = 100$  mm,  $T = 208$  ms,  $E = 7.00$  kV<sub>p-p</sub> at  $f = 25$  kHz.

momentum at each phase of forcing (Whalley and Choi, 2010b). In Figure 5.3 directly above the plasma actuation there are regions of spurious data. This is from the glare and reflection from the white Mylar surface and from the light emitted from the plasma discharge making it not possible to obtain PIV data in this small region.

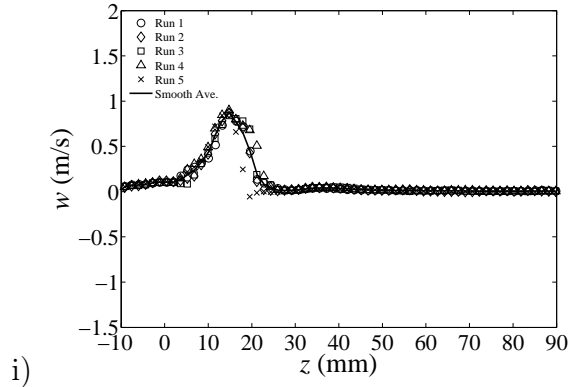
The spanwise velocity distribution at half the distance between the vortex core and wall, ( $y = 5$  mm) for the same test condition as Figure 5.3 with unidirectional forcing is shown in Figure 5.4. For comparison, the spanwise velocity distribution for a range of different forcing periods at  $E = 7.00$  kV<sub>p-p</sub> at  $f = 25$  kHz is shown in Figure 5.5. Each event is repeated five times and phase-averaged at the end of each of the 4-phases (i) to (iv). The velocity distribution (particularly phase (i)) of Figures 5.4 and 5.5 resembles half of the generic two-bump forcing profile, Figure 5.6, that Du *et al.* (2002) had used in their DNSs of spanwise travelling waves. In each of the 4-phases for the data shown in Figure 5.4, there

is a velocity distribution which is spanning a distance on the order of 30 mm ( $\sim 30$  mm). This is a typical length scale for the fluid to move,  $\frac{1}{2}s$ , which is approximately the distance between the adjacent electrodes in the unidirectional forcing configuration, Figure 5.1. This indicates that the fluid is effectively being moved from actuator to actuator through the 4-phases of the travelling wave. The travelling wave has a velocity amplitude  $\sim 1$  m/s (at least for the voltage and frequency applied to the actuators in this test condition) and travels with a wave speed,  $c = \frac{\lambda}{T} = 0.5$  m/s. In Figure 5.5, the time period,  $T$ , of the travelling wave is reduced. Hence, the time that the DBD plasma is on for per phase is reduced and it can be seen that with reduced plasma duration brings a smaller movement of fluid per phase with smaller spanwise velocity magnitude.

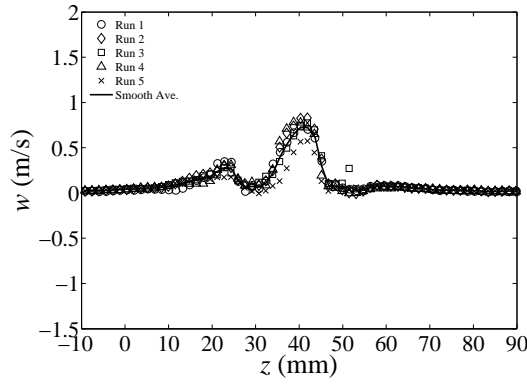
The spanwise velocity distribution as a function of wall-normal distance, through the cores of the starting vortex at the end of each phase for the PIV data presented in Figure 5.3 can be seen in Figure 5.7. The vortex core is distinguishable at  $y = 10$  mm with spanwise velocity at this point being zero. Positive and negative spanwise velocity can be seen under and above the vortex core. At the end of each phase there is a positive spanwise velocity on the order 1 m/s located at half the distance between the vortex core and wall ( $y = 5$  mm), and also a negative spanwise velocity of the same order, typically 0.5 m/s. Hence, the unidirectional spanwise travelling wave creates both large positive and negative spanwise velocity as it moves in the positive spanwise direction. This is because the spanwise travelling wave with DBD plasma is dominated by a vortical flow system.

## The Phase Lag Effect with Unidirectional Forcing

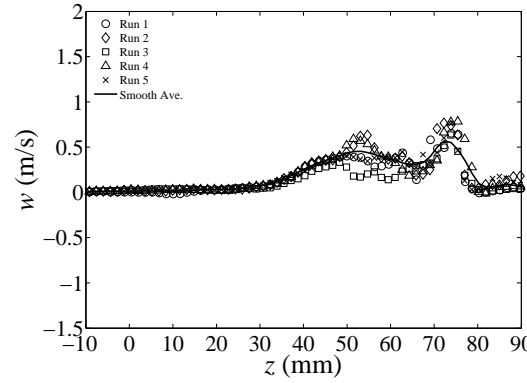
The unidirectional forcing configuration exhibits phase lag through the four phases of the travelling wave. At the end of phase (i), a starting vortex is generated as already shown, Figure 5.3i). Phase (ii) initiates where it takes



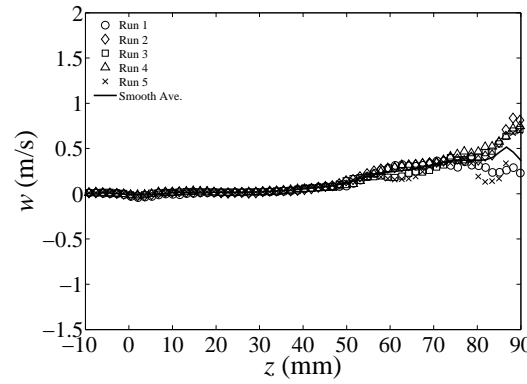
i)



ii)



iii)



iv)

Figure 5.4: Spanwise velocity profiles at  $y = 5$  mm with unidirectional forcing at i)  $\frac{1}{4}T$ , ii)  $\frac{1}{2}T$ , iii)  $\frac{3}{4}T$  and iv)  $T$ .  $\lambda = 100$  mm,  $T = 208$  ms,  $E = 7.00$  kV<sub>p-p</sub> at  $f = 25$  kHz.

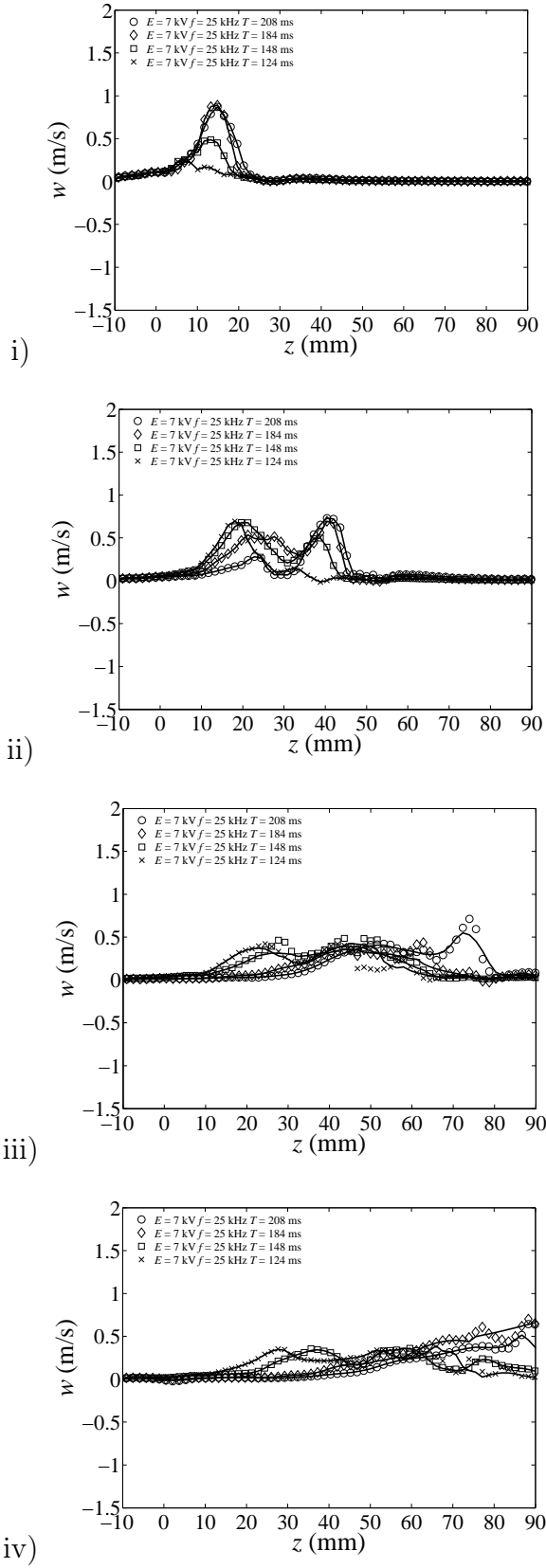


Figure 5.5: Spanwise velocity profiles at  $y = 5 \text{ mm}$  with unidirectional forcing for  $T = 124 \text{ ms}$  to  $T = 208 \text{ ms}$  at i)  $\frac{1}{4}T$ , ii)  $\frac{1}{2}T$ , iii)  $\frac{3}{4}T$  and iv)  $T$ .  $\lambda = 100 \text{ mm}$ ,  $E = 7.00 \text{ kV}_{\text{p-p}}$  at  $f = 25 \text{ kHz}$ .

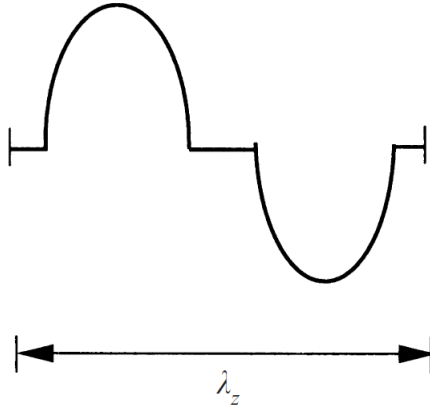


Figure 5.6: Generic two-bump forcing profile used by Du *et al.* (2002).

around 30 ms for the starting vortex that was created during phase (i) to be positioned over the actuator of phase (ii). This phase lag continues throughout the four phases but diminishes through phases (ii) to (iii) to typically 18 ms. At the beginning of phase (iv) there is no noticeable phase lag and the coalesced starting vortex is already positioned over the phase (iv) actuator on initiation of this phase. Hence, the momentum addition by the DBD plasma actuator at each phase of forcing in the unidirectional configuration produces the spanwise travelling wave. This relies on transporting the fluid from the previous phase a distance of  $\frac{1}{2}s$ , such that sequential forcing will entrain and transport fluid from previous phases in the spanwise direction. If the strength of the plasma forcing (amplitude of the travelling wave) or the duration of actuation (time period of the travelling wave), or a combination of both, are too low, the unidirectional travelling-wave mechanism breaks down; fluid is no longer moved from actuator to actuator, hence each actuator acts independently. This is shown in Figure 5.8 with images of vorticity shown at the end of each of the 4-phases. Here, the DBD plasma is operated with  $E = 6.72 \text{ kV}_{\text{p-p}}$  at  $f = 25 \text{ kHz}$  for a period,  $T$ , of 124 ms with each actuator capable of creating a 0.7 m/s wall jet with these plasma parameters. At the end of phase (i), after plasma actuation for  $\frac{1}{4}T$ , a starting vortex has formed. Phase (ii) begins, creating a new co-rotating starting vortex that is unable to entrain the starting vortex of phase (i), having not moved

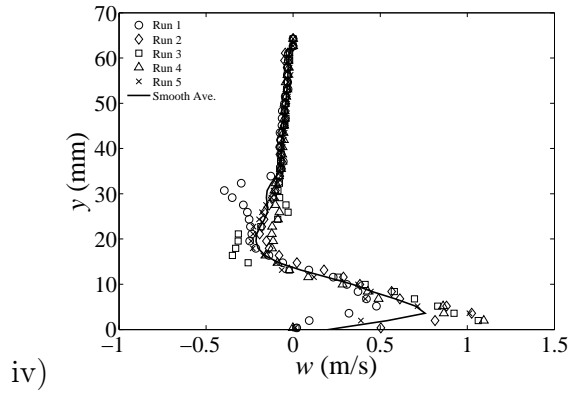
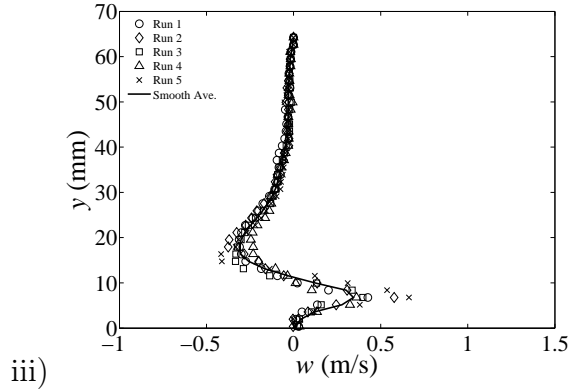
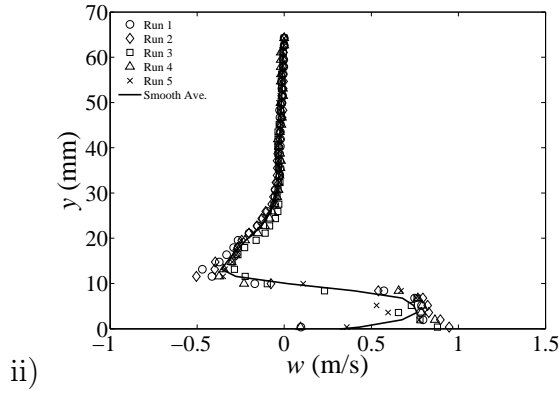
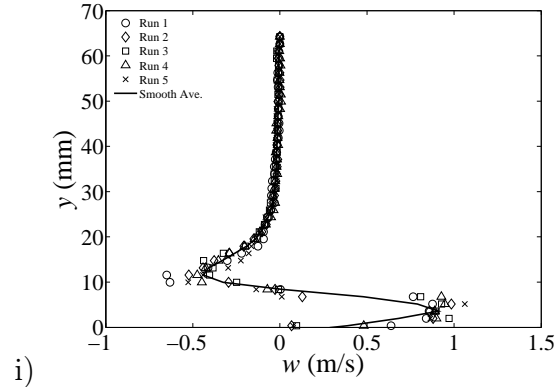


Figure 5.7: Spanwise velocity profiles through the vortex core with unidirectional forcing at i)  $\frac{1}{4}T$ , ii)  $\frac{1}{2}T$ , iii)  $\frac{3}{4}T$  and iv)  $T$ .  $\lambda = 100$  mm,  $E = 7.00$  kV<sub>p-p</sub> at  $f = 25$  kHz.

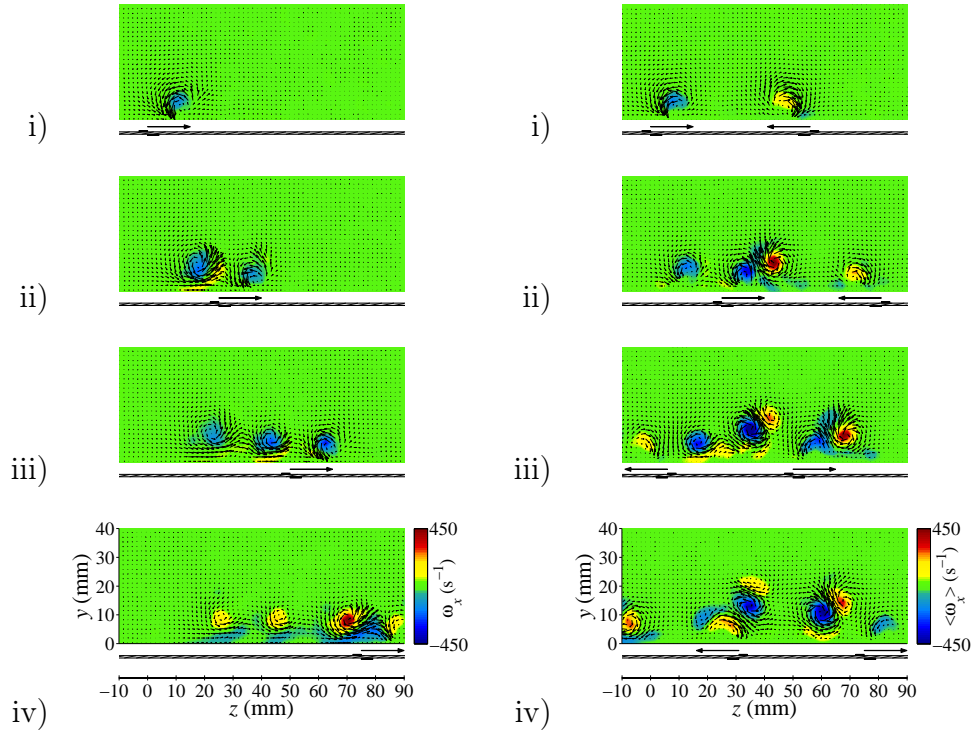


Figure 5.8: Breakdown of the spanwise travelling-wave excitations with unidirectional forcing (left column) with  $E = 6.72 \text{ kV}_{\text{p-p}}$  at  $f = 25 \text{ kHz}$  and bidirectional forcing (right column) with  $E = 6.30 \text{ kV}_{\text{p-p}}$  at  $f = 25 \text{ kHz}$ , i)  $\frac{1}{4}T$ , ii)  $\frac{1}{2}T$ , iii)  $\frac{3}{4}T$  and iv)  $T$ .  $\lambda = 100 \text{ mm}$ ,  $T = 124 \text{ ms}$ .

a distance of  $\frac{1}{2}s$ . This results in two co-rotating starting vortices at the end of phase (ii). Similar results are seen at the end of phases (iii) and (iv), where a system of independent co-rotating starting vortices are travelling in the spanwise direction and the coupling of fluid from phase to phase is redundant, causing a break down of the travelling-wave excitation.

## Bidirectional Forcing PIV Data

Phase-averaged PIV images (over five independent travelling-wave periods) of a spanwise travelling wave with bidirectional forcing in quiescent air are shown in Figure 5.9 through velocity magnitude and vorticity plots. In each of these figures there are 4 images, one taken at the end of phases (i) to (iv). The location of the plasma actuators and the direction of the DBD plasma jets are indicated under each image. The DBD plasma is actuated with  $E = 7.00 \text{ kV}_{\text{p-p}}$  at  $f = 25 \text{ kHz}$

for  $T = 208$  ms. The travelling-wave direction is from left to right. On actuation of DBD plasma a starting vortex is created, in a similar fashion with Chapter 4 and with the unidirectional forcing, Figure 5.3. For the bidirectional forcing there are two actuations per phase in opposite directions, causing two vortices to develop, moving along and away from the wall as seen in Figure 5.9 at the end of phase (i). The vortices have an asymmetric velocity distribution with a maximum velocity on the  $\sim 1$  m/s under the core and have effectively collected fluid in a region close to the phase (ii) actuator. The strong sense of vorticity (right hand column) indicates the core locations at  $y = 10$  mm from the wall, with the secondary vorticities generated due to the no-slip boundary condition. The secondary vorticities are wrapped around the primary rollers, aiding vortex movement away from the wall (Allen and Chong, 2000). Figure 5.9 clearly shows the first movement of the travelling-wave motion at the end of phase (ii). A large stretch of fluid  $\sim 1$  m/s, encapsulated within the first 10 mm of the wall, can be seen emanating away from the second actuation region in the positive  $z$ -direction. This is part of the fluid on the underside of the starting vortex that has been entrained into the region of the plasma actuator by actuation of phase (ii). This region of the fluid is then pushed forwards in the positive  $z$ -direction during this phase of actuation, with similar behaviour (collection and thrusting of fluid) through phases (iii) and (iv). The stretch of fluid has moved further in the positive  $z$ -direction through (i) to (iv) by a combination of fluid entrainment and momentum addition from each actuation of the travelling-wave excitation. As this region of fluid is being transported along the wall in the positive  $z$ -direction, there is also a highly vortical flow structure developing throughout the phases. Secondary vorticity is being generated at the wall which is being moved in the direction of the travelling wave. Other vortical systems are generated on top, behind and in front of the travelling wave, showing a complex system of vortical interactions during the initiation of DBD plasma and the bidirectional travelling-wave excitation.

Du *et al.* (2002) studied using DNS, a continuous spanwise travelling wave implemented with a Lorentz force inside a turbulent channel flow. In their results, there were regions of equal and oppositely signed streamwise vorticity along the wall, which were centered around the regions of maximum force. This is similar to the spanwise travelling waves generated by DBD plasma. However, care must be taken when comparing the spanwise travelling wave of Du *et al.* (2002) and the spanwise travelling wave with DBD plasma, as each spanwise travelling wave is generated by two different forcing techniques. Furthermore, the work presented here is in quiescent air and not inside the turbulent boundary layer. Still, positive and negative streamwise vorticity can be seen close to the wall ( $y < 5$  mm), which is due to the secondary vorticity generated as the starting vortices move over the wall. Similarly, positive and negative streamwise vorticity can be seen in spanwise travelling wave of Du *et al.* (2002), Figure 7.5b), at  $y^+ = 4$  inside a turbulent channel flow. However, this is not to say that the continuous spanwise travelling wave of Du *et al.* (2002) implemented with a Lorentz force has a high vortical system above the wall like in the case of the spanwise travelling wave with DBD plasma.

A cut through the velocity field data, Figure 5.9, at a wall distance of  $y = 5$  mm, half the distance between the vortex core and wall, is presented in Figure 5.10. Each event is repeated five times and phase-averaged at the end of each of the 4-phases (i) to (iv). The velocity distribution (particularly phase (i)) resembles the generic two-bump forcing profile that Du *et al.* (2002) had used in their DNSs of spanwise travelling waves, Figure 5.6. They found that this waveform needed to be actuated at twice the wave speed of the ideal sinusoidal waveform to obtain a similar amount of drag reduction. This was believed to be due to the gaps between the positive and negative action regions of the forcing cycle. However, in their simulations the two-bump profile was still continuous in the sense that it was not operated in phases as is the spanwise travelling wave with DBD plasma presented here. The spanwise velocity in Figure 5.10 has an

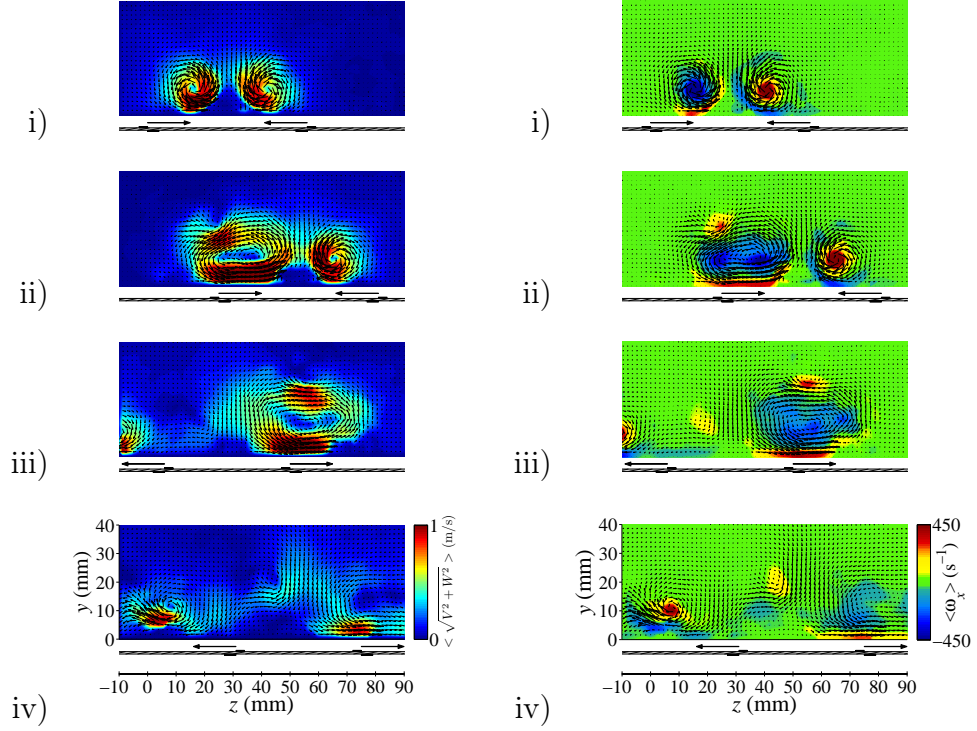


Figure 5.9: PIV results to show the effect of travelling waves in quiescent air with bidirectional forcing on velocity magnitude (left hand column) and streamwise vorticity (right hand column) at i)  $\frac{1}{4}T$ , ii)  $\frac{1}{2}T$ , iii)  $\frac{3}{4}T$  and iv)  $T$ .  $\lambda = 100$  mm,  $T = 208$  ms,  $E = 7.00$  kV<sub>p-p</sub> at  $f = 25$  kHz.

elongated region spanning  $\sim 30$  mm. This is a typical length scale for the fluid to move  $\frac{1}{2}s$  (Figure 5.1), very similar to unidirectional forcing (Figure 5.4) indicating that the fluid is being moved effectively from actuator to actuator through the 4-phases, in this case with a wave speed,  $c = 0.5$  m/s and with an amplitude  $\sim 1$  m/s. An example of the effects of changing the time period,  $T$ , with bidirectional forcing is shown in Figure 5.11. The two-bump velocity profile can be seen for all the time periods shown. However, similar with unidirectional forcing, reducing the time period of the travelling wave by reducing the duration of the plasma creates a reduction in both the spanwise velocity and the spanwise distance that fluid can be moved.

The spanwise velocity distribution as a function of wall-normal distance, through the cores of the starting vortices at the end of each phase for bidirectional forcing can be seen in Figure 5.12. Similar to unidirectional forcing, the vortex core is distinguishable at  $y = 10$  mm and both positive and negative

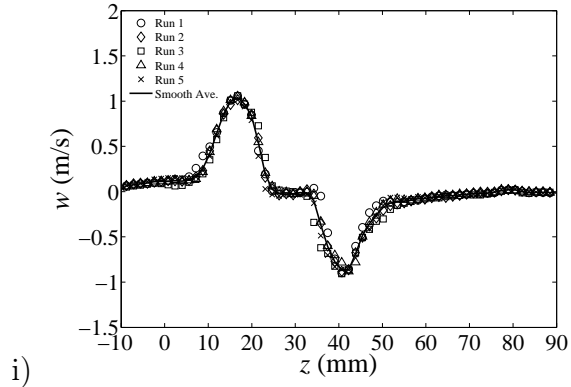
spanwise velocity can be seen under and above the vortex core. Throughout the four phases, the maximum spanwise velocity is typically at 5 mm, hence half the distance between the vortex core and the wall. The positive spanwise velocity is nominally 1 m/s, as was found with unidirectional forcing. However, spanwise velocity up to 1.5 m/s can be seen, for example, at the end phase (iii). There is negative spanwise velocity above the vortex core, which is typically on the order of 0.5 m/s and can reach as high as 1 m/s through the four phases. Hence, the bidirectional spanwise travelling wave creates both large positive and negative spanwise velocity as it moves in the positive spanwise direction, at times, larger than the unidirectional forcing configuration. The positive and negative regions of spanwise velocity are due to the dominating vortical flow system created by the DBD plasma actuators during the bidirectional travelling wave.

## The Phase Lag Effect with Bidirectional Forcing

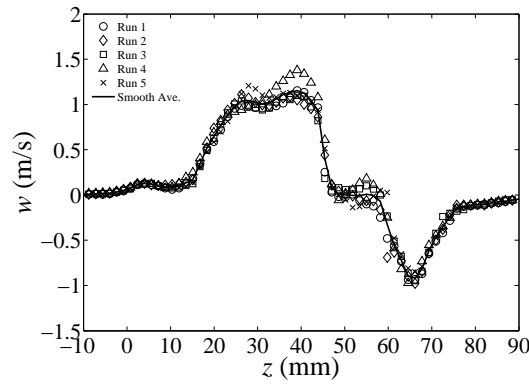
As expressed during the discussion on unidirectional forcing, the travelling wave experiences phase lag. This is also the case for the bidirectional travelling wave. It was found that at the end of phase (i), a pair of starting vortices were created. At the end of phase (ii), a large region of fluid on the order of 1 m/s was seen encapsulated in the first 10 mm of the wall and was moving in the positive spanwise direction, Figure 5.9. This region of fluid lagged the actuation of the travelling wave by typically 30 ms ( $\frac{15}{104}T^+$ ). Hence, the region of fluid moving in the positive spanwise direction arrived over the actuator which was forcing typically 30 ms after the forcing had initiated. A phase lag of around 30 ms was seen throughout the four phase with the bidirectional spanwise travelling wave.

## The Mechanism with Bidirectional Forcing

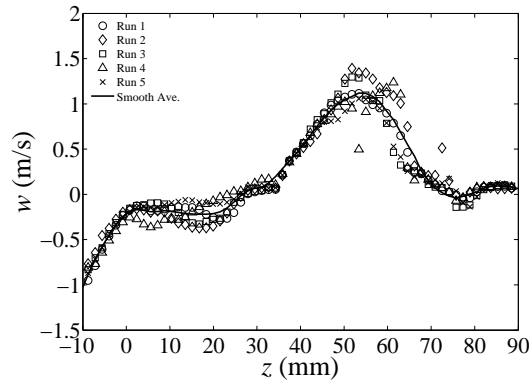
To understand the mechanism in forming the bidirectional travelling wave, Figure 5.13 shows a series of phase-averaged vorticity images taken during phase (ii)



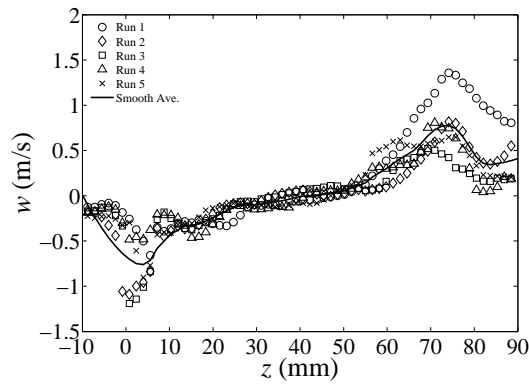
i)



ii)



iii)



iv)

Figure 5.10: Spanwise velocity profile at  $y = 5$  mm with bidirectional forcing at i)  $\frac{1}{4}T$ , ii)  $\frac{1}{2}T$ , iii)  $\frac{3}{4}T$  and iv)  $T$ .  $\lambda = 100$  mm,  $T = 208$  ms,  $E = 7.00$  kV<sub>p-p</sub> at  $f = 25$  kHz.

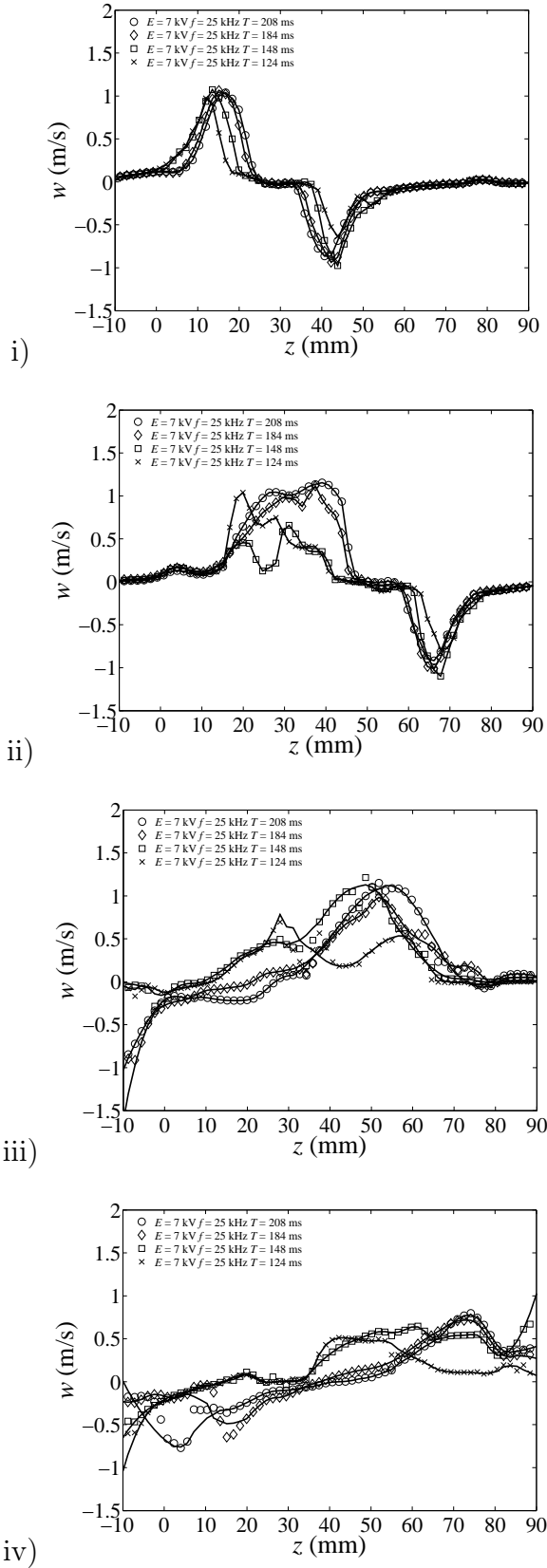
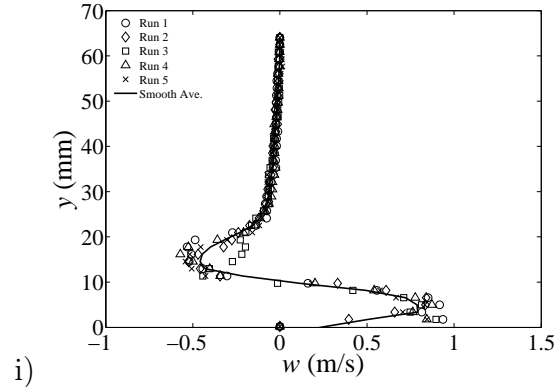
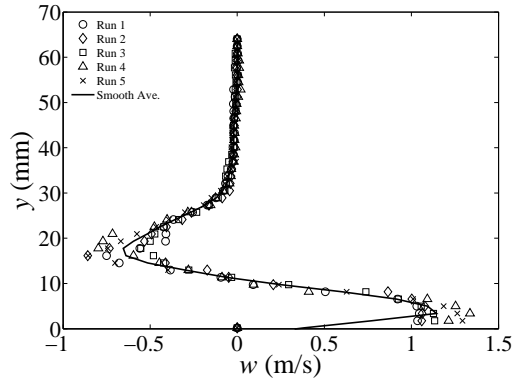


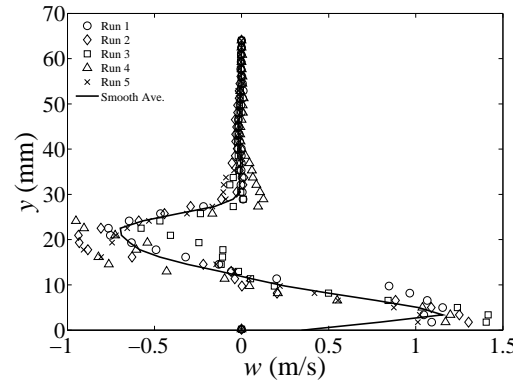
Figure 5.11: Spanwise velocity profiles at  $y = 5$  mm with unidirectional forcing for  $T = 124$  ms to  $T = 208$  ms at i)  $\frac{1}{4}T$ , ii)  $\frac{1}{2}T$ , iii)  $\frac{3}{4}T$  and iv)  $T$ .  $\lambda = 100$  mm,  $E = 7.00$  kV<sub>p-p</sub> at  $f = 25$  kHz.



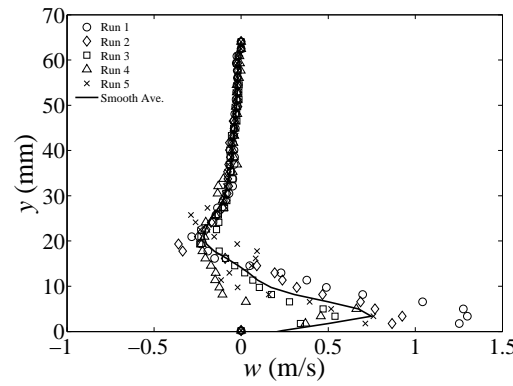
i)



ii)



iii)



iv)

Figure 5.12: Spanwise velocity profiles through the vortex core with bidirectional forcing at i)  $\frac{1}{4}T$ , ii)  $\frac{1}{2}T$ , iii)  $\frac{3}{4}T$  and iv)  $T$ .  $\lambda = 100$  mm,  $E = 7.00$  kV<sub>p-p</sub> at  $f = 25$  kHz.

of the travelling-wave excitation. Figure 5.13a) shows the end of phase (i), where the plasma actuation is 2 ms into phase (ii). The two co- and counter-rotating starting vortices are clearly demonstrated and are collecting fluid in the vicinity of the phase (ii) actuator. Figure 5.13b) is 16 ms into phase (ii) actuation, where two new vortical flow structures can be seen. One of which is located in front of the travelling wave at  $z = 75$  mm and the second at  $z = 35$  mm and are both starting vortices forming due to the phase (ii) DBD plasma initiation. The vortex developing at  $z = 35$  mm is important and is interacting with the previously developed counter-rotating starting vortex of phase (i), causing both the vortical structures to be lifted away from the wall. Figures 5.13c) and d) show further developments at 26 ms and 36 ms into phase (ii) actuation, where the two interacting vortices have been effectively ejected away from the wall at an oblique angle, leaving the phase (ii) actuator entraining fluid from the previous phase and further thrusting the fluid along the wall in the spanwise direction. The two interacting vortices (co- and counter-rotating vortices) eject each other away from the wall due to vortex induction; the vorticity and circulation of each vortex drives the counter-rotating pair away from wall. Figure 5.13e) shows 46 ms into actuation, where now the two ejected vortices have been entrained down towards the wall behind the travelling wave and back into the entrainment region of the phase (ii) actuator. The entrainment towards the wall of the two ejected vortices is due to the downwash that has been caused by the actuation of phase (ii). Also at this time, the counter-rotating vortex from the initiation of phase (ii) has fully developed on the far right of the flow field,  $z = 65$  mm. The fluid transported from phase (ii) is collecting in the region near to the position of the phase (iii) actuator, Figure 5.13f). The fluid is now ready to be entrained by phase (iii) of the travelling wave, and repeat the same process to maintain the travelling-wave excitation. Thus, the spanwise travelling wave is formed by bidirectional forcing through the following mechanism. During phase (i) actuation, fluid is collected from two directions in a region near the second actuation point for phase (ii).

As the actuation for phase (ii) begins, another starting vortex is initiated at the head of the travelling wave. This newly developing starting vortex interacts with the counter-rotating vortex from the previous phase, which causes both vortices to be lifted up and away from the wall at an oblique angle. This now leaves a clear path in the positive  $z$ -direction for the phase (ii) actuator to entrain the previous fluid from phase (i) and add further momentum to the flow, transporting fluid along the wall in the spanwise direction. The interactions of the starting vortices at the beginning of each phase and the necessity to have fluid collected in a region close to the next actuation phase are essential parts to maintaining the travelling-wave excitation when forcing with DBD plasma. If the opposing, counter-rotating vortex that is blocking the travelling-wave motion is not effectively lifted up and away from the wall, then this would stop the movement of the travelling wave in the spanwise direction. Similarly, if the plasma forcing (travelling-wave amplitude) and period of forcing per phase or a combination of both are not large enough to collect fluid in a region which can entrain fluid with the next actuation, the travelling-wave motion is suppressed; this is shown in Figure 5.8 (right column). Here, images of vorticity are presented, one at the end of each of the 4-phases, (i) to (iv), for an applied voltage of  $E = 6.30 \text{ kV}_{\text{p-p}}$  at  $f = 25 \text{ kHz}$  with a period,  $T$ , of 124 ms, with each actuator capable of creating a 0.5 m/s wall jet with these plasma parameters. There is no spanwise travelling wave in this case. Figure 5.8 shows the two starting vortices at the end of phase (i), with little fluid displaced from each actuation. At the end of phase (ii), there has been very little fluid entrained from the previous phase as the fluid displaced through phase (i) has not reached the region of entrainment of phase (ii). This is due to reduced strength and duration of DBD plasma forcing. Opposing, co- and counter-rotating vortices reach but have little energy, causing insufficient vorticity and circulation to lift one another away from the wall, acting as a barrier for spanwise movement along the wall, suppressing travelling-wave motion. Phases (iii) and (iv) continue with a similar outcome of little entrained

fluid and the collisions of co- and counter-rotating vortices that stay close to the wall blocking movement in the spanwise direction. A small change in voltage of  $\Delta E = 0.7 \text{ kV}_{\text{p-p}}$  and a reduced duration of 21 ms each phase yields no travelling-wave excitation.

### 5.3 Chapter Summary

A 4-phase spanwise travelling wave has been successfully implemented with uni and bidirectional forcing using DBD plasma. The development of the travelling waves through each of the 4-phases for both forcing configurations has been studied using time-resolved PIV in quiescent air. It has been observed that on initiation of DBD plasma, starting vortices are created and these vortices are important in the development of the spanwise travelling wave. The mechanisms for transporting fluid in the spanwise direction for both forcing types have been proposed, which have similarity but are inherently different. Successful unidirectional forcing creates a single starting vortex that is transported along the spanwise direction. This is created when each phase moves fluid through a distance of  $\frac{1}{2}s$ , so that actuation entrains the fluid from the previous phase coalescing starting vortices into a single vortex. Phase lag of 30 ms ( $\frac{15}{104}T^+$ ) has been found as the travelling wave initiates. However, this diminishes to zero by the end of the four phases with unidirectional forcing, indicating that the fluid is being accelerated in the spanwise direction, at least in quiescent air. Successful bidirectional forcing creates a complex system of vortices that interact to transport fluid in the spanwise direction. This requires the movement of fluid through a distance  $\frac{1}{2}s$  per phase, which creates co- and counter-rotating vortices. The removal of the counter-rotating vortices from the wall region by the interaction with newly developed co-rotating vortices allows fluid to be transported effectively in the spanwise direction. A phase lag of 30 ms has been observed throughout each phase with this forcing configuration. Both the uni and bidirectional spanwise

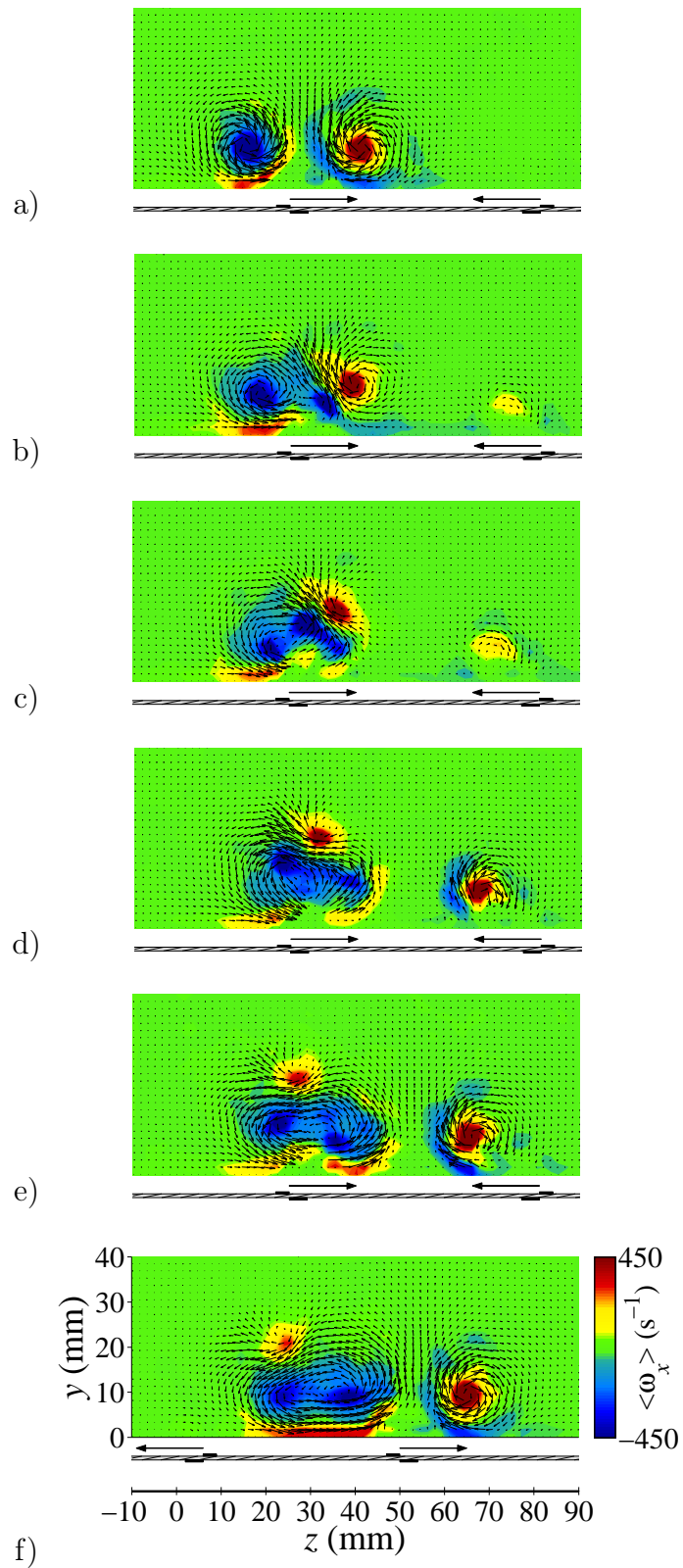


Figure 5.13: PIV vorticity fields of a spanwise travelling wave with bidirectional forcing at a) 2 ms, b) 16 ms, c) 26 ms, d) 36 ms, e) 46 ms and f) 54 ms into phase (ii) actuation.  $\lambda = 100$  mm,  $T = 208$  ms,  $E = 7.00$  kV<sub>p-p</sub> at  $f = 25$  kHz.

travelling wave forcing configurations have shown the ability to move fluid in the spanwise direction over a wavelength of 100 mm ( $\lambda^+ = 500$ ). Hence, both forcing configurations are equally as effective. If the strength of the plasma forcing, duration of actuation, or a combination of both are too low, fluid cannot be transported in the spanwise direction, leading to both mechanisms breaking down. The unidirectional travelling wave was studied by Du *et al.* (2002) and a drag increase was found, although in their study, the parameter space was not extensively studied and therefore it is not known whether unidirectional forcing would always yield a drag increase. The bidirectional travelling wave has been studied extensively both numerically (Du *et al.*, 2002; Zhao *et al.*, 2004; Huang *et al.*, 2011) and experimentally (Xu and Choi, 2006; Itoh *et al.*, 2006), with drag reductions up to 30% being achieved.

# Chapter 6

## Hot-wire Anemometry

### Measurements of Spanwise

### Travelling Waves in the Turbulent

### Boundary Layer

In this chapter, 4-phase spanwise travelling waves with uni and bidirectional forcing are applied to the turbulent boundary layer and studied using hot- and cold-wire anemometry. For all experiments presented the free-stream velocity,  $U_\infty$ , was set to 1.7 m/s producing a boundary-layer thickness,  $\delta$ , of 90 mm at the hot-wire measurement location, 10 mm downstream of the plasma actuators. The Reynolds numbers based on momentum thickness,  $Re_\theta = \frac{U_\infty \theta}{\nu}$  and friction velocity,  $Re_\tau = \frac{u_\tau \delta}{\nu}$  were 1024 and 435 respectively. The data presented has been scaled with friction velocity,  $u_\tau$  and kinematic viscosity,  $\nu$ . Details of obtaining the friction velocity will be presented in this chapter. For the boundary-layer tests presented the spanwise travelling waves were generated with a wavelength,  $\lambda$ , of 100 mm ( $\lambda^+ = \frac{\lambda u_\tau}{\nu} = 500$ ) and with a time period,  $T$ , of 208 ms ( $T^+ = \frac{T u_\tau^2}{\nu} = 82$ ), producing an average wave speed,  $c^+ = \frac{\lambda^+}{T^+} = 6$ . The uni and bidirectional spanwise travelling waves were generated by applying a voltage,  $E$ ,

of  $7 \text{ kV}_{\text{p-p}}$  at a frequency,  $f$ , of 25 kHz to each DBD plasma actuator on the travelling-wave actuator sheet.

## 6.1 Canonical Turbulent Boundary layer

Measurements of the canonical turbulent boundary layer were conducted with the spanwise travelling-wave actuator sheet installed in the wind tunnel. Although for these first sets of measurements the spanwise travelling waves were not operated. A picture showing a Dantec 55P15 boundary-layer type probe being traversed towards the wall can be seen in Figure 6.1a). In this figure the plasma actuator sheet, Figure 3.26, is bonded to the Perspex test plate using double-sided adhesive tape, Figure 3.5, and flush mounted against a Perspex step. The discontinuity between the actuator sheet and step being around  $50 \mu\text{m}$  ( $y^+ = 0.3$ ). The hot-wire measurements were taken 10 mm downstream of the plasma actuators, Figure 6.1b), over the Perspex test plate at four spanwise locations. The hot-wire measurement locations, Z1 to Z4, can be seen in Figure 6.2. The centre of the wind tunnel was located at  $z^+ = 0$ . The first measurement location, Z1, was located at  $z^+ = -65$  with measurements separated by 130 wall units up until Z4 at  $z^+ = 325$ . For each boundary-layer profile, 127 data points were taken at a sampling rate of 1 kHz. The flow was sampled for 90 seconds at each location in the boundary layer.

The viscous sublayer in the turbulent boundary used for this study was very thick ( $y = 1 \text{ mm}$ ), allowing 75 data points to be taken within the first 5 wall units ( $y^+ < 5$ ). This allowed a local measurement of skin friction to be obtained by measuring the near-wall velocity gradient (Andreopoulos *et al.*, 1984). The wall shear stress,  $\tau_w$ , is related to the near-wall velocity gradient by,

$$\tau_w = \mu \frac{\partial \bar{U}}{\partial y} \Big|_{y=0} . \quad (6.1)$$

The wall shear stress can be used to define the friction velocity,  $u_\tau$ , by the ex-

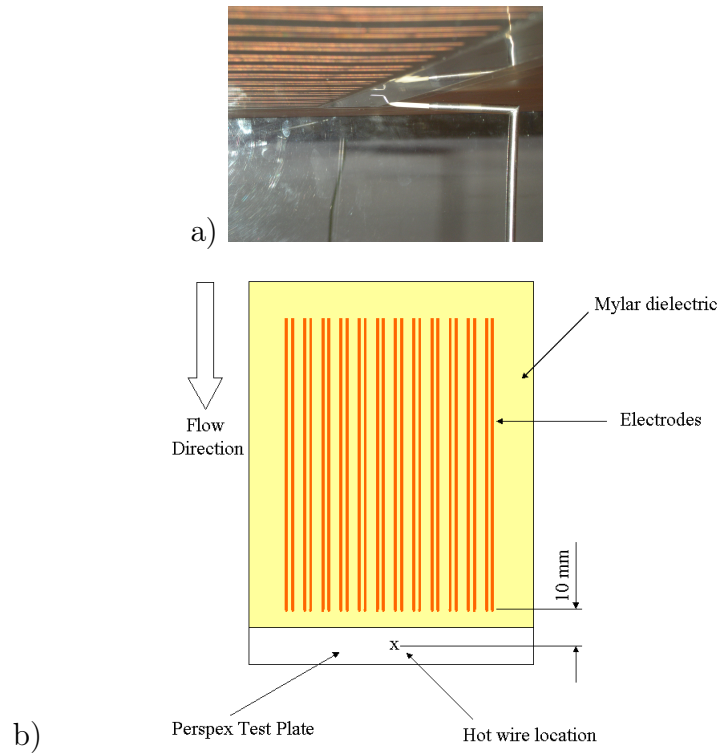


Figure 6.1: A picture showing a) Dantec 55P15 boundary-layer type probe being traversed towards the wall and b) a plan view of the actuator sheet and hot-wire location. Measurements were taken 10 mm downstream of the plasma actuators over a perspex plate (as indicated in b)).

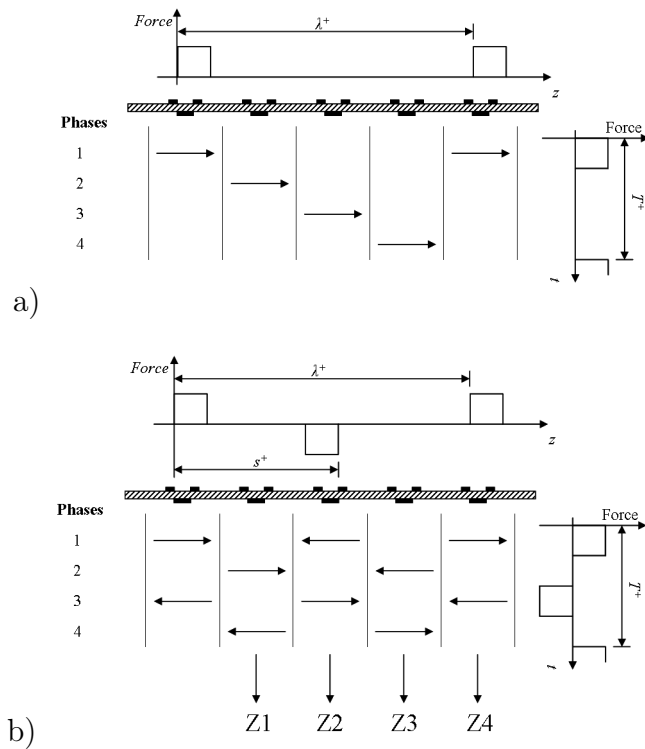


Figure 6.2: Schematic representation of the travelling-wave excitation with a) unidirectional forcing and b) bidirectional forcing taken from Figure 5.1 showing hot-wire measurement locations, Z1 to Z4.

pression,

$$\overline{\tau_w} = \rho u_\tau^2. \quad (6.2)$$

Non-dimensionalising the wall shear stress allows the coefficient of skin friction,  $C_f$ , to be obtained,

$$C_f = \frac{\tau_w}{\frac{1}{2}\rho U_\infty^2} = 2 \left( \frac{u_\tau}{U_\infty} \right)^2. \quad (6.3)$$

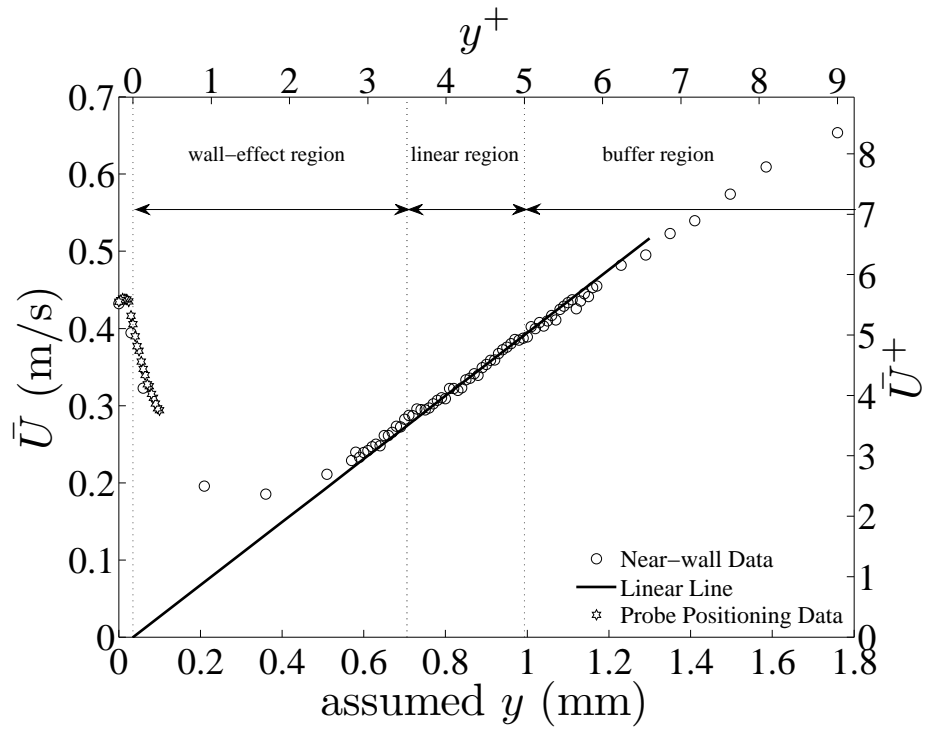
Hence, from Eqns. 6.1 to 6.3, a value of the local skin friction and friction velocity can be obtained from the near-wall velocity gradient of the turbulent boundary layer.

Figure 6.3a) shows an example of velocity data taken within the viscous sub-layer of the turbulent boundary layer. It can be seen that a least squares fit is applied to the data in the linear region  $3.5 < y^+ < 5$  (Hutchins and Choi, 2002), utilising typically 30 of the 75 data points taken within the viscous sublayer. The least squares fit allows the wall shear stress,  $\tau_w$ , to be obtained through Eqn. 6.1 and the friction velocity,  $u_\tau$ , to be obtained through Eqn. 6.2. The value for the friction velocity was 0.0783 m/s and with having a free-stream velocity,  $U_\infty$ , of 1.7 m/s, the coefficient of friction,  $C_f$ , was 0.0042 in this case. It can also be seen in Figure 6.3a) that there is an increase in velocity in the region  $0 < y^+ < 3.5$ . These data are spurious and is called the wall-effect region (Bruun, 1995). It is due to additional heat transfer of the hot-wire probe to the wall of the boundary layer, leading to an increase in measured velocity. It is important to ensure that this region is not used in the linear fitting of the near-wall gradient technique as would lead to inaccurate results. The near-wall gradient technique requires the accurate positioning of the hot wire relative to the wall, to ensure that measurements will be taken in the region of  $y^+ < 5$ . This was addressed by Hutchins and Choi (2002) who developed a technique where the hot wire was traversed towards the wall until one of the hot-wire prongs made contact with the wall, causing a change in the voltage gradient,  $\frac{dE}{dy}$ . This allowed a computer controlled

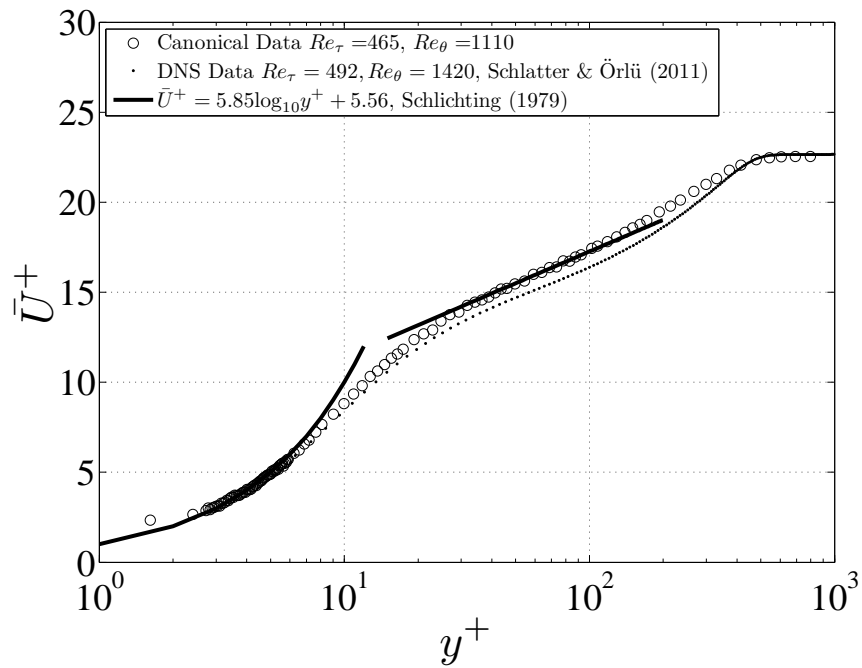
wall positioning approach and is shown in Figure 6.3a) by the probe positioning data for  $y^+ < 0.5$ . It can be seen that close to  $y = 0$  mm, the probe positioning data plateaus indicating that a hot-wire prong has made contact with the wall. From this position the boundary-layer traverse would begin ensuring that data points were taken in the linear region of  $3.5 < y^+ < 5$ . The probe positioning data also served as a guide for fitting the near-wall gradient as the approximate location of the wall was known. The least squares fit in the linear region was extrapolated back to  $\bar{U} = 0$  m/s allowing the true  $y = 0$  mm to be obtained.

The turbulent boundary-layer profile is shown in Figure 6.3b), where the mean streamwise velocity is plotted against wall-normal distance. In this figure, the friction velocity was obtained by the Clauser plot method where the log region was matched to that of Schlichting (1979). The friction velocity and skin-friction coefficient were 0.0795 m/s and 0.0044, which were greater by 1.5% and 5% respectively of the values obtained using the near-wall gradient technique. The Reynolds numbers,  $Re_\tau$  and  $Re_\theta$ , were 465 and 1110 in this case. DNS data of the turbulent boundary layer taken from Schlatter and Örlü (2011) at similar Reynolds numbers ( $Re_\tau = 492$  and  $Re_\theta = 1420$ ) is plotted along with the experimental data for comparison, where profiles appear qualitatively similar. The differences between the profiles is due to the higher Reynolds numbers in the DNS data.

Data taken across four spanwise locations, Z1 to Z4, can be seen in Figure 6.4. The data collapses, as expected, in the canonical boundary layer. In total, 16 turbulent boundary-layer profiles were taken, four at each of the four spanwise locations. The four data sets taken at the four spanwise locations were averaged and the data plotted through Figures 6.5 and 6.6, showing the mean streamwise velocity, turbulence intensity, skewness and kurtosis profiles against wall-normal distance. The experimental data shows similar profiles to the DNS data taken from Schlatter and Örlü (2011), although differences between the hot-wire anemometry and DNS data could be due to an over-stimulation of the



a)



b)

Figure 6.3: Hot-wire anemometry used to obtain a) mean near-wall streamwise velocity and b) mean streamwise velocity profile of the canonical turbulent boundary layer.

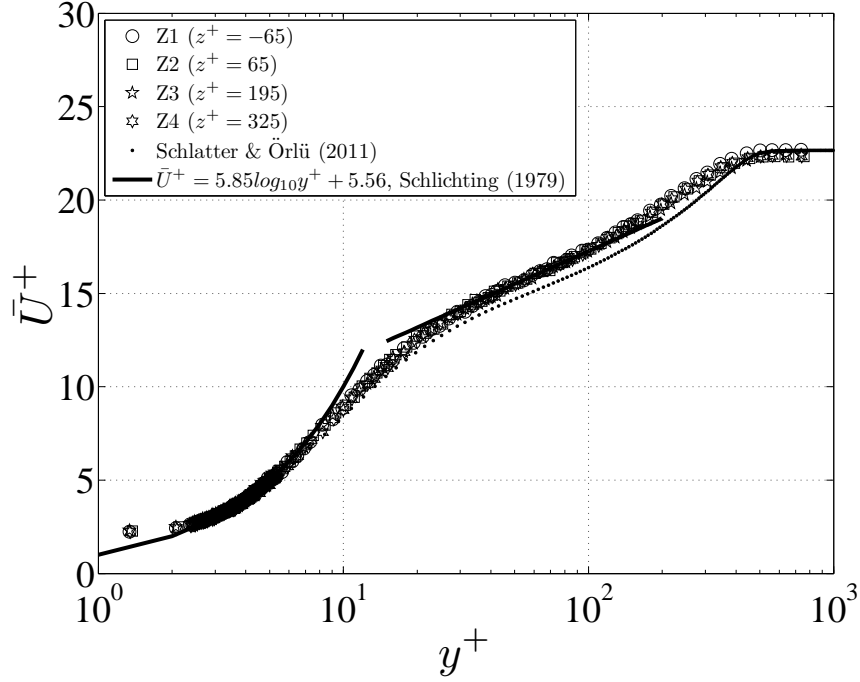


Figure 6.4: Mean streamwise velocity profile at four spanwise locations, Z1 to Z4.

boundary layer caused by the turbulent trip (Erm and Joubert, 1991). The differences in the hot-wire and DNS data can be seen in the mean and turbulence intensity plots clearly, Figure 6.5. There is little difference in higher moments, skewness and kurtosis, as these are normalised quantities, Figure 6.6. The possibility of having an over-stimulated boundary layer due to the tripping device has been discussed in detail in §3.7.3. Throughout the 16 turbulent boundary-layer profiles it was found that the free-stream velocity,  $U_\infty$ , was  $1.70 \pm 0.02$  m/s and the boundary-layer thickness,  $\delta$ , was  $90 \pm 3$  mm. (All uncertainties given are  $\pm 1$  standard deviation). The displacement thickness,  $\delta^*$ , is defined as,

$$\delta^* = \int_0^\delta \left(1 - \frac{\bar{U}}{U_\infty}\right) dy, \quad (6.4)$$

and was  $12.8 \pm 0.5$  mm. The momentum thickness,  $\theta$ , is defined as,

$$\theta = \int_0^\delta \frac{\bar{U}}{U_\infty} \left(1 - \frac{\bar{U}}{U_\infty}\right) dy, \quad (6.5)$$

and was  $9.2 \pm 0.3$  mm and the shape factor,  $H = \frac{\delta^*}{\theta}$ , was  $1.40 \pm 0.01$ . For all the 16 turbulent boundary-layer profiles, the near-wall gradient technique was used to establish the friction velocity. It was found that the friction velocity,  $u_\tau$ , was  $0.0752 \pm 0.0016$  m/s and the coefficient of skin friction,  $C_f$ , was  $0.00400 \pm 0.00011$ . The Reynolds numbers based on friction velocity,  $Re_\tau$ , and momentum thickness,  $Re_\theta$ , were  $435 \pm 17$  and  $1024 \pm 43$  respectively. The uncertainties reported here have been obtained by determining the repeatability of the computed quantities through the streamwise velocity measurements over 16 boundary-layer profiles. The friction velocity and skin-friction coefficient were obtained using the Clauser plot method for the averaged profile and were 0.0747 m/s and 0.0040 respectively, which were within the uncertainty of the values obtained using the near-wall gradient technique.

## 6.2 Turbulent Boundary-Layer Measurements with Spanwise Travelling Waves

In this section, hot- and cold-wire anemometry of the turbulent boundary layer with spanwise travelling waves will be presented. Measurements of the thermal boundary layer have been conducted using a Dantec 55P31, 1  $\mu\text{m}$  diameter cold-wire probe and measurements of the streamwise velocity component have been conducted using a Dantec 55P15, 5  $\mu\text{m}$  diameter hot-wire probe. All measurements have been taken 10 mm downstream of the plasma actuators, with hot-wire measurements taken at four spanwise locations, Z1 to Z4, Figure 6.2, and cold-wire measurements taken at the Z2 location. The turbulent boundary layer was sampled at 1 kHz with duration of 90 seconds without plasma and 60 seconds with plasma at each measurement location for both the hot- and cold-wire anemometry measurements. The plasma is actuated in 3 second bursts with a 3 second gap and a 60 second pause at the end of each acquisition to minimise thermal damage to the electrode sheet, caused by dielectric heating. For

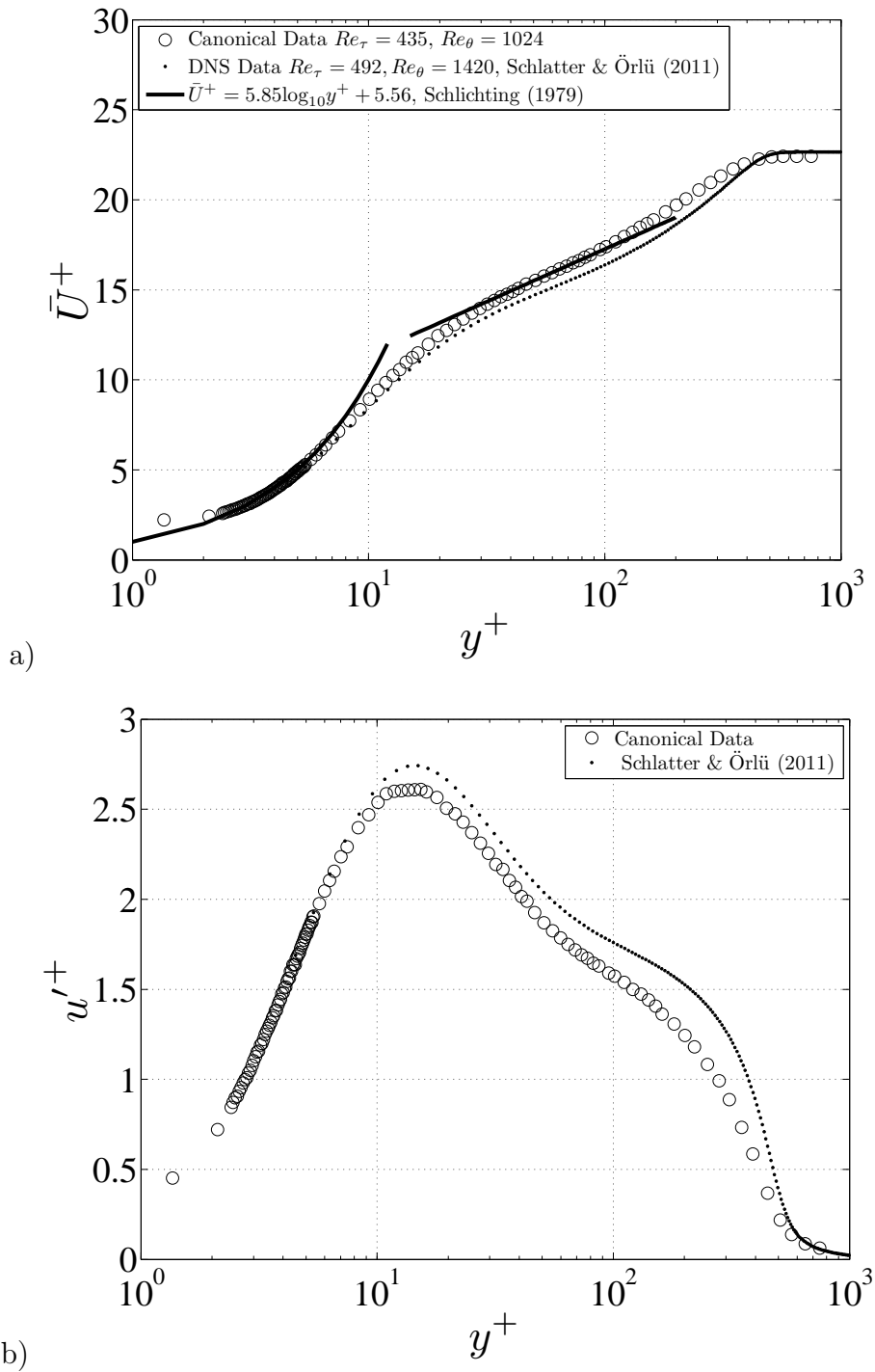


Figure 6.5: Averaged a) mean streamwise velocity profile and b) streamwise turbulence intensity profile of the canonical turbulent boundary layer.

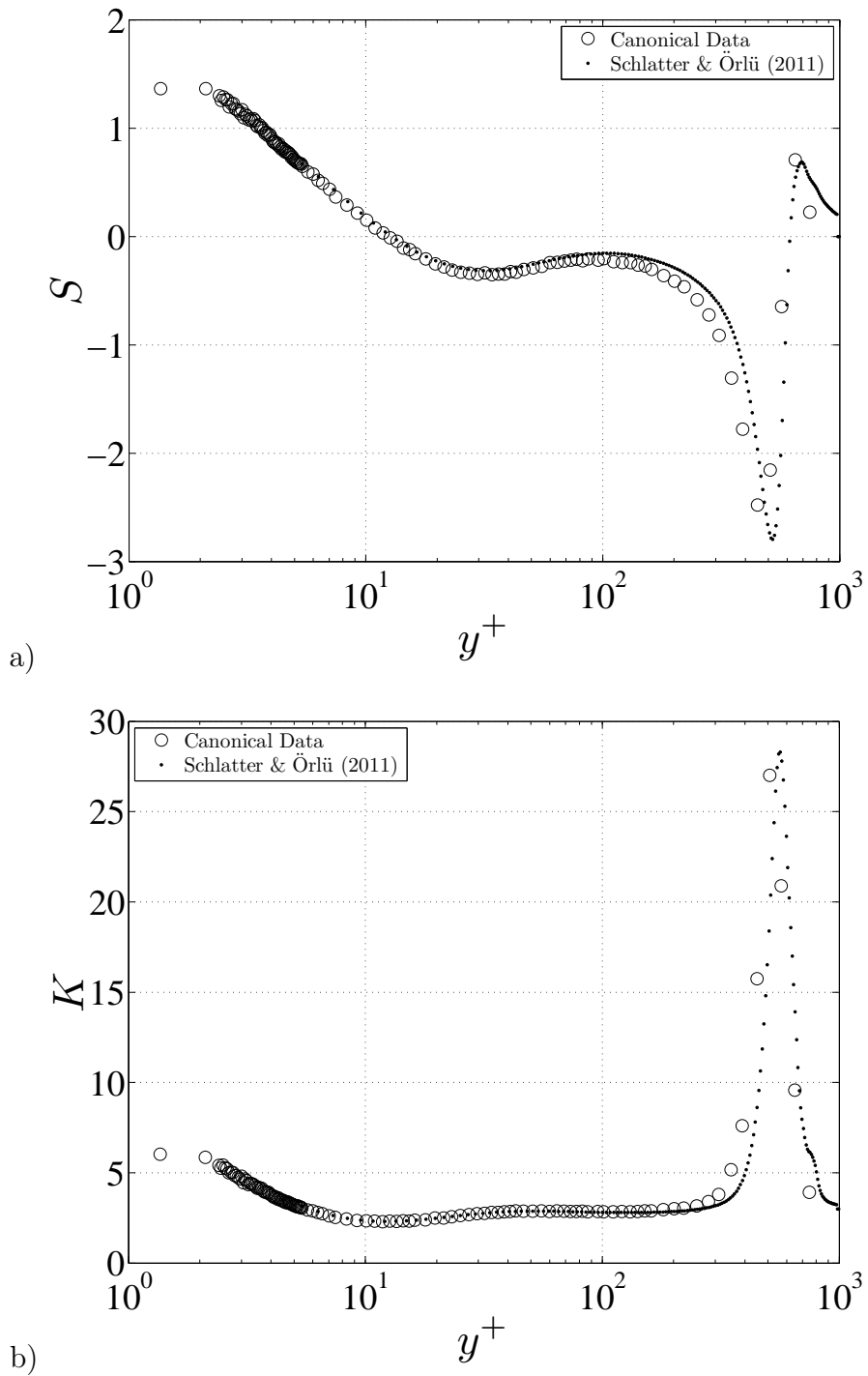


Figure 6.6: Averaged a) skewness and b) kurtosis profiles of streamwise velocity in the canonical turbulent boundary layer.

each boundary-layer profile, 127 data points were taken, where 75 of these were located within the viscous sublayer ( $y^+ < 5$ ). Each boundary-layer profile measurement took 9.5 hours to complete. During each 3 second burst ( $t^+ = 1177$ ), 14 spanwise travelling-wave periods ( $T^+ = 82$ ) were generated. Each 3 second burst is generated by an 8-channel BNC pulse generator, Figure 5.2, which is sampled simultaneously with the hot-wire signals. Hence, the time of plasma forcing (travelling wave) with respect to the hot-wire signals was known. Measurements have been taken 10 mm downstream of the plasma actuators where there will be a natural time delay due to convection. In the near-wall region of the turbulent boundary layer ( $y^+ < 15$ ), the convection velocity of near-wall turbulence is typically  $13u_\tau$  (Johansson *et al.*, 1987). As measurements were taken 10 mm downstream of the plasma actuators this would amount to a time delay on the order of 10 ms. For greater wall-normal distances, ( $y^+ > 15$ ) the convection velocity is equal to the local mean velocity (Kim and Hussain, 1993), giving time delays on the order of 5 ms. The data was sampled at 1 kHz and on observation of the first few data points there was no clear sign that there was noticeable time delay on the velocity signals. Therefore, for all hot-wire analysis, the entire 3 seconds of the 3 second plasma bursts have been used.

### 6.2.1 Thermal Boundary-Layer Measurements

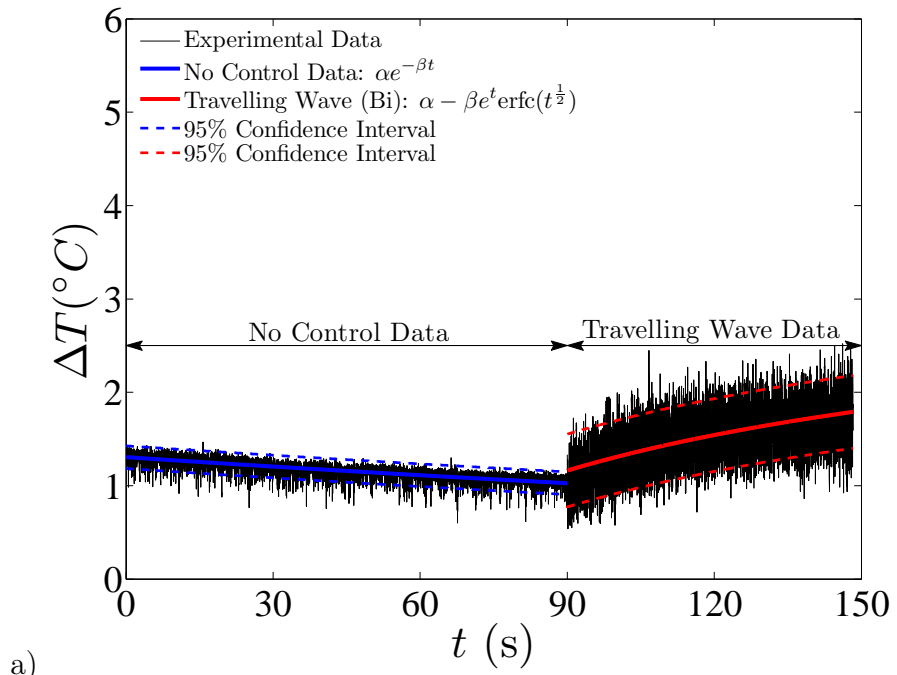
It is known that on application of DBD plasma, a thermal boundary layer is created. This was found by Jukes (2007), who used the same test facility for implementing a spanwise oscillation with DBD plasma and achieved a 45% reduction in turbulent skin friction. In this section, cold-wire anemometry data are presented, showing the thermal boundary layer that is created by the DBD plasma during uni and bidirectional travelling-wave excitation. Figure 6.7a) and b) show temperature time-series at  $y^+ = 5$  with uni and bidirectional forcing respectively. Here,  $\Delta T$  is the change in fluid temperature from the ambient surroundings. A total of 150 seconds is sampled, with 90 seconds of no-control data

and 60 seconds of travelling-wave data (control data). The travelling waves are actuated in 20 bursts of 3 seconds, with a 3 second gap to achieve 60 seconds of plasma data. For the travelling-wave data in Figure 6.7, the 3 second bursts are agglomerated and plotted as a single time-series.

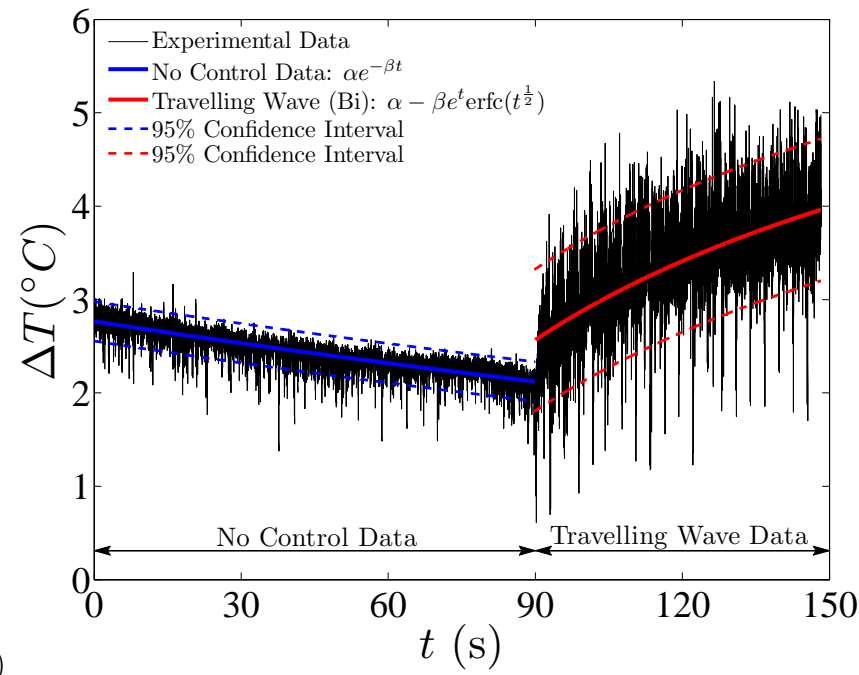
It can be seen for both the uni and bidirectional time-series taken at  $y^+ = 5$  in Figure 6.7, that a temperature change is apparent in both the no-control and travelling-wave data. The no-control data have a change in temperature of approximately  $1^\circ\text{C}$  (unidirectional travelling wave) and  $2.5^\circ\text{C}$  (bidirectional travelling wave). This is due to the residual heat of the dielectric sheet which remains after a 60 second pause between measurement locations. The travelling-wave data have a change in temperature of approximately  $1.5^\circ\text{C}$  and  $3.5^\circ\text{C}$  for the uni and bidirectional travelling waves respectively. There is a larger temperature change for bidirectional forcing than unidirectional forcing throughout the time-series. This is due to unidirectional forcing actuating one plasma actuator per phase and bidirectional forcing actuating two plasma actuators per phase. Hence, application of more plasma leads to larger changes in temperature being generated, as should be expected. It is apparent from these time-series that the thermal effects lead to a non-stationary mean in the temperature measurements. The temperature changes in the no-control data appears to be decaying exponentially, although linear and quadratic functions fit the data equally well, Figures 6.8 and 6.9. The travelling-wave data shows an increase in temperature change as the plasma (travelling wave) is actuated over the 60 seconds. An error function fit, Figure 6.7, has been applied to both data sets and fits the time-series well. Quadratic and cubic function fits to the travelling-wave data can represent the data equally well, Figures 6.8 and 6.9. It is worth mentioning that Jukes *et al.* (2008) performed thermal imagery of a DBD plasma actuator with a  $250\ \mu\text{m}$  thick Mylar dielectric in quiescent air. It was found that the dielectric surface was  $108^\circ\text{C}$  for DBD plasma generated with a square pulse waveform with an applied voltage,  $E$ , of  $7.4\ \text{kV}_{\text{p-p}}$  at a frequency,  $f$ , of  $25\ \text{kHz}$  with 100% duty

cycle. The maximum change in surface temperature after 1 second was approximately  $3.5^{\circ}\text{C}$ . The time evolution of the maximum surface temperature followed an error function fit which was based on 1D unsteady analysis of a semi-infinite solid (Kreith and Bohn, 1993). The plasma parameters used in the Jukes *et al.* (2008) study were similar to the plasma parameters used in the travelling-wave study; a  $250\ \mu\text{m}$  thick Mylar dielectric with similar magnitudes in applied voltage and frequency. Hence, a similar amount of temperature change should be expected.

In Figure 6.10a) and b), the RMS (root-mean-square) temperature profiles throughout the turbulent boundary layer with uni and bidirectional travelling waves are presented respectively. In this figure, the RMS temperature values have been obtained by subtracting the temperature data from the mean of the data set (standard approach for a stationary mean) and also by subtracting the temperature data from the function fits applied to the temperature time-series, which takes into consideration the time-varying mean of the non-stationary data. Figure 6.10 shows that by computing the RMS temperature profiles applying linear, quadratic or exponential functions to the canonical temperature time-series does not change the RMS temperature values. This indicates that any of these functions fit the data equally well. The same holds true for the travelling-wave data, where RMS temperature profiles computed from quadratic, cubic or error function fits to the temperature time-series show little difference throughout the turbulent boundary; this indicates that each fit being equally valid. By taking a mean of the data and calculating the RMS temperature values, (assuming the data have a stationary mean), it can be seen, as expected, that the RMS temperature values are increased when compared to the RMS temperature values calculated from the function fits. For the no-control data, the RMS values calculated by subtracting the mean of the data set are increased until  $y^+ = 10$  (unidirectional travelling wave) and  $y^+ = 15$  (bidirectional travelling wave). Increased RMS temperature values can be seen in the travelling-wave data sets up

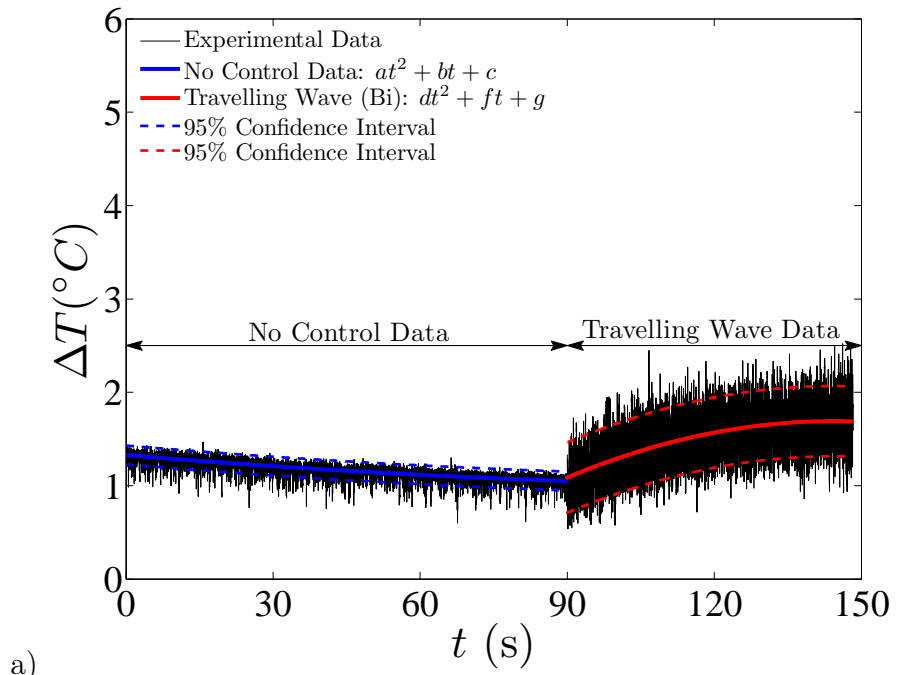


a)

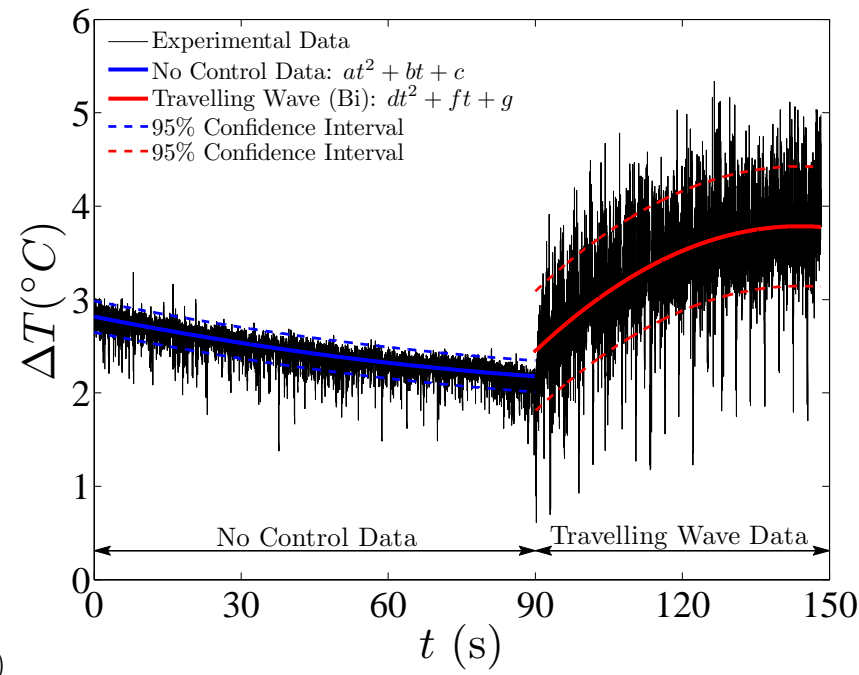


b)

Figure 6.7: Temperature time-series at  $y^+ = 5$  for a) unidirectional forcing and b) bidirectional forcing using exponential fits on no-control data and error function fits on the travelling-wave data.

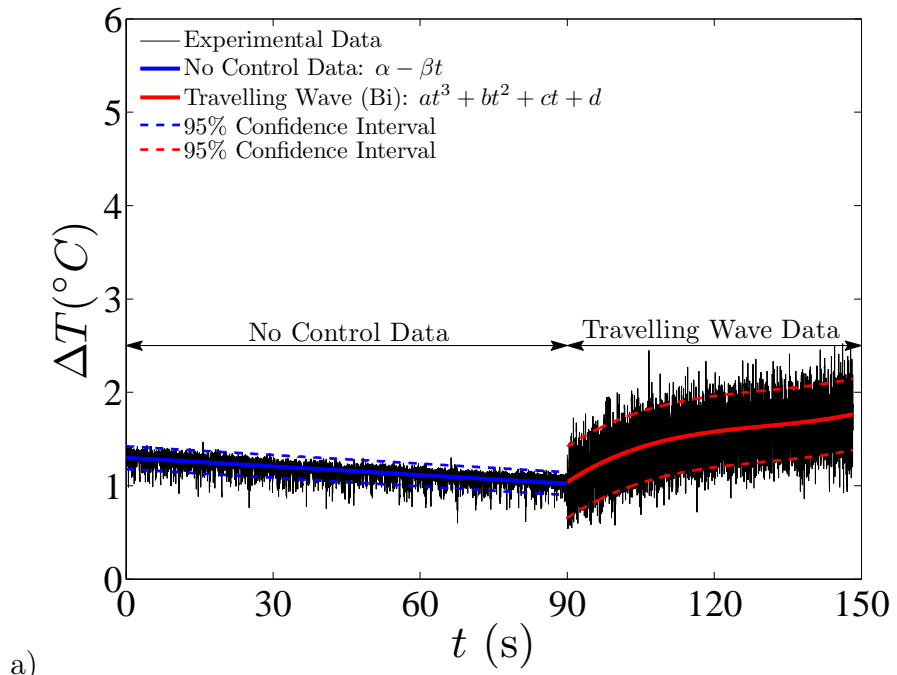


a)

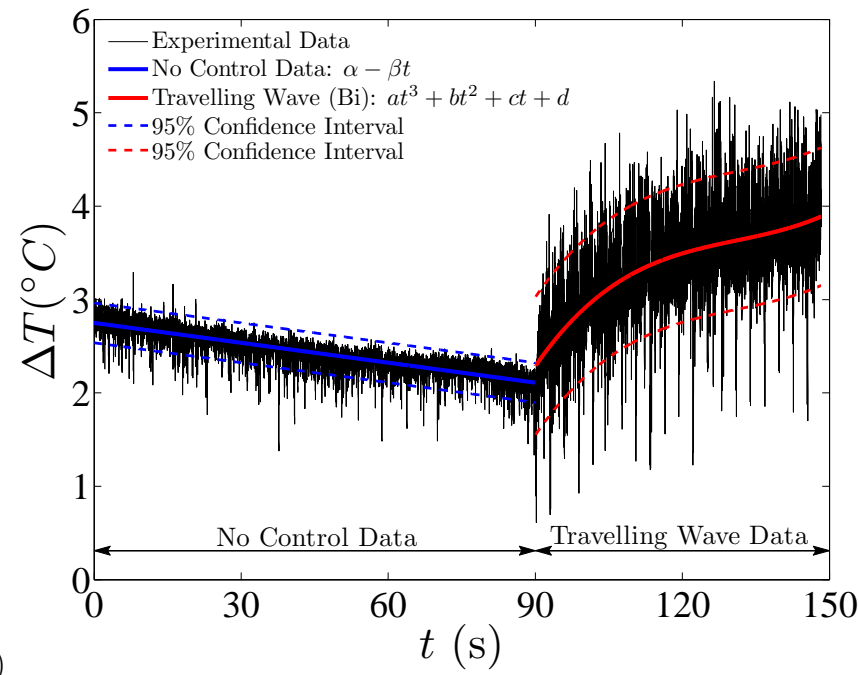


b)

Figure 6.8: Temperature time-series at  $y^+ = 5$  for a) unidirectional forcing and b) bidirectional forcing using quadratic fits on the no-control and travelling-wave data.



a)

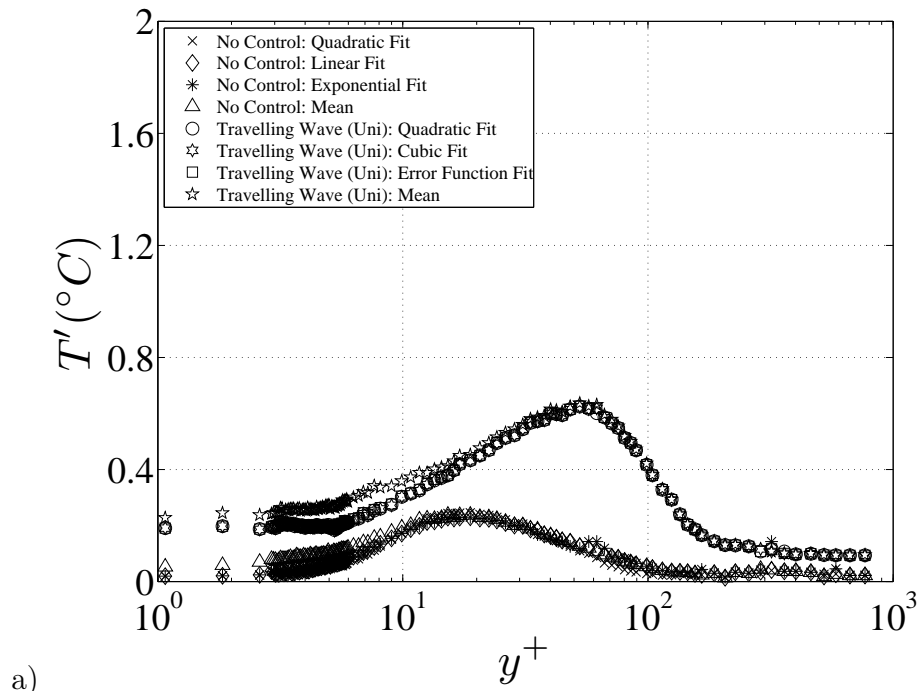


b)

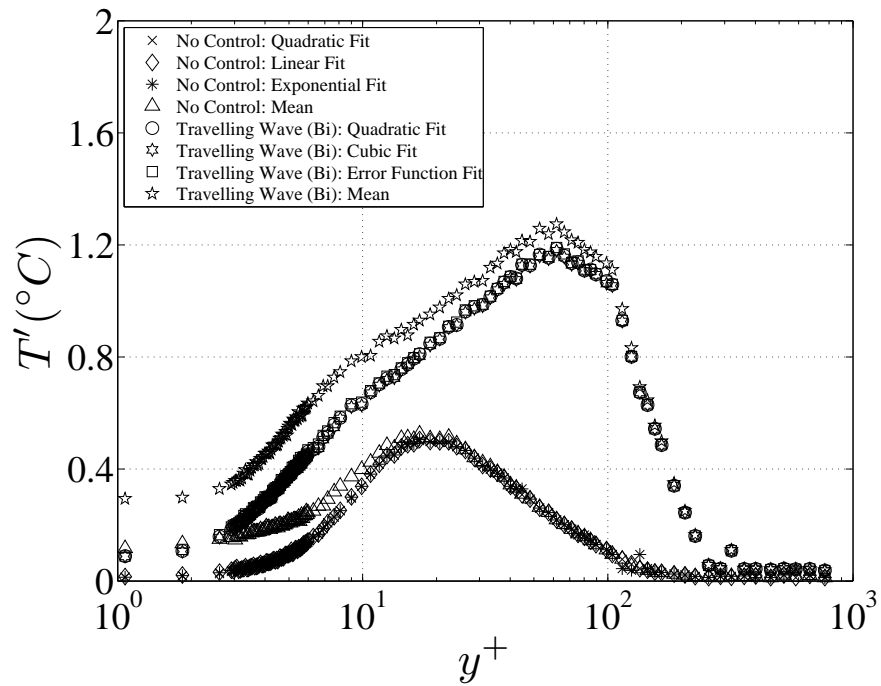
Figure 6.9: Temperature time-series at  $y^+ = 5$  for a) unidirectional forcing and b) bidirectional forcing using linear fits on no-control data and cubic function fits on the travelling-wave data.

until  $y^+ = 30$  with unidirectional forcing and  $y^+ = 100$  with bidirectional forcing. These locations where the RMS temperature profiles generated by subtracting the mean of the data sets and by fitting functions to the data sets join, indicates that there is no temperature effect above these locations. Maximum RMS values for the no-control data are located at  $y^+ = 15$  and have values of  $0.2^\circ\text{C}$  (unidirectional travelling wave) and  $0.6^\circ\text{C}$  (bidirectional travelling wave). This coincides with the location of maximum turbulence intensity in the velocity measurements of the turbulent boundary layer. The maximum values of RMS temperature for the uni and bidirectional travelling waves are located at  $y^+ = 50$  and have values of  $0.6^\circ\text{C}$  and  $1.2^\circ\text{C}$  respectively. In the quiescent air measurements of the spanwise travelling waves, Chapter 5, it was found that the starting vortices generated on initiation of DBD plasma had cores located 10 mm from the wall. In the turbulent boundary layer this would amount to a wall-normal distance of  $y^+ = 50$ . It will be shown in Chapter 7 that when the spanwise travelling waves are studied in the turbulent boundary with PIV, the starting vortices still exist in the flow and have core locations at  $y^+ = 50$ . Hence, it would appear that maximum temperature fluctuation in the travelling-wave data are due to the entrainment of fluid into the vortex cores. Furthermore, large fluctuations in temperature can be seen in Figures 6.7 and 6.10. These temperature fluctuations are thought to be caused by the streamwise vortices generated during the spanwise travelling-wave excitation; the streamwise vortices entrain high-temperature fluid away from the wall and into their cores as they are being transported in the spanwise direction, causing fluctuations in fluid temperature as they pass the stationary cold-wire probe.

To show the effect of thermal boundary, the temperature difference for both the uni and bidirectional travelling waves are shown in Figure 6.11a) and b). The change in temperature has been calculated by taking a mean of the data at each location and subtracting it from the free-stream ambient temperature,  $T_\infty$ . It can be seen that bidirectional forcing generates higher temperatures throughout



a)



b)

Figure 6.10: RMS temperature profiles throughout the turbulent boundary layer for a) unidirectional forcing and b) bidirectional forcing. Both plots contain no-control data as indicated.

the turbulent boundary layer, due to double the amount of plasma being generated by the bidirectional travelling wave. Both travelling waves see a maximum temperature at  $y^+ = 8$ . The no-control data have a maximum temperature difference of  $1.1 \pm 0.1^\circ\text{C}$  (unidirectional travelling wave) and  $2.5 \pm 0.2^\circ\text{C}$  (bidirectional travelling wave). When the travelling waves are applied, larger values of maximum temperature difference can be seen. The uni and bidirectional travelling waves have maximum temperature changes of  $1.9 \pm 0.35^\circ\text{C}$  and  $3.75 \pm 0.8^\circ\text{C}$  respectively. The thermal boundary-layer thickness,  $\Delta$ , is obtained by computing the wall-normal distance when the temperature profile is 1% larger than the ambient free-stream temperature,  $T_\infty$ . The thermal boundary-layer thickness with uni and bidirectional forcing,  $\Delta_p$ , was 35 mm ( $\Delta_p = 0.4\delta, y^+ = 180$ ) and the thermal boundary-layer thickness of the no-control data,  $\Delta_c$ , was 12 mm ( $\Delta_c = 0.13\delta, y^+ = 60$ ).

The core locations of the streamwise vortices (generated due to plasma) inside the turbulent boundary layer during spanwise travelling-wave excitation will be shown to be located at  $y^+ = 50$  with stereoscopic PIV measurements in the  $z$ - $y$  plane of the turbulent boundary layer in Chapter 7. (For a pertinent example, see Figure 7.14 in Chapter 7). It is interesting to note that the location of maximum temperature fluctuation, Figure 6.10, for the travelling-wave data was  $y^+ = 50$ , which coincides with the location of the cores of the streamwise vortices. The profiles of mean temperature difference for the travelling-wave data, Figure 6.11, appear qualitatively similar to the streamwise turbulence intensity profiles, Figure 6.22b) that will be discussed in §6.2.2. Both of the temperature and streamwise velocity turbulence intensity profiles have similar profile shapes with peaks located at  $y^+ = 8$  and  $y^+ = 50$ . This shows that the maximum streamwise turbulence intensity is located at around  $y^+ = 8$ , which is the region of maximum temperature in the turbulent boundary layer with spanwise travelling-wave control by DBD plasma. Hence, the streamwise vortices generated on initiation of DBD plasma are entraining fluid which can be up to  $4^\circ\text{C}$

larger than ambient temperature, in and around the streamwise vortices, leading to maximum temperature fluctuations at the streamwise vortex cores.

The maximum temperature in the turbulent boundary layer would be expected to be located in the plasma formation region (2-3 mm around the upper electrodes of the DBD plasma actuator). The cold-wire measurements, however, have been taken 10 mm downstream of the plasma actuators over a Perspex test plate that is at ambient temperature. The non-dimensional thermal boundary-layer profiles with uni and bidirectional travelling waves (control and no-control) are shown in Figure 6.12a) and b) respectively. The data have been fitted to the  $(\frac{1}{7})^{\text{th}}$  law, Eqn. 6.6, by adjusting the value of the temperature at the wall,  $T_0$ . Here, the assumption is that the wall temperature stays constant (isothermal). Therefore, the wall temperature could be interpreted as the mean surface temperature of the dielectric sheet.

$$\left( \frac{T_0 - T}{T_0 - T_\infty} \right) = \left( \frac{y}{\Delta} \right)^{\frac{1}{7}}. \quad (6.6)$$

It can be seen that the no-control data collapses reasonably well to the  $(\frac{1}{7})^{\text{th}}$  law for  $\frac{y}{\Delta} > 0.1$  ( $y^+ = 8$ ). This location where the no-control data collapses to the  $(\frac{1}{7})^{\text{th}}$  law is after the location of maximum temperature, Figure 6.11, where the temperature profiles begin to diminish to ambient temperature. The wall temperature for the no-control profiles corresponds to  $T_0 = 4^\circ\text{C}$  for the unidirectional travelling wave and  $T_0 = 9^\circ\text{C}$  for the bidirectional travelling wave. There is however, limited travelling-wave data that can be fitted to the  $(\frac{1}{7})^{\text{th}}$  law as seen in Figure 6.12. Hence, extrapolating the wall temperature from a fit with few data points could contain large error and is not considered here for this reason. It is noted, however, that due to the plasma excitation parameters used in this study ( $E = 7 \text{ kV}_{\text{p-p}}$ ,  $f = 25 \text{ kHz}$ ) being similar to those used in the thermal measurements of Jukes *et al.* (2008) ( $E = 7 \text{ kV}_{\text{p-p}}$ ,  $f = 25 \text{ kHz}$ ), it is expected that the surface temperature of the dielectric sheet would be of the same order,  $T_0 \sim 100^\circ\text{C}$ .

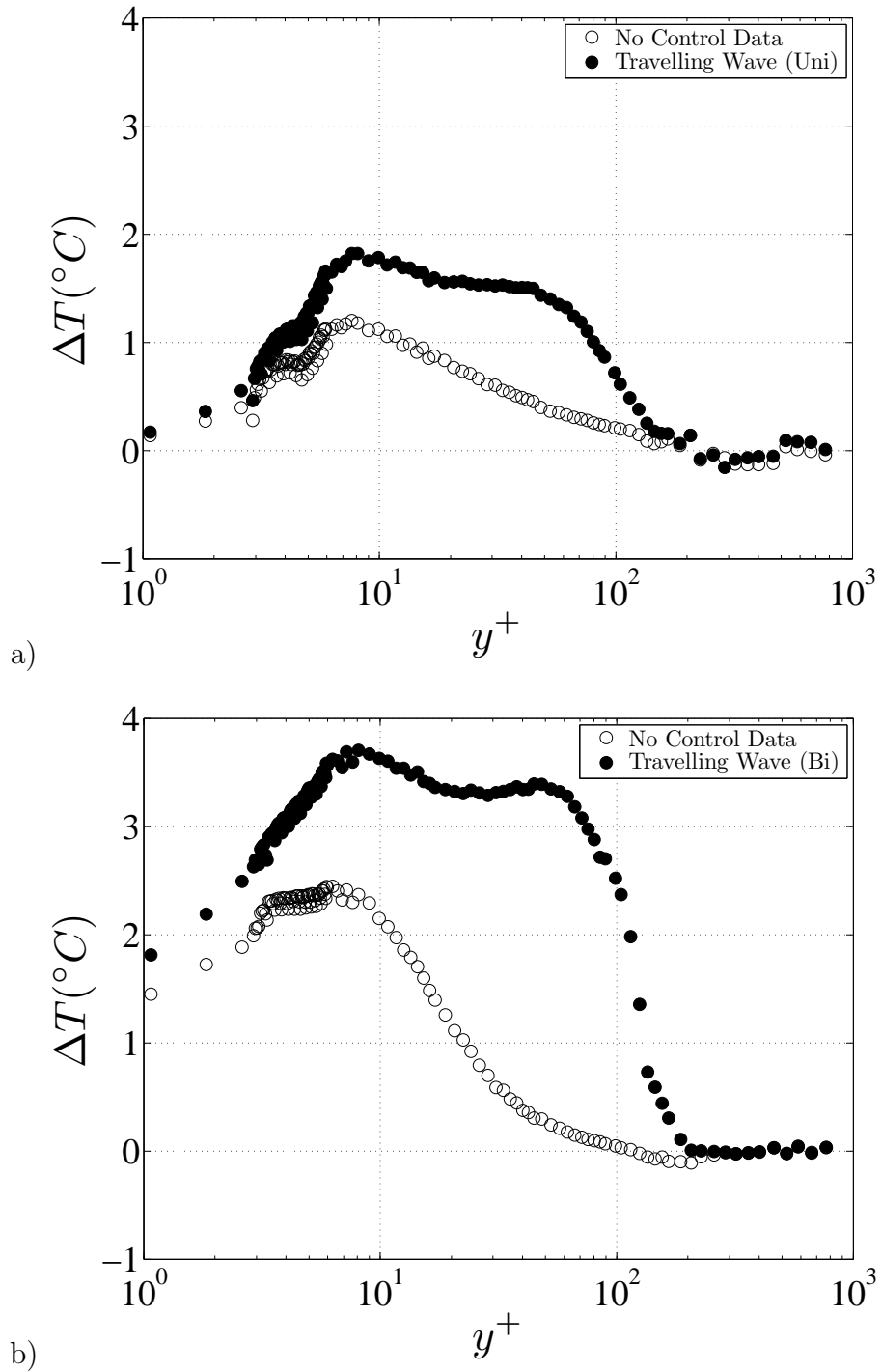


Figure 6.11: Mean temperature difference measurements throughout the turbulent boundary layer for a) unidirectional forcing and b) bidirectional forcing.

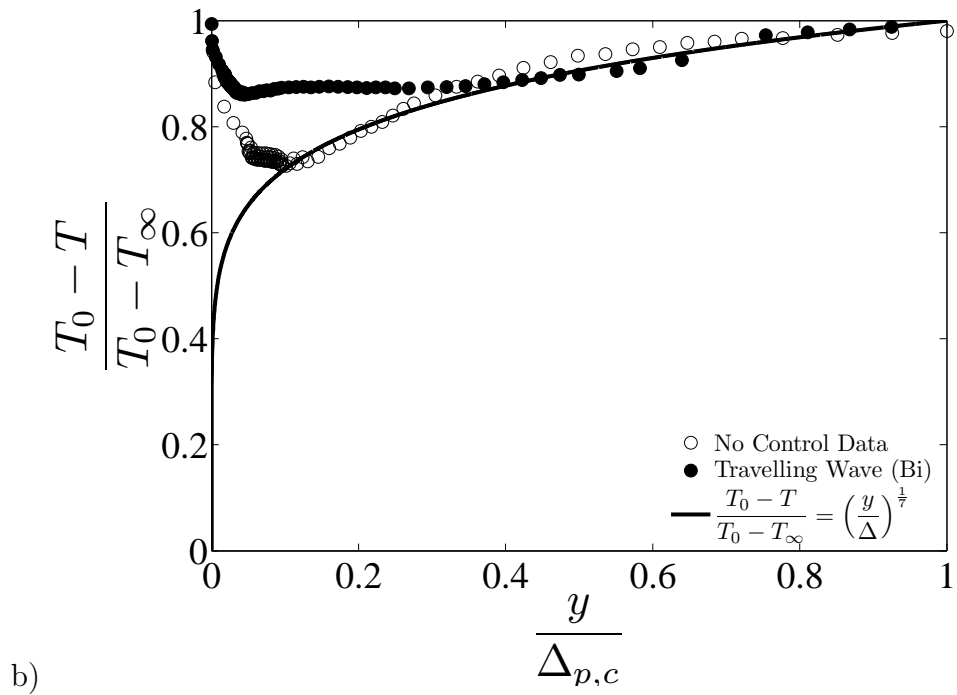
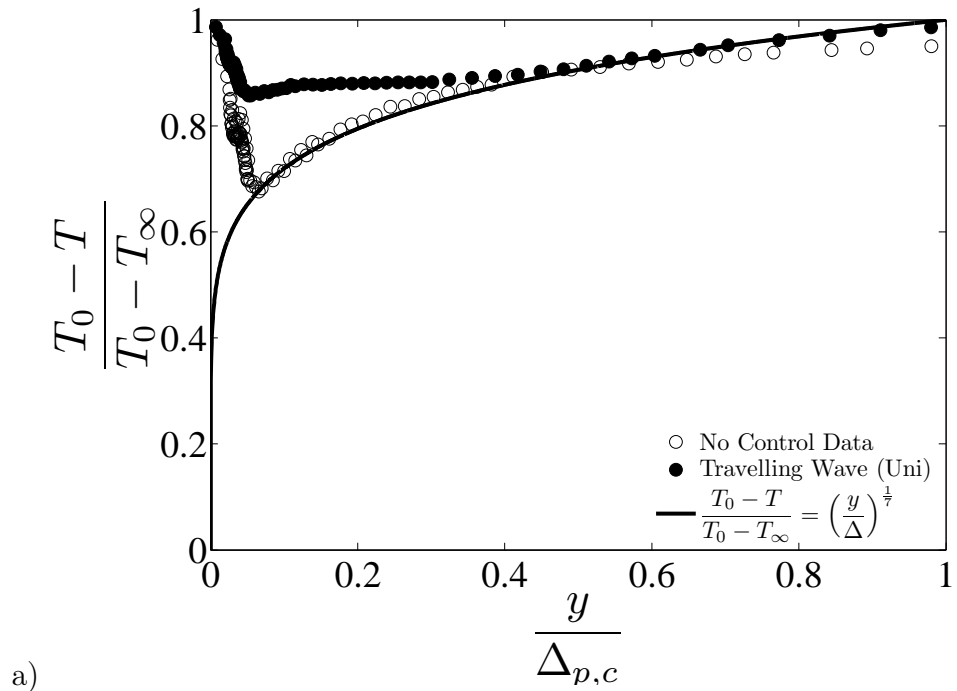


Figure 6.12: Non-dimensional thermal boundary-layer profiles with wall temperature,  $T_0$ , adjusted to fit the  $(\frac{1}{7})^{\text{th}}$  law, a) unidirectional forcing and b) bidirectional forcing.

## 6.2.2 Velocity Measurements

In this section, hot-wire anemometry data are presented showing the changes in the streamwise velocity component throughout the turbulent boundary layer with spanwise travelling-wave excitation. The use of the cold-wire data to compensate the hot-wire data for the thermal boundary layer will be presented and discussed. The turbulent boundary layer was sampled at 1 kHz with duration of 90 seconds without plasma and 60 seconds with plasma at each measurement location. The plasma is actuated in 3 second bursts with a 3 second gap and a 60 second pause at the end of each acquisition to minimise thermal damage to the electrode sheet. For each boundary-layer profile 127 data points were taken, where 75 of these were located within the viscous sublayer ( $y^+ < 5, y < 1$  mm). Each boundary-layer profile took 9.5 hours to complete. As well as temperature correction, the hot-wire data have been corrected for drifts in free-stream velocity. A Dantec 55P51 boundary-layer probe was positioned in the free stream of the turbulent boundary layer. At each measurement location that was sampled by the hot-wire probe that was traversing the boundary layer, the free-stream velocity probe was sampled simultaneously. The mean value of the free-stream velocity from the free-stream probe was then obtained throughout the entire experiment (across all 127 data points),  $\bar{U}_{\infty,FP}$ , along with the value of the free-stream velocity as the traversing probe was traversed through the boundary layer,  $\bar{U}_{\infty,FP}(y)$ . The traversing probe was then compensated for mean drifts in velocity by a multiplication of the ratio,  $\frac{\bar{U}_{\infty,FP}}{\bar{U}_{\infty,FP}(y)}$  at each wall-normal location in the boundary layer.

### 6.2.2.1 Temperature Correction and Considerations

Drifts in ambient temperature and free-stream velocity were corrected using a Dantec 55P15 boundary-layer probe positioned in the free stream and an LM35 temperature sensor respectively. Typically the ambient temperature drift was within 0.5°C and the drift in free-stream velocity was typically 0.05 m/s. The

temperature drifts due to the mean thermal boundary layer were added to the ambient temperature measurement,  $T(y) = T_\infty + \Delta T(y)$ , where the values of  $\Delta T(y)$  were taken from Figure 6.11. Calibrations of the hot-wire probes (Figure 3.11 of Chapter 3) were then interpolated to calculate the velocity signal at each location in the boundary layer. An example of interpolated data between calibration curves is shown in Figure 6.13. In this figure, a temperature of 24°C has been linearly interpolated between calibration curves (2 calibration curves have been shown for clarity). A hot wire is inherently a non-linear device (Bruun, 1995) and care should be taken when using linear interpolation across calibration curves. For the boundary-layer experiments presented here, ten calibration curves were taken in total, each separated by 1°C. If the temperature between the calibration curves is small —1°C is typically the smallest resolution possible for this setup— linear interpolation is valid. Hence, the velocity throughout the boundary layer could be found for a range of temperatures throughout the experiments by using this approach and effectively compensate the hot-wire data. It should be noted that it was ensured that calibration curves for the hot wires were taken at temperatures above and below the working range of the experiments. This was to ensure that velocity data were interpolated and never extrapolated. However, it is worth noting that interestingly, Hultmark and Smits (2010) were recently able to cast similarity variables for both constant temperature and constant current anemometers, that allowed the hot-wire data to be compensated over a large temperature range using a single calibration curve. It was noted in §6.2.1 that the thermal boundary layer had a time-varying mean for  $y^+ < 15$  (no-control data) and  $y^+ < 60$  (travelling-wave data) and function fits were applied to the data to take into consideration the time-varying temperature mean. The effect of correcting the velocity measurements for the thermal boundary layer with a mean temperature change and by correcting the velocity measurements by a time-varying mean of temperature is shown in Figure 6.14. The data in this figure is for bidirectional forcing, where the thermal boundary layer developed by

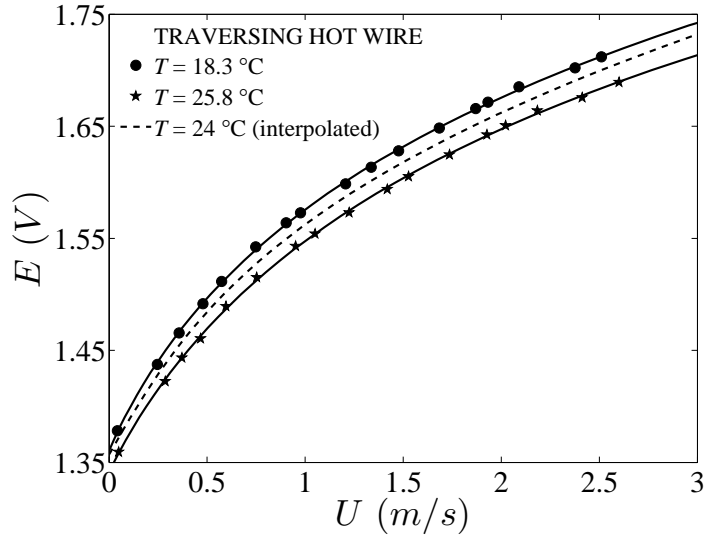


Figure 6.13: An example of temperature correction using the traversing-probe calibration data.

the plasma was largest. It can be seen for both the canonical and travelling-wave data, that correcting the velocity data for the mean temperature change or a time-varying change in temperature has no effect. Time-series of plasma data for bidirectional forcing at  $y^+ = 5$  is shown in Figure 6.15. The data presented in this figure is subjected to thermal effects as shown in Figure 6.9. In Figure 6.15a) the velocity has not been corrected for any thermal effects, in b) the velocity signal has been corrected for mean temperature drift and in c) the velocity has been corrected by applying a cubic function fit to the temperature time-series. It can be seen in Figure 6.15 that the shapes of the velocity time-series for all three plots do not change. There is an increase in mean velocity of the data with no correction (a) to mean correction (b) of 6% in this case. There is a similar increase in mean velocity between the no correction and cubic fit correction (5%). Hence, there is merely a 1% difference in mean velocity change if the data are corrected for mean temperature drift or a time-varying temperature drift. This justifies the correction of the hot-wire data based on the mean temperature change.

Hot-wire measurements have been taken at four spanwise locations, Z1 to Z4, in the turbulent boundary layer, Figure 6.2. These locations were chosen to determine if there were any changes in the turbulent boundary-layer structure

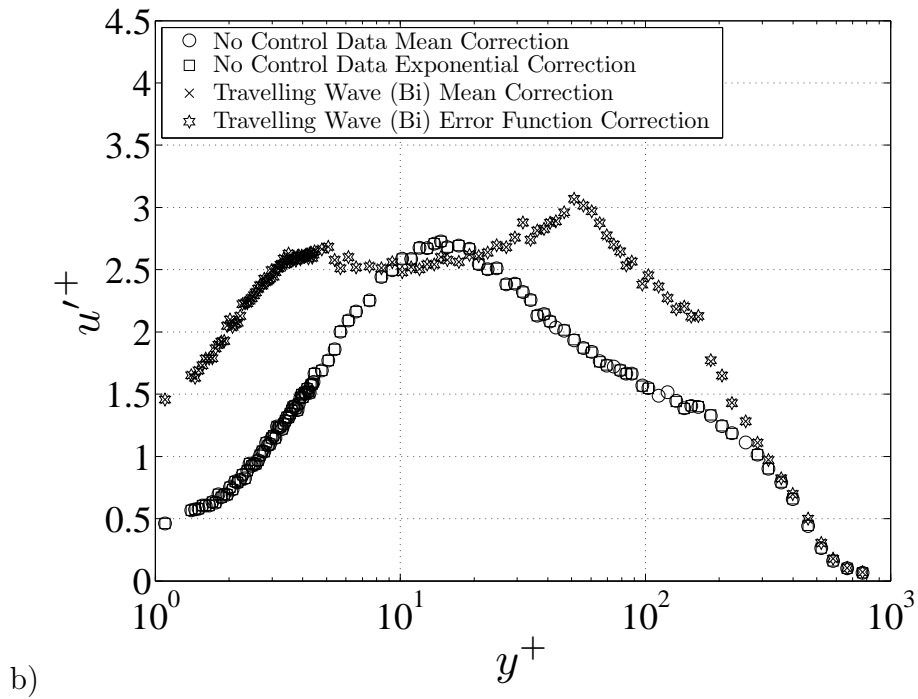
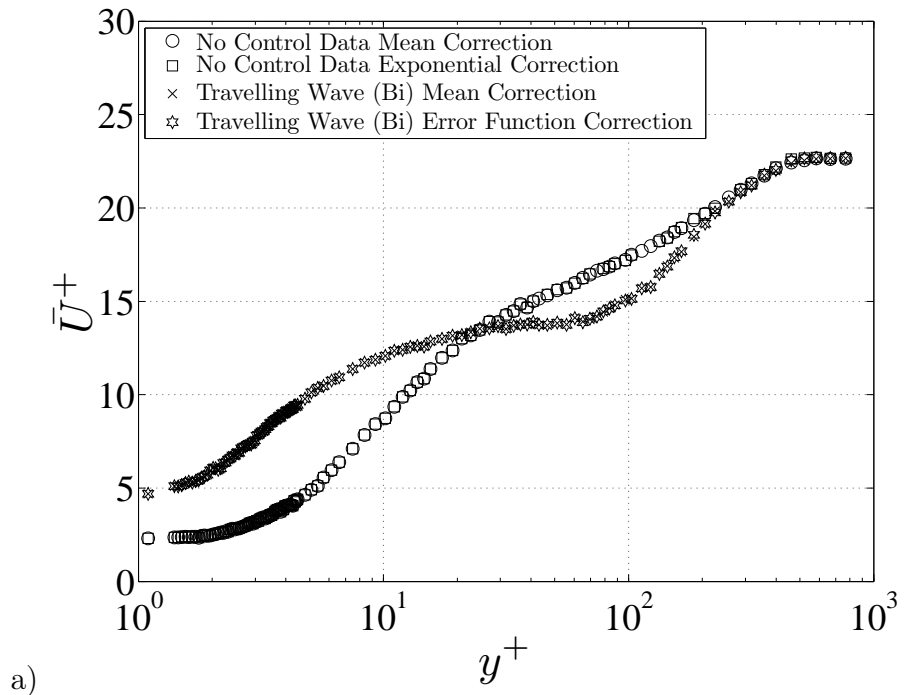


Figure 6.14: Turbulent boundary-layer data corrected for temperature change using different function fits to the thermal boundary-layer data. a) Mean streamwise velocity profiles and b) streamwise velocity turbulence intensity profiles.

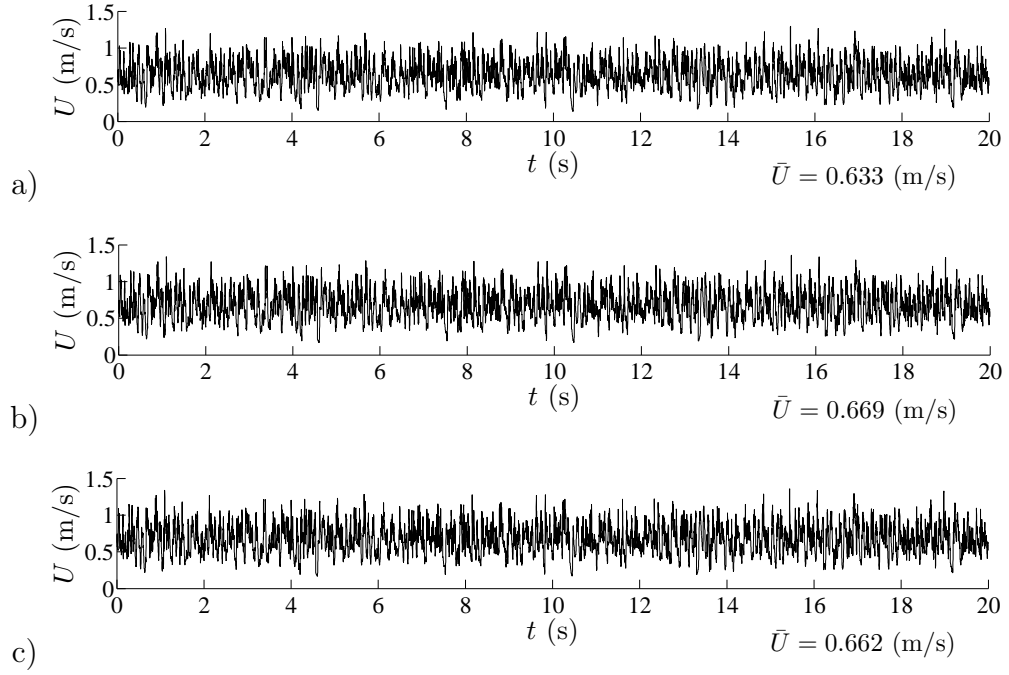


Figure 6.15: Velocity time-series showing the effect of a) no thermal correction, b) mean thermal correction and c) cubic function fit for thermal correction. Data are for bidirectional travelling wave at  $y^+ = 5$ .

as the spanwise travelling waves moved in the spanwise direction. Therefore, 8 boundary-layer profiles were taken in total (one profile at each location for Z1 to Z4 for both uni and bidirectional forcing). Each profile had both no-control and control (travelling-wave) data. The no-control data for both the uni and bidirectional travelling waves were corrected for the mean temperature change in thermal boundary layer and averaged.

The averaged canonical data taken in §6.1 (which is not subjected to any thermal effects from the plasma) is plotted against the averaged no-control data for both the uni and bidirectional travelling waves that have been corrected for the thermal boundary layer in Figures 6.16 and 6.17 respectively. The mean streamwise velocity is shown in Figures 6.16 and 6.17a) and b) with outer and inner scaled variables respectively and the streamwise turbulence intensity is shown in Figures 6.16 and 6.17c). Here, inner scaled variables are quantities found in the inner-region of the turbulent boundary layer, such as friction velocity and viscosity. Outer scaled variables are quantities found in the outer-region of the turbulent boundary layer, such as the free-stream velocity and the boundary-

layer thickness. The no-control data that has been corrected for the thermal boundary is denoted as, No-control Data (Uni) and No-Control Data (Bi) and the data from §6.1 is denoted as Canonical Data. Hence, the canonical data have no influence of any thermal effects from the plasma and the no-control data, although it is taken with no travelling wave forcing, is subjected to small residual heating from the dielectric sheet. It can be seen in Figure 6.16 that after thermal correction, the streamwise velocity and turbulence intensity for the unidirectional travelling-wave data are underestimated by around 8% for  $y^+ < 10$  ( $\frac{y}{\delta} < 0.02$ ). In Figure 6.17, the bidirectional travelling-wave data have a larger underestimate, around 20% in streamwise velocity and 15% for turbulence intensity for  $y^+ < 10$  ( $\frac{y}{\delta} < 0.02$ ).

To look at the thermal effects of the no-control data more closely, plots of the near-wall region will be presented and discussed. As a further comparison, the PIV data in the  $x$ - $z$  plane of the turbulent boundary layer at  $y^+ = 5$  (that will be presented in Chapter 7) will be plotted alongside the hot-wire data. The locations of the hot-wire measurements, Z1 to Z4, in relation to the  $x$ - $z$  plane PIV measurements at  $y^+ = 5$  from Chapter 7 are shown in Figure 6.18a), b) and c), where the time-averaged canonical data, unidirectional and bidirectional travelling-wave data are shown respectively. The time-average for the canonical data was taken over 5250 realisations of the flow at 750 Hz. The time-average of the uni and bidirectional travelling-wave data was taken over 7956 realisations of the flow at 750 Hz, which encompass 51 forcing periods of travelling-wave excitation (10 seconds of data). It should be noted that a Clauser plot cannot be used for a manipulated boundary layer and as a result all data sets have been non-dimensionalised using the no-control friction velocity from herein. It can be seen from this figure, that from a time-average point of view, there are regions of high- and low-speed fluid in bands in the spanwise direction for both the uni and bidirectional travelling waves, Figure 6.18b) and c). The location of the hot-wire measurements are located in high-speed bands across Z1 to Z3. The data from

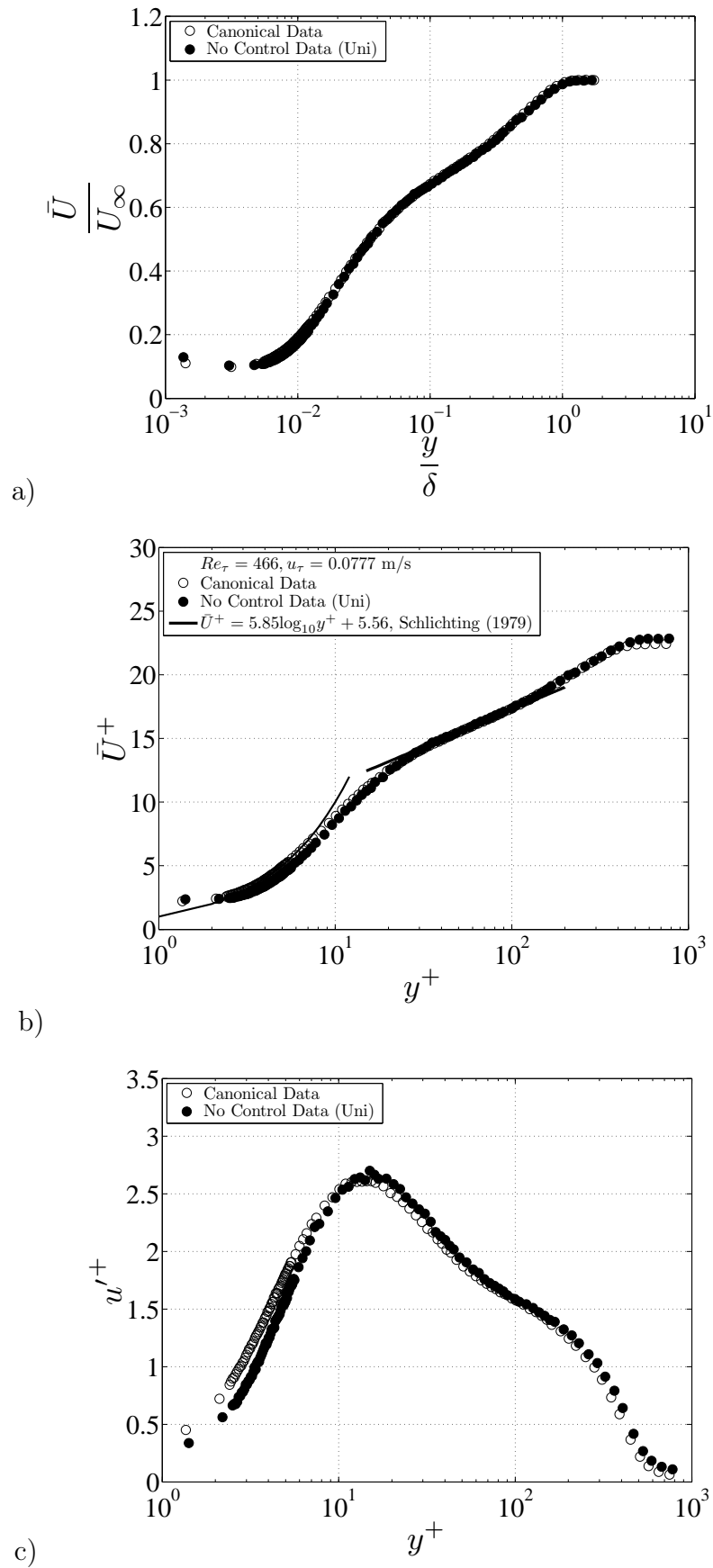


Figure 6.16: The effects of the thermal boundary layer on the unidirectional no-control data after temperature compensation with a) streamwise velocity profile (outer scaling), b) streamwise velocity profile (inner scaling) and c) streamwise velocity turbulence intensity profile.

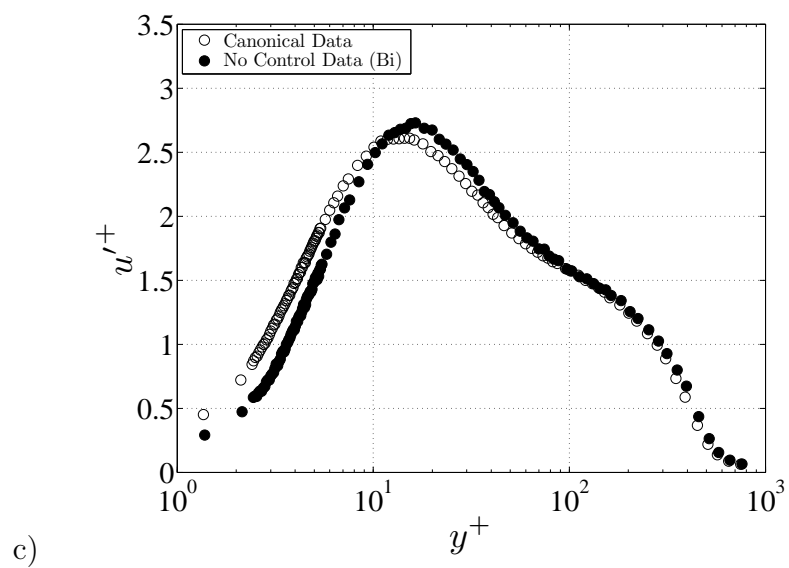
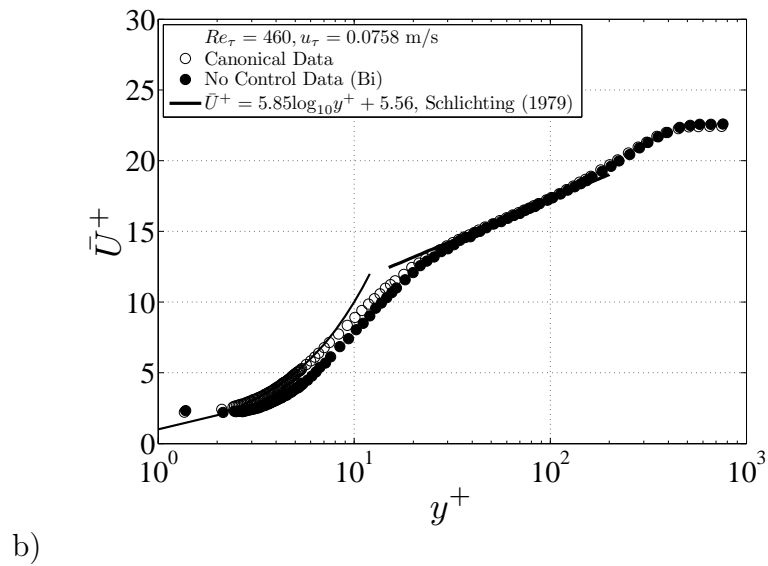
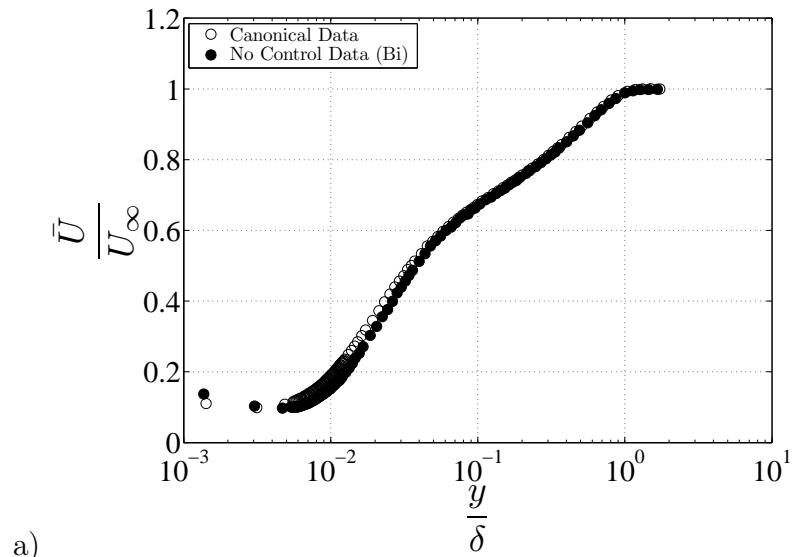


Figure 6.17: The effects of the thermal boundary layer on the bidirectional no-control data after temperature compensation with a) streamwise velocity profile (outer scaling), b) streamwise velocity profile (inner scaling) and c) streamwise velocity turbulence intensity profile.

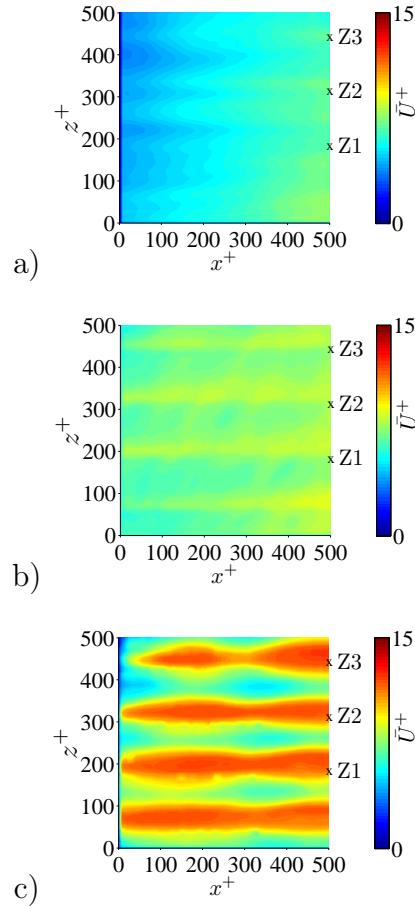


Figure 6.18: Hot-wire measurement locations, Z1 to Z3, in relation to the  $x$ - $z$  plane PIV data at  $y^+ = 5$ , a) time-averaged canonical data, b) time-averaged unidirectional forcing data and c) time-averaged bidirectional forcing data. The data have been scaled with the uncontrolled friction velocity.

this plane ( $y^+ = 5$ ) will be used as a comparison with the near-wall velocity plots taken with hot-wire anemometry in this section.

To look at the thermal effect of the no-control data more closely a plot of the near-wall region at the Z2 location with uni and bidirectional forcing is shown in Figure 6.19. The data for the unidirectional travelling-wave, control and no-control data, can be seen in Figure 6.19a). In this figure, the no-control stream-wise velocity data have been corrected for the thermal boundary layer and shows around an 8% increase (at  $y^+ = 5$ ) in streamwise velocity due to temperature correction. The solid black line, is the averaged canonical data from §6.1 that is not subjected to any thermal effects of the plasma. An error bar showing the uncertainty in the linear fit —to two standard deviations— (and hence, velocity

gradient) is shown at  $y^+ = 5.7$  ( $u_\tau = 0.0752 \pm 2 \times 0.0016$  m/s). The lower bound of the error bar coincides with the no-control streamwise velocity data that has been corrected for the thermal boundary layer, indicating that the no-control data from the unidirectional travelling wave has been successfully corrected for thermal boundary layer effects. Plotted for further comparison, is the time-averaged canonical data from the  $x$ - $z$  plane PIV measurements at  $y^+ = 5$ . The data point is calculated by taking an average in space over  $x$  and  $z$  of the data shown in Figure 6.18a) and is illustrated by the blue circle and has an error bar of  $\pm 5\%$  (Westerweel, 1997).

Plotted on Figure 6.19a) is the unidirectional travelling-wave (control) data. The correction of the thermal boundary layer leads to an increase in velocity of around 5% (at  $y^+ = 5$ ). It is clear that there is an increase in the mean streamwise velocity in the near-wall region when compared to the no-control data, which would ultimately lead to an increase in skin-friction drag. The increase in velocity gradient is shown by the linear fitting of the streamwise velocity in the region of  $3.5 < y^+ < 5$ . The change in gradient between the no-control data and unidirectional travelling-wave data yields a skin-friction drag increase of 20% with unidirectional travelling-wave excitation. However, this should be taken with caution. Plotted on Figure 6.19a) is the PIV data taken in the  $x$ - $z$  plane at  $y^+ = 5$  (red circle), which has been calculated by taking an average in space along the streamwise direction at the Z2 location of the data presented in Figure 6.18b). It should be noted that the  $x$ - $z$  plane PIV data are taken in the centre of the travelling-wave actuator sheet and the hot-wire data are taken a further 850 wall units downstream (10 mm downstream of the plasma actuators). Therefore, streamwise variation in the coefficient of friction is not considered here. The PIV data shows an increase in velocity at  $y^+ = 5$  of 20% from the travelling-wave data taken with hot-wire anemometry. Hence, it would appear that the velocity in the unidirectional travelling-wave data have been underestimated by around 20% at  $y^+ = 5$ . This could be due to additional thermal effects on the

hot-wire data that have not been compensated for and will be discussed later in this section. Therefore, the use of the near-wall gradient technique on the travelling-wave data could contain large errors, which is due to the additional thermal effects on the hot-wire data not being eliminated and is not due to the near-wall gradient technique itself. This is exemplified with the bidirectional travelling-wave data taken in the Z2 location that is presented in Figure 6.19b).

In Figure 6.19b), the no-control streamwise velocity data of the bidirectional travelling wave has been corrected for the thermal boundary layer and shows around an 8% increase with temperature correction. The solid black line, is the averaged canonical data from §6.1 that is not subjected to any thermal effects of the plasma. It can be seen more clearly that there remains around a 20% underestimate (at  $y^+ = 5$ ) of streamwise velocity between the two sets data. To correct for a shift in streamwise velocity of this magnitude an additional 6°C would have needed to be measured during the cold-wire measurements with the bidirectional travelling wave. Due to the underestimate in streamwise velocity in the near-wall region, the near-wall gradient technique cannot be used to determine the friction velocity or the skin-friction coefficient for the no-control data. The underestimated no-control data leads to an underestimate in the friction velocity of 10%, which leads to a 23% underestimate in skin-friction coefficient in this case. The maximum change in temperature from the canonical data measured by the cold wire was 1.1°C and 2.5°C at  $y^+ = 8$  for the uni and bidirectional travelling waves respectively. The no-control data with unidirectional forcing, Figure 6.19a), were successfully corrected for the thermal boundary layer. However, the no-control data with bidirectional forcing were not, due to a larger increase in temperature due to the thermal boundary layer with bidirectional forcing. Therefore, a change in temperature of up to 2.5°C can be compensated appropriately by interpolating over the hot-wire calibration curves but a temperature change of 2.5°C and above is yielding additional thermal errors on the hot wire.

The near-wall streamwise velocity for the bidirectional travelling wave is plot-

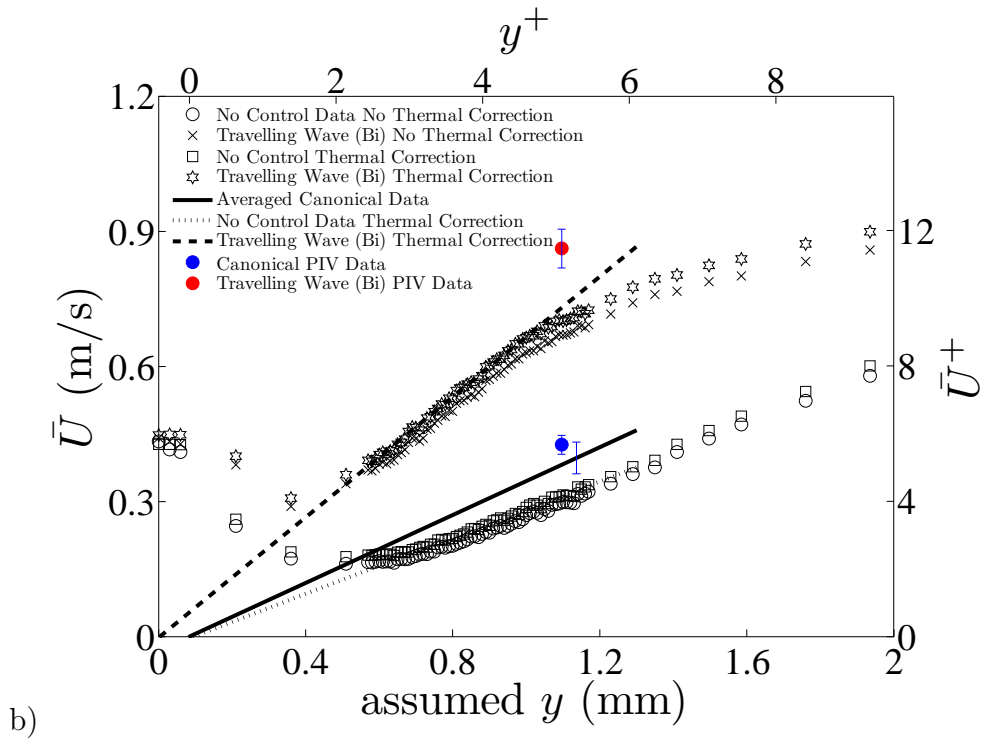
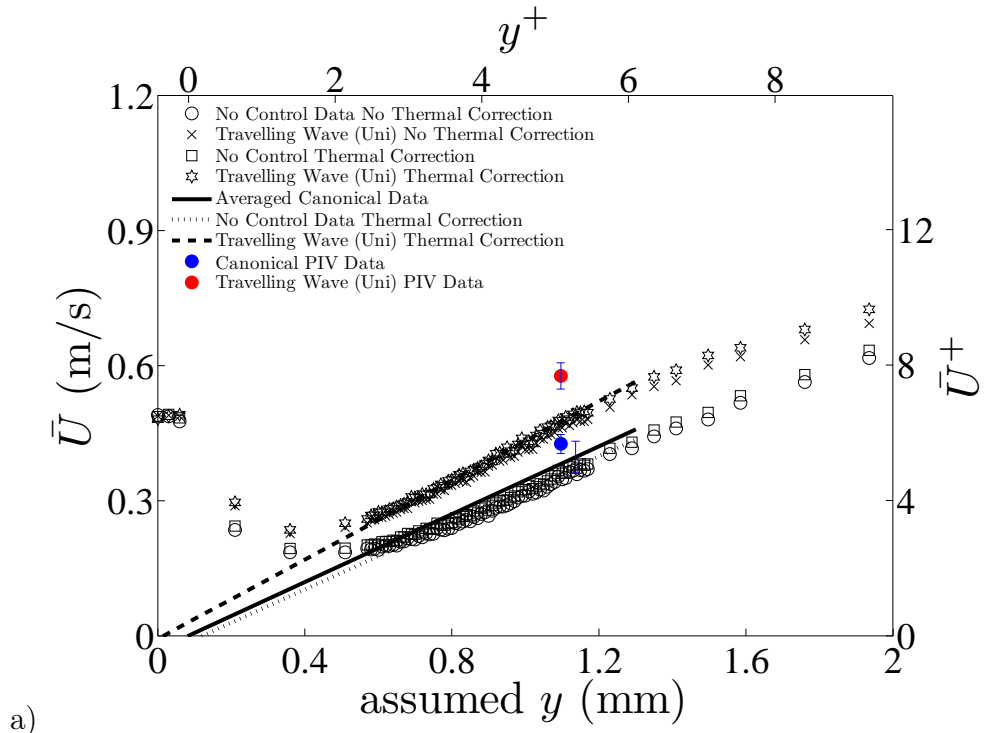


Figure 6.19: Thermal effects in the near-wall region with a) unidirectional forcing and b) bidirectional forcing. The data have been scaled with the uncontrolled friction velocity.

ted in Figure 6.19b). There is a large increase in streamwise velocity in the near-wall region when the bidirectional travelling wave is applied to the boundary layer. A line of least squares fit through the travelling-wave data for  $3.5 < y^+ < 5$  is shown in Figure 6.19b) where it is clear that the gradient of this line has increased when compared with the no-control data, indicating a 75% increase in skin-friction drag in this case. The PIV data taken from Figure 6.18c) is shown by the red circle in Figure 6.19b) which shows that the hot-wire anemometry data for the bidirectional travelling wave has been underestimated by approximately 20% at  $y^+ = 5$ .

It has been seen in both the uni and bidirectional travelling-wave data sets of Figure 6.19, that changes in temperature above  $2.5^\circ\text{C}$  yield underestimates in the streamwise velocity obtained by the hot wire. This creates underestimates in the friction velocity and skin-friction coefficients obtained using the near-wall gradient technique. The no-control bidirectional travelling-wave data underestimated the skin-friction coefficient by 23%. Hence, it would appear that the error in skin-friction measurement with the spanwise travelling waves created with DBD plasma is on the order of 20%. Due to the inaccuracies in the near-wall gradient technique (possibly due to additional thermal effects on the hot-wire data that have not been eliminated), the friction velocity has been obtained from a Clauser plot of the no-control travelling-wave data. This is valid as the underestimates in streamwise velocity were present for  $y^+ < 10$ . The Clauser plot method, Figures 6.16 and 6.17, yielded a friction velocity of 0.0777 m/s and 0.0758 m/s for the uni and bidirectional travelling waves respectively. The no-control friction velocity for both the uni and bidirectional travelling-wave data were within 5% of the friction velocity obtained by the near-wall gradient technique and Clauser plot method with the canonical data in §6.1.

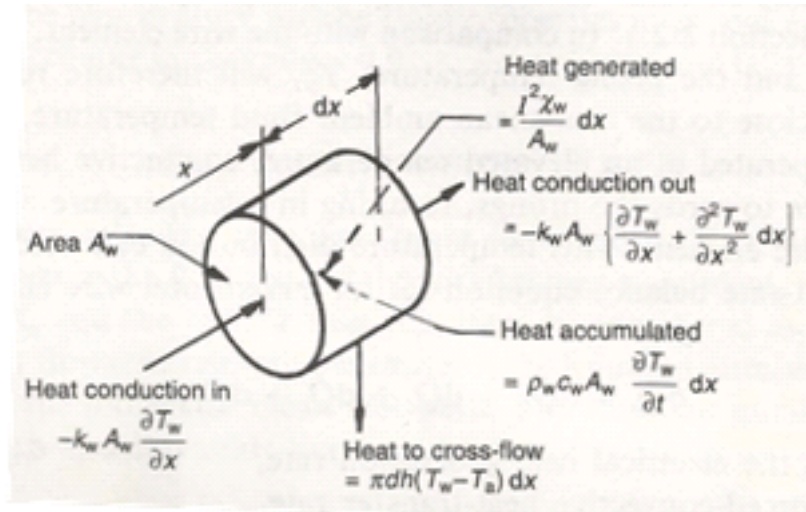


Figure 6.20: Hot-wire geometry and heat balance for an incremental element, Bruun (1995).

### Thermal Errors

It can be seen in Figure 6.19 that the linear fitting of the travelling-wave (control) data does not extend to the same  $U = 0$  m/s location as the no-control data. The same issue was found when DBD plasma was used to create a spanwise oscillation in the turbulent boundary layer (Jukes, 2007). In the spanwise oscillation study, it was thought this was due to  $v$  and  $w$  fluctuations contaminating the  $u$ -component velocity in the viscous sublayer. Increased  $v$  and  $w$  fluctuations would act to increase the measured streamwise velocity as single hot-wire probes are sensitive to magnitude of velocity. Although this is true,  $v$  and  $w$  fluctuations would act to increase the velocity measured by a single hot-wire probe, it does not explain the apparent underestimate in streamwise velocity in the no-control data measured by the hot-wire probe. It is thought that in the current study, the underestimate in the streamwise velocity, the lack of collapse to the same  $U = 0$  m/s position and the inaccuracies in the near-wall gradient technique could be due to additional thermal errors on the hot-wire measurements.

To explain the additional thermal errors that may be present on the hot wire which are causing an underestimate in the streamwise velocity, a diagram is taken from Bruun (1995) and is shown in Figure 6.20. This figure shows a small element

of the wire of a hot-wire probe and the sources of heat transfer acting on the wire. From this figure a heat-rate balance can be determined,

$$d\dot{Q}_e = d\dot{Q}_{fc} + d\dot{Q}_c + d\dot{Q}_{cp} + d\dot{Q}_r + d\dot{Q}_s. \quad (6.7)$$

The total heat transfer (or electrical heat-generation rate) is  $\dot{Q}_e$ , the forced-convective heat transfer rate (the heat transfer due to the flow) is  $\dot{Q}_{fc}$ , the conductive heat transfer (the heat transfer along the wire) is  $\dot{Q}_c$ , the conductive heat transfer from the wire to the hot-wire prongs is  $\dot{Q}_{cp}$ , the heat lost due to radiation (from the wire to the ambient surroundings) is  $\dot{Q}_r$  and the heat storage rate (due to the heat accumulated inside the wire) is  $\dot{Q}_s$ . Under steady state conditions, the wire temperature can be assumed not to change with time (Bruun, 1995) so the heat storage rate,  $\dot{Q}_s$ , can be neglected. Under normal working conditions, the radiation heat-transfer rate is negligible (Bruun, 1995), so that Eqn. 6.7 can be reduced to,

$$d\dot{Q}_e = d\dot{Q}_{fc} + d\dot{Q}_c + d\dot{Q}_{cp}. \quad (6.8)$$

The conductive heat loss,  $\dot{Q}_{cp}$ , from the hot wire to the hot-wire prongs can be expressed as (Bruun, 1995),

$$\dot{Q}_{cp} = 2k_w A_w \frac{(T_w - T_a)}{l_c} \tanh\left(\frac{l}{2l_c}\right). \quad (6.9)$$

In Eqn. 6.9,  $l$  is the active wire length and is 1.25 mm for the 5  $\mu\text{m}$  diameter hot-wire probe used in this study. The area of the wire is  $A_w$  and the thermal conductivity is  $k_w$ . The cold-wire length,  $l_c$ , for a tungsten 5  $\mu\text{m}$  diameter hot-wire probe operated at overheat ratio of 1.8 is typically 150  $\mu\text{m}$  (30 wire diameters). Hence, the conductive heat loss to the hot-wire prongs is proportional to  $(T_w - T_a)$ , where  $T_w$  is the wire temperature which is typically around 230°C and  $T_a$  is the surrounding ambient temperature. For normal working conditions, the hot-wire will be placed in an isothermal flow. Hence the conductive heat

loss to the hot-wire prongs will be constant and not change with time. Small ambient temperature change that drifts slowly over time can be corrected for by interpolating over calibration curves.

It has been shown in Figure 6.11, that on application of the spanwise travelling waves in the turbulent boundary layer, a thermal boundary is developed due to DBD plasma and can generate changes in temperature of up to 4°C within a timescale of 60 seconds. Therefore, it is postulated that the thermal boundary layer developed on application of DBD plasma is causing the hot-wire prongs to be heated, which is reducing the conductive heat loss from the wire to the hot-wire prongs, Eqn. 6.9. Furthermore, the conductive heat loss will not be constant over time due to the non-stationary temperature change with time caused by the plasma, Figure 6.7. As the temperature is decreasing during the no-control data and rising in the control data, there could be a dynamic thermal effect taking place due to the opposite changes in temperature. A reduction in the conductive heat loss to the hot-wire prongs will reduce the total heat transfer sensed by the hot wire, Eqn. 6.8, which will cause a reduction in the measured voltage from the Wheatstone bridge and lead to underestimate in the flow velocity. This underestimate is very difficult to compensate for as the hot-wire calibrations are conducted at constant ambient temperatures, and hence with a constant conductive heat loss from the hot wire to the hot-wire prongs.

The same analogy could be applied to the cold-wire probe. Cold-wire anemometry was performed in constant current mode (not constant temperature mode), where the increase in flow temperature changes the resistance of the wire which in turn causes a change in voltage which is related to temperature (as explained in Chapter 3). The cold-wire probe is operated with a low overheat ratio, close to 1. Hence, the temperature of the wire is approximately equal to the ambient temperature, such that the conductive heat loss,  $\dot{Q}_{cp}$ , from the wire to prongs would be small. As the cold wire is placed into the flow which is subjected to temperature flux, the cold-wire prongs and the wire of the cold wire probe would

be equally heated, hence maintaining a low level of conductive heat loss.

Another possible source of heat transfer is radiative heat transfer from the plasma actuator sheet to the hot-wire prongs. However, this source of heat transfer is thought to be negligible. Black-body radiation is dependant on the temperature of the two bodies—in this case, the plasma actuator sheet and the hot-wire prongs—the distance between the two bodies, the areas of the two bodies and the observation—relative angle—of one body to the other (Kreith and Bohn, 1993). The maximum thermal effects on the hot-wire probe have been seen in the near wall region. In the near-wall region, the radiative heat transfer between the plasma actuator sheet and the hot-wire prongs will be minimum as the relative angle between the bodies—how much one body can see of the other—is small. Furthermore, the temperature difference between the two bodies will be small ( $\sim 200$  °C) along with the area of the hot wire and prongs. The maximum radiative heat transfer will be when the hot-wire probe is far away from the wall. It can be seen in Figures 6.16 and 6.17, and if we look ahead to Figure 6.21, the canonical data, no-control data and the spanwise travelling-wave data collapse for  $y^+ > 200$ , ruling out the possibility of radiative heat transfer.

Therefore, it is expected that the underestimate of streamwise velocity in the near-wall region of the turbulent boundary layer is due to the hot-wire prongs of the hot-wire probe being heated. This is caused by the thermal boundary layer developed by the actuation of DBD plasma inside the turbulent boundary layer, which reduces the conductive heat loss from the wire to the hot-wire prongs, causing a reduction in heat-transfer sensed by the CTA, leading to a reduction in measured velocity. As the streamwise velocity profiles for the no-control data are collapsing to the canonical data for  $y^+ > 20$  (Figure 6.17), it is expected that errors on the hot-wire measurements due to possible additional thermal effects are limited to the inner-region of the boundary layer only.

### 6.2.2.2 Streamwise Velocity Measurements

Streamwise velocity measurements made throughout the turbulent boundary layer at the 4 spanwise locations, Z1 to Z4 are presented in this section. All measurements have been taken with a Dantec 55P15, 5  $\mu\text{m}$  diameter boundary-layer probe. The turbulent boundary layer was sampled at 1 kHz with duration of 90 seconds without plasma and 60 seconds with plasma at 127 locations throughout the boundary layer. The streamwise velocity data have been corrected for the thermal boundary layer effects that have been presented in §6.2.1.

Presented in Figure 6.21a) and b) is the change in mean streamwise velocity of the turbulent boundary layer with uni and bidirectional travelling waves. Profiles have been taken over the four spanwise locations, Z1 to Z4. It can be seen that the data across the four spanwise locations is similar, as expected, with the spread of the data being due to the spanwise travelling waves being produced from discrete actuators. As the data at each spanwise location is similar, an average across the four data sets for each travelling-wave configuration has been performed and is presented in Figure 6.22.

The change in mean velocity inside the turbulent boundary layer with travelling-wave excitation is shown in Figure 6.22a). It can be seen that the turbulent boundary layer was modified up to  $y^+ = 100$  with unidirectional forcing and up to  $y^+ = 200$  with bidirectional forcing. Travelling-wave excitation has led to a velocity deficit in the lower part of the logarithmic region. The velocity reduction with unidirectional forcing can be seen from  $y^+ = 25-100$  by 10% and the velocity reduction with bidirectional forcing can be seen from  $y^+ = 25-200$  by 20%. The reduction in mean streamwise velocity inside the logarithmic region is a feature that was observed when DBD plasma was used to create a spanwise wall oscillation (Jukes, 2007), which was shown to give a turbulent skin-friction reduction of up to 45% (Jukes *et al.*, 2006b; Jukes, 2007). The mean streamwise velocity with wall-normal distance for the spanwise oscillation with DBD plasma can be seen in Figure 6.23, where a reduction in streamwise velocity can also be seen

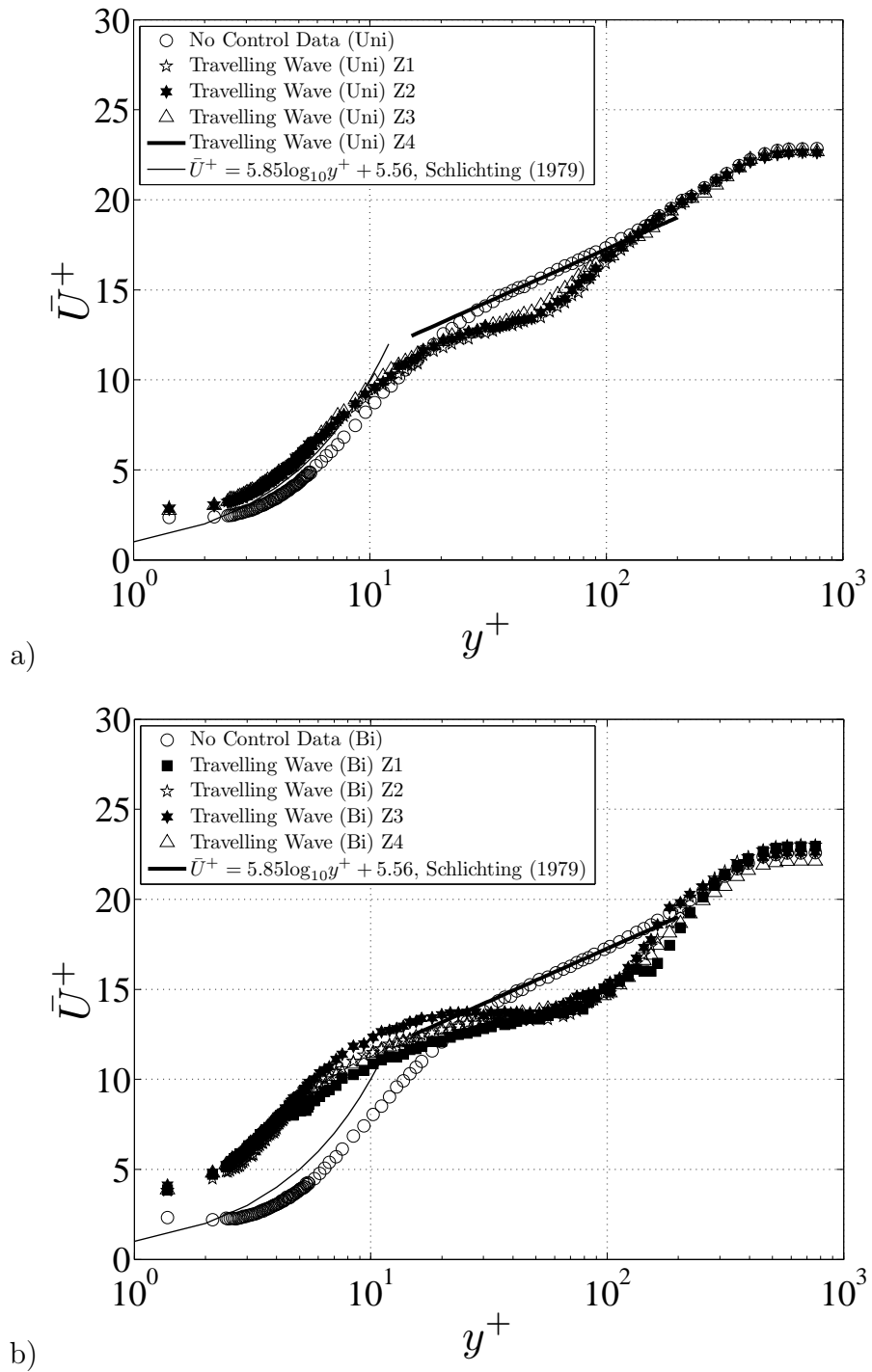


Figure 6.21: Mean streamwise velocity profiles with a) unidirectional forcing and b) bidirectional forcing at spanwise locations Z1 to Z4.

in the logarithmic region ( $10 < y^+ < 100$ ). Hence, for both spanwise oscillation and spanwise travelling wave created by DBD plasma, there are similar changes in turbulent boundary-layer structure. It has already been demonstrated, in Chapter 5 that starting vortices were generated on the initiation of DBD plasma, whose cores were located at  $y = 10$  mm ( $y^+ = 50$ ) with spanwise travelling-wave excitation. It will be shown with the  $z$ - $y$  plane PIV measurements in the turbulent boundary layer (Chapter 7), that the starting vortices form streamwise vortices in the turbulent boundary layer that lift low-speed streamwise velocity from the near-wall region into the logarithmic region. Hence, the streamwise velocity reduction measured in the hot-wire study was due to the upwash of the low-speed fluid from the near-wall region. The increase in streamwise velocity in the near-wall region is thought to be due to the entrainment associated with the plasma actuators. This is a similar trend that has also been observed from streamwise vortices created by a synthetic jet issued from a yawed slit inside a turbulent boundary layer (Di Cicca and Iuso, 2006).

The averaged turbulence intensity profiles are shown in Figure 6.22b), where there is an increase in turbulence intensity with the travelling-wave excitation over the majority of the boundary-layer thickness. There are two peaks in turbulence intensity, in particular at  $y^+ = 5$  and  $y^+ = 60$ , which correspond closely with the maximum temperature changes and temperature fluctuations in the boundary layer, §6.2.1. After  $y^+ > 100$  and  $y^+ > 200$  for the uni and bidirectional travelling waves respectively, there is no effect on the turbulence intensity with spanwise travelling waves. This location corresponds to the upper limit of the velocity reduction observed in the mean streamwise velocity profiles, Figure 6.22a). This indicates the average wall-normal distance ( $y^+ = 100$  and  $y^+ = 200$ ) that the streamwise vortices which are travelling in the spanwise direction, have been lifted to inside the turbulent boundary layer for each travelling-wave configuration.

It can be seen in Figure 6.22b) that for both types of the travelling-wave exci-

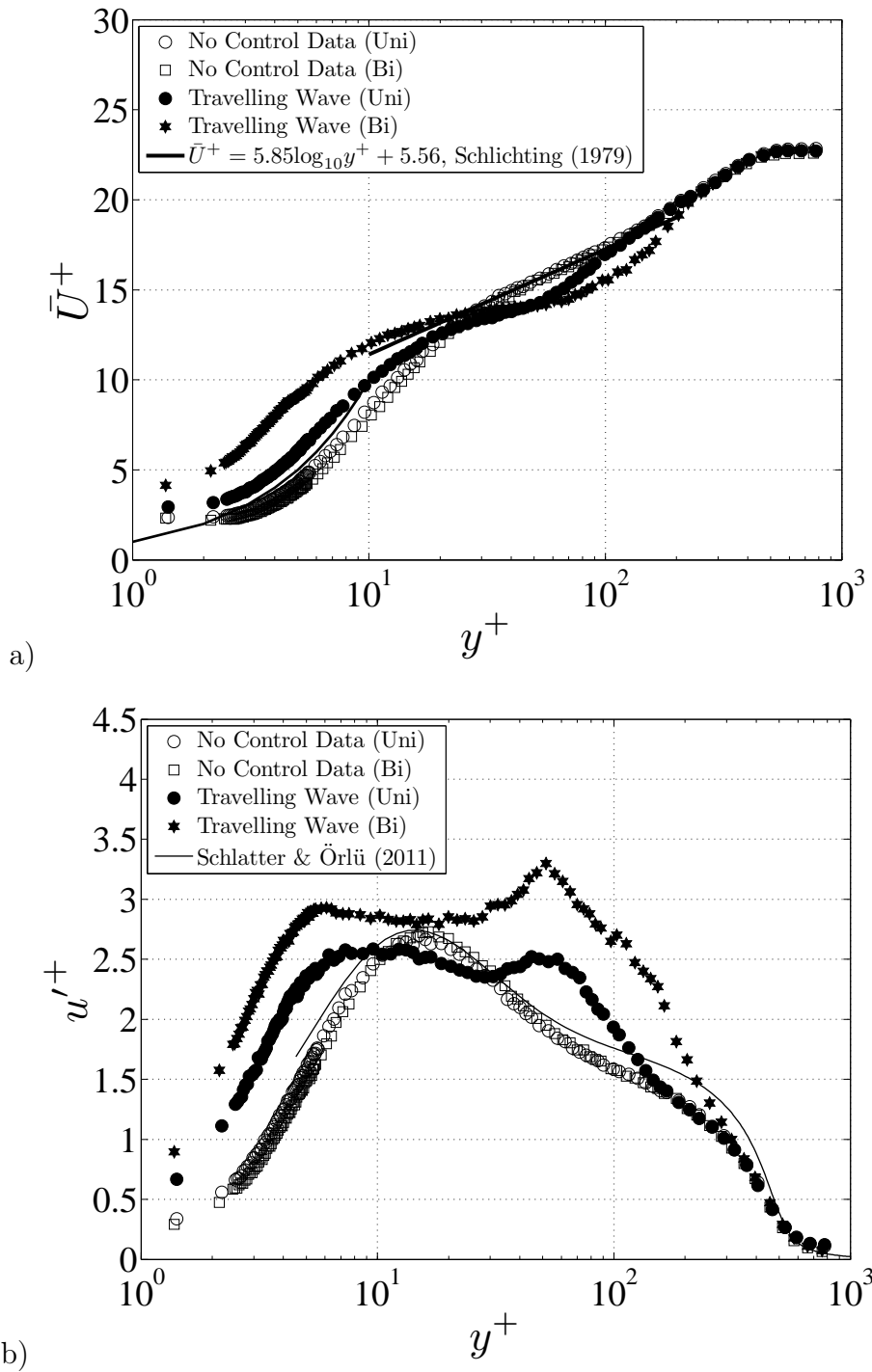


Figure 6.22: Averaged a) mean streamwise velocity profiles and b) streamwise velocity turbulence intensity profiles with uni and bidirectional forcing.

tations, there was a large increase in turbulence intensity in the near-wall region ( $y^+ < 5$ ). It is interesting to compare the turbulence intensity plot of the spanwise travelling waves with the turbulence intensity plot of the spanwise oscillation created with DBD plasma. This is shown in Figure 6.24, where the turbulence intensity with spanwise oscillation is taken from Jukes (2007) and the turbulence intensity plot for the spanwise travelling waves has been non-dimensionalised by the displacement thickness,  $\delta^*$ , and the free-stream velocity,  $U_\infty$ , to compare with the spanwise oscillation data. Figure 6.24b) shows the change in turbulence intensity profiles in the turbulent boundary layer when the distance between the DBD plasma actuators was increased in the spanwise oscillation study. Put simply, the distance between the electrodes,  $s^+$ , in the spanwise oscillation study was the spanwise distance that the starting vortex was able to move (and grow in size to) before it was consumed by the next actuation of DBD plasma. To make a tentative comparison between the spanwise oscillation study and the travelling-wave study, the equivalent distance,  $s^+$ , for the spanwise travelling waves would be the spanwise distance between adjacent DBD plasma actuators. This distance would be approximately  $\frac{1}{2}s^+$  in Figure 6.2, corresponding to 125 wall units ( $s = 25$  mm), which is 2.5 larger than the maximum  $s^+$  tested in the spanwise oscillation study ( $s^+ = 50$ ). It can be seen in Figure 6.24b), that as the distance between the DBD plasma actuators is increased, the turbulence intensity is increased. The data at  $s^+ = 50$  on Figure 6.24b) is very similar to the turbulence intensity plot for the spanwise travelling waves, Figure 6.24a). The increased turbulence intensity for the spanwise travelling waves when compared with the spanwise oscillation study could be due to the distance between the DBD actuators in the spanwise travelling-wave study being larger. In both the spanwise oscillation and the spanwise travelling-wave data, peaks in turbulence intensity can be seen at  $\frac{y}{\delta^*} = 10^{-1}$  and  $10^0$  ( $y^+ = 5$  and  $y^+ = 60$ ). The reason for the increase in turbulence intensity with an increasing distance between the DBD plasma actuators was thought to be due to the strength of the the start-

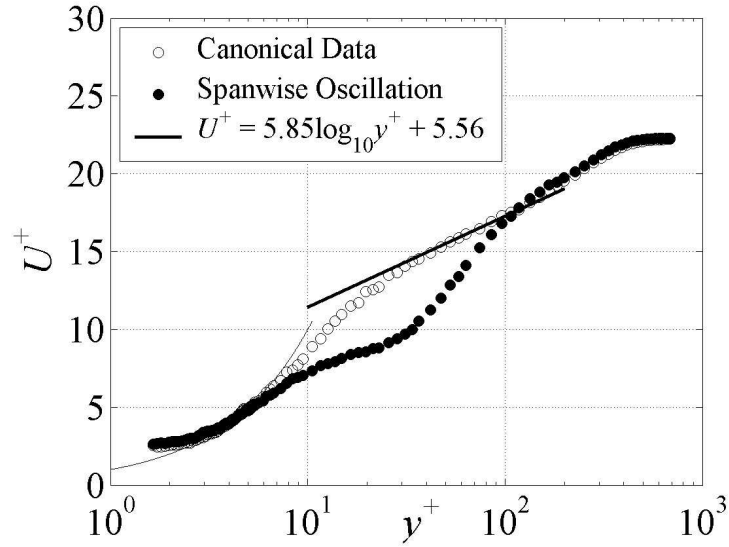
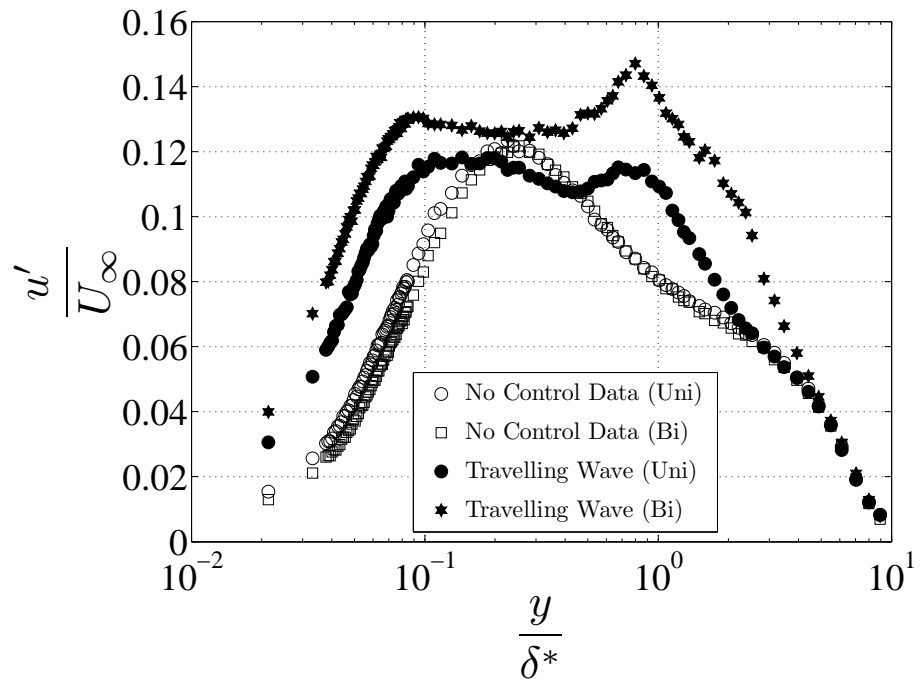
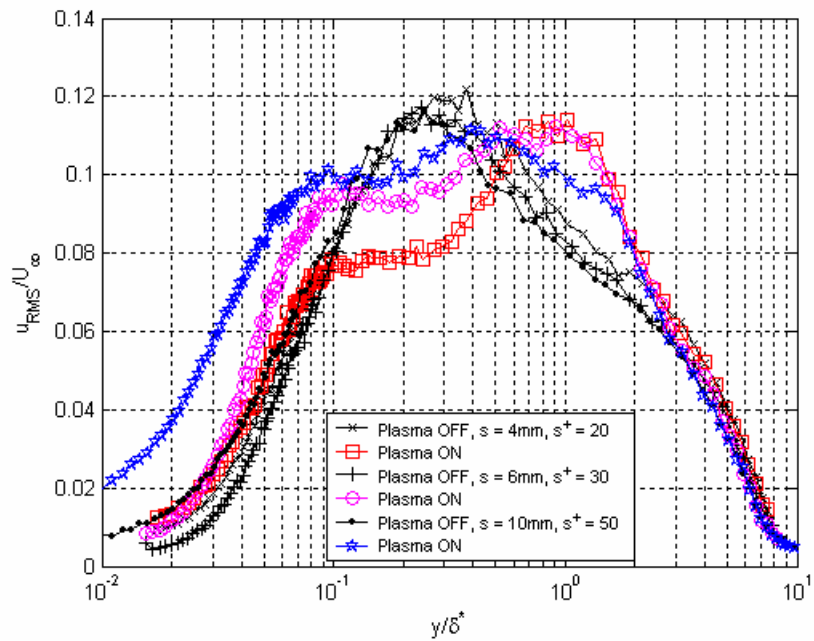


Figure 6.23: Mean streamwise velocity profile with spanwise oscillation created by DBD plasma. Taken from Choi *et al.* (2011).

ing vortex; as we increase the spacing, the velocity on each electrode increases so that the wall jets from each plasma actuator can reach each other. For the spanwise oscillation study the  $s^+ = 50$  data set created a skin-friction drag increase of over 60%. In the spanwise travelling-wave study, the distance between adjacent electrodes was 125 wall units. This was the distance that the fluid was moved (from actuator to actuator in Chapter 5) to create the spanwise travelling waves. It has been seen that with the travelling-wave excitations (both uni and bidirectional forcing), that the starting vortex (or streamwise vortex when inside the turbulent boundary layer) spreads fluid in the spanwise direction from actuator to actuator in each travelling-wave configuration. Although the streamwise vortices are effectively creating movement in the spanwise direction the strength of the streamwise vortices generated by the plasma could be causing increased turbulence intensity in the near-wall region. Reducing the distance between adjacent electrodes with spanwise travelling-wave excitation could lead to improved turbulent boundary-layer control.



a)



b)

Figure 6.24: Comparison of turbulence intensity profiles between a) spanwise travelling waves and b) spanwise oscillation with DBD plasma. The spanwise oscillation data are taken from Jukes (2007).

## Skewness and Kurtosis Profiles

The averaged skewness and kurtosis profiles with spanwise travelling waves are shown in Figure 6.25. There are large changes in both skewness and kurtosis in the near-wall region ( $y^+ < 6$ ) with the spanwise travelling waves. This is an indication that the near-wall structures (sweeps and ejections) have been modified by the spanwise travelling-wave excitations. The unidirectional travelling wave causes increases in both skewness and kurtosis in the near-wall region. This is in agreement with other drag reducing flows, such as spanwise wall oscillation (Choi and Clayton, 2001; Choi, 2002) and riblets (Choi, 1989). In contrast, the bidirectional travelling wave sees a large decrease in both skewness and kurtosis. Du *et al.* (2002) obtained a 30% reduction in turbulent skin friction when a bidirectional travelling wave with Lorentz forcing was applied to a turbulent channel flow. In their study, a decrease in skewness was also observed on application of the spanwise travelling wave. In addition, a flexible sheet undergoing a spanwise travelling-wave motion was applied to the turbulent boundary layer by Itoh *et al.* (2006). In the flexible sheet study, a turbulent skin-friction reduction of 7.5% was obtained and reductions in both skewness and kurtosis were observed. Hence, reductions in skewness and kurtosis with the spanwise travelling wave implemented with DBD plasma are features of drag reducing flows with the spanwise travelling-wave technique.

### 6.2.2.3 Energy Spectra and Probability Density Function

The energy spectra at  $y^+ = 5, 10, 30$  and  $60$  can be seen in Figure 6.26a) to d) respectively. The area under each plot will essentially provide the turbulence intensity squared, hence an increase in energy shows an increase in turbulence. At  $y^+ = 5$ , there is an increase in energy throughout the entire frequency spectrum. This implies that the spanwise travelling waves are adding energy to both large- and small-scale turbulence eddies in the flow. A peak in turbulence intensity

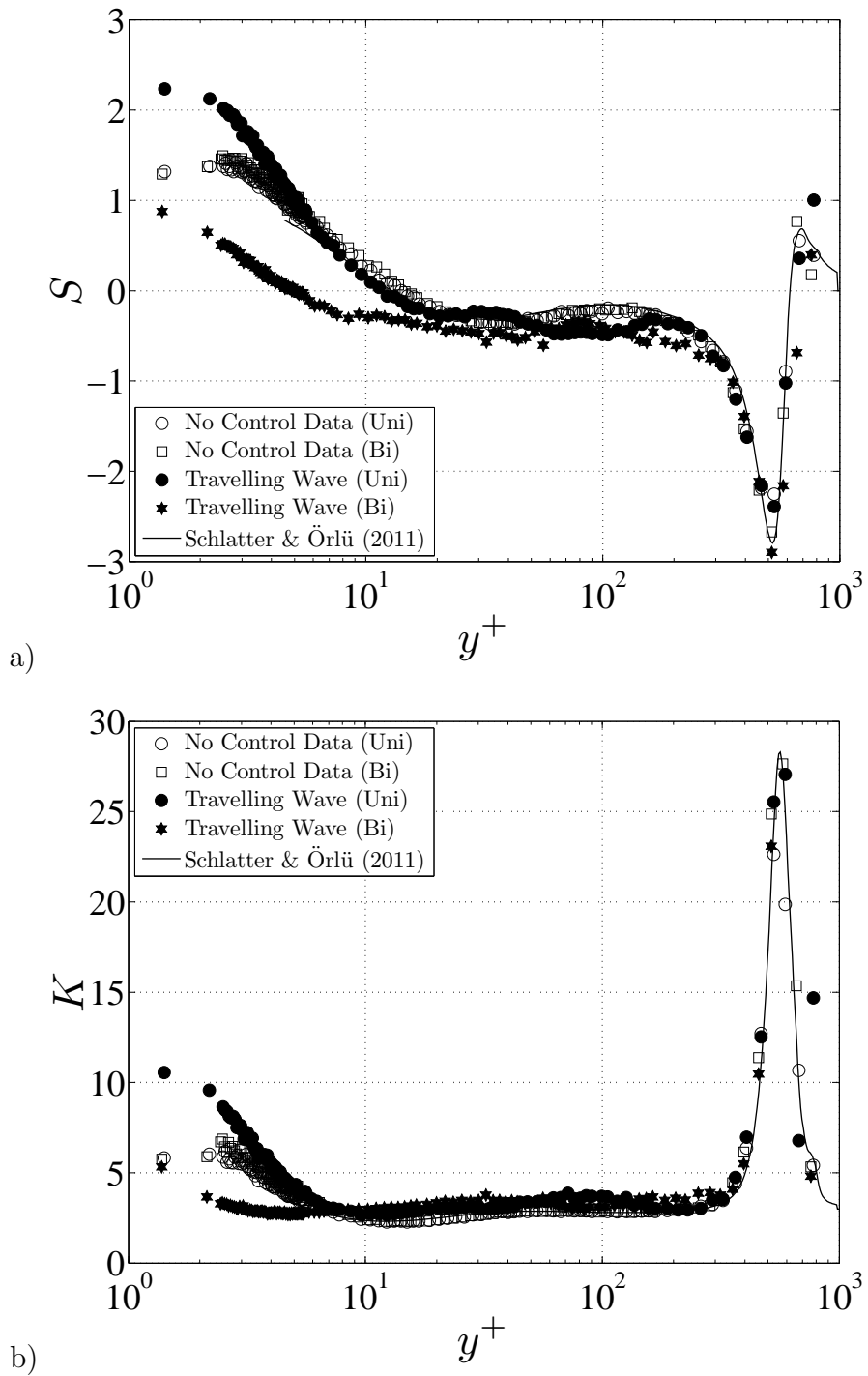


Figure 6.25: Averaged a) skewness and b) kurtosis profiles of streamwise velocity with uni and bidirectional forcing.

was also seen at  $y^+ = 5$  in the boundary layer, Figure 6.22b). At  $y^+ = 10$  and 30, there is a decrease in energy for  $f < 10$  Hz and an increase in energy for  $f > 10$  Hz. This was observed when DBD plasma was used to create a spanwise wall oscillation (Jukes, 2007) and could suggest that the travelling waves at this location are transferring energy from large-scale to small-scale turbulence eddies (Choi and Clayton, 2001). Moving further away from the wall to  $y^+ = 30$  and 60, the energy is increased throughout the frequency spectrum, where similarly increased turbulence intensity was found.

It has been shown in Figure 6.25 that the skewness and kurtosis for  $y^+ < 6$  was increased for the unidirectional travelling wave and reduced for the bidirectional travelling wave. In Figure 6.27a) and b) the fluctuating  $u$ -component time-series and corresponding PDF can be seen at  $y^+ = 5$ . Both the time-series and the PDFs have been normalised by their own standard deviation. When the unidirectional travelling wave is applied, the positive velocity spikes with larger velocity fluctuations being apparent, which led to an increase in skewness and kurtosis by 25% in this case and is illustrated by the change in PDF. When the bidirectional travelling wave was applied, there were large reductions in both skewness and kurtosis at  $y^+ = 5$ . This can be seen clearly with the change in time-series signal and PDF, Figure 6.27b). In this case, the skewness and kurtosis were reduced by 85% and 50% respectively. The values of skewness and kurtosis with the bidirectional travelling wave at  $y^+ = 5$  were 0.16 and 2.83. Hence, the fluctuating  $u$ -component time-series is nearly Gaussian in shape ( $S = 0, K = 3$ ).

The uni and bidirectional travelling waves at  $y^+ = 10$  are presented in Figure 6.28. The PDFs for the no-control data and unidirectional travelling waves can be seen to be similar, with a small reduction in positive skewing and a small increase in kurtosis. The bidirectional travelling wave exhibited a slight negative skewing ( $S = -0.17$ ) in comparison to the slightly positive skewed no-control case ( $S = 0.22$ ). The kurtosis for the uni and bidirectional travelling waves were both increased compared to the no-control cases.

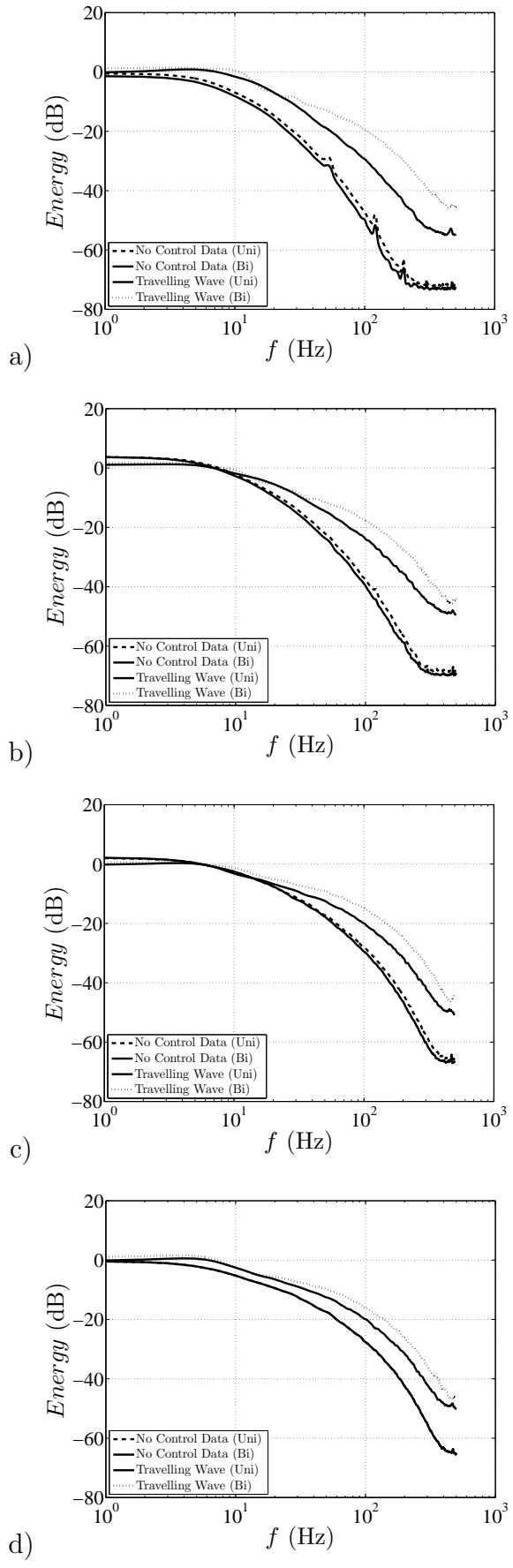


Figure 6.26: Averaged energy spectra with uni and bidirectional forcing at a)  $y^+ = 5$ , b)  $y^+ = 10$ , c)  $y^+ = 30$  and d)  $y^+ = 60$ .

The time-series and PDF for the uni and bidirectional travelling waves at  $y^+ = 30$  and  $60$  can be found in Figures 6.29 and 6.30 respectively. The kurtosis of both time-series was slightly increased when compared with the no-control cases and the skewness is negative with similar values as the no-control cases.

The large changes in skewness and kurtosis with the spanwise travelling waves in the near-wall region are indications that the near-wall structure of turbulence has been modified. It has been noted that increases in skewness and kurtosis have been seen in other drag reducing flows, such as spanwise wall oscillation (Choi and Clayton, 2001; Choi, 2002) and riblets (Choi, 1989). It has been found that the unidirectional spanwise travelling wave causes increases in skewness and kurtosis in the near-wall region, hence, exhibiting the same changes in higher order statistics as some drag reducing flows. Reductions in skewness and kurtosis have been found with the bidirectional travelling wave implemented with DBD plasma. It is interesting to note that a bidirectional travelling wave implemented numerically with a Lorentz force inside a turbulent channel flow (Du *et al.*, 2002) also exhibited a reduction in skewness in the near-wall region. Similarly, a bidirectional travelling wave implemented using a flexible sheet in a turbulent boundary layer was studied experimentally by (Itoh *et al.*, 2006), where reductions in both skewness and kurtosis were found in the near-wall region. Hence, the reductions in skewness and kurtosis observed with the bidirectional travelling wave implemented with DBD plasma, is a common feature of the spanwise travelling-wave technique, which is capable of achieving over a 30% reduction in turbulent skin friction (Du and Karniadakis, 2000; Du *et al.*, 2002; Itoh *et al.*, 2006).

#### **6.2.2.4 Conditional Sampling - VITA Analysis**

To study the bursting phenomena inside the turbulent boundary with and without travelling-wave control, the variable-interval time-averaging (VITA) technique has been used. This technique was first used by Blackwelder and Kaplan (1976) for studying the near-wall region of the turbulent boundary layer. The

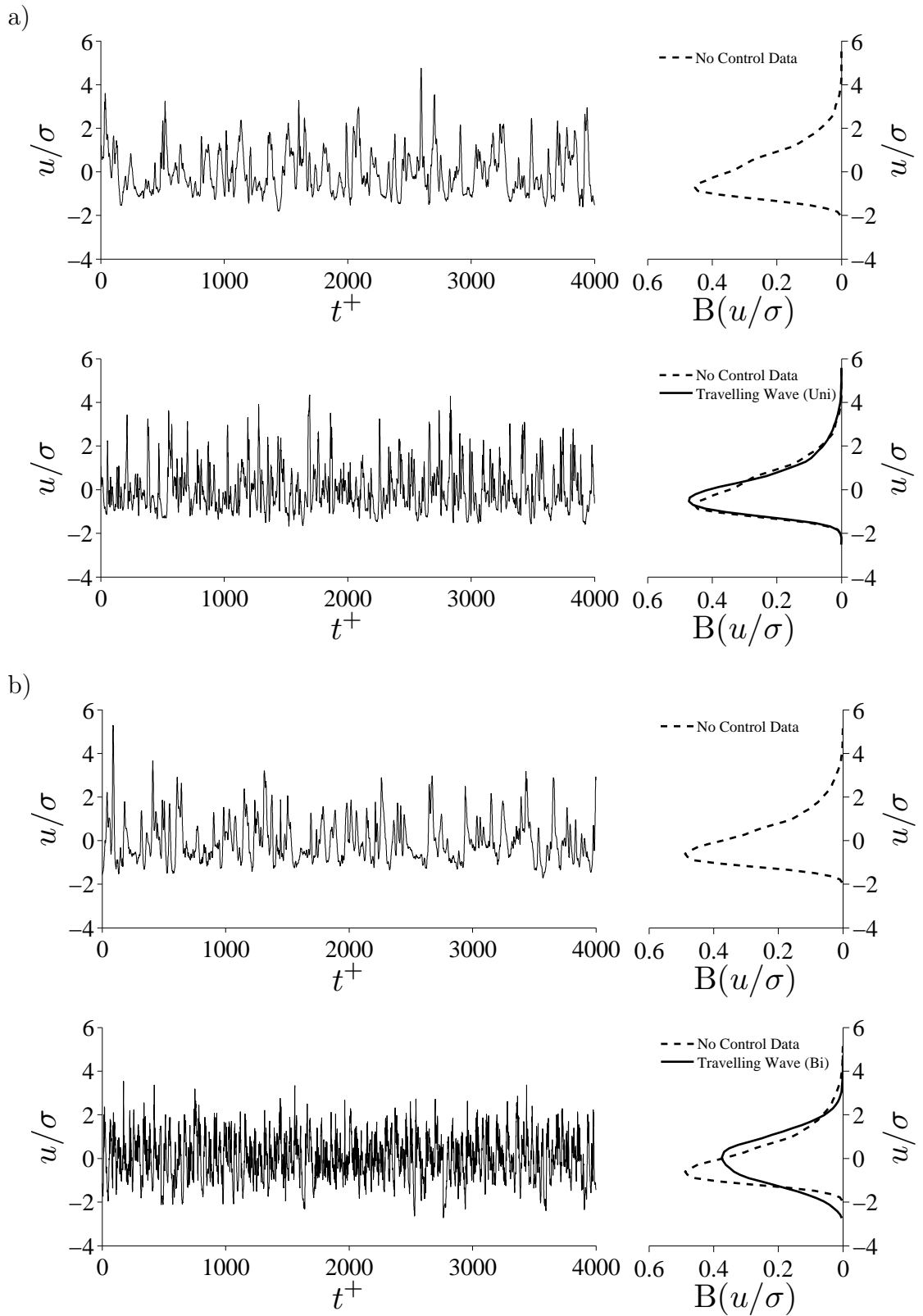


Figure 6.27: Fluctuating streamwise velocity time-series and corresponding PDF at  $y^+ = 5$  with a) unidirectional forcing and b) bidirectional forcing.

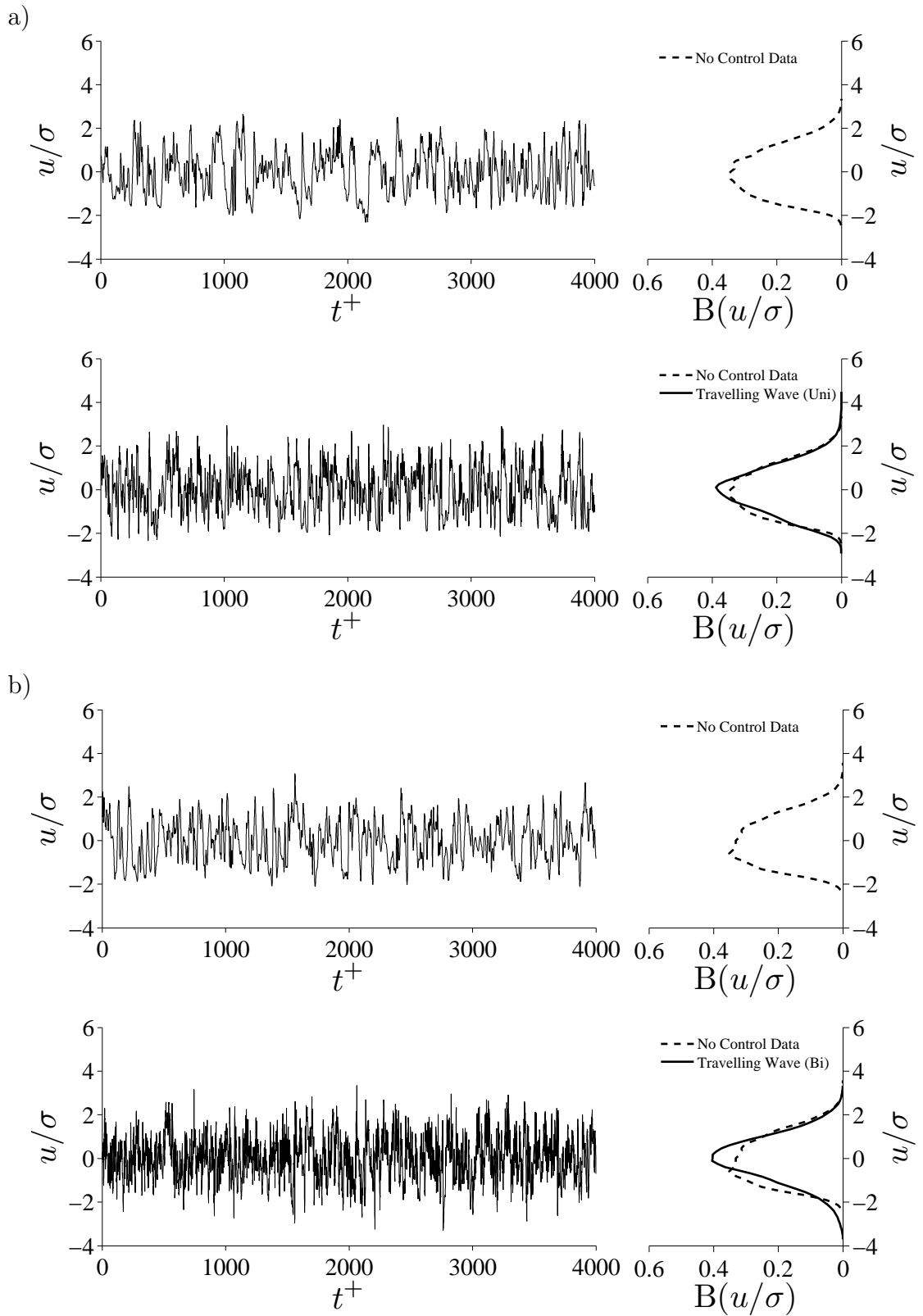


Figure 6.28: Fluctuating streamwise velocity time-series and corresponding PDF at  $y^+ = 10$  with a) unidirectional forcing and b) bidirectional forcing.

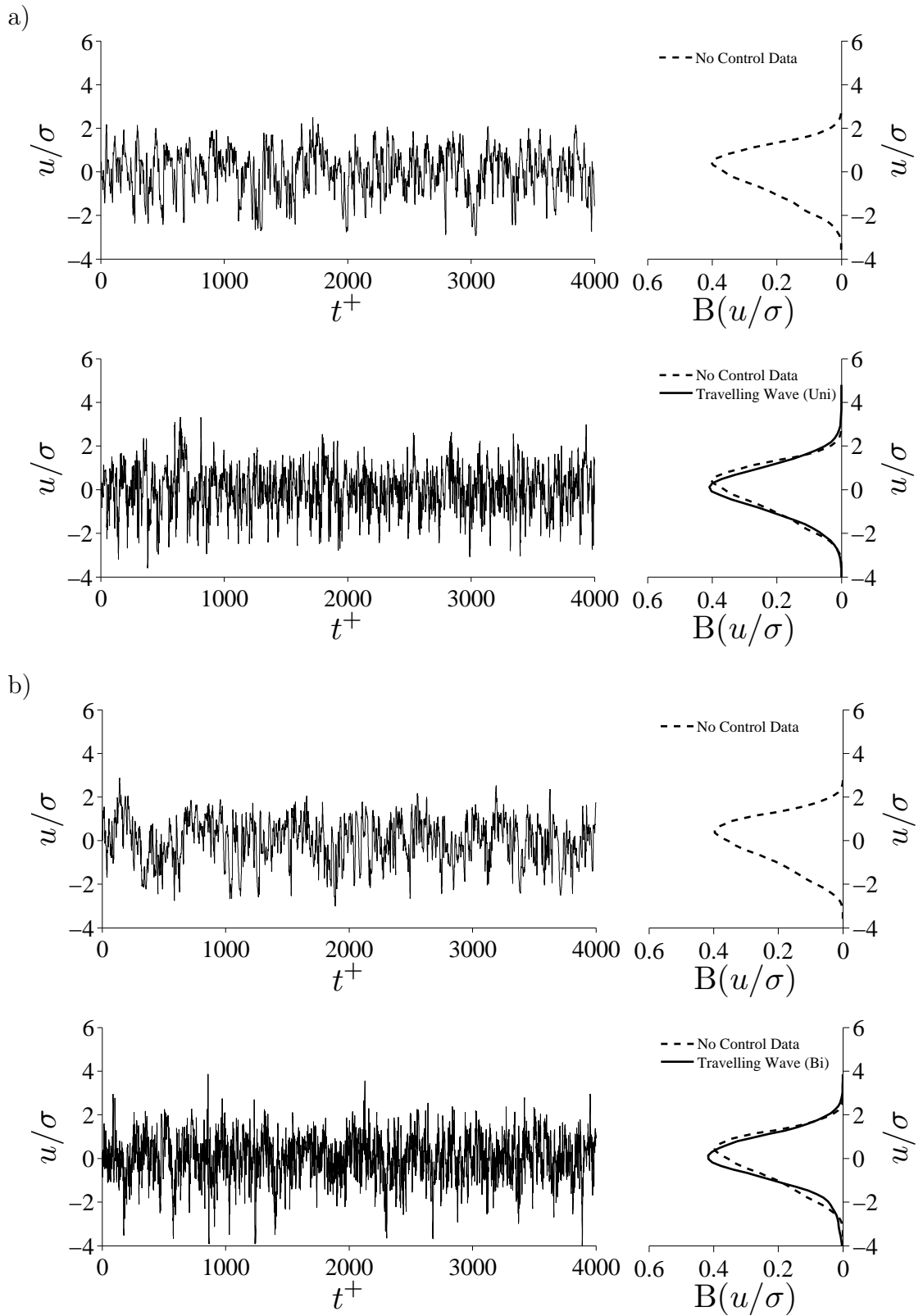


Figure 6.29: Fluctuating streamwise velocity time-series and corresponding PDF at  $y^+ = 30$  with a) unidirectional forcing and b) bidirectional forcing.

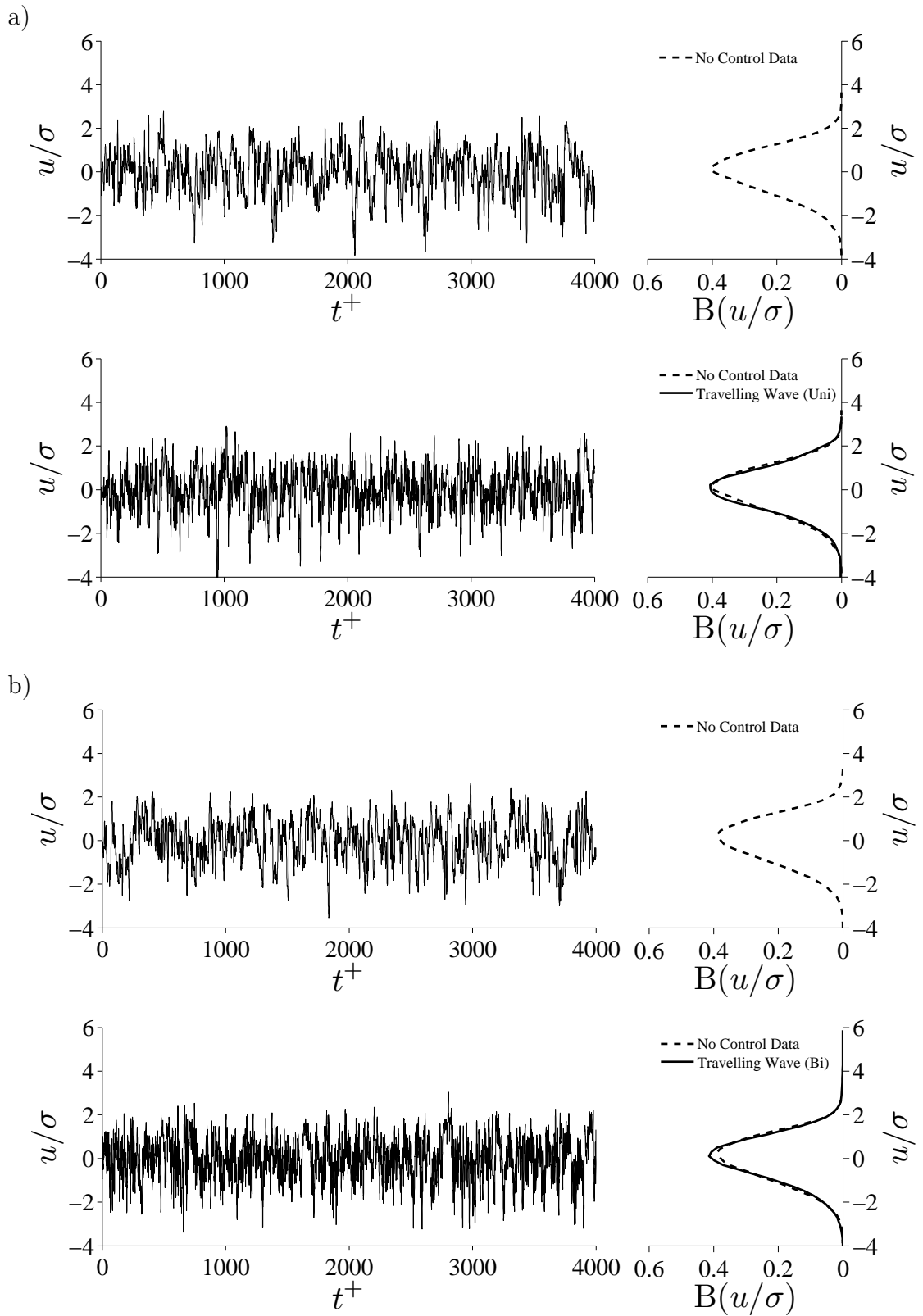


Figure 6.30: Fluctuating streamwise velocity time-series and corresponding PDF at  $y^+ = 60$  with a) unidirectional forcing and b) bidirectional forcing.

VITA technique detects turbulence events (sweep and ejection events), inside the turbulent boundary layer. This is performed by defining a small window,  $T_w$ , which has a typical size of  $T_w^+ = 10$ . This window is moved through the fluctuating  $u$ -component velocity time-series and at each point in the time-series the variance of the signal inside  $T_w$  is calculated. If the variance of the signal inside  $T_w$  is larger than a threshold value, a turbulence event is detected. A review of this technique and other conditional averaging techniques can be found in Antonia (1981).

The local mean,  $\hat{u}(t, T_w)$ , of the fluctuating velocity signal,  $u(t)$ , inside  $T_w$  can be defined as (Bruun, 1995),

$$\hat{u}(t, T_w) = \frac{1}{T_w} \int_{t-\frac{1}{2}T_w}^{t+\frac{1}{2}T_w} u(s) ds. \quad (6.10)$$

The variance of the signal inside  $T_w$  (local variance) can be defined as,

$$\text{Var}(t, T_w) = \hat{u}^2(t, T_w) - [\hat{u}(t, T_w)]^2. \quad (6.11)$$

The variance of the entire signal is defined as,

$$\text{Var}(t) = \lim_{t \rightarrow \infty} \frac{1}{t} \int_0^t u^2(t) dt. \quad (6.12)$$

If the value of the local variance,  $\text{Var}(t, T_w)$  is greater than  $k\text{Var}(t)$ , where  $k$  is a threshold level, then a turbulence event is detected. With this criterion for detection,  $\text{Var}(t, T_w) > k\text{Var}(t)$ , a sweep or an ejection event will be detected. A sweep event is characterised by a positive velocity gradient ( $\frac{du}{dt} > 0$ ) and an ejection event is characterised by negative velocity gradient ( $\frac{du}{dt} < 0$ ). To distinguish between these events, a detector function,  $D(t)$ , was used and defined such that,

$$D(t) = \begin{cases} 1 & \text{if } \text{Var}(t, T_w) > k\text{Var}(t) \text{ and } \frac{du}{dt} > 0 \text{ (sweep event)} \\ 0 & \text{if } \text{Var}(t, T_w) < k\text{Var}(t) \text{ (no event)} \\ -1 & \text{if } \text{Var}(t, T_w) > k\text{Var}(t) \text{ and } \frac{du}{dt} < 0 \text{ (ejection event)} \end{cases} \quad (6.13)$$

In the travelling-wave study, the value of the threshold,  $k$ , was set to 1.2 and the value of  $T_w^+$  was set to 10 (Blackwelder and Kaplan, 1976). To obtain the ensemble-average—a representation of the average VITA event—all events that were detected were averaged over a window with size  $T_{ens}^+$ , where  $T_{ens}^+ > T_w^+$ , with  $T_{ens}^+ = -30$  to 30 in the travelling-wave study. For each VITA event that was detected, the point of detection ( $T_{ens}^+ = 0$ ) was set at the maximum value of  $\frac{du}{dt}$ . One further criterion was added with this VITA scheme and that was to ignore multiple events that were detected inside the ensembling window,  $T_{ens}$ . This was to ensure that packets of turbulence events (Adrian *et al.*, 2000) did not distort the ensemble-average.

In Figure 6.31 and 6.33, the fluctuating  $u$ -component time-series (a), the ratio of local variance to the entire variance of the time-series signal (b) and the detector function of turbulence events (c) can be seen for the no-control data and the unidirectional travelling-wave data respectively at  $y^+ = 5$ . The VITA method of detecting a rapid change in the fluctuating velocity signals can be seen in these two figures, with three sweep events and an ejection event being detected in both figures, 6.31a) and 6.33a).

The individual and ensemble-averaged VITA events for the no-control data can be seen in Figure 6.32. Here, the individual sweep and ejection events are shown by the thin grey lines and the ensemble-average is shown with the thick black line. Sweep events can be seen in Figure 6.32a) and ejection events in Figure 6.32b). In total 32 sweep events and 7 ejection events have been ensemble-averaged in this case, the ratio of sweep and ejection events are a function of wall-normal distance. The individual and ensemble-averaged sweep and ejection

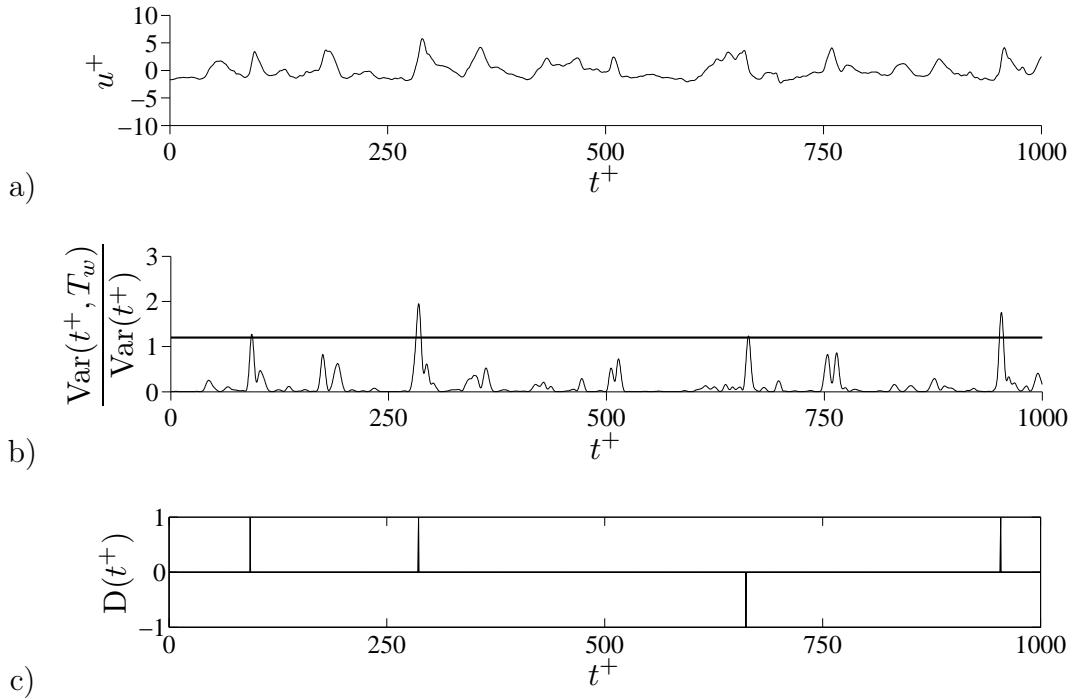


Figure 6.31: No-control data VITA detection at  $y^+ = 5$ . a) Streamwise velocity fluctuation, b) ratio of local variance to the entire signal variance and c) detector function.

events for the unidirectional travelling-wave data can be seen in Figure 6.34a) and b) respectively, where 43 sweep events and 23 ejection events have been ensembled. It should be noted that the detected number of events is of the order 50 and therefore statistically, the ensemble average may not have converged. The VITA analysis for the spanwise travelling waves will focus on sweep events. This is due to sweep events being the major contributor to turbulent skin friction (Kravchenko *et al.*, 1993; Orlandi and Jiménez, 1993).

The VITA events with and without travelling-wave excitation at  $y^+ = 5, 10, 30$  and  $60$  are shown in Figure 6.35a) to d) respectively. The intensity of the sweep has been calculated from the peak to peak value of streamwise velocity of the event and the duration of the sweep event has been calculated from the time separation of the peaks in each sweep signature.

It can be seen in Figure 6.35a) that the intensity of sweep events at  $y^+ = 5$  for both uni and bidirectional forcing have been increased. For uni and bidirectional forcing, the intensity of the sweep event was increased by 34% and 60%

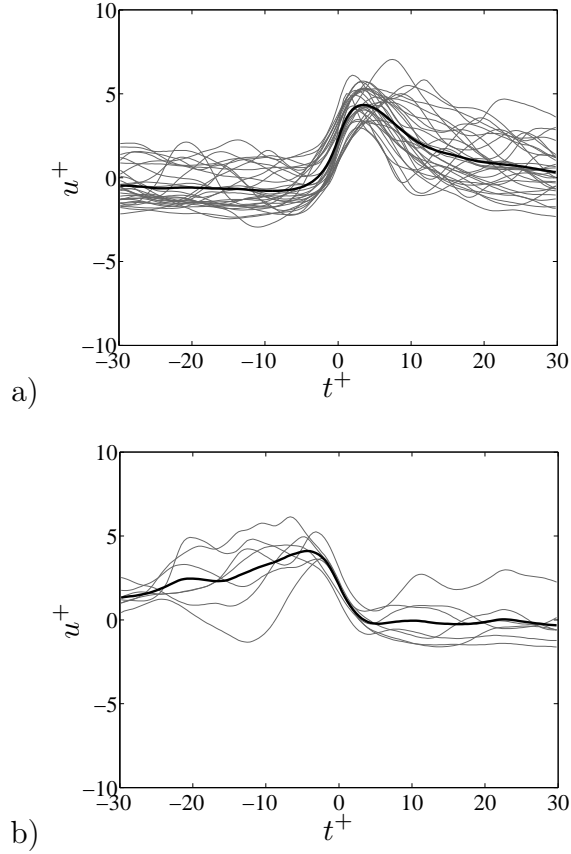


Figure 6.32: No-control data VITA events and ensemble average at  $y^+ = 5$  showing a) sweep events and b) ejection events.

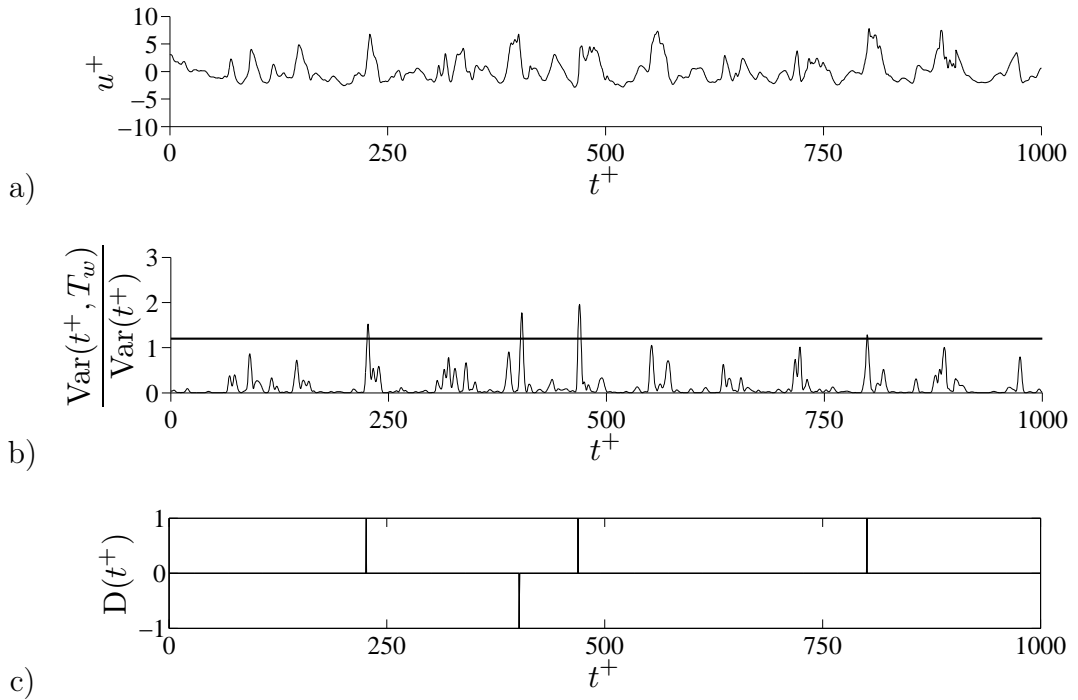


Figure 6.33: Unidirectional VITA detection at  $y^+ = 5$ . a) Streamwise velocity fluctuation, b) ratio of local variance to the entire signal variance and c) detector function.

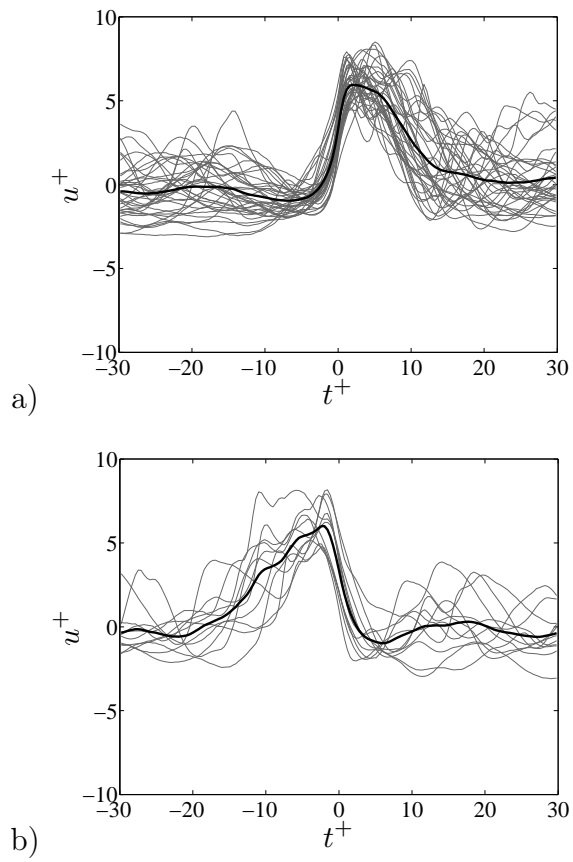


Figure 6.34: Unidirectional VITA events and ensemble average at  $y^+ = 5$  showing a) sweep events and b) ejection events.

respectively and the sweep duration was decreased by 35% and 38% respectively. The increase in sweep intensity at  $y^+ = 5$  is in agreement with the increase in turbulence intensity that has been seen at this location in the boundary layer, §6.2.2.2. It has already been demonstrated that the near-wall region of the turbulent boundary layer has an increase in streamwise velocity. This could be due to the entrainment associated with the plasma actuators and as can be seen in Figure 6.35a), leads to modified sweep events that have greater intensity and most likely causing increased skin friction.

Interestingly, at  $y^+ = 10$  and 30, Figure 6.35b) and c), the intensity of the sweep events for uni and bidirectional forcing have reduced. At  $y^+ = 10$  the reduction in sweep intensity was 10% for both travelling-wave configurations and the sweep duration reduced by 46% and 76% for uni and bidirectional forcing respectively. At  $y^+ = 30$ , the unidirectional travelling wave has reduced sweep intensity and duration by 12% and 57%. The bidirectional travelling wave shows a small increase in sweep intensity of 5% and a reduction in duration of 73%. It is interesting to note that Xu and Choi (2006), who implemented a 4-phase bidirectional travelling wave in a water channel with a Lorentz force found a similar reduction in sweep intensity at  $y^+ = 10$  and 30 in the boundary layer for their skin-friction drag increasing case. At  $y^+ = 60$ , Figure 6.35d), the intensity of the sweep events is increased by 16% and 47% and the duration is reduced by 60% and 70% for uni and bidirectional forcing respectively.

An example of the sweep signature with spanwise wall oscillation, which can achieve up to a 45% reduction in turbulent skin friction, is shown in Figure 6.36 and is taken from Choi and Clayton (2001). There is a strong resemblance (qualitatively) between the shapes of the sweep signature with the mechanical wall oscillation (shown at  $y^+ = 20$ ) and the travelling waves shown in Figure 6.35. This shows great promise that the spanwise travelling waves implemented with DBD plasma are interacting with near-wall turbulence structures to reduce the skin-friction drag. It has been shown throughout the VITA analysis that the

duration of sweep events is largely reduced on application of the spanwise travelling waves. This is a common feature of drag reducing flows. It can be seen in Figure 6.36 taken from Choi and Clayton (2001), that the sweep duration for the mechanical wall oscillation was reduced by nearly 50% when compared with the no-control case. Pang and Choi (2004), who implemented a spanwise oscillation with a Lorentz force in a water channel saw a similar reduction in sweep duration, 50% at  $y^+ = 5$ . A reduction in sweep duration of 50% was observed over riblets by Choi (1989).

The non-dimensional VITA detection frequency as a function of threshold,  $k$ , is plotted in Figure 6.37. Here, the frequency is defined as the total number of sweep events that occur per unit time. Therefore, this will include multiple events that have been discarded in the previous ensemble-average. The results in this figure are similar to the results obtained by Johansson and Alfredsson (1982), where, as the threshold,  $k$ , increases the total number of events decreases in an exponential fashion.

It can be seen for the bidirectional travelling wave, Figure 6.37 (right column), that throughout the turbulent boundary layer more sweep events are detected. At  $y^+ = 5$  and 10, the number of sweep events with travelling-wave excitation was around 2.5 times larger than the no-control flow. At  $y^+ = 30$  and 60, this reduces to around 1.5 times the no-control flow. It should be noted that increased burst frequency is a feature of a drag reduced flow and was observed by Choi (1989) over a riblet surface. It was found that the bursting frequency over a riblet surface was 8 times larger than the canonical flow. It was believed that in this case, the riblets were causing premature sweep events in the turbulent boundary layer. The total number of events for the unidirectional travelling wave, Figure 6.37 (left column), was 3 times the canonical flow at  $y^+ = 5$  and around 2 times the canonical flow at  $y^+ = 10$ . However, at  $y^+ = 30$  and 60, in contrast with the bidirectional travelling wave, the total number of sweep events for travelling-wave excitation and the canonical flow has become equal. Hence, for  $y^+ < 10$

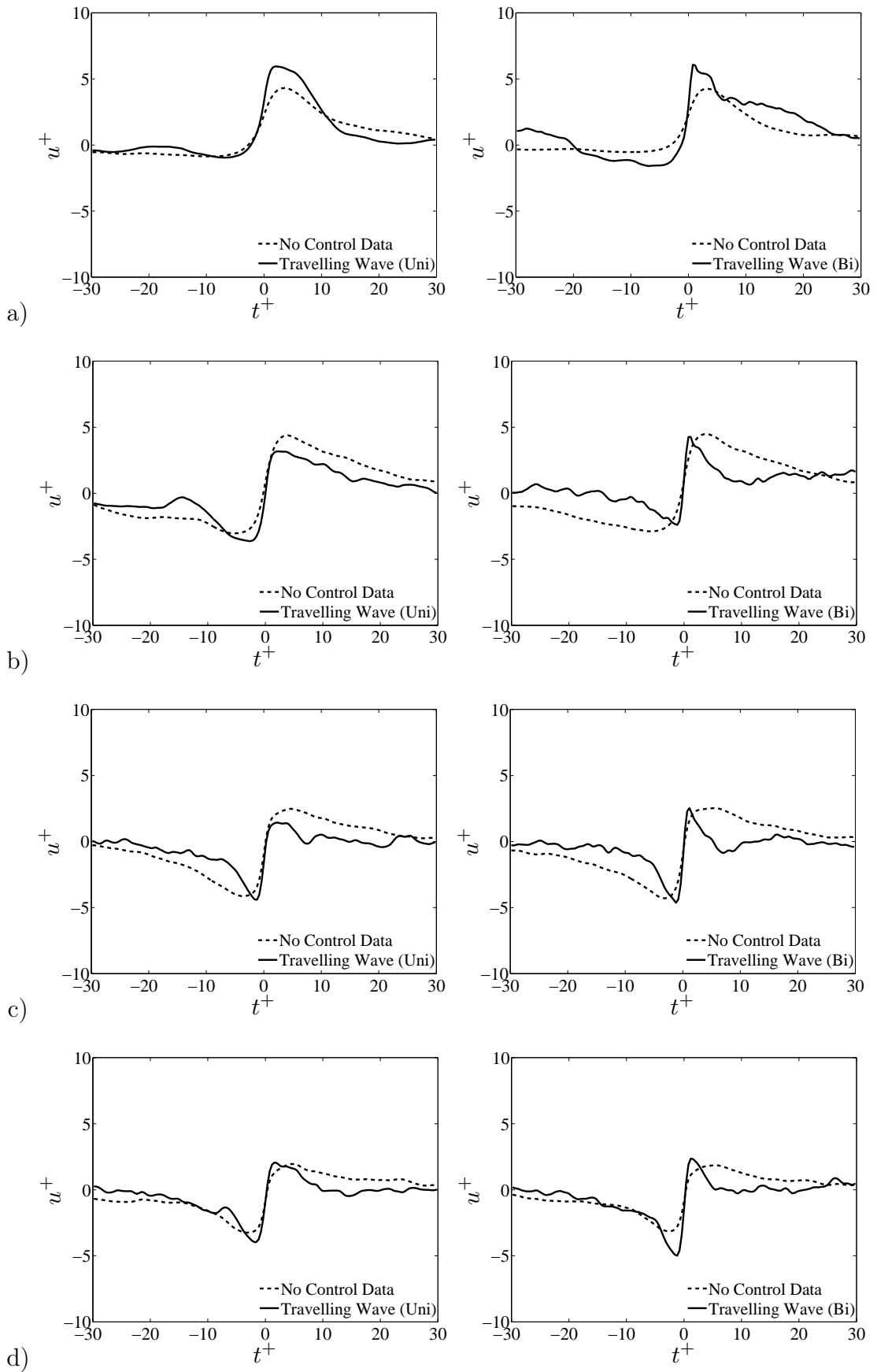


Figure 6.35: Ensemble-averaged VITA events with unidirectional forcing (left column) and bidirectional forcing (right column) at a)  $y^+ = 5$ , b)  $y^+ = 10$ , c)  $y^+ = 30$  and d)  $y^+ = 60$ .

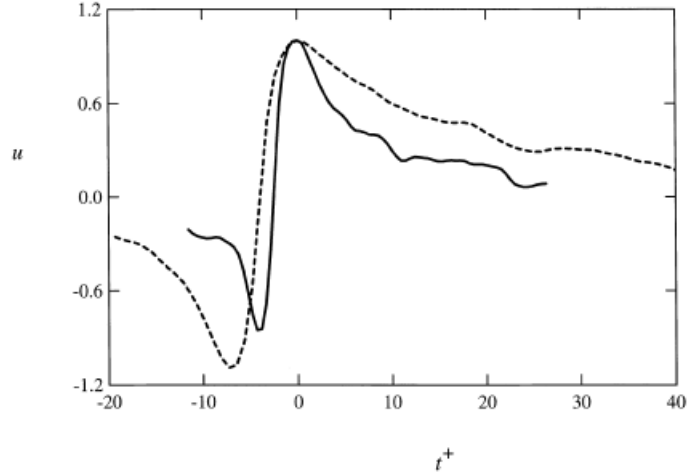


Figure 6.36: An example of VITA for sweep events with an oscillating wall at  $y^+ = 20$ . - - - No-control data and — with wall oscillation. Taken from Choi and Clayton (2001).

for travelling-wave excitations, there was a large increase in the total number of sweep events that have been detected, which have been found to have reduced duration and increased intensity.

### 6.3 Chapter Summary

In this chapter, 4-phase spanwise travelling waves with uni and bidirectional forcing have been applied to the turbulent boundary layer using DBD plasma and studied using hot- and cold-wire anemometry. It has been found that on application of the spanwise travelling waves, the structure of the turbulent boundary layer can be changed up to  $y^+ = 200$ . The unidirectional travelling waves created a streamwise velocity reduction of 10% between  $25 < y^+ < 100$  and the bidirectional travelling waves created a streamwise velocity reduction of 20% between  $25 < y^+ < 200$ . With both forcing configurations, an increase of streamwise velocity has been measured in the near-wall region of the boundary layer ( $y^+ < 10$ ). The turbulence intensity was increased over the majority of the boundary layer, except for unidirectional forcing, where a reduction was observed between  $10 < y^+ < 30$ . Peaks in turbulence intensity were located at  $y^+ = 5$  and  $y^+ = 60$  for both forcing configurations. A comparison has been made with the

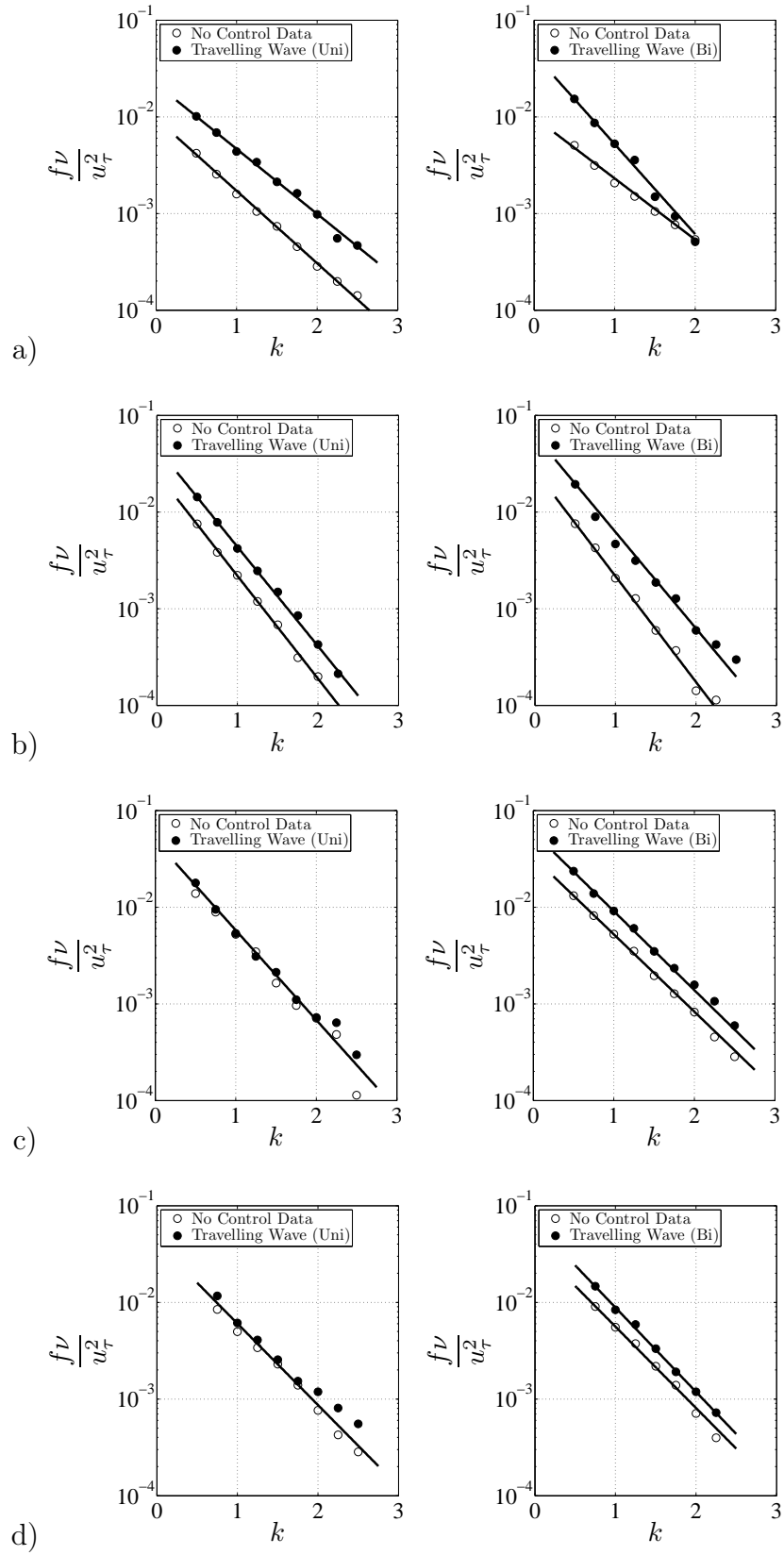


Figure 6.37: Frequency of sweep events as a function of threshold  $k$  for unidirectional forcing (left column) and bidirectional forcing (right column) at a)  $y^+ = 5$ , b)  $y^+ = 10$ , c)  $y^+ = 30$  and d)  $y^+ = 60$ .

study of Jukes (2007) where DBD plasma was used to create a spanwise oscillation in the turbulent boundary layer. Similar increases in turbulence intensity were found in the spanwise oscillation study when the distance between adjacent electrodes was increased. It has been expressed that the increased turbulence intensity in the boundary layer could be due to the strength of the starting vortices created during the spanwise travelling-wave excitation. Hence, lowering the distance between the DBD plasma actuators is thought to reduce the turbulence intensity created and could offer better turbulent boundary-layer control. The canonical data have been compared to those of Schlatter and Örlü (2011) and it has been conjectured that the differences between the data sets could be due to an over-stimulation of the boundary layer due to the turbulent trip (Erm and Joubert, 1991).

It will be shown in Chapter 7, that streamwise vortices are created on application of spanwise travelling waves with DBD plasma in the turbulent boundary layer, which have core locations at  $y^+ = 50$  (Figure 7.14, Chapter 7). It is thought that the streamwise vortices generated on initiation of DBD plasma are lifting low-speed fluid near the wall outwards (upwash) into the logarithmic region causing the reductions in streamwise velocity seen in this hot-wire anemometry study. The downwash of high-speed streamwise velocity into the wall is thought to be due to the downwash associated with the plasma actuators, causing the increased intensity in sweep events and increased streamwise velocity in the near-wall region for both forcing configurations. Hence, it is likely that the downwash of the plasma actuators are causing an increase in skin friction, at least at the measurement locations that have been studied.

A thermal boundary layer was generated on application of DBD plasma inside the turbulent boundary layer. It has been postulated that the thermal boundary layer could have lead to heating of the hot-wire prongs during boundary layer traverses, causing an understimation in the velocity measurements in the near-wall region. Maximum temperature changes of  $1.9^{\circ}\text{C}$  and  $3.75^{\circ}\text{C}$  above ambient

temperature at  $y^+ = 8$  were measured and maximum temperature fluctuations of  $0.6^\circ\text{C}$  and  $1.2^\circ\text{C}$  at  $y^+ = 50$  were measured with uni and bidirectional forcing respectively. Hence, low-speed streamwise velocity, which can be up to  $3.75^\circ\text{C}$  larger than ambient temperature, is being spread in and around the streamwise vortices, leading to maximum temperature fluctuations at the streamwise vortex cores.

# Chapter 7

## PIV Measurements of Spanwise Travelling Waves in the Turbulent Boundary Layer

In this chapter, 4-phase spanwise travelling waves with uni and bidirectional forcing are applied to the turbulent boundary layer. Measurements were obtained using time-resolved 2D and stereoscopic PIV. A time-resolved phase-average over one travelling wave forcing period will be presented along with time- and spanwise-averaged data for both forcing configurations. This will allow the changes in turbulent boundary-layer structure throughout the four phases of the spanwise travelling waves to be seen. For all experiments presented, the free-stream velocity,  $U_\infty$ , was set to 1.7 m/s producing a boundary-layer thickness,  $\delta$ , of 90 mm. The Reynolds numbers based on momentum thickness,  $Re_\theta = \frac{U_\infty \theta}{\nu}$  and friction velocity,  $Re_\tau = \frac{u_\tau \delta}{\nu}$ , were 1024 and 435 respectively. The data presented have been scaled with friction velocity,  $u_\tau$  and kinematic viscosity,  $\nu$ . For the boundary-layer tests presented the travelling waves were generated with a wavelength,  $\lambda$ , of 100 mm ( $\lambda^+ = \frac{\lambda u_\tau}{\nu} = 500$ ) and with a time period,  $T$ , of 208 ms ( $T^+ = \frac{T u_\tau^2}{\nu} = 82$ ). The travelling waves were generated with fixed amplitude by applying a voltage,  $E$ , of 7 kV<sub>p-p</sub> at a frequency,  $f$ , of 25 kHz to each DBD plasma

actuator on the travelling-wave actuator sheet. Hence, the spanwise travelling waves studied in Chapter 6 using hot-wire anemometry are the same spanwise travelling wave that are being studied in this chapter using PIV.

## 7.1 Phase-averaged PIV Measurements

It has been shown in Chapter 5 that a spanwise travelling wave with uni and bidirectional forcing can be generated with DBD plasma in quiescent air. In this section, the spanwise travelling waves that were generated in quiescent air are applied to the turbulent boundary layer. Measurements were taken in the  $x$ - $z$  and  $z$ - $y$  planes of the turbulent boundary layer using 2D and stereoscopic PIV respectively.

The  $x$ - $z$  plane measurements were taken at a wall-normal distance,  $y$ , of 1 mm ( $y^+ = 5$ ), within the viscous sublayer, parallel to the wall. This was very close to the wall of the boundary layer and alignment of the laser sheet parallel to the surface without glare from the copper electrodes or white Mylar surface was crucial. The travelling-wave actuator sheets were bonded to a Perspex substrate that was 10 mm thick using double sided adhesive tape. The perspex used in this study varied by around 200  $\mu\text{m}$  (in thickness) across the total length of the actuator sheet (408 mm). The travelling-wave actuator sheet and test plate were flush mounted into the wind tunnel by four thumb screws. This allowed fine adjustment of the actuator sheet with the wind tunnel test surface and also to the parallel laser light sheet. In addition, the laser head was mounted on a custom made traverse system that allowed the adjustment of the laser sheet in the wall-normal direction (parallel to the wall) by two screw threads. The combination of the thumb screws that flush mounted the travelling-wave actuator sheet into the wind tunnel and the custom made traverse for the laser head allowed the light sheet to be kept close and parallel to the wall with an accuracy of  $\pm 0.5$  mm ( $\pm 2.5$  wall units). PIV images were taken prior to measurements to

ensure that glare from the surface was not an issue. It was important to ensure that the laser sheet was well focused to a nominal 1 mm thickness ( $y^+ = 5$ ) over the measurement region. As the light sheet had a finite thickness, data would be phase-averaged through the light sheet thickness. Before and after the measurement region, the laser sheet would diverge and cause glare from the actuator surface.

The travelling-wave actuator sheet, §5.1, had 24 electrodes which enabled spanwise travelling waves over three wavelengths,  $3\lambda$  ( $\lambda = 100$  mm,  $\lambda^+ = 500$ ), to be generated. Each actuator, and hence travelling wave, had an active length of  $x = 336$  mm ( $x^+ = 1720$ ). The 2D PIV presented in the  $x$ - $z$  plane has a field of view of 100 mm x 100 mm (500 x 500 wall units), or  $1\lambda^+ \times 1\lambda^+$  and positioned such that  $(x^+, z^+) = (250, 250)$  was the centre of the travelling-wave actuator sheet. The measurements in the  $z$ - $y$  plane of the turbulent boundary layer are performed using stereoscopic PIV. The stereoscopic PIV presented has a field of view of 100 mm x 40 mm (500 x 200 wall units), or  $1\lambda^+ \times 0.4\lambda^+$  and positioned such that  $(z^+, y^+) = (250, 0)$  was the centre of the travelling-wave actuator sheet with  $y^+ = 0$  being the location of the wall. With respect to the  $x$ - $z$  plane measurements, the measurements in the  $z$ - $y$  plane are taken at  $x^+ = 200$ . For the boundary-layer tests presented the travelling waves were actuated over the entire  $3\lambda^+$ . Unidirectional forcing requires 12 of the 24 electrodes (1 actuator per phase through 4-phases over 3 wavelengths) and 8 plasma power supplies and bidirectional forcing requires 24 of the 24 electrodes (2 actuator per phase through 4-phases over 3 wavelengths) and 12 plasma power supplies. For each experiment, the spanwise travelling waves were actuated continuously for 14 forcing periods,  $14T^+$ . Data were acquired with a frequency of 750 Hz for the last 3 of the 14 forcing periods. This sampling rate provided 156 realisations over each forcing period. Each experiment was repeated 17 times, capturing in total 51 forcing periods. A phase-average over the 51 forcing periods was performed. This allowed a time-resolved phase-average over one forcing period with spanwise travelling-

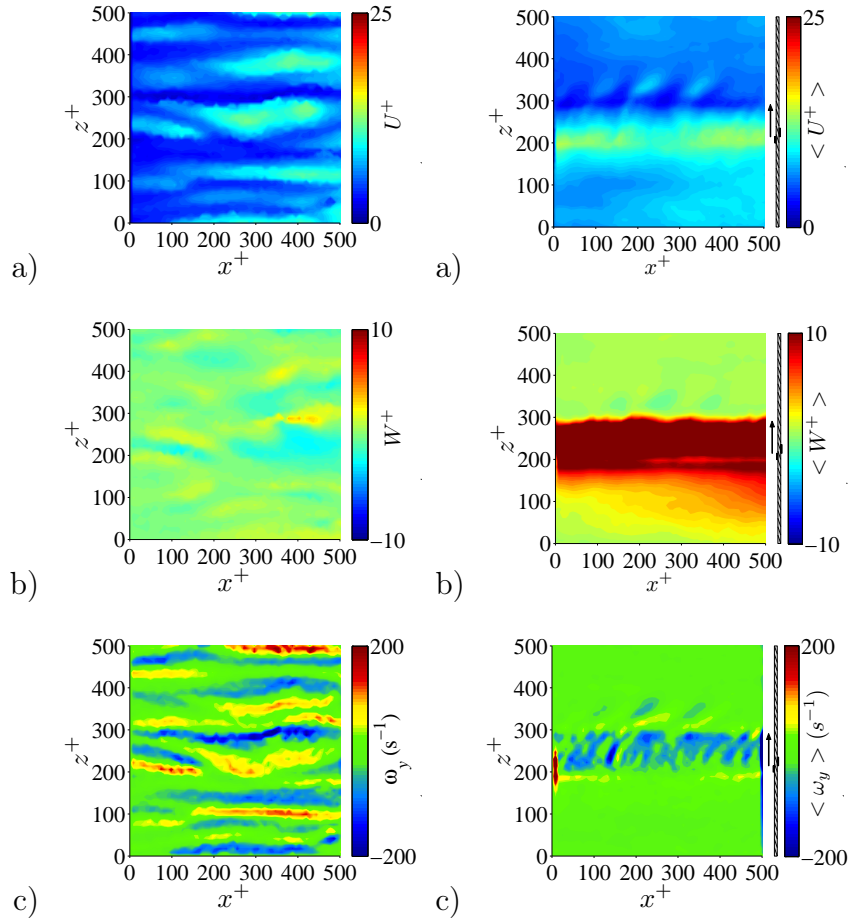


Figure 7.1: A comparison of instantaneous canonical flow (left column) and unidirectional forcing (right column) at  $\frac{1}{2}T^+$  in the  $x$ - $z$  plane of a turbulent boundary layer at  $y^+ = 5$  with a) streamwise velocity, b) spanwise velocity and c) wall-normal vorticity.  $\lambda^+ = 500$ ,  $T^+ = 82$ .

wave excitation, enabling the changes in turbulent boundary-layer structure to be seen.

### $x$ - $z$ Plane Measurements with Unidirectional Forcing

Presented in Figure 7.1 is a comparison between canonical flow and the changes in turbulent boundary-layer structure on application of a 4-phase unidirectional spanwise travelling wave in the  $x$ - $z$  plane at  $y^+ = 5$ . Figure 7.1a) (left column) shows an instantaneous snapshot of streamwise velocity in the viscous sublayer. The boundary-layer flow direction is from left to right. The existence of low- and high-speed streaks (Kline *et al.*, 1967; Kim *et al.*, 1971) can clearly be seen, which appear to have a characteristic spacing of  $z^+ = 100$  (Smith and Metzler, 1983).

These streaks if viewed temporally would be seen meandering through the flow and would eventually disappear from the viewing plane at  $y^+ = 5$ . It is known that the near-wall streaks are lifted away from the wall and dissipated in the outer regions of the boundary layer as part of the bursting process (Schoppa and Hussain, 2002). The low- and high-speed streaks are thought to be due to the induction of the legs of hairpin vortices present in the turbulent boundary layer (Offen and Kline, 1975; Robinson, 1991; Adrian, 2007). Low-speed fluid (the low-speed streaks) is collected on the upwash side of hairpin legs, the so called quasi-streamwise vortices —although quasi-streamwise vortices do not necessarily exist in pairs (Robinson, 1991)—, and the high-speed fluid (high-speed streaks) caused by the downwash side of hairpin legs. The downwash of high-speed fluid from the outer regions of the boundary layer being a major contributor to turbulent skin friction (Kravchenko *et al.*, 1993; Orlandi and Jiménez, 1993).

On application of the unidirectional travelling wave, Figure 7.1a) (right column), there is a very different picture when compared to the canonical case. In this image, the boundary-layer flow is moving in the positive  $x$ -direction and the travelling wave is moving in the positive  $z$ -direction. The position of the activated plasma actuator can be seen on the right hand side of the image. The data presented are the phase-averaged streamwise velocity at the end of phase (ii) at  $\frac{1}{2}T^+$ . It can be seen that when the unidirectional travelling wave is applied, the near-wall structure is changed. Some of the low- and high-speed streaks of the canonical flow have been eliminated and replaced by a wide ribbon of low-speed fluid that is being pushed in the positive  $z$ -direction. The low-speed ribbon extends for around 100 wall units in the spanwise direction in this case and is persistent along the streamwise direction. It is important to note, however, that not all the near-wall streaks can be eliminated otherwise turbulence would not be able to sustain itself (Jiménez and Pinelli, 1999). The elimination of the near-wall streaky structure into a wide ribbon of low-speed fluid on application of a spanwise travelling wave has been found numerically (Du and Karniadakis, 2000;

Du *et al.*, 2002) and experimentally (Xu and Choi, 2006) leading to a 30% reduction in turbulent skin friction. Du *et al.* (2002) from their numerical simulations believe that the mechanism of the turbulent boundary-layer control with a spanwise travelling wave is the stabilisation of the near-wall streaks which leads to changes in the turbulence regeneration cycle. With the changes to the canonical flow that have been shown in Figure 7.1a), it would appear that the unidirectional spanwise travelling wave with DBD plasma is acting in a similar fashion to the previous Lorentz force studies (Du and Karniadakis, 2000; Du *et al.*, 2002; Xu and Choi, 2006).

From the canonical data, it can be seen that there is little spanwise velocity, 7.1b), in the near-wall region of the turbulent boundary layer. In Figure 7.1c), the wall-normal vorticity effectively shows the locations of the low- and high speed-streaks that have been discussed in Figure 7.1a). The unidirectional travelling wave introduces a strong spanwise component of velocity in the near-wall region, Figure 7.1b). This high-speed region of spanwise velocity extends for over 100 wall units and is due to the spanwise forcing of the plasma actuator. As the unidirectional travelling wave is applied and the low-speed streaks amalgamated, there is a large change in wall-normal vorticity, Figure 7.1c). The wall-normal vorticity is largely confined to  $200 < z^+ < 300$ , which is over the low- and high-speed ribbon formed by the actuation of DBD plasma. As the travelling wave has eliminated some of the near-wall streaks, wall-normal vorticity cannot be seen over the entire measurement region. The magnitude of the wall-normal vorticity generated by the unidirectional forcing is on the same order as the canonical data ( $200 \text{ s}^{-1}$ ) and is less spread in the spanwise direction. This could be an indication that the wall-normal vorticity at  $y^+ = 5$  is reduced by the unidirectional travelling wave.

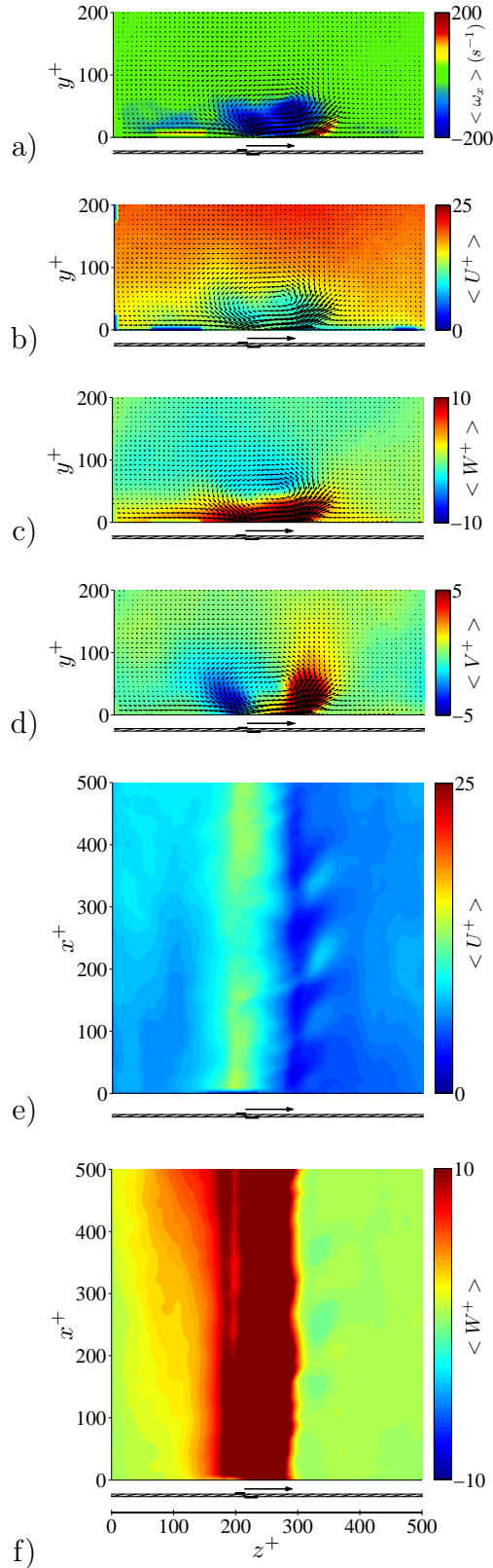


Figure 7.2: A comparison of data in the  $z$ - $y$  and  $x$ - $z$  planes at  $\frac{1}{2}T^+$  with unidirectional forcing in a turbulent boundary layer showing a) streamwise vorticity ( $z$ - $y$  plane), b) streamwise velocity ( $z$ - $y$  plane), c) spanwise velocity ( $z$ - $y$  plane), d) wall-normal velocity ( $z$ - $y$  plane), e) streamwise velocity ( $x$ - $z$  plane) and f) spanwise velocity ( $x$ - $z$  plane).  $\lambda^+ = 500$ ,  $T^+ = 82$ .

## ***z-y* Plane Measurements with Unidirectional Forcing**

The  $x$ - $z$  plane data with unidirectional forcing that have been presented in Figure 7.1 is compared with  $z$ - $y$  plane data in Figure 7.2. In Figure 7.2, the boundary-layer flow is in the positive  $x$ -direction and the travelling wave is moving in the positive  $z$ -direction. With the  $z$ - $y$  plane measurements, the boundary-layer flow is moving into the plane of the paper and images are taken at a streamwise distance of  $x^+ = 200$  in relation with the  $x$ - $z$  plane data. Figure 7.2a) shows streamwise vorticity in the  $z$ - $y$  plane of the turbulent boundary with unidirectional forcing. A streamwise vortex can be seen by the strong negative vorticity with arrows of  $V$  and  $W$  components of velocity. There appears to be two distinct regions of negative vorticity. The negative vorticity on the left hand side of the streamwise vortex is due to the vorticity generated from the previous phase of forcing, hence, the streamwise vortex from phase (i) in this case. The vorticity on the right of the streamwise vortex is due to the vorticity generated from the current phase of forcing, phase (ii). During forcing over the phase, the two streamwise vortices coalesce to create the single streamwise vortex shown in Figure 7.2a). This confirms that on application of DBD plasma in the turbulent boundary layer, the starting vortex still remains in the flow. From herein as the starting vortex is inside the turbulent boundary layer, it will be referred to as a streamwise vortex. The streamwise vortex generated during unidirectional forcing is entraining low-speed streamwise velocity from the near-wall region into the core of the streamwise vortex and around its periphery, Figure 7.2b). The wall-normal velocity distinguishing the areas of upwash and downwash can be found in Figures 7.2d). The streamwise velocity data in the  $x$ - $z$  plane can be found in Figures 7.2e), where a low-speed ribbon can be seen. Behind the head of the travelling-wave front (or above the plasma actuator), there is a region of high-speed streamwise velocity. The region of high-speed fluid coincides with the region of downwash, Figure 7.2d), from the plasma actuator. The spanwise velocity generated during the travelling-wave excitation can be found in Figure 7.2c)

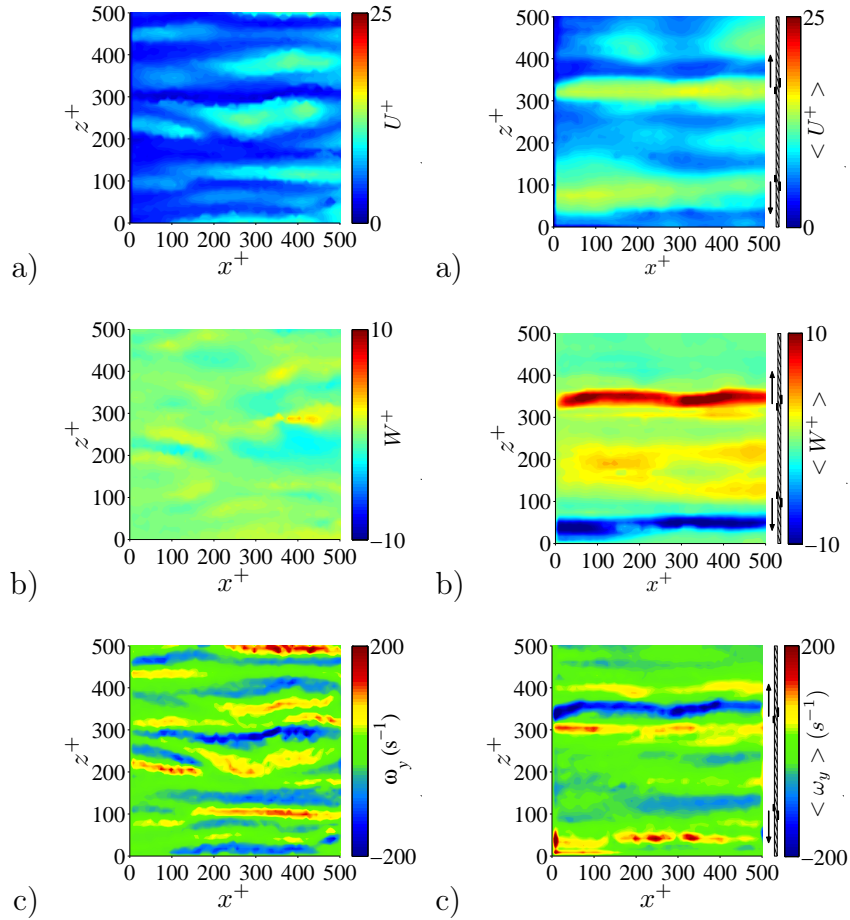


Figure 7.3: A comparison of instantaneous canonical flow (left column) and bidirectional forcing (right column) at  $\frac{3}{4}T^+$  in the  $x$ - $z$  plane of a turbulent boundary layer with a) streamwise velocity, b) spanwise velocity and c) wall-normal vorticity.  $\lambda^+ = 500$ ,  $T^+ = 82$ .

and f). The spanwise velocity emanates from the plasma actuator and typically extends in the boundary layer up to  $y^+ = 50$ .

### $x$ - $z$ Plane Measurements with Bidirectional Forcing

A comparison of a bidirectional travelling wave and canonical flow can be found in Figure 7.3. The boundary-layer flow is in the positive  $x$ -direction and the travelling-wave direction is in the positive  $z$ -direction. For the bidirectional travelling wave (right column), the plasma is actuated in two opposite directions per phase. The directions in which the plasma actuators are fired can be found on the right hand side of the images. The bidirectional travelling-wave images are taken at the end of phase (iii) at  $\frac{3}{4}T^+$ . There are similarities with the uni and

bidirectional travelling-wave excitations. It can be seen in Figure 7.3a), that the near-wall streaky structure inside the viscous sublayer is substantially altered when compared with the canonical case. There is again an elimination of some naturally occurring low- and high-speed streaks in the near-wall region and instead, a region of low-speed fluid can be seen moving in the positive  $z$ -direction at  $z^+ > 350$ . There is a region of low-speed streamwise velocity entering the image at  $z^+ < 50$  which is the low-speed fluid that was collected during the same forcing period from the first wavelength on the travelling-wave sheet. The collected low-speed fluid at  $z^+ < 50$  is being pushed upwards in the positive spanwise direction ready for the next forcing period to transport it further in the positive spanwise direction. Similar to unidirectional forcing, there are regions of high-speed streamwise velocity above the plasma actuators,  $z^+ = 100$  and  $z^+ = 300$ .

The bidirectional travelling wave requires the plasma to activate in two opposite directions per phase. This causes spanwise velocity to emanate away from the regions of the plasma actuators in two opposite directions, Figure 7.3b) (right column). The spanwise extent of the spanwise velocity and regions of low-speed streamwise velocity are around 50 wall units, which is typically half of the footprint of the low- and high-speed streamwise and spanwise velocity regions found with unidirectional forcing. Two bands of wall-normal vorticity of different sign can be seen in Figure 7.3c) (right column). The changes in wall-normal vorticity can be found at  $300 < z^+ < 400$  and  $z^+ < 100$ , where bands of thin strips of positive and negative wall-normal vorticity can be seen. Similar to unidirectional forcing, it appears that the magnitude of wall-normal vorticity with bidirectional forcing and canonical flow is of the same order, typically  $200 \text{ s}^{-1}$ . From observation of Figure 7.3c) (right column) it would appear that bidirectional forcing creates less wall-normal vorticity than the canonical flow. This is because the regions of wall-normal vorticity are located around the regions of high- and low-speed streamwise velocity. The bidirectional travelling wave has removed some of

the naturally occurring low- and high-speed streaks, resulting in less wall-normal vorticity over the entire measurement region.

### ***z-y* Plane Measurements with Bidirectional Forcing**

Figure 7.4 compares *x-z* and *z-y* plane data with bidirectional forcing at  $\frac{3}{4}T^+$ . The boundary-layer flow is in the positive *x*-direction and the travelling wave is moving in the positive *z*-direction. With the *z-y* plane measurements, the boundary-layer flow is moving into the plane of the paper and images are taken at a streamwise distance of  $x^+ = 200$  with respect to the *x-z* plane data. Streamwise vortices can be seen in Figure 7.4a) when the bidirectional travelling wave is applied to the turbulent boundary layer. Above the plasma actuator that is firing at  $z^+ = 325$ , there is a co-rotating streamwise vortex illustrated by negative vorticity and a counter-rotating vortex (positive vorticity) that is being lifted by the co-rotating vortex. Throughout the text, the co-rotating streamwise vortex is the streamwise vortex which has negative vorticity and is travelling in the direction of the travelling wave (positive *z*-direction). The counter-rotating streamwise vortex is the streamwise vortex which has positive vorticity and is travelling in the opposite direction to the travelling wave. This scenario of co- and counter-rotating vortices lifting one another away from the wall was found in quiescent air in Chapter 5 with bidirectional forcing. There is another counter-rotating vortex that has developed on the left hand side of the image at  $z^+ = 75$ , as with bidirectional forcing there are two DBD plasma actuators fired each phase. Similar to unidirectional forcing, the streamwise vortex is lifting low-speed streamwise velocity from the near-wall region out into the boundary layer, Figure 7.4b), and spreading low-speed streamwise velocity in the near-wall region, Figure 7.4e). Another similarity with the unidirectional forcing is the two distinct regions of negative vorticity around the co-rotating streamwise vortex. Again, the negative vorticity on the left hand side of the streamwise vortex is due to the vorticity generated from the previous phase of forcing, hence, the streamwise vortex from

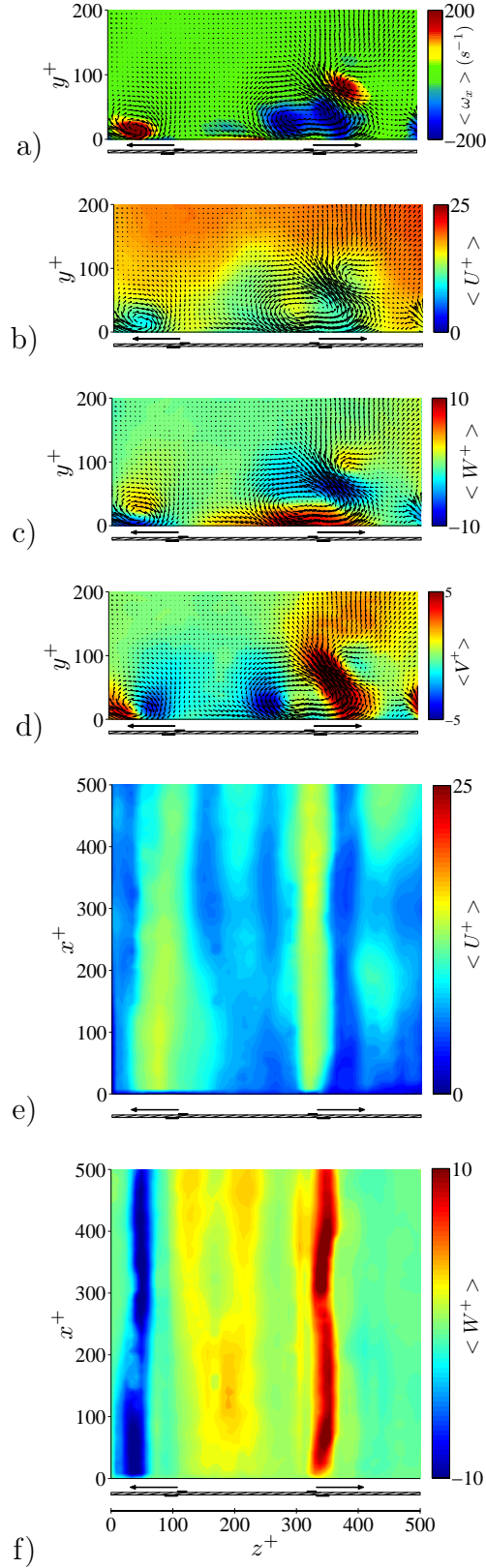


Figure 7.4: A comparison of data in the  $z$ - $y$  and  $x$ - $z$  planes at  $\frac{3}{4}T^+$  with bidirectional forcing in a turbulent boundary layer showing a) streamwise vorticity ( $y$ - $z$  plane), b) streamwise velocity ( $y$ - $z$  plane), c) spanwise velocity ( $y$ - $z$  plane), d) wall-normal velocity ( $x$ - $z$  plane), e) streamwise velocity ( $x$ - $z$  plane) and f) spanwise velocity ( $x$ - $z$  plane).  $\lambda^+ = 500$ ,  $T^+ = 82$ .

phase (ii) in this case. The vorticity on the right of the streamwise vortex is due to the vorticity generated from the current phase of forcing, phase (iii). During forcing over the phase, the two streamwise vortices coalesce to create the single (although elongated) streamwise vortex shown in Figure 7.4a). Spanwise velocity in the  $z$ - $y$  plane is coinciding with the spanwise velocity in the  $x$ - $z$  plane, Figure 7.4c) and f) which again extends to  $y^+ = 50$ . There are regions of negative spanwise velocity in the  $z$ - $y$  plane located at  $z^+ = 50$  and  $350$  with the bidirectional forcing due to the induction of the streamwise vortices. The wall-normal velocity in the  $z$ - $y$  plane is shown in Figure 7.4d) where the location of negative (downwash) wall-normal velocity closely corresponds to the locations of increases in streamwise velocity in the  $x$ - $z$  plane, Figure 7.4e).

## Comparison with Lorentz Forcing

Images taken from Karniadakis and Choi (2003) can be found in Figure 7.5, with Figure 7.5a) showing the instantaneous streamwise velocity during a bidirectional spanwise travelling wave implemented with a Lorentz force studied numerically using DNS. A bidirectional travelling wave with Lorentz forcing has obtained a skin-friction drag reduction on the order of 30% (Du and Karniadakis, 2000; Du *et al.*, 2002). Figures 7.1a) and 7.3a) of the uni and bidirectional travelling waves with DBD plasma and Figure 7.5a) of a bidirectional travelling wave with a Lorentz force show similar near-wall streamwise velocity distributions. With the DBD plasma forcing, the travelling waves are collecting and spreading the near-wall low-speed streamwise velocity in the spanwise direction, which is in line with the presented DNS results. Therefore, it would be expected that the DBD plasma forcing is interacting with the turbulent structures to reduce turbulent skin friction by stabilising the near-wall streaks leading to changes in the turbulence regeneration cycle (Du *et al.*, 2002). There are regions of high-speed streamwise velocity transferring momentum to the wall with DBD plasma forcing, which could be increasing turbulent skin friction locally. Spanwise velocity distri-

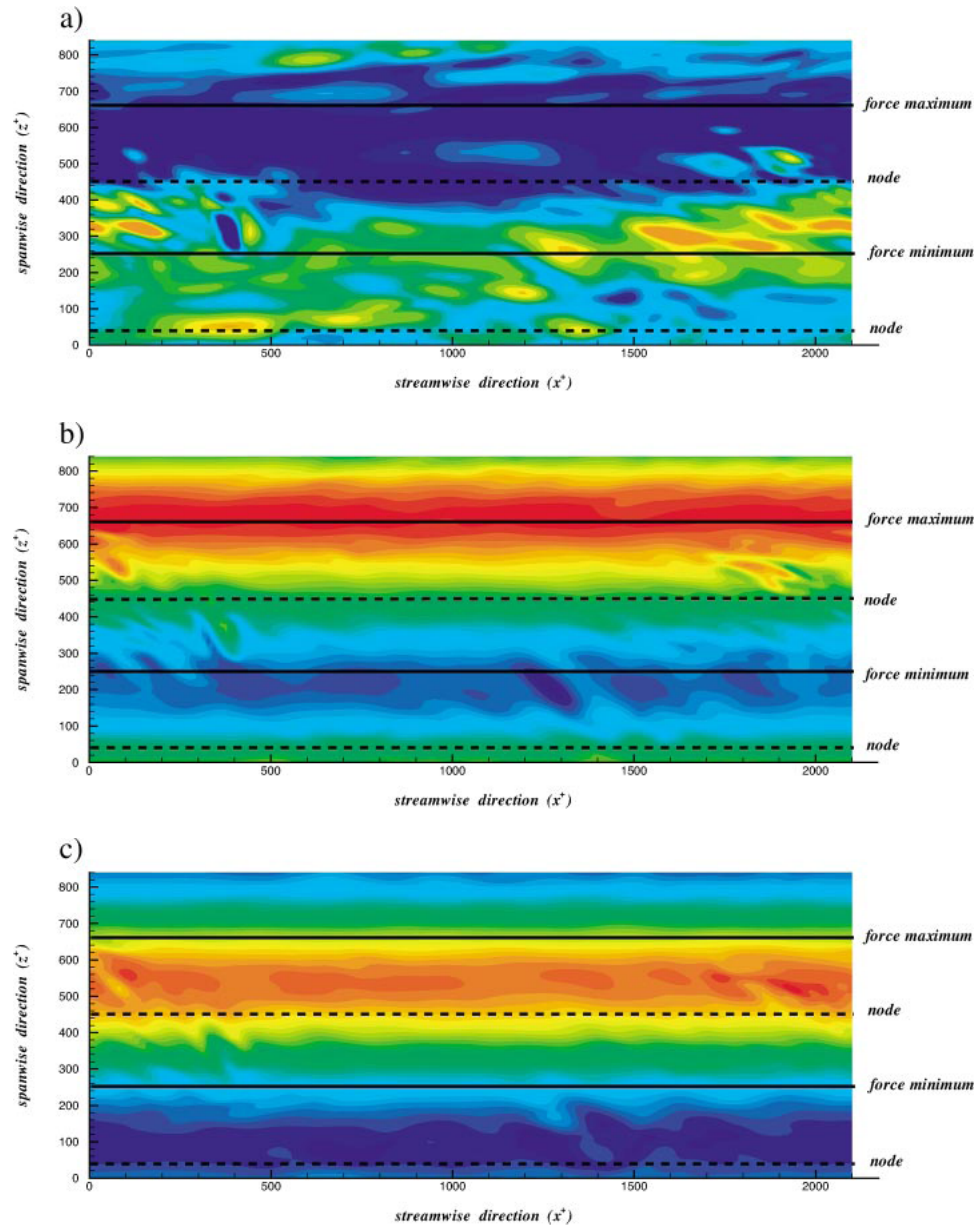


Figure 7.5: Visualisation of instantaneous a) streamwise velocity, b) streamwise vorticity and c) spanwise velocity at  $y^+ = 4$  from the wall controlled by a transverse travelling wave. High values (red), low (or negative) values (blue). Taken from Karniadakis and Choi (2003).

butions with the uni and bidirectional forcing can be found in Figures 7.1b) and 7.3b) and with Lorentz forcing in Figure 7.5c). Further similarities between DBD plasma and Lorentz forcing exist. The regions of high-speed spanwise velocity and the locations of the wide ribbons of low-speed fluid coincide. The exception is that the region of low-speed fluid has spread over typically 100 wall units in the spanwise direction for DBD plasma forcing. Whereas, the Lorentz forcing spreads the low-speed streaks over typically 200 wall units. This could be due to the difference in control parameters that have been employed between the DBD plasma forcing and Lorentz forcing travelling wave. The span of the low-speed ribbon with DBD plasma could also be inhibited by the high-speed region of entrained fluid above the plasma actuator. Regions of high-speed fluid above the region of forcing are not apparent in the Lorentz forcing travelling wave. Furthermore, Lorentz and plasma forcing are fundamentally different. The Lorentz force is maximum at the wall and decays exponentially, whereas on initiation of DBD plasma, a starting vortex is created which leads to the production of a laminar wall jet under continual forcing. The similarity between the DBD plasma forcing and Lorentz forcing travelling waves shows that DBD plasma has the ability to modify the near-wall turbulence of the turbulent boundary layer positively. The amalgamation of low-speed streaks into wide ribbons of low-speed fluid is clearly apparent and has been shown by Du *et al.* (2002) to lead to reductions in turbulent skin friction of up to 30% when the control parameters have been optimised.

### **Skin-friction Signature**

The data that have been taken on the  $x$ - $z$  plane of the turbulent boundary layer is located within the viscous sublayer,  $y^+ = 5$ . This is very close to the wall, to the extent where the distribution of velocity could represent the skin-friction signature on the wall (Choi *et al.*, 2011). Presented in Figure 7.6 is the stream-wise velocity (left column), spanwise velocity (middle column) at  $y^+ = 5$  and

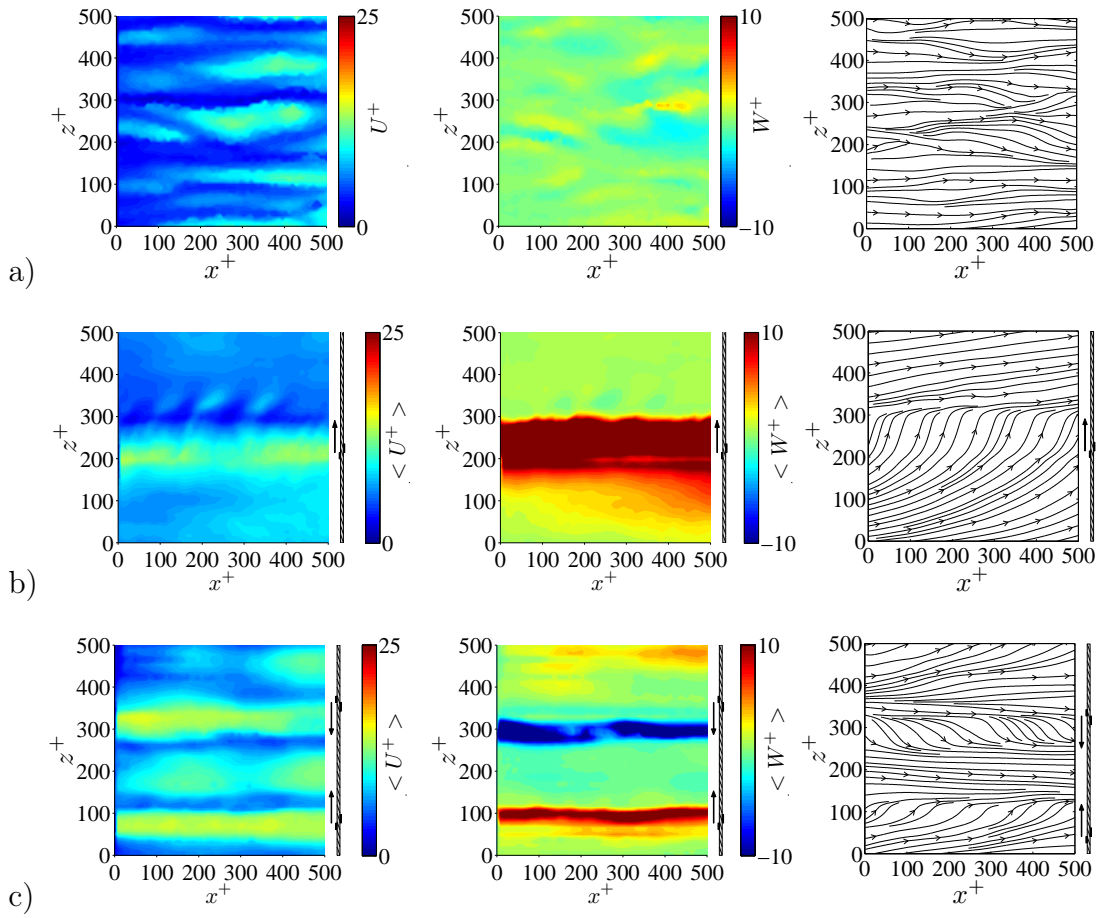


Figure 7.6: Streamwise velocity (left column), spanwise velocity (middle column) and a representation of the skin-friction field (right column) a) canonical data, b) unidirectional travelling wave ( $\frac{1}{2}T^+$ ) and c) bidirectional travelling wave ( $\frac{1}{4}T^+$ ).

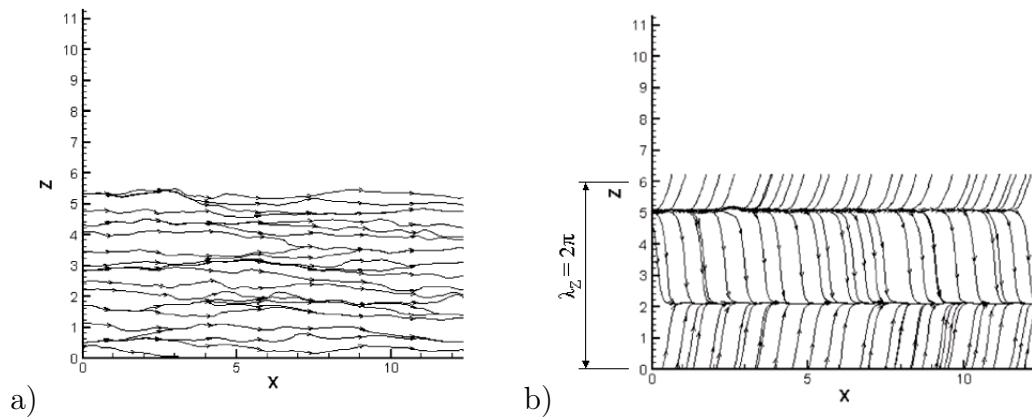


Figure 7.7: Instantaneous skin-friction field taken from Zhao *et al.* (2004) with a) no-control and b) spanwise travelling-wave control. Vector lines of  $|\tau_w|$ .

a representation of the skin-friction signature (right column) on the wall in the  $x$ - $z$  plane of a turbulent boundary layer for a) canonical data, b) a unidirectional travelling wave and c) a bidirectional travelling wave. The lines to represent the skin-friction signature have been generated by computing the streamlines from the  $U$  and  $W$  velocity components at  $y^+ = 5$ . Figure 7.6a) represents the streamwise velocity, spanwise velocity and corresponding skin-friction signature over the turbulent boundary layer wall with no-control. With the streamwise velocity data, the near-wall streaky structure can easily be seen meandering through the flow in the near-wall region. The corresponding representation of the skin-friction signature appears sporadic with vectors straying in both the positive and negative spanwise directions. On application of the unidirectional travelling wave, Figure 7.6b), the near-wall streaky structure is annihilated leaving a large ribbon of low-speed fluid being pushed in the positive spanwise direction at the head of the travelling wave. There is a high-speed region behind the head of the travelling wave pushing the low-speed ribbon in the spanwise direction. The representation of the skin-friction signature with unidirectional forcing shows large changes when compared with the canonical data. The skin-friction signature has been heavily twisted in the spanwise direction due to the spanwise forcing of the travelling wave. The skin-friction signature is no longer sporadic, it has become regularised due to the unidirectional forcing. The representation of the canonical and unidirectional skin-friction signature is qualitatively similar to the DNS results of Zhao *et al.* (2004), who obtained a skin-friction drag reduction on the order of 30% using a spanwise travelling wave implemented by a flexible wall. An example of the skin-friction signature obtained by Zhao *et al.* (2004) is shown in Figure 7.7. Figure 7.7a) shows the skin-friction field on an uncontrolled wall, which appear remarkably similar to the canonical case presented in Figure 7.6a). It appears using the  $U$  and  $W$  velocity components to compute streamlines at  $y^+ = 5$  produces a reasonable estimation of the skin-friction signature on the wall of the turbulent boundary layer. Note that in these figures, the low-speed

regions (blue) would correspond to low skin friction and high-speed regions (red) would correspond to high skin friction. Figure 7.7b) shows the skin-friction field of a spanwise travelling wave implemented using a flexible wall. In this figure, the travelling wave produced a near sinusoidal near-wall spanwise velocity distribution which had a wavelength,  $\lambda_z$ , of  $2\pi$  in the DNS simulation as indicated in Figure 7.7. The skin-friction signature of Zhao *et al.* (2004) has been twisted in both the positive and negative spanwise directions due to the positive and negative spanwise velocities introduced by the flexible wall. The representation of the skin-friction signature with the unidirectional spanwise travelling wave resembles half of the skin-friction signature of Zhao *et al.* (2004), as there is forcing in one direction only. The representation of skin-friction signature with the bidirectional spanwise travelling wave is presented in Figure 7.6c). As bidirectional forcing creates forcing in two opposing directions, the representation of the skin-friction signature is twisted in both the positive and negative spanwise directions, qualitatively similar to the skin-friction field of Zhao *et al.* (2004) with a flexible wall, Figure 7.7b).

## Transient Behaviour with Unidirectional Forcing

The development through phases (i) to (iv) of the phase-averaged streamwise velocity, spanwise velocity and wall-normal vorticity with a unidirectional travelling wave can be found in Figure 7.8. In all images, the position of the actuator is indicated on the right hand side of the images. It can be seen that the low-speed ribbon of streamwise velocity formed with unidirectional forcing is transported further in the positive spanwise direction through phases (i) to (iv). This is due to the spanwise velocity that is generated by each DBD plasma actuator through each phase. The low-speed streamwise velocity coincides with the high-speed spanwise velocity region. As the low-speed ribbon of streamwise velocity is transported in the spanwise direction, a ribbon of wall-normal vorticity can be seen propagating in the spanwise direction.

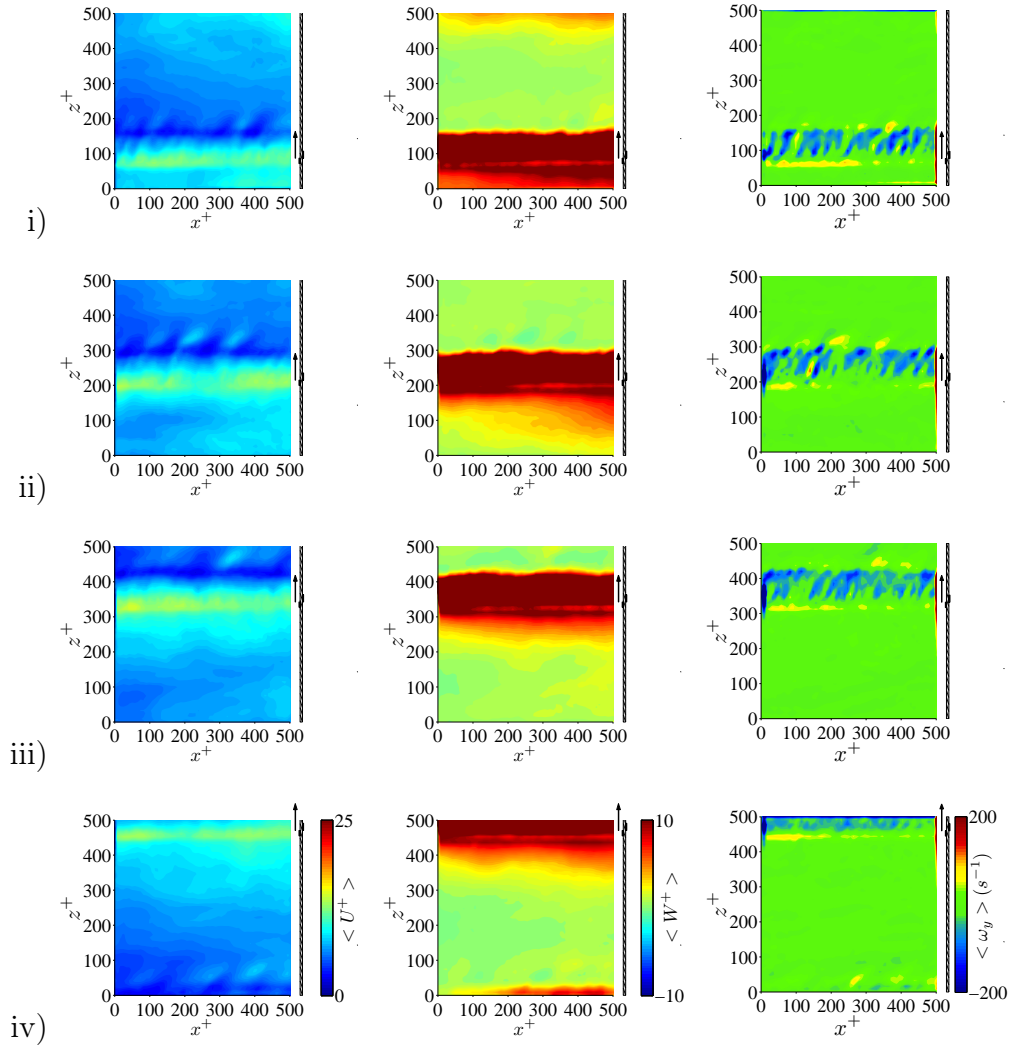


Figure 7.8: Phase-averaged streamwise velocity (left column), and spanwise velocity (middle column) and wall-normal vorticity (right column) in the  $x$ - $z$  plane of a turbulent boundary layer with unidirectional forcing at a)  $\frac{1}{4}T^+$ , b)  $\frac{1}{2}T^+$ , c)  $\frac{3}{4}T^+$  and d)  $T$ .  $\lambda^+ = 500$ ,  $T^+ = 82$ .

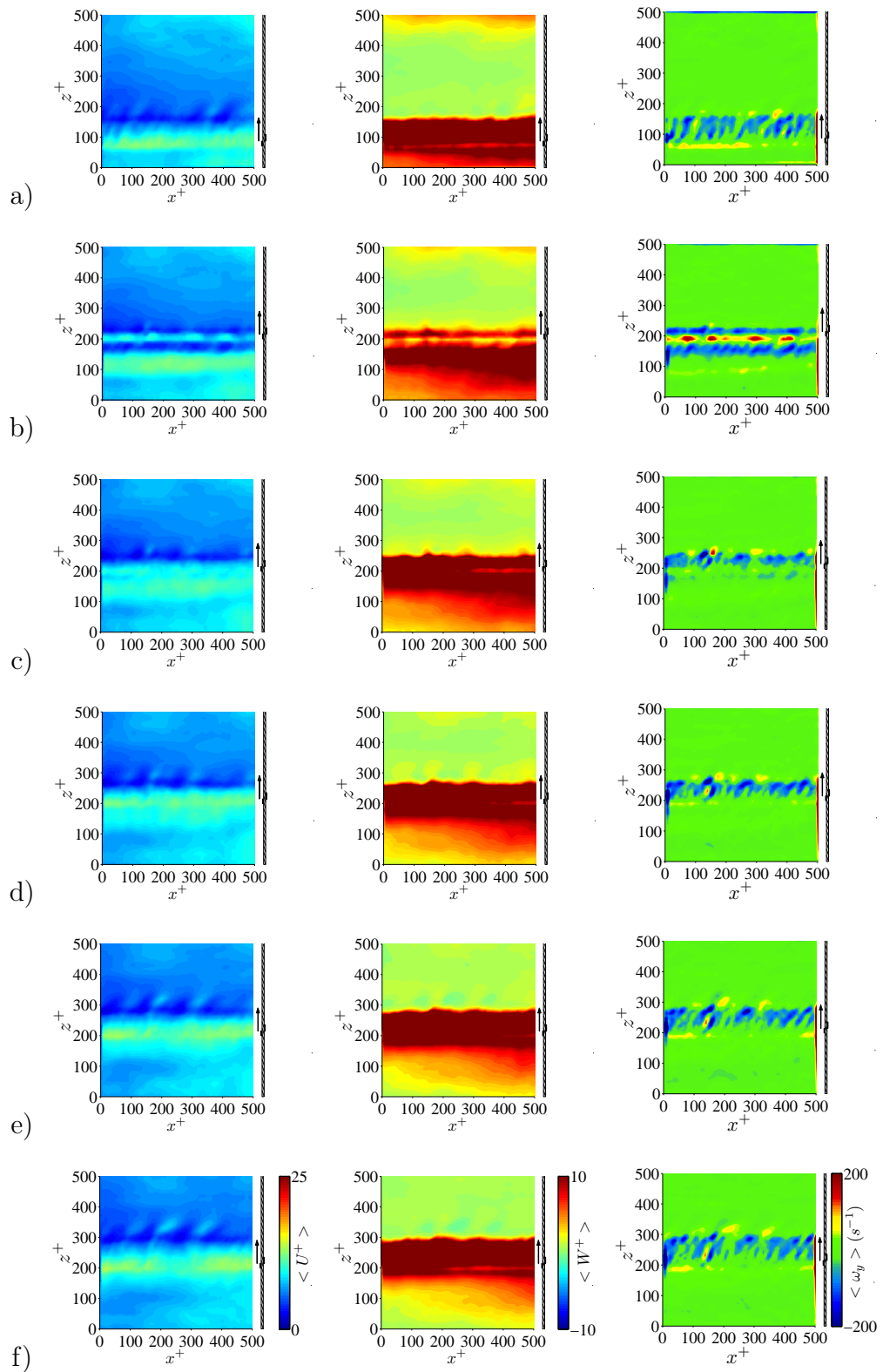


Figure 7.9: Phase-averaged streamwise velocity (left column), spanwise velocity (middle column) and wall-normal vorticity (right column) in the  $x$ - $z$  plane of a turbulent boundary layer with unidirectional forcing through phase (ii) at a)  $\frac{5}{20}T^+$ , b)  $\frac{6}{20}T^+$ , c)  $\frac{7}{20}T^+$ , d)  $\frac{8}{20}T^+$ , e)  $\frac{9}{20}T^+$  and f)  $\frac{10}{20}T^+$ .  $\lambda^+ = 500$ ,  $T^+ = 82$ .

Figure 7.9 presents the development of the phase-averaged streamwise velocity (left column), spanwise velocity (middle column) and wall-normal vorticity (right column) through phase (ii) of the unidirectional travelling wave. Figure 7.9a) is a phase-average taken at the end of phase (i),  $\frac{1}{4}T^+$ . The plasma actuator has effectively amalgamated and spread low-speed streamwise velocity in the spanwise direction inside the viscous sublayer. Figure 7.9b) shows the starting point of phase (ii). The plasma actuator fires at  $z^+ = 200$ , which is in the centre of the amalgamated low-speed region, causing ribbons of low- and high-speed streamwise velocity. The plasma actuator thrusts the low-speed fluid further in the positive spanwise direction, Figure 7.9c), causing the amalgamation of the low-speed ribbon. Through Figures 7.9d) to f),  $\frac{8}{20}T^+$  to  $\frac{10}{20}T^+$ , the low-speed ribbon of streamwise velocity is thrust further in the spanwise direction, completing the movement through phase (ii). Figure 7.9a) and f) show the ends of phases (i) and (ii) respectively. Both of these images appear qualitatively and quantitatively similar and when compared it can be seen that the low-speed fluid has moved through a distance of  $\frac{1}{4}\lambda^+$  ( $z^+ = 175$  to  $z^+ = 300$ ) in a time period of  $\frac{1}{4}T^+$ . Hence, the fluid is being moved with an average wave speed,  $c^+ = \frac{\lambda^+}{T^+} = 6$ .

It can be seen through Figure 7.9 that there is large spanwise velocity introduced by the unidirectional travelling wave which extends in the spanwise direction for  $z^+ = 100$ . If the locations of the spanwise velocity (middle column) and streamwise velocity (left column) are compared, the regions of high streamwise velocity are in the regions of high spanwise velocity. This supports the concept that as the plasma actuators push fluid in the spanwise direction, by continuity, high-speed fluid from the outer regions of the boundary layer is being entrained into the near-wall region, causing a local increase in streamwise velocity. The presence of wall-normal vorticity (right column) is dependent on two terms;  $\frac{\partial U}{\partial z}$  and  $\frac{\partial W}{\partial x}$ . The spanwise velocity introduced into the turbulent boundary layer by the unidirectional travelling wave appears uniform along the streamwise direction. However, the plasma forcing at each phase of the travelling

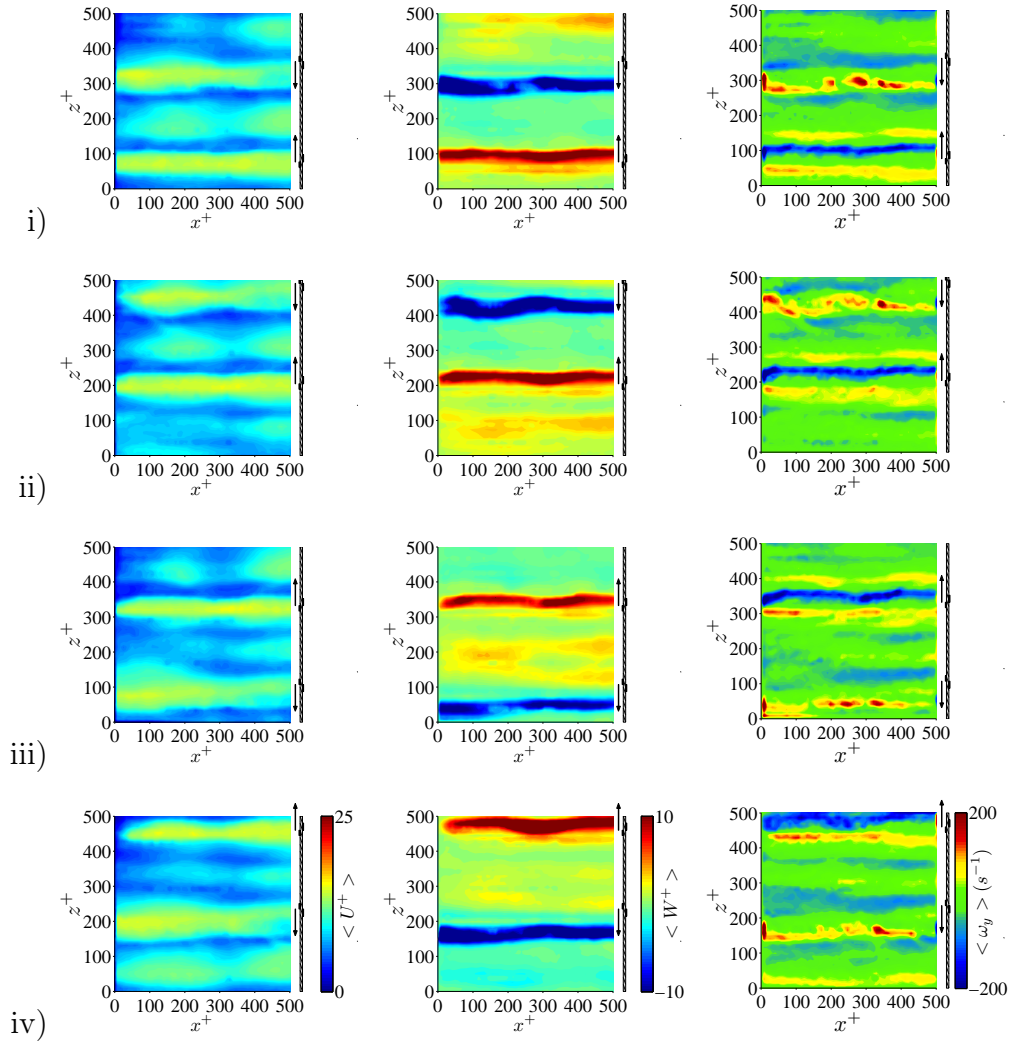


Figure 7.10: Phase-averaged streamwise velocity (left column), spanwise velocity (middle column) and wall-normal vorticity (right column) in the  $x$ - $z$  plane of a turbulent boundary layer with bidirectional forcing at a)  $\frac{1}{4}T^+$ , b)  $\frac{1}{2}T^+$ , c)  $\frac{3}{4}T^+$  and d)  $T$ .  $\lambda^+ = 500$ ,  $T^+ = 82$ .

wave generates both low- and high-speed ribbons of streamwise velocity which propagate in the spanwise direction. Hence, the  $\frac{\partial U}{\partial z}$  term becomes dominant in the wall-normal vorticity calculation. Strips of low- and high-speed fluid can be seen in each image of the figure as the travelling wave develops through phase (ii), which generates strips of positive and negative wall-normal vorticity.

## Transient Behaviour with Bidirectional Forcing

The development through phases (i) to (iv) of the phase-averaged streamwise velocity, spanwise velocity and wall-normal vorticity with a bidirectional travelling

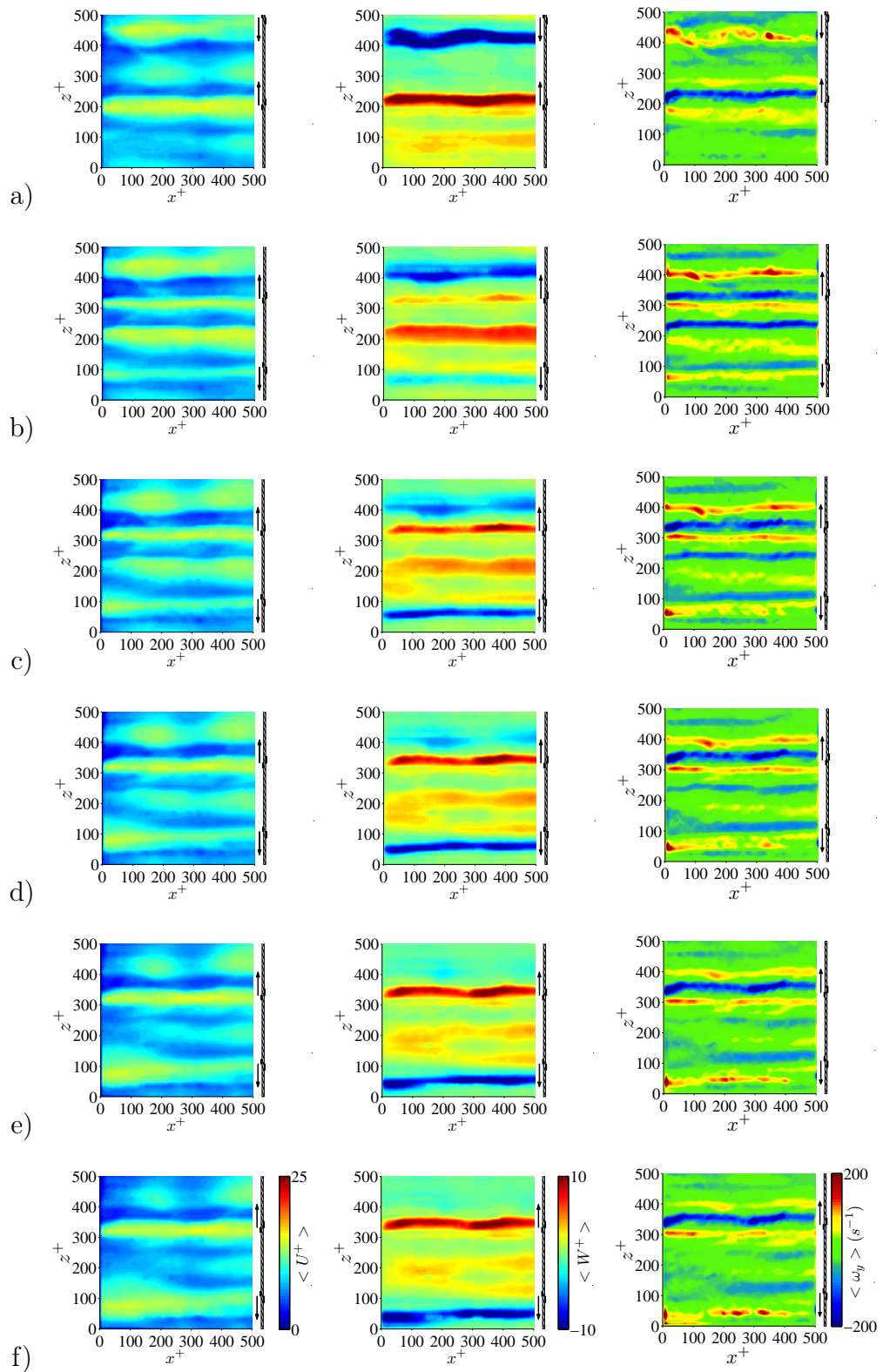


Figure 7.11: Phase-averaged streamwise velocity (left column), and spanwise velocity (left column) and wall-normal vorticity (right column) in the  $x$ - $z$  plane of a turbulent boundary layer with bidirectional forcing through phase (iii) at a)  $\frac{10}{20}T^+$ , b)  $\frac{11}{20}T^+$ , c)  $\frac{12}{20}T^+$ , d)  $\frac{13}{20}T^+$ , e)  $\frac{14}{20}T^+$  and f)  $\frac{15}{20}T^+$ .  $\lambda^+ = 500$ ,  $T^+ = 82$ .

wave can be found in Figure 7.10. With the bidirectional travelling wave, two DBD plasma actuators are actuated each phase in opposite directions. This is illustrated by the positive and negative spanwise velocity created by each actuator. There is a resultant positive spanwise velocity due to the travelling wave transporting fluid in the positive spanwise direction. This can be seen in Figure 7.10 (middle column) where, for example, in phase (ii) there is a large region of positive spanwise velocity for  $z^+ < 200$  and for phase (iii), for  $100 < z^+ < 300$ . As the spanwise velocity is moving in the spanwise direction, low-speed streamwise velocity (left column) is being transported in the spanwise direction. In between the actuators of phase (i) there are two regions of low-speed streamwise velocity located at  $z^+ = 100$  and  $250$  that both extend for 50 wall units in the spanwise direction. These two regions are separated by a slightly higher region of streamwise velocity, which is due to the downwash of high-speed streamwise velocity from the outer boundary layer from previous phases of the travelling wave, which could be inhibiting the spanwise growth of the low-speed ribbons of fluid with the bidirectional travelling wave. As the low-speed ribbons of streamwise velocity are transported in the spanwise directions, strips of positive and negative wall-normal vorticity (right column) can be seen propagating in the spanwise direction.

The development through phase (iii) of the phase-averaged streamwise velocity (left column), spanwise velocity (middle column) and wall-normal vorticity (right column) are shown in Figure 7.11. The boundary-layer flow is moving from left to right and the travelling wave is actuated to move in the positive  $z$ -direction. Figure 7.11a) shows the end of phase (ii) at  $\frac{1}{2}T^+$ . There are two high-speed regions of streamwise velocity above the locations of the plasma actuators located at  $z^+ = 200$  and  $z^+ = 485$  and a low-speed ribbon between,  $250 < z^+ < 400$ . The low-speed ribbon can be split up into three sections. There are two clear low speed-regions located at  $z^+ = 250$  and  $z^+ = 400$ , and a region of increased streamwise velocity sandwiched in between the two low-speed regions located at

$z^+ = 300$ . The increased streamwise velocity at  $z^+ = 300$  is due to the high-speed streamwise velocity that was entrained from phase (i) of the travelling-wave excitation. The travelling-wave excitation of phase (ii), Figure 7.11a), is trying to push the low-speed fluid from  $z^+ = 250$  and  $z^+ = 400$  in opposite directions so that the two low-speed regions will merge into one around  $z^+ = 300$  forming one wide ribbon of low-speed fluid. This is nearly accomplished. However, the high-speed fluid from phase (i) remains persistent through a time scale of  $\frac{1}{4}T^+$ . Phase (iii) actuation has initiated with Figure 7.11b), where the low-speed fluid that was collected between  $250 < z^+ < 400$  is being pushed further in the positive spanwise direction. As was evident at the end of phase (ii), Figure 7.11a), the high-speed streamwise velocity from the previous phase restricts the bidirectional movement in the spanwise direction. The high-speed streamwise velocity introduced by phase (ii) can be seen remaining persistent at  $z^+ = 200$  and  $z^+ = 450$ . Throughout the development of phase (iii), Figures 7.11b) to f), the high-speed streamwise velocity from phase (ii) ( $z^+ = 200$  and  $450$ ) deteriorates and the low-speed streamwise velocity collected from phase (iii) is pushed further in the spanwise direction, forming a wide low-speed ribbon for  $z^+ > 350$ . For successful bidirectional forcing, the two DBD plasma actuators which are actuated each phase collect low-speed fluid in the viscous sublayer in a region mid-way between both actuators. The following phase pushes the previously collected low-speed fluid (and newly collected low-speed fluid) further in the spanwise direction, creating a wide ribbon of low-speed fluid moving in the positive spanwise direction.

The wall-normal vorticity development through phase (iii) of the bidirectional travelling wave is shown in the right column of Figures 7.11. Similar with unidirectional forcing, the wall-normal vorticity is indicating the locations of the low- and high-speed streamwise velocity regions generated by the plasma actuators. As the bidirectional travelling wave has double the actuators per phase in comparison with unidirectional forcing, multiple strips of positive and negative

wall-normal vorticity can be seen throughout the development of phase (iii).

## Spanwise Velocity Profiles

The spanwise velocity profiles for uni and bidirectional forcing through phases (i) to (iv) are shown in Figures 7.12 and 7.13 respectively. Each spanwise velocity profile is generated by averaging the phase-averaged spanwise velocity over a streamwise distance of  $x = 100$  mm ( $x^+ = 500$ ) with a resolution of  $x = 1.6$  mm ( $x^+ = 8$ ), providing an average over 62 spanwise velocity profiles.

Figure 7.12 shows the spanwise velocity profiles for the unidirectional travelling wave. At the end of each phase, (i) to (iv), there is a well defined bell-shaped velocity profile, resembling half a sinusoid. The maximum phase-averaged spanwise velocity through phases (i) to (iv) is  $\langle W^+ \rangle = 25$ , and on average the maximum phase-averaged spanwise velocity is  $\langle W^+ \rangle = 22$ . This is equal to the free-stream velocity. Hence, for unidirectional forcing the spanwise to free-stream velocity ratio,  $\frac{\langle W^+ \rangle}{U_\infty}$  is 1. If the peak phase-average spanwise velocity location is compared in phases (i) and (iv), it can be seen that the travelling wave moves through a distance of  $z^+ = 375$  ( $\frac{3}{4}\lambda^+$ ) in a time scale of  $\frac{3}{4}T^+$ , visually confirming an average travelling wave speed of,  $c^+ = 6$ . Hence, Figure 7.12 illustrates that an applied voltage of  $E = 7$  kV<sub>p-p</sub> at a frequency  $f = 25$  kHz (each actuator capable of creating a 1 m/s wall jet with these plasma parameters) can generate a spanwise travelling wave with DBD plasma in a unidirectional forcing configuration with an amplitude of  $\langle W^+ \rangle = 22$  with a wave speed of  $c^+ = 6$  over a wavelength,  $\lambda^+ = 500$ .

In Chapter 5, the spanwise velocity profile in still air for unidirectional forcing was estimated by taking a spanwise cut of the data at half the distance between the starting vortex core and wall,  $y^+ = 25$ , Figure 5.4. There are both similarities and differences between the spanwise velocity profiles found in quiescent air and in the turbulent boundary layer. In both quiescent air and in the turbulent boundary layer, there is a well defined bell-shape velocity profile travelling in the

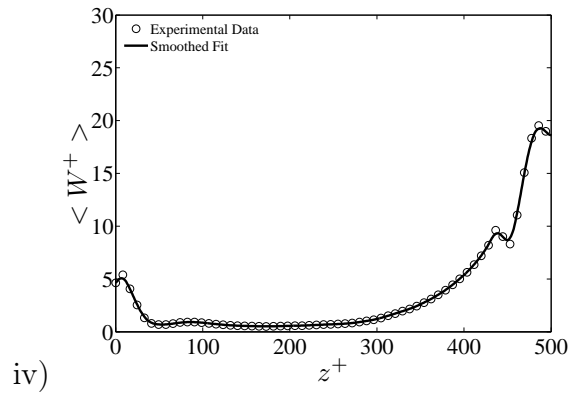
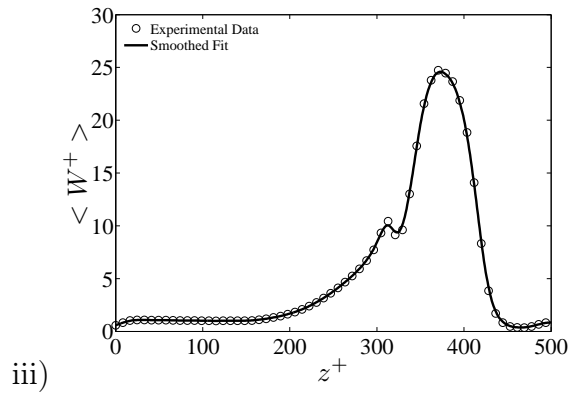
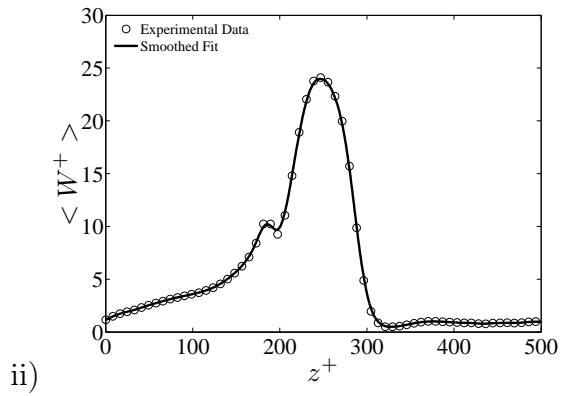
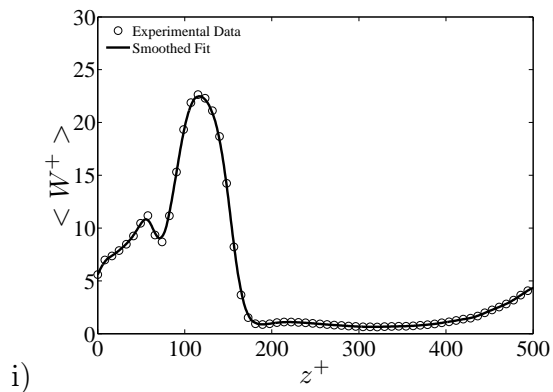


Figure 7.12: Spanwise velocity profiles with unidirectional forcing at  $y^+ = 5$  at i)  $\frac{1}{4}T^+$ , ii)  $\frac{1}{2}T^+$ , iii)  $\frac{3}{4}T^+$  and iv)  $T^+$ .  $\lambda^+ = 500$ ,  $T^+ = 82$ .

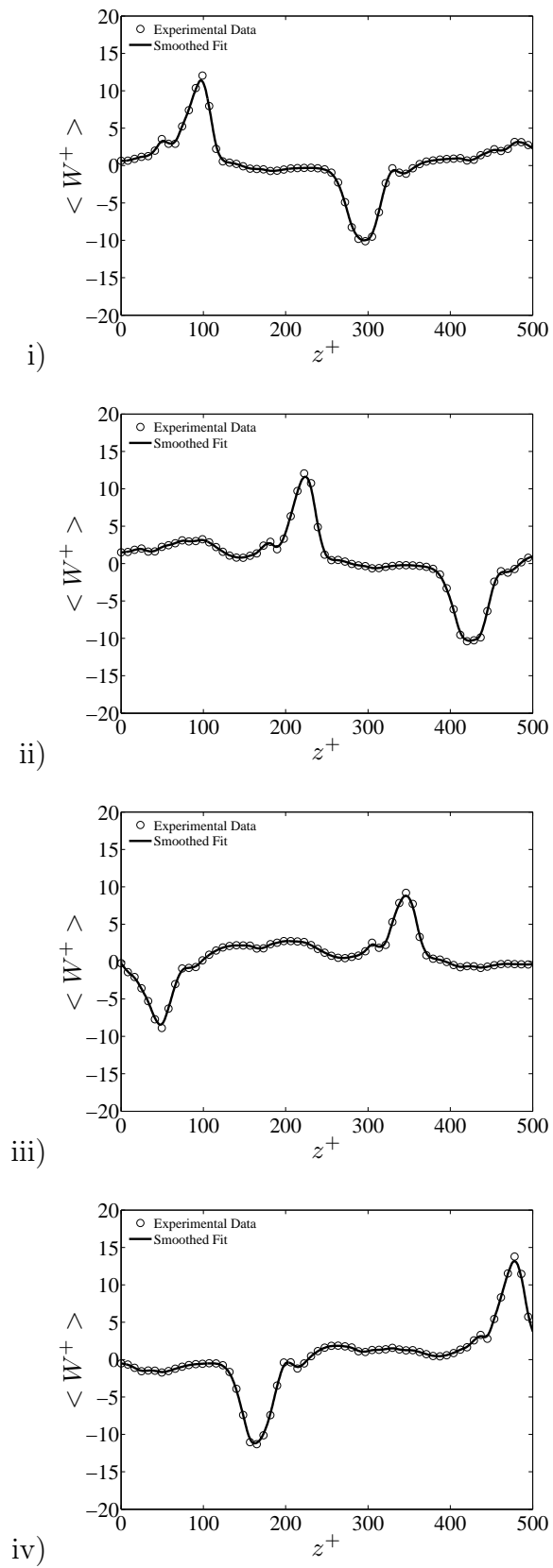


Figure 7.13: Spanwise velocity profiles with bidirectional forcing at  $y^+ = 5$  at i)  $\frac{1}{4}T^+$ , ii)  $\frac{1}{2}T^+$ , iii)  $\frac{3}{4}T^+$  and iv)  $T^+$ .  $\lambda^+ = 500$ ,  $T^+ = 82$ .

spanwise direction across phases (i) to (iv). This spanwise velocity profile resembles half of the two-bump forcing profile that Du *et al.* (2002) had used in their DNS of spanwise travelling waves. The two-bump forcing profile that Du *et al.* (2002) used in their DNS was presented in Chapter 5 in Figure 5.6. This forcing profile is a discontinuous sinusoid and the spanwise velocity profile for the unidirectional forcing resembles half this forcing profile. The spanwise velocity profile of the unidirectional travelling wave in quiescent air, appears 40% smaller than the spanwise velocity profile found inside the turbulent boundary layer. This could be partly due to the spanwise velocity profile in the turbulent boundary layer being taken very close to the wall,  $y = 1 \text{ mm}$  ( $y^+ = 5$ ), where the spanwise velocity induced by the plasma is higher. The more likely reasons are due to how the experiments in quiescent air and in the turbulent boundary layer were conducted. Firstly, in the quiescent air measurements of the unidirectional travelling wave, one wavelength of the travelling-wave actuator sheet was used and not all three as in the case for the turbulent boundary-layer measurements. Secondly, for the measurements in quiescent air, data was obtained for the unidirectional travelling wave over the first period of forcing only. In the turbulent boundary-layer measurements, data was taken after 11 forcing periods of the unidirectional travelling-wave excitation. Hence, fluid had already been coupled from actuator to actuator over several forcing periods where momentum and spanwise velocity would have increased before measurements began. These are the reasons for the spanwise velocity (the amplitude of the unidirectional travelling wave) being measured larger inside the turbulent boundary when compared with the quiescent air results. In both quiescent air and inside the turbulent boundary layer, Figures 5.4 and 7.12, the DBD plasma actuators are effectively moving fluid in the spanwise direction over the entire wavelength of the spanwise travelling wave.

The phased-averaged spanwise velocity profile taken at  $y^+ = 5$  with bidirectional forcing is shown in Figure 7.13 through phases (i) to (iv). The velocity

profile resembles a two-bump function, similar to the forcing profile of Du *et al.* (2002), Figure 5.6. The positive and negative spanwise velocity is due to the plasma actuators firing in two opposite direction per phase with the bidirectional forcing configuration. The maximum phase-averaged spanwise velocity through phases (i) to (iv) is  $\langle W^+ \rangle = 12$ , which is on the order of the free-stream velocity and gives a spanwise to free-stream velocity ratio of  $\frac{\langle W^+ \rangle}{U_\infty} = 0.54$ . If the location of the positive peaks in the phase-average spanwise velocity are compared in phases (i) and (iv), it can be seen that the travelling wave moves with wave speed of  $c^+ = 6$ . Hence, Figure 7.13 illustrates that an applied voltage of  $E = 7 \text{ kV}_{\text{p-p}}$  at a frequency  $f = 25 \text{ kHz}$  can generate a spanwise travelling wave with DBD plasma in a bidirectional forcing configuration with an amplitude of  $\langle W^+ \rangle = 12$ , with a wave speed of  $c^+ = 6$ , over a wavelength,  $\lambda^+ = 500$ . The applied voltage and frequency to the DBD plasma actuators was equal for both the uni and bidirectional forcing configurations, yet the amplitude of the unidirectional travelling wave appears 45% larger when compared with the bidirectional travelling wave.

## Comparison with Quiescent Air

Comparing the spanwise velocity profiles for the bidirectional travelling wave in quiescent air, Chapter 5, Figure 5.10 and the phase-averaged spanwise velocity profiles inside the turbulent boundary layer, Figure 7.13, similarities and differences can be seen. The two-bump spanwise velocity profile of the bidirectional forcing can be seen in both figures and the measured maximum spanwise velocity in quiescent air and in the turbulent boundary layer is nearly equal,  $\langle W^+ \rangle = 12$ ,  $w = 1 \text{ m/s}$ . The spanwise velocity profile of the bidirectional travelling wave in quiescent air is stretched and elongated in the spanwise direction. In contrast, the phase-averaged spanwise velocity profile taken inside the turbulent boundary layer remains as a regular two-bump spanwise velocity profile spreading over 75 wall units in the spanwise direction. In addition, and as

already noted, the phase-averaged spanwise velocity with unidirectional forcing is 45% larger than bidirectional forcing in the turbulent boundary layer. As was explained with unidirectional travelling wave in quiescent air; the experiments in quiescent air and inside the turbulent boundary layer were conducted differently. The quiescent air measurements for the uni and bidirectional travelling waves were conducted in the same way. Firstly, the bidirectional travelling waves were conducted over one wavelength in quiescent air and inside the turbulent boundary layer all three wavelengths on the travelling-wave actuator sheet were used. Secondly, the quiescent air measurements considered the bidirectional travelling-wave excitation over the first forcing period. Inside the turbulent boundary layer, the bidirectional travelling-wave measurements were taken after 11 forcing periods. Hence, it would be expected (like in the unidirectional travelling wave case) that the momentum coupling and phase-averaged spanwise velocity measured in the turbulent boundary would be greater than quiescent air, however this is not the case. This is due to the high-speed streamwise velocity that is being entrained into the near-wall region. This has been shown in Figure 7.10, when the streamwise velocity in the  $x$ - $z$  plane of the turbulent boundary layer was analysed over the four phases of the bidirectional travelling-wave excitation. It was found that in between the opposing actuators, low speed-ribbons were formed. In between the low-speed ribbons, large streamwise velocity was present due to the entrained high-speed streamwise velocity from previous phases that still remained close to the wall during the subsequent phase of forcing. The entrained fluid with large streamwise velocity inhibits the travelling-wave motion in the turbulent boundary layer. The bidirectional travelling wave is still transporting low-speed fluid in the spanwise direction and is still amalgamating the low- and high-speed streaks into low-speed ribbons, but is less effective in the boundary layer when compared with the unidirectional travelling wave for this reason. The unidirectional travelling wave does not have this same issue of large streamwise fluid from previous phases inhibiting spanwise movement as the DBD plasma forcing is in one direction only.

The large streamwise velocity that is entrained into the near-wall region appears to have convected downstream by a time-scale of  $T^+$ , Figure 7.8. In other words, although high-speed streamwise fluid is entrained with unidirectional forcing it does remain in the near-wall region by the time the next travelling-wave period occurs, hence, having no effect on the travelling-wave excitation in this case.

## Unidirectional Spanwise Travelling-Wave Mechanism

In all figures presented of the  $z$ - $y$  plane data, the free-stream velocity is into the plane of the paper and the spanwise travelling waves are moving in the positive  $z$ -direction. The direction and location of the activated plasma actuators can be seen in each image. It has previously been shown when the  $z$ - $y$  plane data was compared with the  $x$ - $z$  plane data that on application of DBD plasma in the turbulent boundary layer with both a uni and a bidirectional travelling wave, streamwise vortices are generated. The streamwise vortex development through a single phase and also over the four phases will be presented for both forcing configurations. Alongside streamwise vorticity, the  $U$ ,  $V$  and  $W$  components of velocity and Reynolds stress will be presented to show how the travelling-wave excitations have changed the turbulent boundary-layer structure throughout the four phases of excitation.

Illustrated in Figure 7.14 is the development of streamwise vorticity through phase (ii) of the unidirectional travelling wave in the  $z$ - $y$  plane of the turbulent boundary layer. In Figure 7.14a), at the end of phase (i), it can be seen that there is a coherent streamwise vortex located at  $y^+ = 50$  that has been created due to DBD plasma. The arrows in each image are of the  $V$  and  $W$  velocity components, indicating the roll up of fluid around a vortex core of concentrated negative streamwise vorticity. Secondary vorticity is generated along the wall to preserve the no-slip boundary condition (Allen and Naitoh, 2007), with a thin area of secondary vorticity being wrapped around the primary roller. Phase (ii) begins, Figure 7.14b), and a new co-rotating vortex is initiated. The two co-

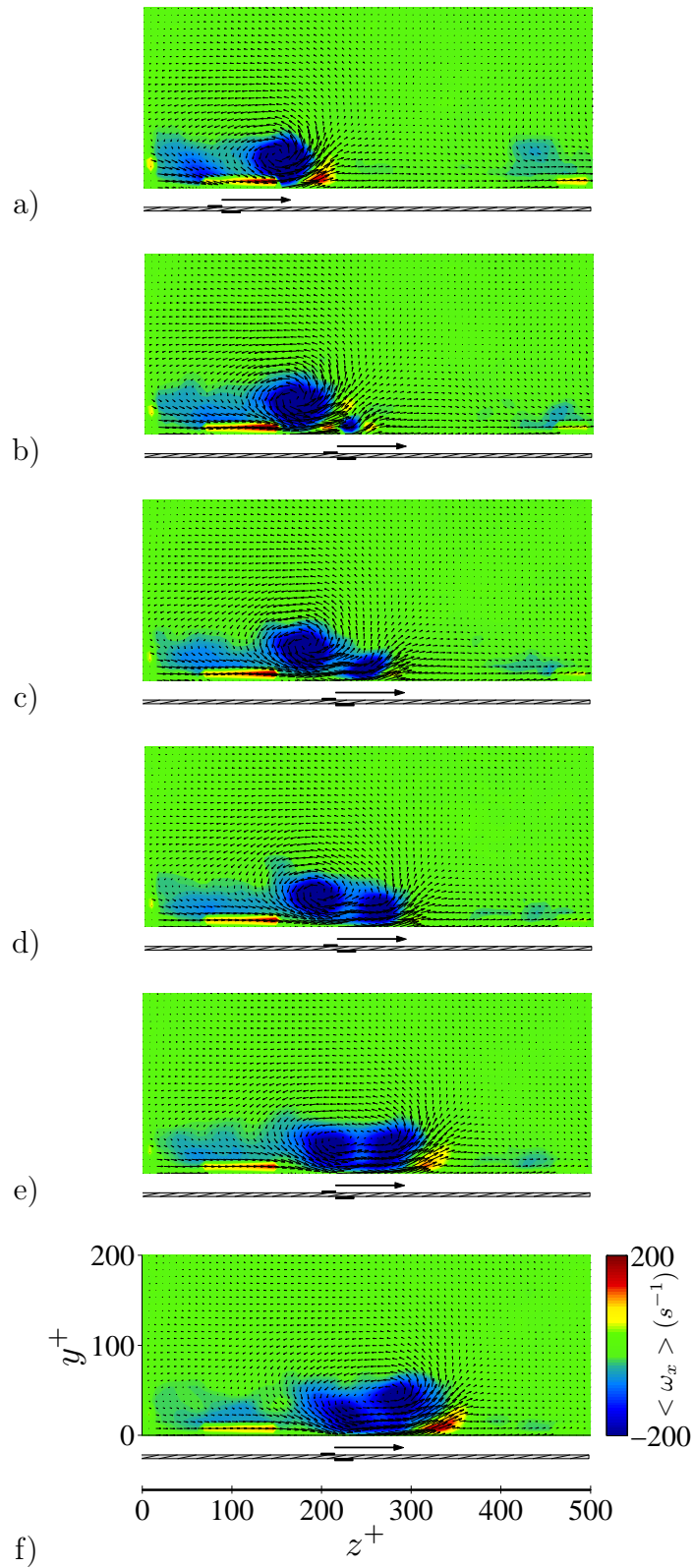


Figure 7.14: Phase-averaged streamwise vorticity in the  $z$ - $y$  plane of a turbulent boundary layer with unidirectional forcing at a)  $\frac{5}{20}T^+$ , b)  $\frac{6}{20}T^+$ , c)  $\frac{7}{20}T^+$ , d)  $\frac{8}{20}T^+$ , e)  $\frac{9}{20}T^+$  and f)  $\frac{10}{20}T^+$ .  $\lambda^+ = 500$ ,  $T^+ = 82$ .

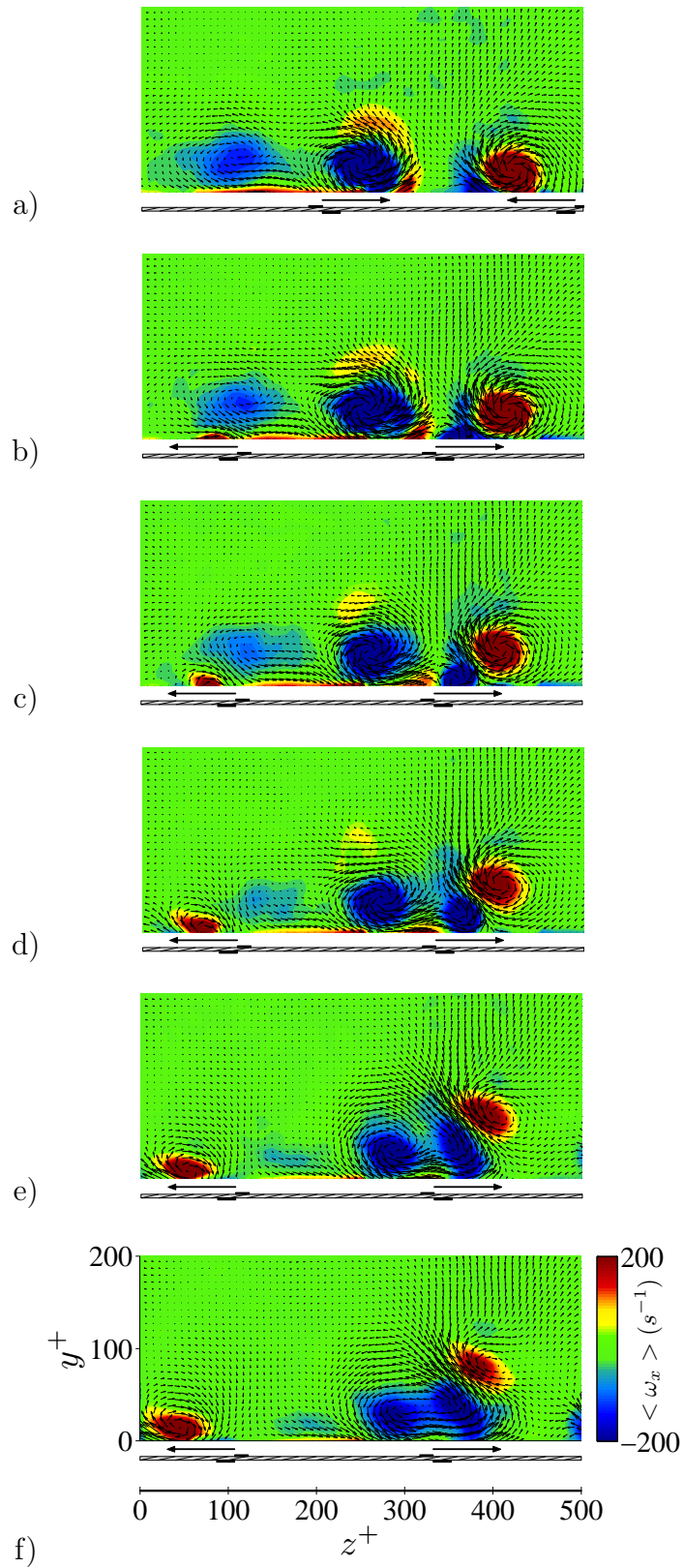


Figure 7.15: Phase-averaged streamwise vorticity in the  $z$ - $y$  plane of a turbulent boundary layer with bidirectional forcing at a)  $\frac{10}{20}T^+$ , b)  $\frac{11}{20}T^+$ , c)  $\frac{12}{20}T^+$ , d)  $\frac{13}{20}T^+$ , e)  $\frac{14}{20}T^+$  and f)  $\frac{15}{20}T^+$ .  $\lambda^+ = 500$ ,  $T^+ = 82$ .

rotating vortices begin to coalesce, elongating and stretching along the spanwise direction, forming by the end of phase (ii), a single streamwise vortex of negative vorticity whose core has remained at  $y^+ = 50$ , Figure 7.14f). As the two vortices merge through phase (ii), the negative streamwise vorticity is spread along the spanwise direction of the turbulent boundary covering a distance of 150 wall units. The mechanism of vortex amalgamation inside the turbulent boundary layer appears similar to that found when the unidirectional spanwise travelling wave was applied in quiescent air.

### **Bidirectional Spanwise Travelling-Wave Mechanism**

The development of streamwise vorticity through phase (iii) of the bidirectional travelling wave is presented in Figure 7.15. At the end of phase (ii), Figure 7.15a), there are two counter-rotating vortices whose cores are located at  $z^+ = 275$  and  $425$  and are located at a wall-normal distance of  $y^+ = 50$ . Another vortex, located at  $z^+ = 100$  can be seen. This is the remnants of phase (i). The counter-rotating vortices have concentrated regions of positive and negative vorticity and the secondary vorticity which has been generated to preserve the no-slip boundary condition can be seen wrapped around each vortex core. Phase (iii) begins, Figure 7.15b), and the two newly activated plasma actuators produce two more streamwise vortices. The plasma actuator located at  $z^+ = 325$  produces a streamwise vortex of negative vorticity in the vicinity of the existing streamwise vortex located at  $z^+ = 425$ . The newly formed and existing streamwise vortex form a counter-rotating pair that begin to interact. The plasma actuator ( $z^+ = 325$ ) activated through phase (iii), Figure 7.15b) to f), is adding momentum and vorticity to the flow and causing the negatively signed streamwise vortex to grow and lift the existing positively signed vortex up and away from the wall at an angle of  $45^\circ$  in the opposite direction to the spanwise travelling wave. At the same time, the co-rotating vortices (the existing vortex travelling in the positive  $z$ -direction from phase (ii) and the newly created streamwise vortex from phase (iii)) begin to co-

alesce. By the end of phase (iii), Figure 7.15f) there is a stretched and elongated region of negative streamwise vorticity spanning from  $z^+ = 250$  to  $z^+ = 400$  with the streamwise positively signed vortex (opposing the travelling-wave motion) generated from phase (ii) being lifted up and away from the wall with a core location of  $y^+ = 90$ . The interaction of co- and counter-rotating vortices, coalescing and being lifted up and away from the wall is an important aspect of the travelling wave-excitation with bidirectional forcing and was found when the bidirectional spanwise travelling wave was actuated in quiescent air, (Whalley and Choi, 2010b).

The bidirectional travelling wave actuates in two directions with two plasma actuators per phase. The other plasma actuator of phase (iii) is located at  $z^+ = 100$  and produces a positively signed streamwise vortex travelling in the opposite direction to the travelling wave. This is because this actuator is part of the next on-coming travelling wave from the first wavelength on the travelling-wave actuator sheet. The streamwise vortex which was located at  $z^+ = 100$  in Figure 7.15a) and was the remnants of phase (i) has been consumed during the actuation of phase (ii).

Figures 7.14f) and 7.15f) show the phase-averaged streamwise vorticity of the uni and bidirectional travelling waves at the end of phases (ii) and (iii) respectively. If these two figures are compared, it can be seen that the amalgamation of the co-rotating vortices in both forcing configurations appears qualitatively and quantitatively similar, both producing a stretched and elongated region of negative streamwise vorticity spanning 150 wall units. Hence, with both forcing configurations the starting vortices coalesce to create a streamwise vortex that is travelling in the spanwise direction.

## Comparison of Uni and Bidirectional Forcing

The phase-averaged streamwise velocity and streamwise vorticity through phases (i) to (iv) with the uni and bidirectional travelling waves are shown in Figures 7.16

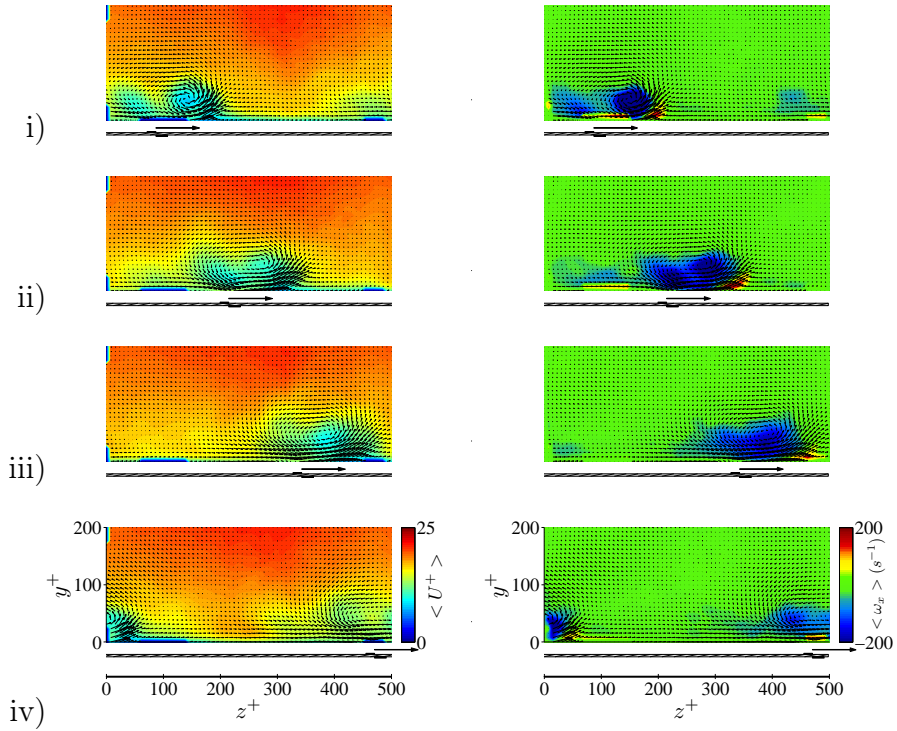


Figure 7.16: Phase-averaged streamwise velocity (left column) and streamwise vorticity (right column) in the  $z$ - $y$  plane of a turbulent boundary layer with unidirectional forcing at a)  $\frac{1}{4}T^+$ , b)  $\frac{1}{2}T^+$ , c)  $\frac{3}{4}T^+$  and d)  $T$ .  $\lambda^+ = 500$ ,  $T^+ = 82$ .

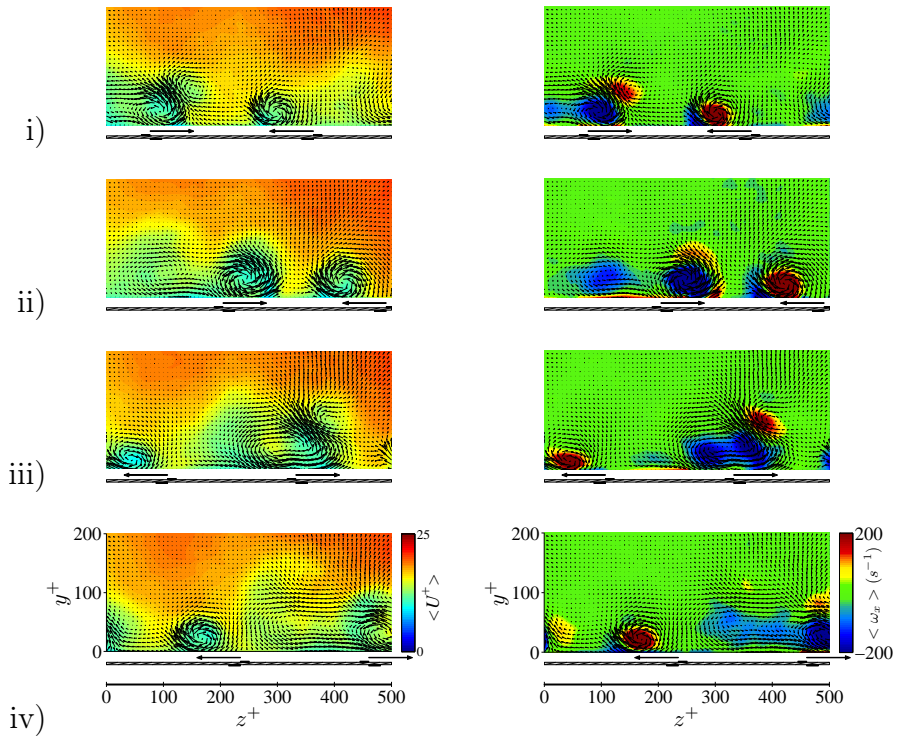


Figure 7.17: Phase-averaged streamwise velocity (left column) and streamwise vorticity (right column) in the  $z$ - $y$  plane of a turbulent boundary layer with bidirectional forcing at a)  $\frac{1}{4}T^+$ , b)  $\frac{1}{2}T^+$ , c)  $\frac{3}{4}T^+$  and d)  $T$ .  $\lambda^+ = 500$ ,  $T^+ = 82$ .

and 7.17 respectively. In both the uni and bidirectional travelling waves, the streamwise vortices, created on the initiation of DBD plasma, are causing low-speed fluid to be spread along the spanwise direction and into the outer regions of the turbulent boundary layer. It is expected that the low-speed streamwise velocity from the viscous sublayer is being transported into the logarithmic region through vortex induction and simultaneously the streamwise vortex at the head of the travelling wave front is collecting and spreading the low-speed streamwise velocity within the viscous sublayer in the spanwise direction, confirming the visualisations of the  $x$ - $z$  plane. Hence, the streamwise vortex generated during the travelling-wave excitation is causing the formulation of the wide ribbon of low-speed fluid in the near-wall region of the turbulent boundary layer. This same result has recently been found in the DNSs of Huang *et al.* (2011), who implemented a bidirectional spanwise travelling wave with a Lorentz force inside a turbulent channel flow and achieved more than a 35% reduction in turbulent skin-friction drag. It is clear with both forcing configurations, through phases (i) to (iv), Figures 7.16 and 7.17, that the presence of the streamwise vortices that are travelling in the spanwise direction creates low-speed bulges of streamwise velocity within the turbulent boundary layer. Throughout each phase of forcing, the low-speed regions are spread across the entire wavelength of the travelling wave, with low-speed fluid reaching greater distances from the wall where the starting vortices are present. With unidirectional forcing, the fluid through phases (i) to (iv) reaches typically 100 wall units,  $y^+ = 100$ . With bidirectional forcing, the low-speed fluid is expelled to greater wall-normal distances, typically to a distance of 150 wall units,  $y^+ = 150$ . The expulsion of low-speed fluid to greater wall-normal distances with the bidirectional spanwise travelling wave is due to the interaction between the counter-rotating vortices, which lift each other away from the wall and into the outer regions of the turbulent boundary layer.

It is interesting to note that studies of the interaction of a yawed synthetic jet (Di Cicca and Iuso, 2006) on a turbulent boundary layer have yielded similar

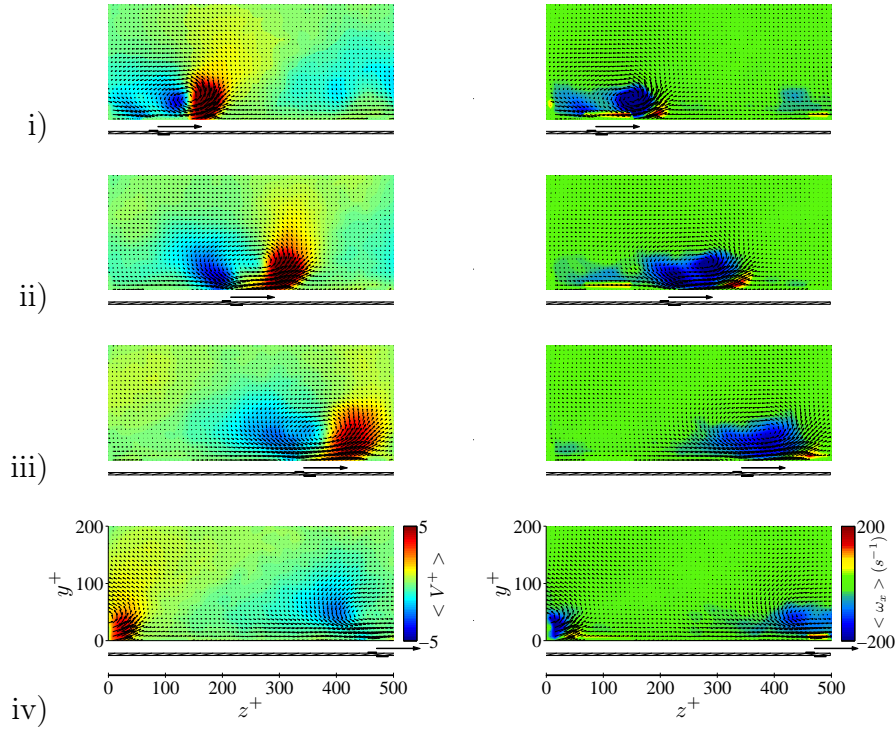


Figure 7.18: Phase-averaged wall-normal velocity (left column) and streamwise vorticity (right column) in the  $z$ - $y$  plane of a turbulent boundary layer with unidirectional forcing at a)  $\frac{1}{4}T^+$ , b)  $\frac{1}{2}T^+$ , c)  $\frac{3}{4}T^+$  and d)  $T$ .  $\lambda^+ = 500$ ,  $T^+ = 82$ .

results to those presented within this section. It was shown (Di Cicca and Iuso, 2006) that the streamwise vortices created by a yawed synthetic jet caused a large time-averaged velocity deficit (22% at  $y^+ = 50$ ) within the logarithmic region and a slight increase in time-averaged velocity in the near-wall region of the turbulent boundary layer. These effects were put down to the upwash and downwash generated by the streamwise vortices issued from the synthetic jet.

## Wall-normal Velocity

The development of the wall-normal velocity for uni and bidirectional forcing through phases (i) to (iv) are shown in Figures 7.18 and 7.19 respectively. The streamwise vorticity is plotted on the right of each image to indicate clearly the location of the streamwise vortices during each phase of forcing. For the unidirectional travelling wave, the streamwise vortex at the end of phase (i) is located at  $z^+ = 175$  and it is possible to see both positive and negative wall-normal velocity on the order of  $V^+ = 5$  due to the upwash and downwash of the streamwise

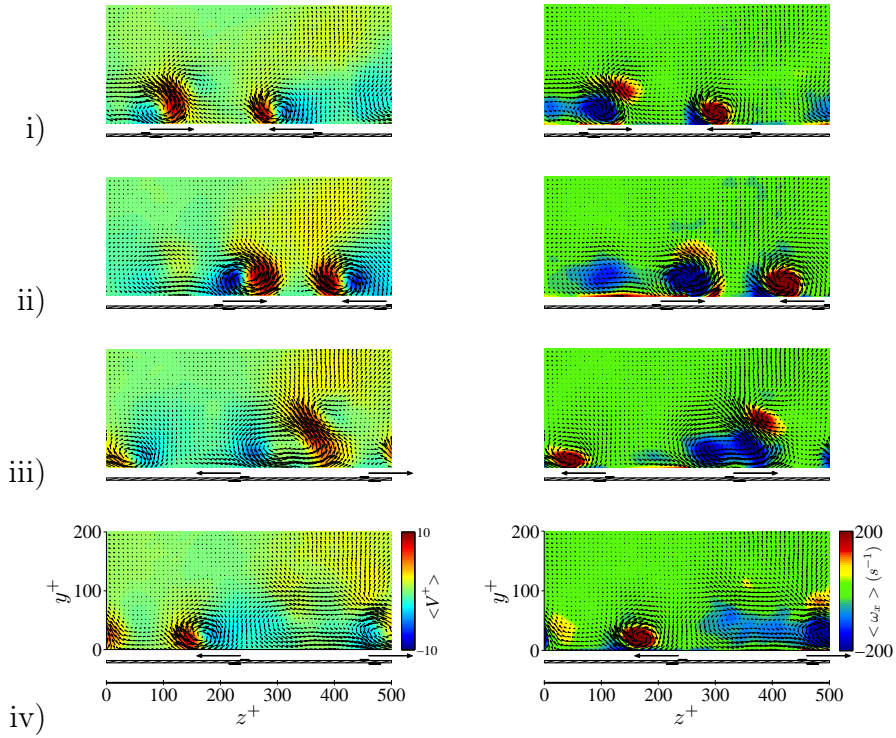


Figure 7.19: Phase-averaged wall-normal velocity (left column) and streamwise vorticity (right column) in the  $z$ - $y$  plane of a turbulent boundary layer with bidirectional forcing at a)  $\frac{1}{4}T^+$ , b)  $\frac{1}{2}T^+$ , c)  $\frac{3}{4}T^+$  and d)  $T$ .  $\lambda^+ = 500$ ,  $T^+ = 82$ .

vortex. The upwash appears more intense and is spread over a larger area. The downwash, can be found directly above and behind the plasma actuator. The action of upwash and downwash will be transferring momentum into and away from the near-wall region of the turbulent boundary layer and can be seen throughout the four phases, (i) to (iv), as the streamwise vortex is moving in the spanwise direction. The entrainment of high-speed streamwise velocity into the viscous sublayer of the turbulent boundary has already been demonstrated, Figure 7.2, with the PIV taken in the  $x$ - $z$  plane at  $y^+ = 5$ . This was caused by the downwash of streamwise velocity through the entrainment associated with the plasma actuators. This is similar to the wall-normal velocity with the bidirectional travelling wave through phases (i) to (iv), which are presented in Figure 7.19. The pairs of counter-rotating streamwise vortices have both positive and negative areas of wall-normal velocity due to upwash and downwash on the order of 10 wall units ( $V^+ = 10$ ).

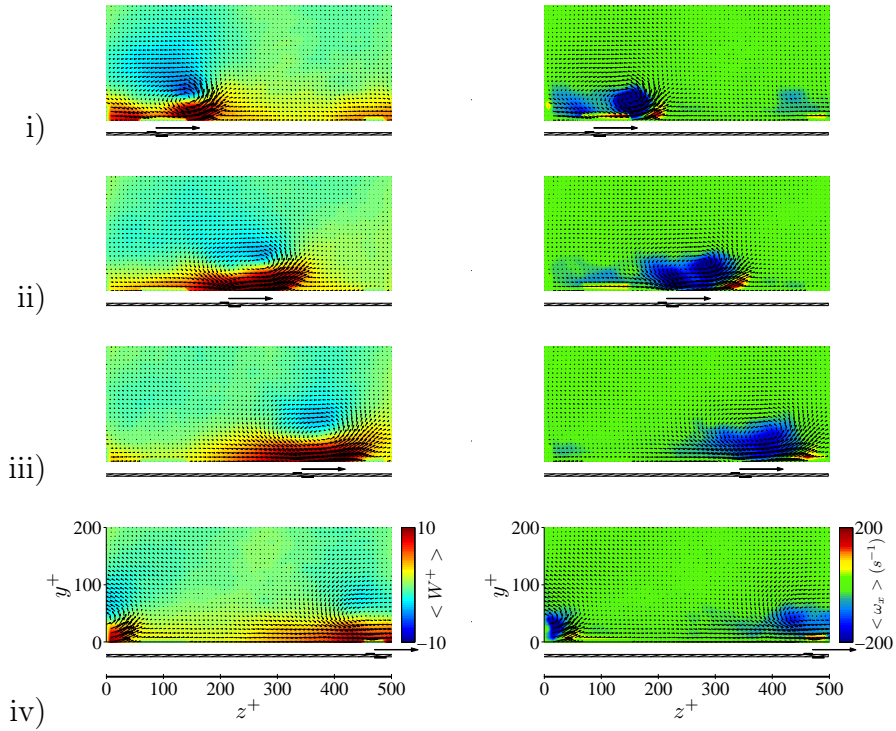


Figure 7.20: Phase-averaged spanwise velocity (left column) and streamwise vorticity (right column) in the  $z$ - $y$  plane of a turbulent boundary layer with unidirectional forcing at a)  $\frac{1}{4}T^+$ , b)  $\frac{1}{2}T^+$ , c)  $\frac{3}{4}T^+$  and d)  $T$ .  $\lambda^+ = 500$ ,  $T^+ = 82$ .

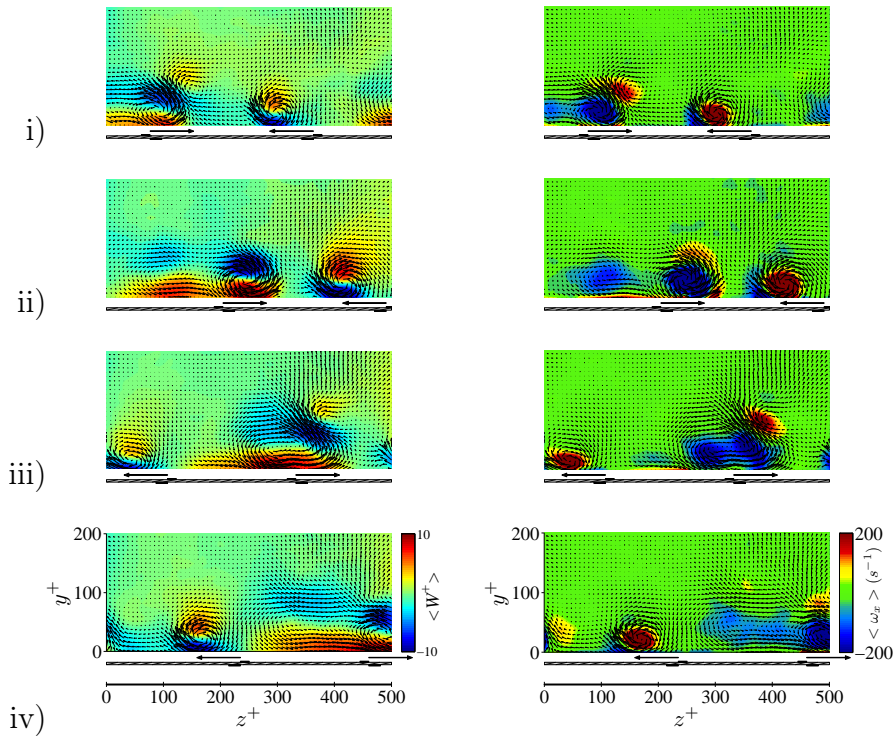


Figure 7.21: Phase-averaged spanwise velocity (left column) and streamwise vorticity (right column) in the  $z$ - $y$  plane of a turbulent boundary layer with bidirectional forcing at a)  $\frac{1}{4}T^+$ , b)  $\frac{1}{2}T^+$ , c)  $\frac{3}{4}T^+$  and d)  $T$ .  $\lambda^+ = 500$ ,  $T^+ = 82$ .

## Spanwise Velocity

The developments of spanwise velocity through phases (i) to (iv) of the uni and bidirectional travelling waves is presented in Figures 7.20 and 7.21 respectively. With the unidirectional travelling wave through phases (i) to (iv) a positive component of spanwise velocity encapsulated between  $y^+ = 50$  and the wall can be seen over the entire wavelength of the travelling wave. There is a more intense region of spanwise velocity which spans typically 200 wall units around the actuated plasma actuator, which has already been found to have a magnitude of  $\langle W^+ \rangle = 22$ , Figure 7.12. There is a region of negative spanwise velocity above  $y^+ = 50$  throughout phases (i) to (iv). With comparison to the streamwise vorticity which is shown to the right of each image, the negative spanwise velocity is due to the streamwise vortex. Above the region of the vortex core ( $y^+ = 50$ ) there is flow reversal due to the velocity profile of the streamwise vortex. It can be seen clearly in Figure 7.20 that the unidirectional travelling wave is pushing fluid in the spanwise direction through phases (i) to (iv) in the positive spanwise direction.

The development of spanwise velocity for the bidirectional travelling wave is shown in Figure 7.21. Through phases (i) to (iv), a positive spanwise velocity component cannot be seen over the entire wavelength of the travelling wave, as the plasma actuators fire in both the positive and negative spanwise directions. Instead a spanwise velocity component spreading over 250 wall units can be seen propagating in the positive  $z$ -direction. Above the location of the vortex core ( $y^+ = 50$ ), there is an area of negative spanwise velocity throughout the phases of the travelling wave. The negative spanwise velocity at times can appear more intense when compared with the unidirectional travelling wave. This occurs when the co- and counter-rotating vortices interact and the co-rotating vortex lifts the counter-rotating vortex away from the wall. The locations of the interactions between the co- and counter-rotating vortices can be seen in the streamwise vorticity plots to the right of each image. The areas of negative spanwise velocity above

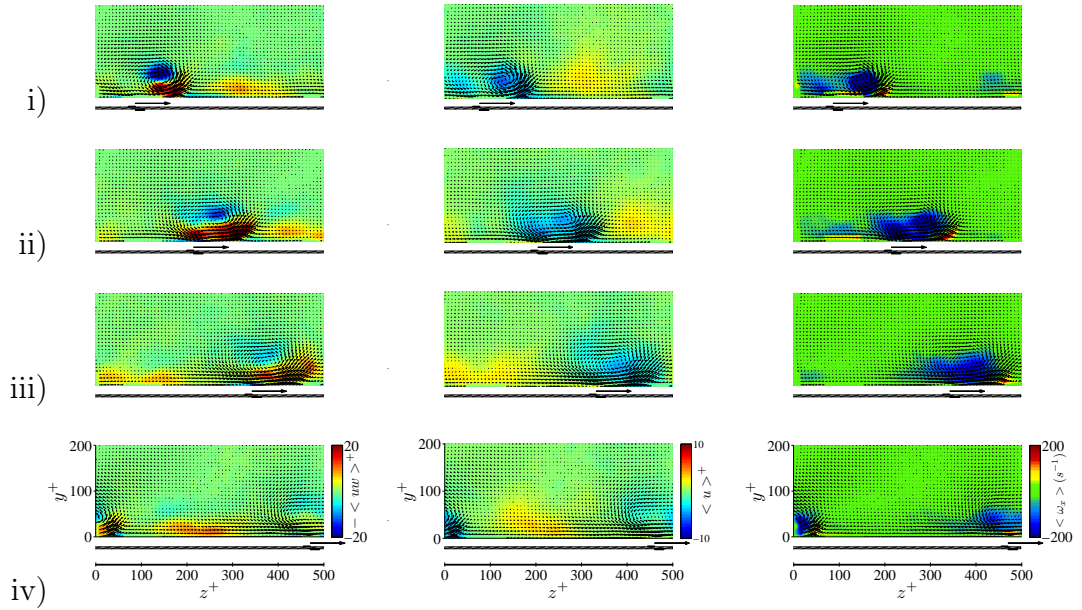


Figure 7.22: Phase-averaged  $-\langle uw^+ \rangle$  Reynolds stress (left column), streamwise velocity fluctuation (middle column) and streamwise vorticity (right column) in the  $z$ - $y$  plane of a turbulent boundary layer with unidirectional forcing at a)  $\frac{1}{4}T^+$ , b)  $\frac{1}{2}T^+$ , c)  $\frac{3}{4}T^+$  and d)  $T$ .  $\lambda^+ = 500$ ,  $T^+ = 82$ .

the vortex core are as in the case of unidirectional forcing, due to the reversed flow introduced by the streamwise vortices. It can be seen throughout each phase of the bidirectional travelling wave that fluid is effectively being transported from actuator to actuator in the positive spanwise direction.

## Reynolds Stresses

The phase-averaged  $-\langle uw^+ \rangle$  Reynolds stress through phases (i) to (iv) of the uni and bidirectional travelling waves are shown in Figures 7.22 and 7.23 respectively. Throughout the development of the spanwise travelling waves, low-speed streamwise velocity has been seen wrapped in and around the streamwise vortices that are travelling in the spanwise direction. This low-speed streamwise velocity (middle column) coupled with the high-speed spanwise velocity pushing the travelling wave in the positive spanwise direction causes the positive  $-\langle uw^+ \rangle$  Reynolds stress seen encapsulated within the first 50 wall units of the turbulent boundary layer. The negative  $-\langle uw^+ \rangle$  Reynolds stress is either found above the vortex core, where there are regions of negative spanwise velocity

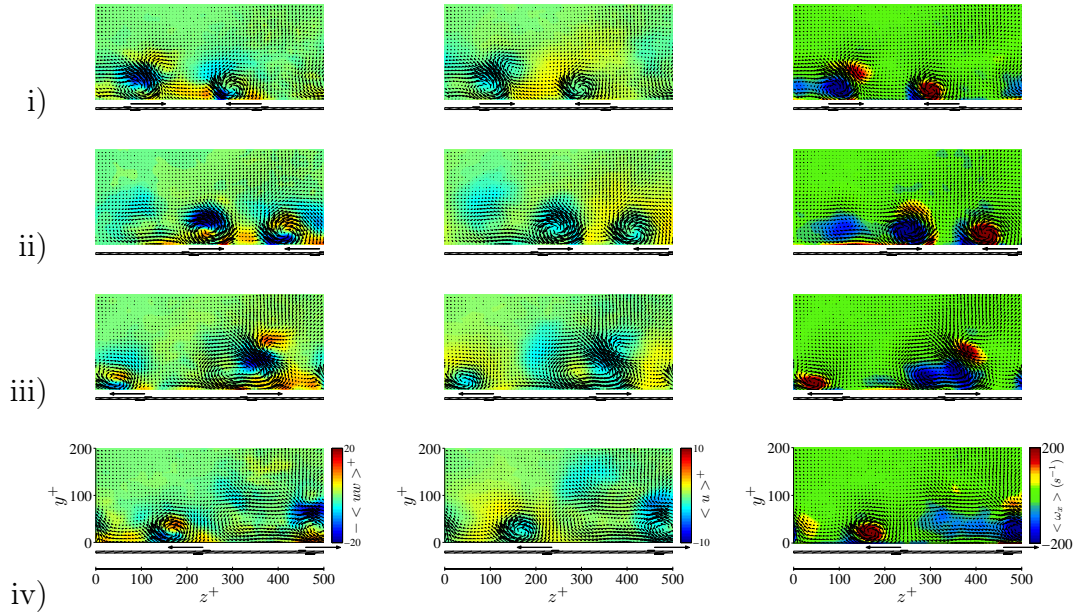


Figure 7.23: Phase-averaged  $-\langle uw^+ \rangle$  Reynolds stress (left column), streamwise velocity fluctuation (middle column) and streamwise vorticity (right column) in the  $z$ - $y$  plane of a turbulent boundary layer with bidirectional forcing at a)  $\frac{1}{4}T^+$ , b)  $\frac{1}{2}T^+$ , c)  $\frac{3}{4}T^+$  and d)  $T$ .  $\lambda^+ = 500$ ,  $T^+ = 82$ .

due to the velocity profile of the streamwise vortex, or (in the case of bidirectional forcing) due to one of the two actuators causing negative spanwise velocity. With bidirectional forcing, co- and counter-rotating vortices interact, causing regions of positive  $-\langle uw^+ \rangle$  Reynolds stress for  $y^+ > 100$ . This is due to the negative spanwise velocity from the counter-rotating vortex that is lifted away from the wall by the co-rotating vortex.

The development of  $-\langle vw^+ \rangle$  Reynolds stress throughout the four phases of the spanwise travelling wave can be seen in Figures 7.24 and 7.25. Images of fluctuating spanwise velocity (middle column) and streamwise vorticity (right column) throughout each phase are shown to the right of the figures so that the location of the streamwise vortices and velocity distribution can easily be identified. Negative quantities of wall-normal velocity are generated through the entrainment of fluid towards the wall by the plasma actuators. This coupled with the positive spanwise velocity for the unidirectional forcing and both positive and negative spanwise velocity for the bidirectional forcing close to the wall generates positive and negative  $-\langle vw^+ \rangle$  Reynolds stress above and behind the plasma

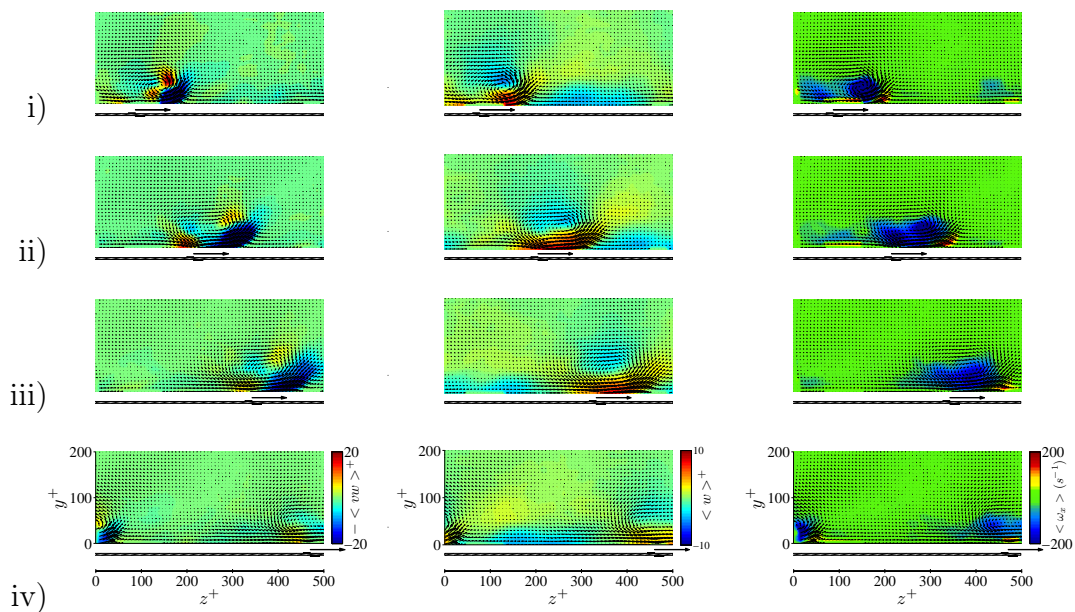


Figure 7.24: Phase-averaged  $\langle vv^+ \rangle$  Reynolds stress (left column), spanwise velocity fluctuation (middle column) and streamwise vorticity (right column) in the  $z$ - $y$  plane of a turbulent boundary layer with unidirectional forcing at a)  $\frac{1}{4}T^+$ , b)  $\frac{1}{2}T^+$ , c)  $\frac{3}{4}T^+$  and d)  $T$ .  $\lambda^+ = 500$ ,  $T^+ = 82$ .

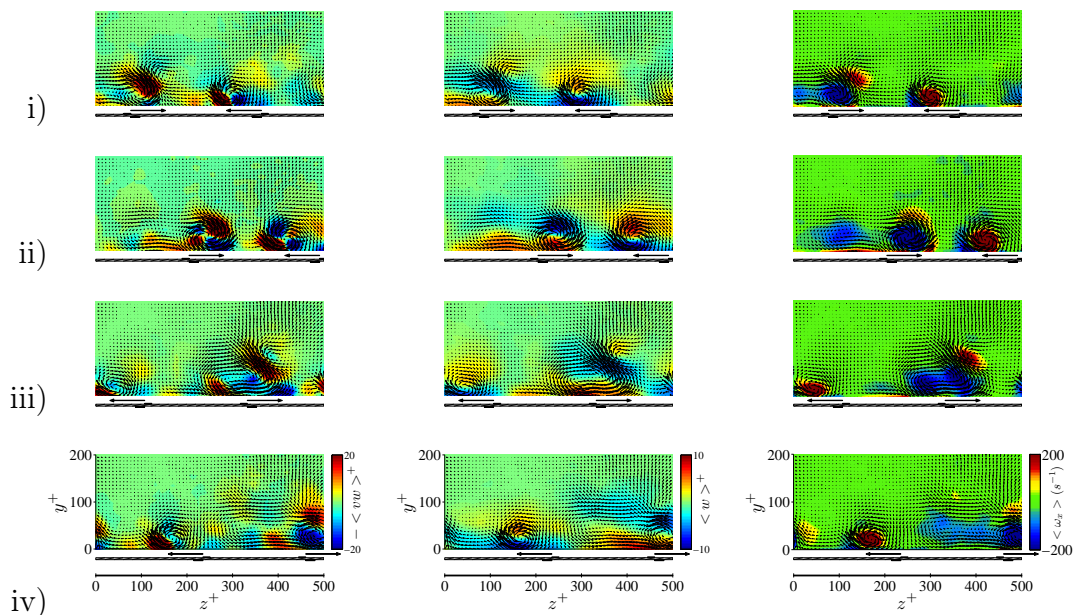


Figure 7.25: Phase-averaged  $\langle vv^+ \rangle$  Reynolds stress (left column), spanwise velocity fluctuation (middle column) and streamwise vorticity (right column) in the  $z$ - $y$  plane of a turbulent boundary layer with bidirectional forcing at a)  $\frac{1}{4}T^+$ , b)  $\frac{1}{2}T^+$ , c)  $\frac{3}{4}T^+$  and d)  $T$ .  $\lambda^+ = 500$ ,  $T^+ = 82$ .

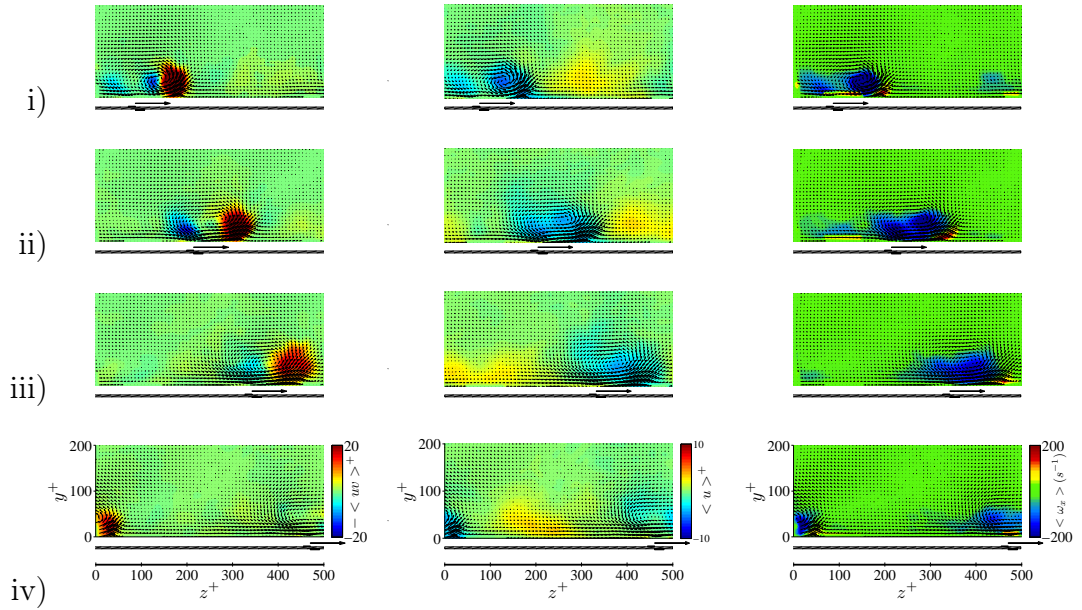


Figure 7.26: Phase-averaged  $-\langle uv^+ \rangle$  Reynolds stress (left column), streamwise velocity fluctuation (middle column) and streamwise vorticity (right column) in the  $z$ - $y$  plane of a turbulent boundary layer with unidirectional forcing at a)  $\frac{1}{4}T^+$ , b)  $\frac{1}{2}T^+$ , c)  $\frac{3}{4}T^+$  and d)  $T$ .  $\lambda^+ = 500$ ,  $T^+ = 82$ .

actuators with both forcing configurations. Hence, the positive and negative  $-\langle vw^+ \rangle$  Reynolds stress found directly above and behind the plasma actuator is a consequence of high spanwise velocity being pushed towards the wall of the turbulent boundary layer. This could be thought of as a modified sweep event causing increased spanwise wall shear stress.

The development of  $-\langle uv^+ \rangle$  Reynolds stress with uni and bidirectional travelling waves through phases (i) to (iv) can be seen in Figures 7.26 and 7.27 respectively. Again, the corresponding streamwise velocity fluctuation (middle column) and streamwise vorticity (right column) are plotted to the side of each image to indicate the location of the streamwise vortices. Positive values of  $-uv$  Reynolds stress are produced by sweep and ejection events. A sweep event is caused by high momentum fluid being splashed onto the wall and is a major contributor to turbulent skin-friction drag. An ejection event is produced when low-speed fluid is expelled outwards away from the wall and into the outer regions of the boundary layer. Hence, both sweep and ejection events cause turbulence production. The two forcing configurations have similar  $-\langle uv^+ \rangle$  Reynolds

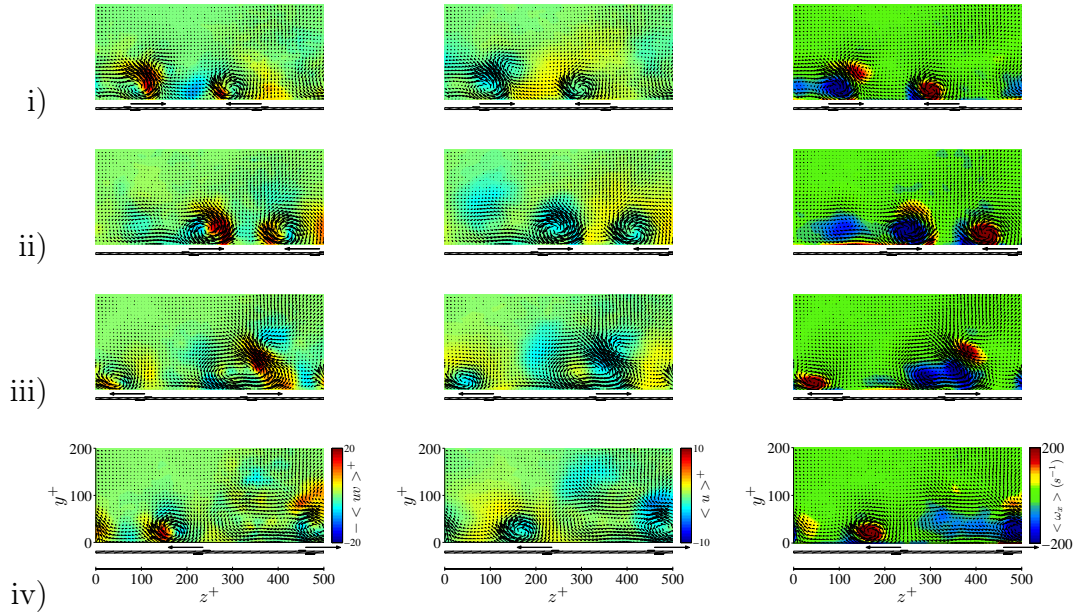


Figure 7.27: Phase-averaged  $-\langle uv^+ \rangle$  Reynolds stress (left column), stream-wise velocity fluctuation (middle column) and streamwise vorticity (right column) in the  $z$ - $y$  plane of a turbulent boundary layer with bidirectional forcing at a)  $\frac{1}{4}T^+$ , b)  $\frac{1}{2}T^+$ , c)  $\frac{3}{4}T^+$  and d)  $T$ .  $\lambda^+ = 500$ ,  $T^+ = 82$ .

stress fields. The streamwise vortices generated during the spanwise travelling waves have both positive and negative contributions to  $-\langle uv^+ \rangle$  Reynolds stress. Low-speed fluid lifted up and away from the wall on the upwash side of the streamwise vortices produces positive  $-\langle uv^+ \rangle$  Reynolds stress. This could be interpreted as a modified ejection event within the turbulent boundary layer as low-speed streamwise velocity is being ejected from the wall. On the downwash side of the streamwise vortices, there is a negative contribution to  $-\langle uv^+ \rangle$  Reynolds stress. During downwash, low-speed streamwise velocity is being pushed down into the wall. This could be interpreted as a modified wall-ward motion. The  $-\langle uv^+ \rangle$  Reynolds stress fields that are presented in Figures 7.26 and 7.27 are very similar to the results of Huang *et al.* (2011), who have also shown that positive and negative  $-\langle uv^+ \rangle$  Reynolds stress is found on the upwash and downwash sides respectively of the streamwise vortices generated during spanwise travelling-wave excitation. Huang *et al.* (2011) found that the negative  $-\langle uv^+ \rangle$  Reynolds stress on the downwash side of the streamwise vortices results in the overall reduction in turbulent skin-friction drag. Hence,

the  $-\langle uv^+ \rangle$  Reynolds stress fields presented in Figures 7.26 and 7.27 for the uni and bidirectional forcing is a very promising and encouraging result for the spanwise travelling waves implemented with DBD plasma.

## 7.2 Time- and Spanwise-averaged PIV Measurements

In this section, a time-average through 51 forcing periods of the spanwise travelling waves in the  $z$ - $y$  plane will be presented. The data were taken at a frequency of 750 Hz and the travelling wave forcing period,  $T$ , was 208 ms ( $T^+ = 82$ ) which amounts to a time-average over 2652 flow realisations. The time-averaged fields are spanwise-averaged over the wavelength of the travelling waves,  $z = 100$  mm ( $\lambda^+ = 500$ ), with a resolution of 1.5 mm ( $z^+ = 7.5$ ) and plotted as functions of wall-normal distance. This will allow the effects of each phase of the travelling wave to be linked to the time-averaged changes in the turbulent boundary-layer structure.

### Velocity and Streamwise Vorticity

The time-averaged velocity and streamwise vorticity profiles for both the unidirectional (left column) and bidirectional (right column) spanwise travelling waves are presented in Figure 7.28. The time-averaged streamwise vorticity is shown in Figure 7.28a). The unidirectional forcing shows negative streamwise vorticity over the entire travelling-wave wavelength up to a wall-normal distance of  $y^+ = 75$ . It was shown throughout the four phases of excitation that a streamwise vortex was formed during unidirectional forcing which travelled in the positive spanwise direction, Figure 7.16. On a time-average point of view, it is this streamwise vortex travelling in the spanwise direction that has created the negative vorticity across the spanwise direction of the turbulent boundary layer. The streamwise vorticity for the bidirectional travelling wave has some similarity. Negative and

positive streamwise vorticity can be seen across the spanwise direction up to a wall-normal distance of  $y^+ = 75$ . With bidirectional forcing, the DBD plasma actuators fire in two opposite directions each phase. This creates both co- and counter-rotating vortices inside the turbulent boundary layer throughout the four phases of excitation, Figure 7.17. Hence, the regions of negative vorticity seen in the time-averaged vorticity field of Figure 7.28a) are due to the co-rotating vortices which move in the positive spanwise direction and the positive vorticity is due to the counter-rotating vortices which form and move in the negative spanwise direction.

The time-averaged streamwise vorticity fields that have been presented in Figure 7.28a) have been spanwise-averaged and are plotted as a function of wall-normal distance in Figure 7.29a). As the unidirectional travelling wave generates negative streamwise vorticity only, larger amounts of negative streamwise vorticity can be seen when compared with the bidirectional forcing excitation. With the unidirectional forcing above  $y^+ = 75$  there appears to be little amounts of streamwise vorticity in the boundary layer. With bidirectional forcing, both positive and negative streamwise vorticity can be seen as a function of wall-normal distance. The first two data points (within 3 mm of the wall) are on average positive streamwise vorticity, which change to negative streamwise vorticity at greater wall-normal distances until a peak of negative streamwise vorticity at  $y^+ = 40$ . Above the locations of the streamwise vortex cores ( $y^+ = 50$ ) the streamwise vorticity changes sign and becomes positive. This is caused by the ejected counter-rotating vortices away from the wall by the interactions with the co-rotating vortices, Figure 7.15.

The time-averaged streamwise velocity for both the uni and bidirectional travelling waves can be seen in Figure 7.28b). There is a reduction in streamwise velocity across the spanwise direction of the turbulent boundary layer due to the streamwise vortices of each phase of forcing entraining low-speed streamwise velocity from the near-wall region into and around the streamwise vortex cores. A

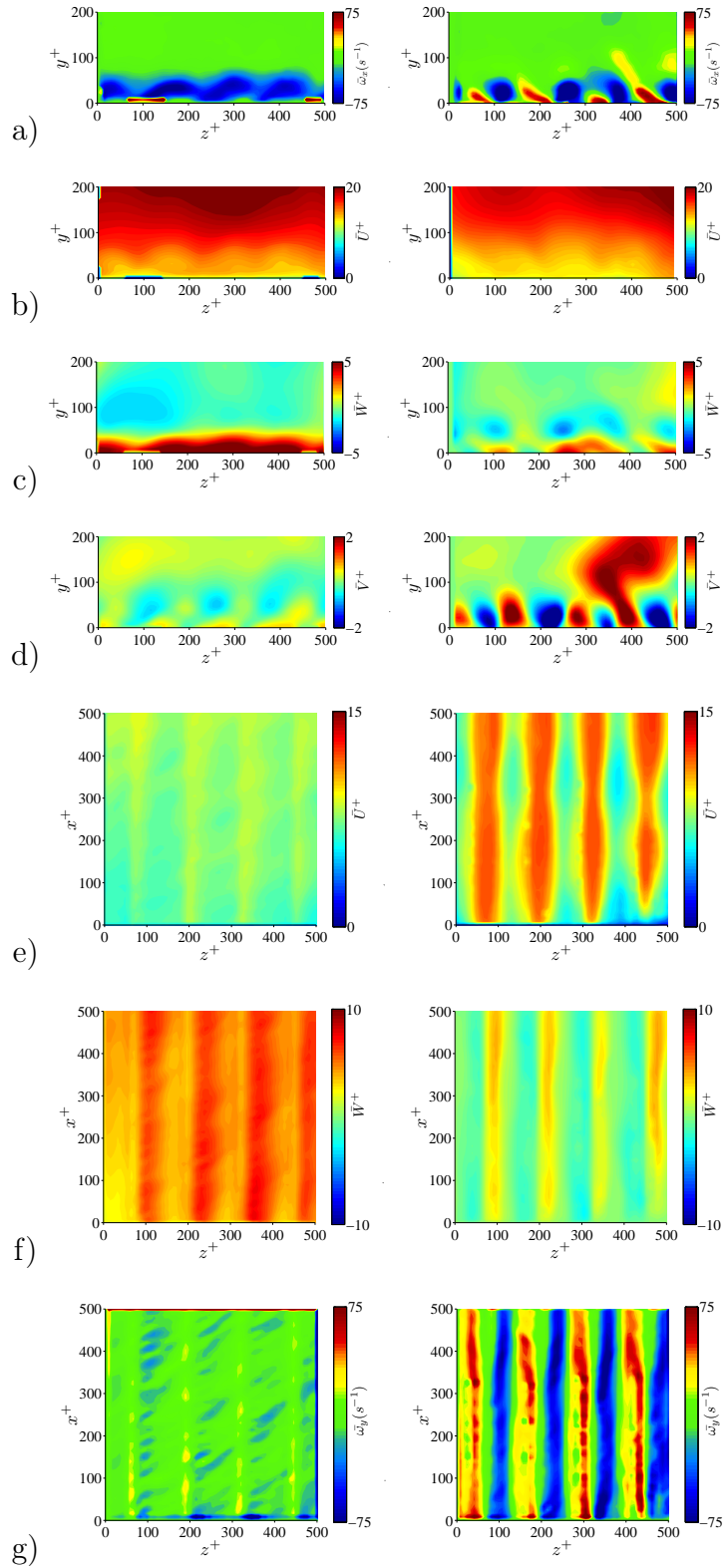


Figure 7.28: A comparison of time-averaged data in the  $z$ - $y$  and  $x$ - $z$  planes with unidirectional forcing (left column) and bidirectional forcing (right column) in a turbulent boundary layer showing a) streamwise vorticity ( $z$ - $y$  plane), b) streamwise velocity ( $z$ - $y$  plane), c) spanwise velocity ( $z$ - $y$  plane), d) wall-normal velocity ( $z$ - $y$  plane), e) streamwise velocity ( $x$ - $z$  plane), f) spanwise velocity ( $x$ - $z$  plane) and g) wall-normal vorticity ( $x$ - $z$  plane).  $\lambda^+ = 500$ ,  $T^+ = 82$ .

spanwise-average of these data are presented in Figure 7.29b). The data for the uni and bidirectional forcing is plotted against canonical data, where it is clear that there is a reduction in streamwise velocity for both forcing configurations. The velocity reduction is on the order of 15% and spans from  $20 < y^+ < 125$ . This is a similar amount of streamwise velocity reduction over the same region of the boundary layer as found with hot-wire anemometry, Chapter 6. Hence, the streamwise vortices generated with both the uni and bidirectional spanwise travelling waves cause the velocity reduction seen in the logarithmic region of the turbulent boundary layer.

The time-averaged spanwise velocity is presented in Figure 7.28c). With unidirectional forcing (left column) there is a single region of positive spanwise velocity spread across the spanwise direction of the boundary layer and encapsulated within the first 50 wall units ( $y^+ = 50$ ). With bidirectional forcing (right column) the positive spanwise velocity is of lower magnitude and has regions of negative spanwise velocity for  $y^+ < 50$  as the bidirectional forcing actuates plasma in two opposite directions per phase. A spanwise-average across both the time-averaged spanwise velocity fields is shown in Figure 7.29c), where it can be seen that both uni and bidirectional forcing creates a positive spanwise velocity up to  $y^+ = 50$ . The magnitude of the spanwise velocity for unidirectional forcing is larger as was shown with the phase-averaged spanwise velocity profiles taken in the  $x$ - $z$  plane at  $y^+ = 5$ , Figures 7.12 and 7.13. Above the streamwise vortex core,  $y^+ > 50$ , the spanwise velocity is negative for both forcing configurations and is on the same order,  $\langle \bar{W}^+ \rangle = -1$ . This negative spanwise velocity is due to the reverse flow caused by the streamwise vortices that are travelling in the positive spanwise direction, Figures 7.20 and 7.21.

The time-averaged wall-normal velocity for both forcing configurations is presented in Figure 7.28d). Regions of positive and negative wall-normal velocity can be seen throughout both forcing configurations due to the upwash and downwash of the streamwise vortices and the entrainment associated with the plasma

actuators. This was seen through the development of each forcing configuration through the four phases of excitation, Figures 7.18 and 7.19. The locations of downwash (negative wall-normal velocity) coincide with the regions of the high-speed streamwise velocity which are presented in Figure 7.28d) of the streamwise velocity in the  $x$ - $z$  plane. The areas of upwash and downwash for the bidirectional travelling wave are of greater magnitude when compared with unidirectional forcing. Likewise, the areas of high-speed streamwise velocity in the  $x$ - $z$  plane spread over a larger spanwise distance and are larger in magnitude than the unidirectional case. A spanwise-average over the wall-normal velocity data are shown in Figure 7.29d). There is very little change in wall-normal velocity in a spanwise-average sense with either forcing configuration. This is due to the regions of positive and negative wall-normal velocity equaling each other over the wavelength of the spanwise travelling waves. It can be seen that the travelling wave data are on the order of the canonical wall-normal velocity data, 0.5 wall units (0.03 m/s). Compared with the spanwise velocity data, Figure 7.29c), the wall-normal velocity with both forcing configurations is small.

The time-averaged spanwise velocity in the  $x$ - $z$  plane of the boundary layer is shown in figure 7.28f). Bands of high-speed positive spanwise velocity can be seen with unidirectional forcing and bands of positive and negative spanwise velocity with bidirectional forcing. The bands of high-speed positive and negative spanwise velocity show the locations of the plasma actuators. The time-averaged wall-normal vorticity in the  $x$ - $z$  plane is shown in Figure 7.28g). For both forcing configurations, bands of positive and negative wall-normal vorticity can be found due to the bands of low- and high-speed streamwise velocity caused by the travelling waves in the near-wall region. The intensity of the wall-normal vorticity is larger for the bidirectional forcing configuration as the streamwise velocity entrained into the near-wall region is of larger magnitude.

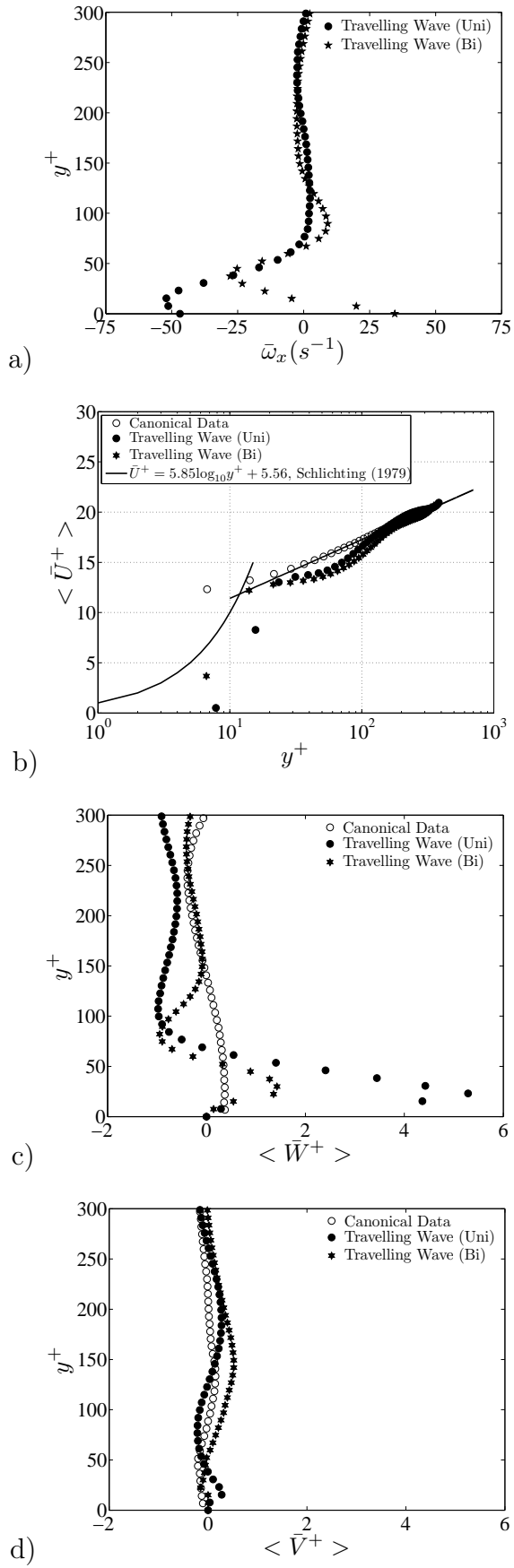


Figure 7.29: Spanwise-averaged data of Figure 7.28 showing a) streamwise vorticity, b) streamwise velocity, c) spanwise velocity and d) wall-normal velocity.

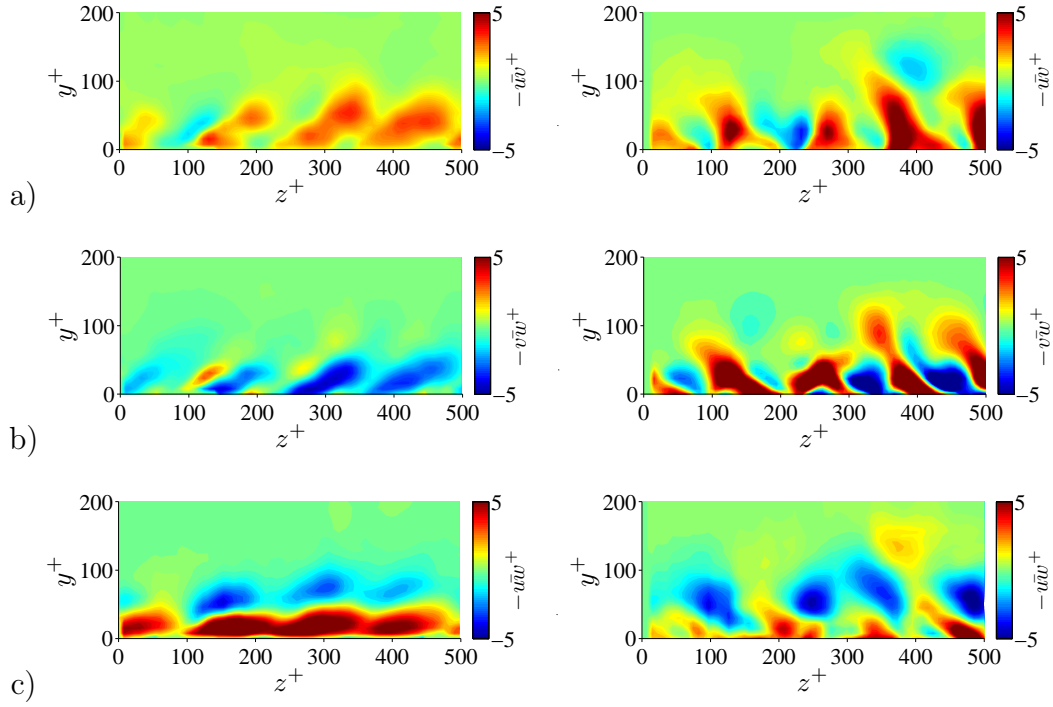


Figure 7.30: A comparison of time-averaged Reynolds stress in the  $z$ - $y$  plane with unidirectional forcing (left column) and bidirectional forcing (right column) in a turbulent boundary layer showing a)  $-\overline{uv}^+$ , b)  $-\overline{vw}^+$  and c)  $-\overline{uw}^+$ .  $\lambda^+ = 500$ ,  $T^+ = 82$ .

## Reynolds Stresses

The time-averaged  $-\overline{uv}^+$  Reynolds stress is given in Figure 7.30a). For both the uni and bidirectional travelling waves, positive and negative  $-\overline{uv}^+$  Reynolds stress can be seen throughout the spanwise direction in the  $z$ - $y$  plane of the turbulent boundary layer. The positive  $-\overline{uv}^+$  Reynolds stress is caused either by the upwash of low-speed streamwise velocity from the streamwise vortices or is due to the downwash of high-speed streamwise velocity from the outer regions of the boundary layer by the plasma actuators. The negative  $-\overline{uv}^+$  Reynolds stress is due to the low-speed streamwise velocity being pushed into the wall on the downwash side of the streamwise vortices. This has been discussed in §7.1 and has been shown in Figures 7.26 and 7.27 for the uni and bidirectional travelling waves respectively. A spanwise-average of the time-averaged  $-\overline{uv}^+$  Reynolds stress is shown in Figure 7.31a). It can be seen that the  $-\langle \overline{uv}^+ \rangle$  Reynolds stress for the uni and bidirectional forcing both have peak values of  $-\langle \overline{uv}^+ \rangle = 1.25$  and are

both larger than the canonical case throughout the turbulent boundary layer. The canonical  $-\langle \overline{uv}^+ \rangle$  Reynolds stress data has non-physical point of inflection at  $y^+ = 100$ . This could be due to over-stimulation of the turbulent boundary layer caused by the turbulent trip (Erm and Joubert, 1991) or, it could be due to error associated with pixel locking (Christensen, 2004). Pixel locking can occur when the measured velocity causes particle displacements less than a pixel. This is often found when PIV data is being used to compute velocity fluctuations, which is necessary in the calculations of Reynolds stress. Pixel locking occurs when the sub-pixel estimator cannot accurately determine the sub-pixel displacements of the PIV seeding particles, causing the estimated displacements to be locked towards integer values. Westerweel (1997) showed that using a Gaussian sub-pixel estimator —over centroid or quadratic fits to the cross-correlation peaks— can significantly reduce the error associated with pixel locking. In addition, it should be ensured that the PIV images are not under-resolved (Westerweel, 1997; Christensen, 2004), by having  $\frac{d_r}{d_p} > 2$ . Here,  $d_r$  is the diameter of the PIV particles used to seed the flow and  $d_p$  is the diameter of a pixel. By ensuring that the PIV seeding particles fill more than a single pixel of the CCD camera, allows the sub-pixel estimator to locate the cross-correlation peak inside each interrogation area more accurately, reducing error associated with pixel locking. For the PIV used in this thesis, it was ensured that  $\frac{d_r}{d_p} > 2$  and that a Gaussian sub-pixel estimator was used in all data analysis. In Figure 7.31b) and c), non-zero  $-\langle \overline{vw}^+ \rangle$  Reynolds stress and  $-\langle \overline{uw}^+ \rangle$  Reynolds stress can be seen in the canonical data. It is possible that this could be due to error associated with pixel locking (Christensen, 2004). The error will double when computing products of velocity fluctuation, which is necessary for calculations of Reynolds stress. Moreover, perhaps more error could be associated with the  $-\langle \overline{uw}^+ \rangle$  Reynolds stress calculation. This is due to the  $u$ -component of velocity being deduced from solving four displacement equations simultaneously (Lee, 2008), which use the  $V$ - and  $W$ - components of velocity, which both may contain errors

due to pixel locking.

The time-averaged  $-\overline{vw}^+$  Reynolds stress is presented in Figure 7.30b) for the uni and bidirectional travelling waves. The  $-\overline{vw}^+$  Reynolds stress fields appear different for the two forcing configurations. For the unidirectional forcing there is mainly negative  $-\overline{vw}^+$  Reynolds stress which is created when high-speed spanwise velocity is being ejected away from the wall by the upwash of the streamwise vortices that are travelling in the positive spanwise direction. Regions of positive  $-\overline{vw}^+$  Reynolds stress can be seen to the left of the negative  $-\overline{vw}^+$  Reynolds stress regions. The positive  $-\overline{vw}^+$  Reynolds Stress for the unidirectional travelling wave is created due to two reasons. The first is due to the low-speed spanwise velocity that is ejected away from the wall above the streamwise vortex core. The second is due to high-speed spanwise velocity being pushed into the wall region by the entrainment of the plasma actuators behind (to the left of) the streamwise vortex. The distributions of the  $-\overline{vw}^+$  Reynolds stress for the unidirectional travelling waves through the four phases, (i) to (iv), has been shown in Figure 7.24. The contrast of the  $-\overline{vw}^+$  Reynolds stress between the uni and bidirectional travelling waves is more clearly demonstrated in the spanwise-averaged data presented in Figure 7.31b). In this figure it is clear that the unidirectional travelling wave creates on average negative  $-\langle \overline{vw}^+ \rangle$  Reynolds stress and the bidirectional travelling wave creates on average positive  $-\langle \overline{vw}^+ \rangle$  Reynolds stress. The distribution for the  $-\langle \overline{vw}^+ \rangle$  Reynolds stress appears quite symmetric about the origin for the two forcing configurations. With bidirectional forcing, Figure 7.30b), regions of negative  $-\overline{vw}^+$  Reynolds stress is created due to two reasons. As with unidirectional forcing, the high-speed spanwise velocity is being ejected away from the surface by the upwash of the streamwise vortices creating negative  $-\overline{vw}^+$  Reynolds stress. Also, high-speed spanwise fluid that is moving in the opposite direction to the travelling wave (as bidirectional forcing fires two actuators in opposite directions) is pushed into the wall by the entrainment of the plasma actuators, which is essentially causing modified sweep events in the span-

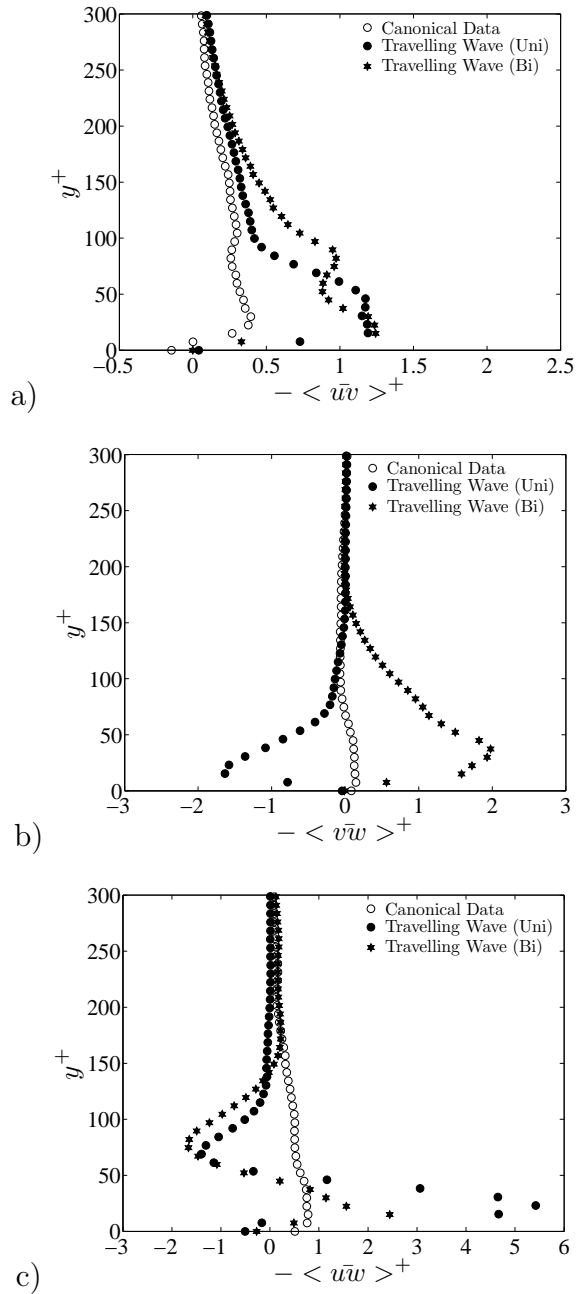


Figure 7.31: Spanwise-averaged data of Figure 7.28 showing a)  $- \langle \overline{u'w'} \rangle^+$  Reynolds stress, b)  $- \langle \overline{v'w'} \rangle^+$  Reynolds stress and c)  $- \langle \overline{u'w'} \rangle^+$  Reynolds stress.

wise direction. The positive  $-\overline{vw}^+$  Reynolds stress that is more dominant during bidirectional forcing is created for two reasons. Firstly, the high-speed spanwise fluid that is travelling in the same direction as the travelling wave is pushed into the wall by the entrainment of the plasma actuators, this was also found with unidirectional forcing. Secondly, the negative spanwise velocity is being ejected away from the wall. The ejection of the negative spanwise velocity is due to the interaction of the co- and counter-rotating vortices, where it has been seen that the co-rotating vortex lifts the counter-rotating vortex upwards away from the wall, Figure 7.15. The positive  $-\overline{vw}^+$  Reynolds stress is also created by the high-speed negative spanwise velocity on the upwash side of the counter-rotating vortices.

The time-averaged  $-\overline{vw}^+$  Reynolds stress is presented in Figure 7.30c) and the spanwise-averaged  $-\langle \overline{vw}^+ \rangle$  Reynolds stress is presented in Figure 7.31c) for the uni and bidirectional travelling waves. The spanwise-averaged  $-\langle \overline{vw}^+ \rangle$  Reynolds stress indicates that both forcing configurations generate positive  $-\langle \overline{vw}^+ \rangle$  Reynolds stress below the streamwise vortex core,  $y^+ < 50$  and negative  $-\langle \overline{vw}^+ \rangle$  Reynolds stress after the core. The positive  $-\langle \overline{vw}^+ \rangle$  Reynolds stress for the uni and bidirectional travelling waves is caused by the high-speed spanwise velocity pushing the low-speed streamwise velocity that was entrained from the streamwise vortices in to the spanwise direction. The negative  $-\langle \overline{vw}^+ \rangle$  Reynolds stress above the cores of the streamwise vortices,  $y^+ > 50$ , is the low-speed streamwise fluid that has been lifted away from the wall and is being transported in the negative spanwise direction due to the streamwise vortices. In addition, negative  $-\langle \overline{vw}^+ \rangle$  Reynolds stress is created with bidirectional forcing below the streamwise vortex core,  $y^+ < 50$ , due to low-speed streamwise velocity being transported in the spanwise direction by the counter-rotating vortices.

## 7.3 Chapter Summary

It has been shown that spanwise travelling waves with uni and bidirectional forcing configurations can be implemented with DBD plasma inside a turbulent boundary layer. They were generated with amplitudes of  $\langle W^+ \rangle = 22$  and 12 respectively, over a fixed wavelength of  $\lambda^+ = 500$ , with a time period of  $T^+ = 82$ , yielding a wave speed of  $c^+ = 6$ . It has been found that the unidirectional travelling wave creates streamwise vortices in sequence, which move as a single vortex, engulfing the neighbouring vortices from previous phases. The bidirectional travelling wave activates plasma in two opposite directions per phase, causing a complex interaction of co- and counter-rotating streamwise vortices that lift one another away from the wall to maintain the travelling-wave excitation. It has been seen that both forcing configurations generate a streamwise vortex that travels in the spanwise direction spreading the low-speed fluid within the viscous sublayer, creating wide ribbons of low-speed fluid. This result is in line with DNS studies (Du *et al.*, 2002; Huang *et al.*, 2011) and it is conjectured by Huang *et al.* (2011) that the co-rotating streamwise vortex has an important role in the reduction of Reynolds stress and the spreading of low-speed fluid in the near-wall region leading to a reduction in turbulent skin friction. High-speed fluid has been observed above the regions of plasma actuation. This is thought to be due to the downwash associated with the entrainment that occurs directly above the plasma actuators. It is thought that this could be leading to a local increase in skin friction. The velocity field within the viscous sublayer has been used to estimate the representation of the skin-friction signature on the wall. It has been shown that the skin-friction vectors are heavily twisted in the spanwise direction during the travelling-wave excitations, a feature found in other drag reducing flows (Zhao *et al.*, 2004).

# Chapter 8

## Conclusions and Future

## Recommendations

Discussions and summaries have been included in each chapter of the thesis. In this final chapter, the key findings from each chapter will be collated to provide an overall summary in §8.1. A list of novel outcomes from the thesis will be given in §8.2, some suggestions for future work will be given in §8.3 and the publications from the thesis will be given in §8.4.

### 8.1 Conclusions

A single, asymmetric DBD plasma actuator was applied in quiescent air in Chapter 4. It was found that on initiation of DBD plasma, a starting vortex is created, which appeared qualitatively similar to the junction vortex of Allen and Naitoh (2007). It has been shown that the movement of the starting vortex core scales with  $t^{0.71}$  in both the horizontal and vertical directions and the vortex core makes an angle of  $31^\circ$  to the wall for a range of voltage and frequencies applied to the actuator. The growth rate of  $t^{0.71}$  for the starting vortex has been related to the rate of change of momentum which was imparted by the plasma actuator into quiescent air. It has been found that the DBD plasma actuator couples momentum linearly with time to the flow, resulting in a constant force being applied

by the actuator. The applied force by the plasma actuator was estimated using a momentum balance of the PIV data and it was found to be on the order of 1 mN/m. The starting vortex velocity field has been predicted to scale with  $t^{-\frac{1}{3}}$  from the analysis set out by Cantwell (1986) and it has been shown that this prediction is in excellent agreement with the experimental data, with the velocity field of the starting vortex scaling in a self-similar fashion. The mechanism of the starting vortex formation is thought to be due to continuity, with laterally ejected fluid created by the plasma wall jet being replenished by entrainment above the plasma region, creating circulation. Secondary vorticity was generated to preserve the no-slip boundary condition and was found to be wrapped around the starting vortex as it moved along and away from the wall. It is considered that this could aid the movement of the starting vortex away from the wall.

In Chapter 5, 4-phase uni and bidirectional spanwise travelling waves have been successfully applied in quiescent air using DBD plasma. The development of the travelling waves through each of the 4-phases for both forcing configurations has been studied using time-resolved PIV. It has been observed that the starting vortices are important in the development of the spanwise travelling waves. Successful unidirectional forcing creates a single starting vortex that is transported along the spanwise direction. This is created when each phase moves fluid through a distance of  $\frac{1}{2}s$ , so that actuation entrains the fluid from the previous phase coalescing starting vortices into a single vortex. Phase lag of 30 ms ( $\frac{15}{104}T^+$ ) has been found as the travelling wave initiates, however, this diminishes to zero by the end of the four phases. Successful bidirectional forcing creates a complex system of vortices that interact to transport fluid in the spanwise direction. This requires the movement of fluid through a distance  $\frac{1}{2}s$  per phase. A phase lag of 30 ms ( $\frac{15}{104}T^+$ ) has been observed throughout each phase with this forcing configuration. Both the uni and bidirectional spanwise travelling wave forcing configurations have shown the ability to move fluid in the spanwise direction over a wavelength of 100 mm. Hence, both forcing configuration have been

shown to be equally as effective in quiescent air. If the strength of the plasma forcing, duration of actuation, or a combination of both are too low, fluid cannot be transported in the spanwise direction as effectively.

The spanwise travelling waves have been studied with hot- and cold-wire anemometry in Chapter 6. It has been found that on application of the spanwise travelling waves, the structure of the turbulent boundary layer can be changed up to  $y^+ = 200$ . The unidirectional travelling waves created a streamwise velocity reduction of 10% between  $25 < y^+ < 100$  and the bidirectional travelling waves created a streamwise velocity reduction of 20% between  $25 < y^+ < 200$ . With both forcing configurations, an increase of streamwise velocity has been measured in the near-wall region of the boundary layer ( $y^+ < 10$ ), which is consistent with an increase in skin-friction drag. The turbulence intensity was increased over the majority of the boundary layer, except for unidirectional forcing where a reduction was observed between  $10 < y^+ < 30$ , which is again, consistent with an increase in skin-friction drag. Peaks in turbulence intensity were located at  $y^+ = 5$  and  $y^+ = 60$  for both forcing configurations. A thermal boundary layer was generated on application of DBD plasma, which ruled out estimates of skin friction from estimates of the sublayer mean velocity gradient. Maximum temperature changes of  $1.9^\circ\text{C}$  and  $3.75^\circ\text{C}$  above ambient temperature at  $y^+ = 8$  were measured and maximum temperature fluctuations of  $0.6^\circ\text{C}$  and  $1.2^\circ\text{C}$  at  $y^+ = 50$  were measured with uni and bidirectional forcing respectively. Hence, low-speed streamwise velocity, which can be up to  $3.75^\circ\text{C}$  larger than ambient temperature, is being spread in and around the streamwise vortices, leading to maximum temperature fluctuations at the streamwise vortex cores.

In chapter 7, 2D and stereoscopic PIV has been used to look at the structure of the turbulent boundary throughout the four phases of the travelling wave. They travelling waves were generated with amplitudes of  $W^+ = 22$  and  $12$  respectively over a fixed wavelength of  $\lambda^+ = 500$  with a time period of  $T^+ = 82$ , yielding a wave speed of  $c^+ = 6$ . It has been found that the unidirectional travelling wave

creates streamwise vortices in sequence, which move as a single vortex engulfing the neighbouring vortices from previous phases. The bidirectional travelling wave activates plasma in two opposite directions per phase, causing a complex interaction of co- and counter-rotating streamwise vortices that lift one another away from the wall to maintain the travelling-wave excitation. It has been seen that both forcing configurations generate a streamwise vortex that travels in the spanwise direction spreading the low-speed fluid within the viscous sublayer, creating wide ribbons of low-speed fluid. Alongside the spreading of low-speed sublayer streaks, the streamwise vortex lifts low-speed fluid from the near-wall region outwards into the outer boundary layer due to vortex induction. The low-speed streamwise velocity around the vortex, leads to low-speed streamwise velocity being pushed into the wall (a modified wallward motion) which is similar to the latest findings of Huang *et al.* (2011). These results are in line with DNS studies (Du *et al.*, 2002; Huang *et al.*, 2011) and it is conjectured by Huang *et al.* (2011) that the streamwise vortex has an important role in the reduction of Reynolds stress and the spreading of low-speed fluid in the near-wall region, leading to a reduction in turbulent skin friction. High-speed fluid has been observed above the regions of plasma actuation. This is thought to be due to the downwash associated with the entrainment that occurs directly above the plasma actuators. It is thought that this could be leading to a local increase in skin friction. The velocity field within the viscous sublayer has been used to estimate the representation of the skin-friction signature on the wall. It has been shown that the skin-friction vectors are heavily twisted in the spanwise direction during the travelling-wave excitations, a feature found in other drag reducing flows (Zhao *et al.*, 2004).

## 8.2 Novel Outcomes

1. The starting vortex produced on initiation of DBD plasma exhibits self-similar scaling, with the vortex core scaling with  $t^{0.71}$  in both the horizontal

and vertical directions.

2. The velocity field of the starting vortex scales in a self-similar fashion, scaling with  $t^{-\frac{1}{3}}$ , which is in excellent agreement with analytical predictions formulated from the Euler equations.
3. The starting vortex travels with an angle of  $31^\circ$  to the wall.
4. An asymmetric DBD plasma actuator couples momentum linearly —with constant force— to the surrounding flow.
5. Successful spanwise travelling waves with two different forcing configurations —uni and bidirectional forcing— have been created in quiescent air with DBD plasma.
6. Uni and bidirectional spanwise travelling waves have been found to be equally effective at transporting fluid in quiescent air.
7. When applied to the turbulent boundary layer, the spanwise travelling waves have significantly altered the near-wall structure of the turbulent boundary layer. The streamwise vortices on initiation of DBD plasma have creating wide ribbons of low-speed streamwise velocity, which is in line with previous numerical simulations and experiments of spanwise travelling waves created by Lorentz forcing.
8. The structure of the turbulent boundary layer can be modified up to  $y^+ = 200$  with spanwise travelling-wave excitation.
9. Successful unidirectional forcing creates streamwise vortices in sequence, which engulf neighbouring vortices into a single streamwise vortex, which travels in the spanwise direction, effectively spreading the sublayer streaks.
10. Successful bidirectional forcing generates a complex system of interacting co- and counter-rotating vortices that lift one another away from the wall

to maintain the spanwise travelling wave excitation. Similar to unidirectional forcing, a single streamwise vortex travels in the spanwise direction, effectively spreading the sublayer streaks.

### 8.3 Future Recommendations

Throughout this thesis, 4-phase spanwise travelling waves have been created using DBD plasma upon which a good set of experimental data have been obtained to help understand the drag reduction mechanism. It has been shown that there is an increase in streamwise velocity in the near-wall region due to downwash associated with the entrainment of the plasma actuators. In addition, large increases in turbulence intensity have been measured throughout the boundary layer. However, it has been shown that the spanwise travelling waves have had positive effects on the near-wall region of the turbulent boundary layer, creating wide ribbons of low-speed streamwise velocity within the viscous sublayer, which is in line with the latest DNS results, obtaining over 30% reduction in turbulent skin-friction drag with the spanwise travelling-wave technique. Hence, there is great promise that the spanwise travelling waves implemented with DBD plasma could be refined to improve the interactions with the turbulence structures.

It is recommended that the number of phases of the travelling wave be increased. For example, with an 8-phase spanwise travelling wave there would be double the amount of actuators in comparison with the 4-phase spanwise travelling wave. This would mean that the distance that the fluid needs to move to pass from actuator to actuator each phase of forcing is smaller. In other words, the applied voltage to each actuator is lower and the duration of each actuation period is reduced. This in turn would create a starting vortex that is weaker which is expected to create less turbulence intensity in the boundary layer compared to the starting vortex of the 4-phase travelling wave. In addition, the weaker plasma forcing and reduced plasma duration would yield less downwash associated with

the entrainment of the plasma actuators. These changes should be possible whilst still maintaining the amalgamation of the low-speed streaks in the near-wall region into wide ribbons of low-speed fluid. It should also be possible to increase the phases further, for example 16 phases. The limit to the number of phases would be the physical distance that must be kept between adjacent electrodes before the plasma would break down into an arc. This is typically 3 mm for the applied voltages and frequencies used in this study. It should also be noted that by increasing the number of phases, the spanwise travelling-wave motion will become more continuous. This is not to say that the spanwise travelling wave with DBD plasma would create a continuous forcing profile as seen in the DNS studies, but it will begin to resemble a more sinusoidal-like wave pattern when applied to the boundary layer.

Dielectric heating could be responsible for the additional thermal errors on the hot-wire measurements of Chapter 6. Dielectric heating could be reduced by careful choice of dielectric materials. It is recommended that Kapton, Cirlex and Teflon are tried over Mylar. In addition, operating the DBD plasma at lower AC frequency, around 1 kHz is recommended. This will further reduce dielectric heating.

A further recommendation would be to try LDA (Laser-Doppler Anemometry) as a point measurement technique rather than hot-wire anemometry. This is because LDA is an optical measurement technique and it will not suffer from the drawbacks of heat flux generated by the plasma. However, it should be noted that sampling times required in the viscous sublayer are expected to be very long, a drawback when compared with hot-wire anemometry.

Throughout this study, the near-wall gradient technique could not be used to establish a local measurement of skin friction with and without spanwise travelling-wave control, due to the possible residual heating effects of the hot wire in the near-wall region. Therefore, it would be desirable and recommended that a direct measurement of skin-friction drag be used, such as a Fibre-Bragg

grating system, to quantify the changes in global skin-friction drag on application of spanwise travelling waves with DBD plasma.

The latest DNS results of Quadrio *et al.* (2009) and Viotti *et al.* (2009) show great application for surface based techniques such as DBD plasma. It is therefore recommended that streamwise travelling waves and standing waves be tested with DBD plasma.

## 8.4 Publications

### Journal Publications

1. CHOI, K.-S., JUKES, T.N. and WHALLEY, R. (2011). Turbulent boundary-layer control with plasma actuators. *Philosophical Transactions of the Royal Society A*, 369, 1443-1458.
2. WHALLEY, R. and CHOI, K.-S. (2010). Starting, traveling and colliding vortices: Dielectric-barrier-discharge plasma in quiescent air. *Physics of Fluids*, 22, 901105.

Three further journal publications are expected from the thesis. A journal paper will be written documenting the results of the starting vortex, Chapter 4 and a further two journal papers will be written documenting the turbulent boundary-layer control with spanwise travelling waves, Chapters 6 and 7.

### Conference Papers

1. WHALLEY, R. and CHOI, K.-S. (2011). Turbulent boundary-layer control with spanwise travelling waves. In: *13<sup>th</sup> European Turbulence Conference, 12<sup>th</sup> - 15<sup>th</sup> September, Warsaw, Poland*.
2. WHALLEY, R. and CHOI, K.-S. (2010). Changes in turbulent boundary-layer structure by spanwise travelling waves created by DBD plasma actu-

- ators. In: *Proceedings of the European Drag Reduction and Flow Control Meeting, 2<sup>nd</sup> - 4<sup>th</sup> September, Kyiv, Ukraine.*
3. WHALLEY, R. and CHOI, K.-S. (2010). Turbulent boundary-layer control by DBD plasma: A spanwise travelling wave. In: *5<sup>th</sup> AIAA Flow Control Conference, 28<sup>th</sup> - 1<sup>st</sup> July, Illinois, Chicago.*
  4. WHALLEY, R. and CHOI, K.-S. (2010). Turbulent boundary-layer control by spanwise travelling waves created by DBD plasma. In: *Proceedings of the 9<sup>th</sup> International Workshop on Magneto-Plasma Aerodynamics, 13<sup>th</sup> - 15<sup>th</sup> April, Moscow, Russia.*
  5. WHALLEY, R.D, JUKES, T.N. and CHOI, K.-S. (2008). On the development of a starting vortex by Dielectric Barrier Discharge plasma. In: *Proceedings of the 5<sup>th</sup> International Conference on Flow Dynamics, 17<sup>th</sup> - 19<sup>th</sup> November, Sendai, Japan.*
  6. WHALLEY, R.D, JUKES, T.N. and CHOI, K.-S. (2008). On the development of a starting vortex in still air at the initiation of Dielectric Barrier Discharge plasma. In: *Proceedings of the European Drag Reduction and Flow Control Meeting, 8<sup>th</sup> - 11<sup>th</sup> September, Ostritz, Germany.*

## Invited Lectures

1. WHALLEY, R. and CHOI, K.-S. (2010). Turbulent boundary-layer control with spanwise travelling waves. *Beijing University of Aeronautics and Astronautics, 20<sup>th</sup> October, Beijing, China.*

# Bibliography

- ACARE (2004). Strategic Research Agenda Volume 1 Advisory Council for Aeronautics Research in Europe October 2004.
- ADRIAN, R. J. (2007). Hairpin vortex organization in wall turbulence. *Physics of Fluids*, 19, 041301.
- ADRIAN, R. J., MEINHART, C. D. and TOMKINS, C. D. (2000). Vortex organization in the outer region of the turbulent boundary layer. *Journal of Fluid Mechanics*, 422, 1–54.
- ALLEN, J. J. and CHONG, M. S. (2000). Vortex formation in front of a piston moving through a cylinder. *Journal of Fluid Mechanics*, 416, 1–28.
- ALLEN, J. J. and NAITOH, T. (2007). Scaling and instability of a junction vortex. *Journal of Fluid Mechanics*, 574, 1–23.
- ANDREOPOULOS, J., DURST, F., ZARIC, Z. and JOVANOVIĆ, J. (1984). Influence of Reynolds number on characteristics of turbulent wall boundary layers. *Experiments in Fluids*, 2, 7–16.
- ANTONIA, R., ZHU, Y. and SOKOLOV, M. (1995). Effect of concentrated wall suction on a turbulent boundary layer. *Physics of Fluids*, 7, 2465–2474.
- ANTONIA, R. A. (1981). Conditional sampling in turbulence management. *Annual Review Fluid Mechanics*, 13, 131–156.

- BERNARD, P. S., THOMAS, J. M. and HANDLER, R. A. (1993). Vortex dynamics and the production of Reynolds stress. *Journal of Fluid Mechanics*, 253, 385–419.
- BLACKWELDER, R. F. and KAPLAN, R. E. (1976). On the wall structure of the turbulent boundary layer. *Journal of Fluid Mechanics*, 76, 89–112.
- BOEUF, J. P., LAGMICH, Y., CALLEGARI, T. and PITCHFORD, L. C. (2007a). EHD force in dielectric barrier discharges parametric study and influence of negative ions. In: *45th AIAA Aerospace Sciences Meeting and Exhibit*, AIAA, 2007-183.
- BOEUF, J. P., LAGMICH, Y., CALLEGARI, T. and PITCHFORD, L. C. (2007b). Electrohydrodynamic force in dielectric barrier discharge plasma actuators. *Journal of Physics D: Applied Physics*, 40, 652–662.
- BOEUF, J. P. and PITCHFORD, L. C. (2005). Electrohydrodynamic force and aerodynamic flow acceleration in surface dielectric barrier discharge. *Journal of Physics*, 97, 103307–103307–10.
- BRUUN, H. H. (1995). *Hot-wire Anemometry*. Oxford University Press.
- CANTWELL, B. J. (1981). Organized motion in turbulent flow. *Annual Review Fluid Mechanics*, 13, 457–515.
- CANTWELL, B. J. (1986). Viscous starting jets. *Journal of Fluid Mechanics*, 173, 159–189.
- CATTAFESTA III, L. and SHEPLAK, M. (2010). Actuators for active flow control. *Annual Review Fluid Mechanics*, 43, 247–272.
- CHERNYSHENKO, S. I. and BAIG, M. F. (2005). The mechanism of streak formation in near-wall turbulence. *Journal of Fluid Mechanics*, 544, 99–131.
- CHOI, K.-S. (1989). Near-wall structure of a turbulent boundary layer with riblets. *Journal of Fluid Mechanics*, 208, 417–458.

- CHOI, K.-S. (2002). Near-wall structure of the turbulent boundary layer with spanwise-wall oscillation. *Physics of Fluids*, 14, 2530–2542.
- CHOI, K.-S. and CLAYTON, B. R. (2001). The mechanism of turbulent drag reduction with wall oscillation. *International Journal of Heat and Fluid Flow*, 22, 1 – 9.
- CHOI, K.-S., DEBISSCHOP, J.-R. and CLAYTON, B. R. (1998). Turbulent boundary-layer control by means of spanwise wall-oscillation. *AIAA Journal*, 36, 1157–1163.
- CHOI, K.-S., JUKES, T. N. and WHALLEY, R. (2011). Turbulent boundary-layer control with plasma actuators. *Philosophical Transactions of the Royal Society A*, 369, 1443–1458.
- CHOI, K.-S., YANG, X., CLAYTON, B. R., GLOVER, E., ATLAR, M., SEMENOV, B. N. and KULIK, V. (1997). Turbulent drag reduction using compliant surfaces. *Proceedings of the Royal Society A*, 453, 2229–2240.
- CHRISTENSEN, K. T. (2004). The influence of peak-locking errors on turbulence statistics computed from PIV ensembles. *Experiments in Fluids*, 36, 484–497.
- CLAUSER, F. H. (1954). Turbulent boundary layers in adverse pressure gradients. *Journal of Aeronautical Sciences*, 21, 91–108.
- CORINO, E. R. and BRODKEY, R. S. (1969). A visual investigation of the wall region in turbulent flow. *Journal of Fluid Mechanics*, 37, 1–30.
- CORKE, T., POST, M. and ORLOV, D. M. (2007). SDBD plasma enhanced aerodynamics: concepts, optimization and applications. *Progress in Aerospace Science*, 43, 193–217.
- CORKE, T. C., ENLOE, C. L. and WILKINSON, S. P. (2010). Dielectric barrier discharge plasma actuators for flow control. *Annual Review Fluid Mechanics*, 42, 505–529.

- CORKE, T. C. and POST, M. L. (2005). Overview of plasma flow control: Concepts, optimization, and applications. In: *43rd AIAA Aerospace Sciences Meeting and Exhibit*, AIAA.
- DI CICCA, G. M. and IUSO, G. (2006). On large-scale vortical structures produced by a yawed synthetic jet - turbulent boundary layer interaction. In: *3rd AIAA Flow Control Conference*, AIAA.
- DU, Y. and KARNIADAKIS, G. E. (2000). Suppressing wall turbulence by means of a transverse travelling wave. *Science*, 288, 1230–1234.
- DU, Y., SYMEONIDIS, Y. and KARNIADAKIS, G. E. (2002). Drag reduction in wall-bounded turbulence via a transverse travelling wave. *Journal of Fluid Mechanics*, 457, 1–34.
- ENLOE, C. L., MCHARG, M. G. and MCCLAUGHLIN, T. E. (2008). Time-correlated force production measurements of the dielectric barrier discharge plasma aerodynamic actuator. *Journal of Applied Physics*, 103, 073302–10.
- ENLOE, C. L., MCCLAUGHLIN, T. E., VANDYKEN, R. D., KACHNER, K. D., JUMPER, E. J. and CORKE, T. (2004a). Mechanisms and responses of a single dielectric barrier plasma actuator: Plasma morphology. *AIAA Journal*, 42, 589–594.
- ENLOE, C. L., MCCLAUGHLIN, T. E., VANDYKEN, R. D., KACHNER, K. D., JUMPER, E. J., CORKE, T., POST, M. and HADDED, O. (2004b). Mechanisms and responses of a single dielectric barrier plasma actuator: Geometrics effects. *AIAA Journal*, 42, 595–604.
- ERM, L. P. and JOUBERT, P. N. (1991). Low-reynolds-number turbulent boundary layers. *Journal of Fluid Mechanics*, 230, 1–44.
- FALCO, R. (1977). Coherent motions in the outer region of turbulent boundary layers. *Physics of Fluids*, 20, S124–S132.

- FONT, G. and MORGAN, W. (2005). Plasma discharges in atmospheric pressure oxygen for boundary layer separation. In: *35th AIAA Fluid Dynamics Conference and Exhibition*, 2005-4632.
- FORTE, M., JOLIBOIS, J., MOREAU, E., TOUCHARD, G. and CAZALENS, M. (2006). Optimization of a dielectric barrier discharge actuator by stationary and instationary measurements of the induced flow velocity, application to airflow control. In: *3rd AIAA Flow Control Conference, San Francisco*, AIAA, 2006-2863.
- GIBALOV, V. I. and PIETSCH, G. J. (2000). The development of dielectric barrier discharges in gas gaps and on surfaces. *Journal of Physics D: Applied Physics*, 33, 2618–2636.
- GRASS, A. J. (1971). Structural features of turbulent flow over smooth and rough boundaries. *Journal of Fluid Mechanics*, 50, 233–255.
- GRUNDMANN, S. and TROPEA, C. (2007). Experimental transition delay using glow discharge plasma actuators. *Experiments in Fluids*, 42, 653–657.
- GRUNDMANN, S. and TROPEA, C. (2008). Active cancelation of artificially introduced Tollmein-Schlicting waves using plasma actuators. *Experiments in Fluids*, 44, 795–806.
- GRUNDMANN, S. and TROPEA, C. (2009). Experimental damping of boundary-layer oscillations using DBD plasma actuators. *International Journal of Heat and Fluid Flow*, 30, 394–402.
- GAD-EL HAK, M. and BANDYOPADHYAY, P. (1994). Reynolds number effects in wall-bounded turbulent flows. *Applied Mechanics Reviews*, 47, 307–365.
- HAMBLETON, W. T., HUTCHINS, N. and MARUSIC, I. (2006). Simultaneous orthogonal-plane particle image velocimetry measurements in a turbulent boundary layer. *Journal of Fluid Mechanics*, 560, 53–64.

- HE, C. and CORKE, T. C. (2009). Plasma flaps and slats: An application of weakly-ionized plasma actuators. *Journal of Aircraft*, 46, 864.
- HEAD, M. R. and BANDYOPADHYAY, P. (1981). New aspects of turbulent boundary-layer structure. *Journal of Fluid Mechanics*, 107, 297–338.
- HUANG, L. P., BAOCHUN, F. and DONG, G. (2010). Turbulent drag reduction via a transverse wave traveling along streamwise direction induced by Lorentz force. *Physics of Fluids*, 22, 015103.
- HUANG, L. P., CHOI, K.-S. and BAOCHUN, F. (2011). Near-wall turbulence structures subject to spanwise travelling wave leading to a formation of low-speed ribbons. *To be Submitted*.
- HUANG, X. and ZHANG, X. (2008). Streamwise and spanwise plasma actuators for flow-induced cavity noise control. *Physics of Fluids*, 037101, 037101.
- HULTMARK, M. and SMITS, A. J. (2010). Temperature corrections for constant temperature and constant current hot-wire anemometers. *Measurement Science and Technology*, 21, 105404.
- HUTCHINS, N. and CHOI, K.-S. (2002). Accurate measurements of local skin friction coefficient using hot-wire anemometry. *Progress in Aerospace Science*, 38, 421–446.
- HUTCHINS, N., HAMBLETON, W. T. and MARUSIC, I. (2005). Inclined cross-stream stereo particle image velocimetry measurements in turbulent boundary layers. *Journal of Fluid Mechanics*, 541, 21–54.
- ITOH, M., TAMANO, S., YOKOTA, K. and TANIGICHI, S. (2006). Drag reduction in a turbulent boundary layer on a flexible sheet undergoing a spanwise travelling wave motion. *Journal of Turbulence*, 7, 1–17.
- JAYARAMAN, B., CHO, Y.-C. and SHYY, W. (2008). Modeling of dielectric

- barrier discharge plasma actuator. *Journal of Applied Physics*, 103, 0503304–15.
- JIMÉNEZ, J. and PINELLI, A. (1999). The autonomous cycle of near-wall turbulence. *Journal of Fluid Mechanics*, 389, 335–359.
- JOHANSSON, A. V. and ALFREDSSON, P. H. (1982). On the structure of turbulent channel flow. *Journal of Fluid Mechanics*, 122, 295–314.
- JOHANSSON, A. V., ALFREDSSON, P. H. and ECKELMANN, H. (1987). On the evolution of shear-layer structures in near-wall turbulence. In: *Advances in Turbulence, Proceedings of the first European Turbulence Conference, Lyon*.
- JUKES, T. N. (2007). *Turbulent Drag Reduction using Surface Plasma*. Ph.D. thesis, University of Nottingham.
- JUKES, T. N. and CHOI, K.-S. (2009a). Control of unsteady flow separation over a circular cylinder using dielectric-barrier-discharge surface plasma. *Physics of Fluids*, 21, 094106.
- JUKES, T. N. and CHOI, K.-S. (2009b). Flow control around a circular cylinder using pulsed dielectric barrier discharge surface plasma. *Physics of Fluids*, 21, 084103.
- JUKES, T. N., CHOI, K.-S., JOHNSON, G. A. and SCOTT, S. J. (2006a). Characterisation of surface plasma-induced wall flows through velocity and temperature measurement. *AIAA Journal*, 44, 764.
- JUKES, T. N., CHOI, K.-S., JOHNSON, G. A. and SCOTT, S. J. (2006b). Turbulent drag reduction by surface plasma through spanwise flow oscillation. In: *3rd AIAA Flow Control Conference*, AIAA.
- JUKES, T. N., CHOI, K.-S., SEGAWA, T. and YOSHIDA, H. (2008). Jet flow induced by a surface plasma actuator. In: *Proceedings of the Institution of*

- Mechanical Engineers Part I: Journal of Systems and Control Engineering*, volume 222, volume 222, 347–356.
- JUNG, W., MANGIACACCHI, N. and AKHAVAN, R. (1992). Suppression of turbulence in wall-bounded flows by high frequency spanwise oscillation. *Physics of Fluids*, 4, 1605–1607.
- KARNIADAKIS, G. E. and CHOI, K.-S. (2003). Mechanisms on transverse motions in turbulent wall flows. *Annual Review Fluid Mechanics*, 35, 45–62.
- KIM, H. T., KLINE, S. J. and REYNOLDS, W. C. (1971). The production of turbulence near a smooth wall in a turbulent boundary layer. *Journal of Fluid Mechanics*, 50, 133–160.
- KIM, J. and HUSSAIN, F. (1993). Propagation velocity of perturbations in turbulent channel flow. *Physics of Fluids*, 5, 0899–8213.
- KIM, W., DO, H., MUNGAL, M. G. and CAPPELLI, M. A. (2007). On the role of oxygen in dielectric barrier discharge actuation of aerodynamic flows. *Applied Physics Letters*, 91, 181501–3.
- KLEBANOFF, P. S. (1954). *Characteristics of turbulence in a boundary layer with zero pressure gradients*. Technical Report TN 3178, NASA.
- KLINE, S. J., REYNOLDS, W. C., SCHRAUB, F. A. and RUNSTADLER, P. W. (1967). The structure of turbulent boundary layers. *Journal of Fluid Mechanics*, 30, 741–773.
- KRAMER, M. O. (1961). The dolphin’s secret. *Naval Engineers Journal*, 73, 103–107.
- KRAVCHENCKO, A. G., CHOI, H. and MOIN, P. (1993). On the relation of near-wall streamwise vortices to wall skin friction in turbulent boundary layers. *Physics of Fluids*, 5, 3307–3309. Brief Communications.

- KREITH, F. and BOHN, M. S. (1993). *Principles of Heat Transfer*. West Publishing Company, New York.
- KUNHARDT, E. (2000). Generation of large volume atmospheric pressure nonequilibrium plasmas. *IEEE Transactions on Plasma Science*, 28, 189–199.
- LANGMUIR, I. (1928). Oscillations in ionized gases. *Proceedings of the National Academy of Sciences*, 14, 627–637.
- LEE, T.-W. (2008). *Thermal and flow measurements*. CRC Press.
- LIKHANSKII, A. V., SHNEIDER, M. N., MACHERET, S. O. and MILES, R. B. (2008). Modeling of dielectric barrier discharge plasma actuator in air. *Journal of Applied Physics*, 103, 053305–13.
- LU, S. S. and WILLMARTH, W. W. (1973). Measurements of the structure of the Reynolds stress in a turbulent boundary layer. *Journal of Fluid Mechanics*, 60, 481–511.
- MCLAUGHLIN, T. E., MUNSKA, M. D., VAETH, J. P., DAUWALTER, T. E., GOODE, J. R. and SIEGEL, S. G. (2004). Plasma-based actuators for cylinder wake vortex control. In: *2nd AIAA Flow Control Conference*, AIAA.
- MERKLE, C. and DEUTSCH, S. (1989). Drag reduction in liquid boundary layers by gas injection. In: *Viscous drag Reduction in Boundary layers*, AIAA, 203–261.
- MOREAU, E. (2007). Airflow control by non-thermal plasma actuators. *Journal of Physics D: Applied Physics*, 40, 605.
- MOREAU, E., ROBERTO, S. and GUILLERMO, A. (2008). Electric wind produced by surface plasma actuators: a new dielectric barrier discharge based on a three-electrode geometry. *Journal of Physics D*, 41, 115204.

- MUNSKA, M. D. and MCLAUGHLIN, T. E. (2003). Circular cylinder flow control using surface plasma actuators. In: *43rd AIAA Aerospace Sciences Meeting and Exhibit*, AIAA.
- OFFEN, G. R. and KLINE, S. J. (1975). A proposed model of the bursting process in turbulent boundary layers. *Journal of Fluid Mechanics*, 70, 209–228.
- OKITA, Y., JUKES, T. N., CHOI, K.-S. and NAKUMURA, K. (2008). Flow reattachment over an airfoil using surface plasma actuator. In: *4th Flow Control conference*, AIAA, 2008-4203.
- ORLANDI, P. and JIMÉNEZ, J. (1993). On the generation of turbulent wall friction. *Physics of Fluids*, 6, 634–641.
- ORLOV, D. M. and CORKE, T. (2005). Numerical simulations of aerodynamic plasma actuator effects. In: *43rd AIAA Aerospace Sciences Meeting and Exhibit*, 2005-1083.
- ORLOV, D. M., CORKE, T. and PATEL, M. (2006). Electric circuit model for aerodynamic plasma actuator. In: *44th AIAA Aerospace Sciences Meeting and Exhibit*, 2006-1206.
- PANG, J. and CHOI, K.-S. (2004). Turbulent drag reduction by Lorentz force oscillation. *Physics of Fluids*, 16, 1071–6631.
- PANTON, R. L. (2001). Overview of the self-sustaining mechanisms of wall turbulence. *Progress in Aerospace Science*, 37, 341–383.
- PATEL, M. P., NG, T. T., VASUDEVAN, S., CORKE, T. C., POST, M. L., MCLAUGHLIN, T. E. and SUCHOMEL, C. F. (2008). Scaling effects of an aerodynamic plasma actuator. *Journal of Aircraft*, 45, 223–236.
- PORTER, C., MCLAUGHLIN, T., ENLOE, C. L., FONT, G., RONEY, J. and BAUGHN, J. (2007). Boundary layer control using a DBD plasma actuator. In: *45th AIAA Aerospace Scienced Meeting and Exhibit*, 2007-786.

- POST, M. L. (2004). *Plasma actuators for separation control on stationary and unstationary airfoils*. Ph.D. thesis, University of Notre Dame.
- POST, M. L. and CORKE, T. C. (2003). Separation control on high angle of attack airfoil using plasma actuators. *AIAA Journal*, 42, 2177–2184.
- QUADRIO, M., RICCO, P. and VIOTTI, C. (2009). Streamwise-travelling waves of spanwise wall velocity for turbulent drag reduction. *Journal of Fluid Mechanics*, 627, 161–178.
- RATHNASINGHAM, R. and BREUER, K. (2003). Active control of turbulent boundary layers. *Journal of Fluid Mechanics*, 495, 209–233.
- REYNOLDS, O. (1883). An experimental investigation of the circumstances which determine whether the motion of water shall be direct or sinous and the laws of resistance in pallel channels. *Philosophical Transactions of the Royal Society London*, 174, 51.
- ROBINSON, M. (1962). A history of the electric wind. *American Journal of Physics*, 30, 366–372.
- ROBINSON, S. K. (1991). Coherent motions in the turbulent boundary layer. *Annual Review of Fluid Mechanics*, 23, 601–639.
- ROTH, J. R. (1995). *Industrial Plasma Engineering. Vol 1: Principles*, volume 1. Institute of Physics Publishing.
- ROTH, J. R. (2003). Aerodynamic flow acceleration using paraelectric and peristaltic electrohydrodynamic (EHD) effects of a One Atmosphere Uniform Glow Discharge Plasma (OAUGDP). *Physics of Plasmas*, 10, 1070–664.
- ROTH, J. R. and SHERMAN, D. M. (1998). Boundary layer flow control with a One Atmospheric Uniform Glow Discharge Surface Plasma. In: *36th Aerospace sciences meeting and exhibit, January 12-15*, AIAA, AIAA 98-0328.

- SANTHANAKRISHNAN, A. and JACOB, J. D. (2006a). Flow control using plasma actuators and linear/annular plasma synthetic jet actuators. In: *3rd AIAA Flow Control Conference*, AIAA, 2006-3033.
- SANTHANAKRISHNAN, A. and JACOB, J. D. (2006b). On plasma synthetic jet actuators. In: *44th AIAA*, AIAA, 2006-0317.
- SAVILL, A. and MUMFORD, J. (1988). Manipulation of turbulent boundary layers by outer-layer devices: skin-friction and flow-visualization results. *Journal of Fluid Mechanics*, 191, 389–418.
- SCHLATTER, P. and ÖRLÜ, R. (2011). DNS of a turbulent zero-pressure gradient boundary layer. *Journal of Fluid Mechanics*. (to appear).
- SCHLATTER, P., ÖRLÜ, R., LI, Q., BRETHOUWER, G., FRANSSON, J. H. M., JOHANSSON, A. V., ALFREDSSON, P. H. and HENNINGSON, D. S. (2009). Turbulent boundary layers up to  $Re_\theta = 2500$  studied through simulation and experiment. *Physics of Fluids*, 5, 051702–4. Letters.
- SCHLICHTING, H. (1979). *Boundary-Layer Theory*. McGraw-Hill New York.
- SCHOPPA, W. and HUSSAIN, F. (2002). Coherent structure generation in near-wall turbulence. *Journal of Fluid Mechanics*, 453, 57–108.
- SEGAWA, T., H., Y., TAKEKAWA, S., JUKES, T. N. and CHOI, K.-S. (2008). Coaxial annular jet produced by DBD plasma actuator. *The Japan Society of Fluid Mechanics*, 27, 65–72.
- SMITH, C. R. and METZLER, S. P. (1983). The characteristics of low-speed streaks in the near-wall region of a turbulent boundary layer. *Journal of Fluid Mechanics*, 129, 27–54.
- SMITS, A. J. and LIM, T. T. (Editors) (2000). *Flow Visualisation Techniques and Examples*. Imperial College Press.

- TENNEKES, H. and LUMLEY, J. L. (1972). *A first course in turbulence*. The MIT Press.
- THEODORSEN, T. (1952). Mechanisms of turbulence. In: *Proceedings 2nd Midwestern Conference of Fluid Mechanics*.
- VIOTTI, C., QUADRIO, M. and LUCHINI, P. (2009). Streamwise oscillation of spanwise velocity at the wall of a channel for turbulent drag reduction. *Physics of Fluids*, 21, 115109.
- VIRK, P. (1975). Drag reduction fundamentals. *AIChE Journal*, 21, 625–656.
- WALLACE, J. M., ECKELMANN, H. and BRODKEY, R. S. (1972). The wall region in turbulent shear flow. *Journal of Fluid Mechanics*, 54, 39–48.
- WESTERWEEL, J. (1997). Fundamentals of digital particle image velocimetry. *Measurement Science and Technology*, 8, 1379–1392.
- WHALLEY, R. and CHOI, K.-S. (2010a). Starting, traveling and colliding vortices: Dielectric-barrier-discharge plasma in quiescent air. *Physics of Fluids*, 22, 091105.
- WHALLEY, R. and CHOI, K.-S. (2010b). Turbulent boundary layer control with DBD plasma: A spanwise travelling wave. In: *5th AIAA Flow Control Conference*, AIAA.
- WILKINSON, S. P. (2003). Investigation of an oscillating surface plasma for turbulent drag reduction. In: *41st AIAA Aerospace and Sciences Meeting and Exhibit*, 2003-1023.
- WILLMARTH, W. W. and LU, S. S. (1972). Structure of the Reynolds stress near the wall. *Journal of Fluid Mechanics*, 55, 65–92.
- XU, P. and CHOI, K.-S. (2006). Boundary layer-control for drag reduction by Lorentz forcing. In: *Proceedings of the IUTAM Symposium on Flow Control and MEMS*.

ZHAO, H., WU, J.-Z. and LUO, J.-S. (2004). Turbulent drag reduction by traveling wave of flexible wall. *Fluid Dynamics Research*, 34, 175.

ZHOU, J., ADRIAN, R. J., BALACHANDER, S. and KENDALL, T. (1999). Mechanisms for generating coherent packets of hairpin vortices in channel flow. *Journal of Fluid Mechanics*, 387, 353–396.